Durham University

Durham E-Theses

Methods for constructing 3D geological and geophysical models of flood basalt provinces

NELSON, CATHERINE,ELIZABETH

How to cite:

NELSON, CATHERINE,ELIZABETH (2010) *Methods for constructing 3D geological and geophysical models of flood basalt provinces*, Durham theses, Durham University. Available at Durham E-Theses Online: http://etheses.dur.ac.uk/488/

Use policy

The full-text may be used and/or reproduced, and given to third parties in any format or medium, without prior permission or charge, for personal research or study, educational, or not-for-profit purposes provided that:

- a full bibliographic reference is made to the original source
- a link is made to the metadata record in Durham E-Theses
- the full-text is not changed in any way

The full-text must not be sold in any format or medium without the formal permission of the copyright holders.

Please consult the full Durham E-Theses policy for further details.

Academic Support Office, The Palatine Centre, Durham University, Stockton Road, Durham, DH1 3LE
e-mail: e-theses.admin@durham.ac.uk Tel: +44 0191 334 6107
http://etheses.dur.ac.uk

METHODS FOR CONSTRUCTING 3D GEOLOGICAL AND GEOPHYSICAL MODELS OF FLOOD BASALT PROVINCES

Catherine E. Nelson

A thesis submitted for the degree of

Doctor of Philosophy

Department of Earth Sciences

Durham University

2010

METHODS FOR CONSTRUCTING 3D GEOLOGICAL AND GEOPHYSICAL MODELS OF FLOOD BASALT PROVINCES

Catherine E. Nelson

ABSTRACT

In this thesis, realistic 3D geological models of flood basalt provinces are constructed. These models are based on outcrop observations and remote sensing data from the North Atlantic Igneous Province, collected by a variety of methods including terrestrial laser scanning. Geophysical data are added to the models to make them suitable for generating synthetic seismic data.

Flood basalt provinces contain a number of different volcanic facies, distinguished by their outcrop appearance and physical properties. These include tabular-classic and compound-braided lava flows, intrusions and hyaloclastites. 3D models are constructed for tabular-classic lava flows based on satellite data from Iceland and laser scanning data from a variety of locations. Models for compound-braided lava flows are based on terrestrial laser scanning data and field observations from the Faroe Islands and the Isle of Skye.

An additional finding of this work is that volcanic facies can be differentiated in wireline log data from boreholes. Facies show characteristic velocity distributions which can be linked to onshore observations and used to understand volcanic facies in offshore boreholes. Data from boreholes on the Faroe Islands are used to add seismic velocities to the 3D geological models above.

This thesis also develops methods and workflows for constructing 3D geological models of flood basalt lava flows. The collection of digital 3D data using terrestrial laser scanning is evaluated, and data processing workflows are developed.

Copyright © by Catherine E. Nelson

The copyright of this thesis rests with the author. No quotation from it should be published without prior written consent and information derived from it should be acknowledged.

In memory of

Peter F. Nelson

1949-2008

Acknowledgements

There are many people I'd like to thank for their help during my PhD:

Firstly, I'd like to thank my supervisors, Dr Volcano and the Wizard (also known as Dougal Jerram and Richard Hobbs), for devising the project, funding it, coming up with excellent ideas, always being available, being so supportive, getting me to write papers and making substantial improvements to the draft of this thesis.

Thanks to the people who helped with fieldwork: Richard Walker in the Faroe Islands; and Terry Spry, Jo Garland and Mike Lewis on Skye.

Thanks to the BGS for their help with obtaining the GSI3D software, and troubleshooting when I had problems. In particular, I'd like to thank Charlotte Vye, Holger Kessler, Ricky Terrington, Ben Wood and Diarmad Campbell for their help.

I'd also like to thank Aeron Buchanan for all his time and help developing awesome new methods for building 3D models.

Thanks also to everyone in Durham who made this possible, in particular Dave and Gary for IT help, and Max for letting me use his PC. And thanks to everyone in the Open Plan area for fun times.

My family have made all this possible through their continuing support. Thanks Mum for always being there for me. This thesis is dedicated to my Dad, who I think of often.

And finally I'd like to thank Mike for being there through all the ups and downs, for distractions, putting up with bad moods and complaints, carrying equipment around, proof-reading, and generally being the most fantastic person I've ever had the good fortune to spend time with.

Table of Contents

ABSTRACT i

ACKNOWLEDGEMENTS iv

1. INTRODUCTION 1

1.1 PROJECT MOTIVATION: THE PROBLEMS 1

1.1.1 Problems with seismic imaging through flood basalts 1

1.1.2 Problems with mapping flood basalt lava flows 2

1.2 3D MODELLING 5

1.2.1 Geological models from outcrop observations 5

1.3 AIMS AND GENERAL APPROACH 6

1.4 THESIS OUTLINE 8

2. BACKGROUND: FACIES ARCHITECTURE OF FLOOD BASALT PROVINCES AND VOLCANIC MARGINS, AND EFFECTS ON GEOPHYSICAL PROPERTIES 10

2.1 CHAPTER SUMMARY 10

2.2 FLOOD BASALT PROVINCES AND HYDROCARBON EXPLORATION 10

2.2.1 Introduction to flood basalt provinces and volcanic rifted margins 10

2.2.2 Exploration problems in flood basalts, volcanic rifted margins and associated basins 13

2.2.3 The developing field of detailed facies analysis in flood basalt terrains 15

2.3 FLOOD BASALTS AND VOLCANIC RIFTED MARGINS – A FACIES ARCHITECTURE APPROACH 17

2.3.1 How to define key volcanic facies 17

2.3.2 Scales of heterogeneity 1 – intrafacies 17

2.3.3 Scales of heterogeneity 2 – flow facies and facies associations 19

2.3.4 Scales of heterogeneity 3 – seismic scale 23

2.4 A GEOPHYSICAL PERSPECTIVE 27

2.4.1 Relating basaltic facies to geophysical properties 28

2.4.2 How does heterogeneity affect seismic data? 30

2.5 CONCLUSIONS 32

3. METHODOLOGY AND DATASETS 35

3.1 CHAPTER SUMMARY 35

3.2 BOREHOLE DATA 35

3.3 TERRESTRIAL LASER SCANNING 36

3.3.1 Principles and equipment details 36

3.3.2 Data acquisition 38
3.3.3 Data processing 40
3.3.4 Previous work 43
3.4 THE GSI3D SOFTWARE 45
3.4.1 Background 45
3.4.2 The GSI3D methodology 46
3.4.3 Previous work 49
3.5 GOCAD 49
3.5.1 Introduction to the software 49
3.5.2 Key concepts 50
3.5.3 Model creation with GOCAD® 52
4. FLOOD BASALT FACIES FROM BOREHOLE DATA 54
4.1 CHAPTER SUMMARY 54
4.2 INTRODUCTION 54
4.2.1 The internal structure of flood basalt lava flows 54
4.2.2 Terminology 56
4.2.3 Interpreting wireline log data in flood basalt provinces 56
4.3 FAROESE CASE STUDY 58
4.3.1 Analysis of the Lopra-1/1A, Vestmanna-1, and Glyvursnes-1 borehole data 58
4.3.2 Methodology 60
4.3.3 Results of data analysis 64
4.3.4 Understanding the lava flow signature: Comparing tabular-classic and compound-braided facies 66
4.4 IDENTIFYING FACIES DISTRIBUTIONS IN UNCONSTRAINED DATA 69
4.4.1 Velocity distributions for the unconstrained boreholes 70
4.5 DISCUSSION AND CONCLUSIONS 73
5. CAPTURING 3D DATA IN FLOOD BASALT PROVINCES 77
5.1 CHAPTER SUMMARY 77
5.2 CASE STUDIES 77
5.2.1 Ljosa Quarry, Faroe Islands 79
5.2.2 Talisker Bay, Skye 80
5.3 COLLECTION AND PROCESSING THE LASER SCAN DATA 80
5.3.1 Ljosa quarry 80
5.3.2 Talisker Bay 81
5.3.3 Data processing 83
5.4 BUILDING 3D MODELS FROM THE LASER SCAN DATA 85

5.4.1 Picking key horizons 85
5.4.2 Extending the horizons laterally 86
5.4.3 Interrogating the block models 89
5.5 Evaluation of terrestrial laser scanning 93
5.6 An alternative approach: structure from motion 94
5.6.1 Theoretical principles 95
5.6.2 Pilot study: Hyaloclastites in Iceland 96
5.7 Discussion 101

6. DEFINING AND MODELLING LAVA FLOW SURFACE ROUGHNESS 102

Chapter summary 102
6.1 Introduction to random models and previous work 102
6.1.1 Spectral analysis and basalts as fractals 102
6.1.2 Previous work 104
6.1.3 Requirement for new data 105
6.2 Datasets 105
6.2.1 Remote sensing data from Iceland 105
6.2.2 Laser scan data from the Faroe Islands 108
6.2.3 Laser scan data from Ethiopia 111
6.2.4 Data preparation 111
6.3 Data analysis 113
6.4 Building random surfaces 116
6.5 Discussion 120

7. INTEGRATED GEOLOGICAL AND GEOPHYSICAL MODELS 122

7.1 Chapter summary 122
7.2 3D geological and geophysical modelling 122
7.3 Tabular-classic flow model 122
7.3.1 Approach and source data 122
7.3.2 Methods 127
7.3.3 Analysis 131
7.4 Compound-braided flow models: combined deterministic and random models 133
7.4.1 Approach 133
7.4.2 Methods 137
7.4.3 Analysis 142
7.5 Compound-braided flow models: fully random models 143
7.5.1 Approach, source data and methods 143
7.5.2 Analysis 145

7.6 DENSITY 146
7.7 DISCUSSION AND CONCLUSIONS 148
7.7.1 Tabular-classic flow model 148
7.7.2 Compound-braided flow models 148
7.7.3 Conclusions 149

8. CONCLUSIONS, FURTHER WORK AND SYNTHETIC SEISMIC DATA 152

8.1 CONCLUSIONS 152
8.1.1 3D data in flood basalt provinces 152
8.1.2 Borehole analysis and velocity data 152
8.1.3 Methods for 3D modelling 152
8.1.4 Applications to synthetic seismograms 153
8.2 FURTHER WORK 153
8.3 AN INITIAL LOOK AT SYNTHETIC SEISMIC DATA 155
8.3.1 1D reflectivity modelling 155
8.3.2 3D synthetic seismic data 161

REFERENCES 165

APPENDICES 180

List of figures

Figure 1.1 Typical exposure in flood basalt provinces. a) Eysturoy, Faroe Islands. b) Streymoy, Faroe Islands. c) Etendeka, NW Namibia. 3

Figure 1.2 Well-exposed areas of flood basalt provinces. a) Neist sea cliffs, Skye, UK. b) Talisker Bay, Skye, UK. c) Flow termination, Etendeka, Namibia. 4

Figure 1.3 Construction of a 3-D model from surfaces identified on correlation panels. a) Fully geo-spatially constrained logs and correlation panels. Data based on detailed satellite located logs. b) A correlation panel of key surfaces is constructed through logged data (e.g. Jerram et al., 1999). c) Panels orientated into true 3-D position, key surfaces identified from the 3 correlation panels, and 3-D surfaces reconstructed as GOCAD™ interpolated surfaces (adapted from Jerram and Robbe, 2001). 7

Figure 2.1 a) Location map of major flood basalt provinces, North Atlantic Igneous Province (NAIP) is highlighted. b) Schematic map of the NAIP showing location of onshore exposure. c) Schematic E-W cross-section from Greenland to Shetland, showing large scale lateral facies variations (adapted from Jerram and Widdowson, 2005). 12

Figure 2.2 Seismic reflection data from the FAST profile, Faroe-Shetland Basin (England et al., 2005). The source was designed to maximise penetration through basalts, using large airguns to increase low-frequency energy. A long offset was used, allowing better multiple suppression by normal moveout strategies. 13

Figure 2.3 Examples of the internal heterogeneity present in flood basalt provinces. Sections were produced from field sketches made by D. Jerram. Note that the scale is the same for each example. It can be seen that there is a wide variation in the internal architecture of a flood basalt province - flow thicknesses, numbers and associations all vary within a province and between provinces. Provinces are, however, made of the same "building blocks" allowing classification schemes to be developed, as discussed in Section 2.3. 16

Figure 2.4 The intrafacies classification scheme. a) The components which make up the various facies are indicated next to the diagrams. The abbreviations are as follows: a aphanitic margin, b bole material, c concentric banding, f foreset bedding, i injection structure, j regular jointing, l loading structure, m massive, p porphyritic texture, ra rubbly surface, rp ropy surface, si inclined sheet, t tuffaceous material, v vesiculated, xl medium to coarsely crystalline. Other intrafacies include Flow base, Flow top (unweathered), Sill, Pillow lava and Volcaniclastic. b) Descriptions of the different intrafacies shown in a). c) An example of various intrafacies from Talisker Bay, Skye, NAIP. There is a high degree of complexity evident in this one small area. For further details on all the intrafacies and their components, see Single and Jerram, 2004. 18

Figure 2.5 The volcanic facies classification scheme. 3D examples of different facies are shown, together with a list of the facies from the classification scheme of Jerram (2002). 20

Figure 2.6 Examples of facies types. a) is a cliff section from Talisker Bay, Skye, NAIP. b) shows the interpretation. Two flows are present, both showing the tabular-classic facies type. The upper flow shows a well-developed entablature and colonnade structure. The ponded flow facies type is also present here, on the right of the photograph. Also note the onlapping relationship between the two flows. Examples of facies associations: Large scale onlap-offlap facies variations in Ethiopia and Deccan.. c) is from the Ethiopian Traps, Africa. d) is from the Deccan Traps, India. Note that the scale is similar - in both areas, this facies association is present on a scale of hundreds of metres. Modified from Jerram 2002; Jerram and Widdowson 2005. 21

Figure 2.7 Section through the Etendeka flood basalts, NW Namibia. Compound-braided and tabular-classic flow facies can both be observed here, as well as onlap disconformity and sediment interlayer facies associations. 22

Figure 2.8 Facies observed in seismic sections and onshore analogues. a) Section of GFA-99 line 205 interpreted as showing tabular-type facies. The GFA-99 seismic data was collected approximately 60km SE of the Faroe Islands in the Faroe-Shetland Basin. b) Example of thick tabular flows from Talisker Bay, Skye. c) Section of GFA-99 line 107 showing dipping reflector sequences interpreted as hyaloclastite facies. Section changed from W-E to E-W for comparison with onshore analogue. d) Cliff section in the Nausuaq area, West Greenland shows hyaloclastites dipping and prograding eastwards onto Jurassic sediments. The hyaloclastites are covered by subaerial compound and tabular flows; this section is interpreted as filling a water-filled basin. Photograph courtesy of D.G. Pearson. e) Section of GFA-99 line 203 showing contrasting seismic signatures. f) These different seismic signatures are interpreted as compound braided facies overlain by tabular classic facies. An example of compound braided facies is shown from NW Streymoy, Faroe Islands. Seismic data courtesy of Western-Geco. 25

Figure 2.9 Schematic representation of the effects of basalt heterogeneity on the velocity profile through a lava pile. All elements of this diagram are on approximately the same scale. Photo from Skye Main Lava Series showing a typical layered basalt sequence. A seismic wavelet is included for comparison at a frequency of approximately 40Hz, as is commonly used in exploration. A frequency of 10Hz would be four times larger. The velocity profile is taken from ODP Hole 642E (Eldholm et al., 1987) and shows the wide and rapid variation in P-wave velocity. 27

Figure 2.10 Physical properties of different intrafacies. a) P-wave velocities for the different intrafacies. It can be seen that there is a wide velocity range. Massive intrafacies such as dykes and flow cores are faster, while more vesicular intrafacies such as boles are slower. The inflated sheet flow shows a range. b) Densities for the different intrafacies. Again, there is a wide range, from high density flow cores to low density boles. Data from the SIMBA database.29

Figure 2.11 Classification of scattering problems in heterogeneous media. Regions where different methods of analysis can be used are highlighted. *L* is the extent of the heterogeneous region, or the distance the seismic wave travels (the travel path). *a* is the size of the heterogeneity. *k* (the wavenumber) is where λ is the wavelength. Adapted from Wu and Aki, 1988. 31

Figure 3.1 Schematic view of Riegl LMS-Z420i terrestrial laser scanner. Image from http://www.riegl.com. (1) Range finder electronics. (2) Laser beam. (3) Reflective polygon - rotates rapidly to fire and collect laser beam. (4) Rotating optical head allows 360° coverage. (5) TCP/IP Ethernet interface. (6) Ruggedized laptop. (7) Nikon D70 digital camera. (8) USB camera interface. 37

Figure 3.2 The LMS-Z420i equipment in action in the Faroe Islands. 37

Figure 3.3 Range data for the LMS-Z420i laser scanner. From http://www.riegl.com. This graph assumes a flat target, average brightness and a perpendicular angle of incidence. 38

Figure 3.4 Data acquisition on Skye. a) Transporting the equipment. b) Setup procedures. c) Operating the equipment. 39

Figure 3.5 a) TLS point cloud for Brancepeth Castle. b) Panorama made from stitched photographs from one scan position. c) The point cloud coloured from the digital photographs. 41

Figure 3.6 Initial data processing using Riscan Pro. a) Photograph showing positions of reflectors. b) Fine scan of a 22cm reflector. 42

Figure 3.7 Merging scans. a) Scan from the centre of the courtyard. b) Scan from the rooftop. c) Merged scans. 44

Figure 3.8 Example of a complete GSI3D model from the BGS. Sudbury area, Suffolk, UK. From Kessler et al., 2009. 45

Figure 3.9 Screenshot of GSI3D version 2.6, showing the map, 3D and cross-section windows. 47

Figure 3.10 1200 km^2 model of the Sudbury – Ipswich – Felixstowe area, East Anglia. From Kessler et al., 2009. a) Imported geological map. b) Correlated cross-section. c) Fence diagram. d) Unit distribution. e) Completed block model. 48

Figure 3.11 Creating a GOCAD® surface from points. a) Imported points from GSI3D. b) Completed GOCAD® surface. 50

Figure 3.12 The default configuration for creating a surface from a grid of points in GOCAD® 51

Figure 3.13 Example of an empty voxet showing cells, with grid lines every 40 cells. 51

Figure 3.14 Model creation in GOCAD® from stratigraphic log data. From Single and Jerram, 2004. 52

Figure 4.1 Principles of interpreting wireline log data. As discussed in the text, variation in velocity and density can be used to subdivide lava flows into their crust, core and base regions. Photo from Ljosa quarry, Eysturoy, Faroe Islands. This is at a different scale to the log data, but this three-part division has been shown to be independent of scale (e.g. Self et al., 1997). Schematic flow structure from Self et al. (1997). Log data from the Lopra-1/1A borehole. 55

Figure 4.2 Location map of boreholes used in this chapter. 57

Figure 4.3 Location map of Faroese onshore boreholes and their stratigraphic positions. After Passey and Bell (2007). Borehole depths from Japsen et al. (2005). 59

Figure 4.4 Velocity histograms of various volcanic facies. Tabular-classic, hyaloclastite and dyke data from the Lopra-1/1A borehole; compound-braided data from the Glyvursnes-1 borehole. 62

Figure 4.5 Examples of P-wave velocity (V_p) data from different volcanic facies, divided into individual lava flows and showing intraflow variations where appropriate. Compound data from the Glyvursnes-1 borehole, other data from the Lopra-1/1A borehole. 64

Figure 4.6 Example of log data divided into core and crust. Core has high velocity, high density, low neutron porosity and low gamma ray. Crust has decreasing velocity and density, increasing neutron porosity and often a high spike in the gamma ray. Data from the Lopra-1/1A borehole.67

Figure 4.7 Plot of core proportion (core thickness divided by total flow thickness) versus flow thickness. Beinisvørð Formation data from the Lopra-1/1A borehole. 69

Figure 4.8 Velocity histograms for the boreholes with no nearby onshore analogues, as described in the text. 71

Figure 4.9 Well 164/07-1 histogram plotted with synthetic histograms constructed from tabular-classic and compound-braided data. The tabular data is a 300m selection from the Lopra-1/1A borehole of almost entirely tabular flows, while the compound data is a 150m selection from the Glyvursnes-1 borehole. These are normalised to the number of sample points. 73

Figure 4.10 a) Comparison between the borehole data in this chapter and cross-sections through a variety of flood basalt provinces from Chapter 2. b) Possible lateral variations. 74

Figure 5.1 Summary of the workflow used in this study. The data collection and processing steps follow standard procedures (e.g. Buckley et al., 2008). Enge et al. (2007) provide a similar workflow for model building. 78

Figure 5.2 Map of part of the NAIP and locations of case studies used in this chapter. 79

Figure 5.3 Overview photo of Ljosa quarry and map of the scanning setup, showing the scan positions and the reflector positions. 81

Figure 5.4 a) Overview photo of the Talisker Bay case study, showing the small sea stack, cliff section and wave-cut platform. b) The TLS equipment in action. c) The large sea stack. d) The case study area at high tide, showing the cliff section and both sea stacks. 82

Figure 5.5 Map of the scan setup at Talisker Bay. The complex layout meant several scans were carried out; two on the platform halfway up the large sea stack. Two scans were carried out at one position, one of which was tilted at an angle of 30° to the horizontal, in order to capture the top of the sea stack. 83

Figure 5.6 The completed laser scan point clouds, coloured from the digital photos. a) Talisker Bay data. b) Ljosa Quarry data. 84

Figure 5.7 Interpreted 3D lines from the Talisker Bay case study 86

Figure 5.8 The completed 3D model of the Ljosa Quarry case study constructed in GSI3D. a) Final model - lighter colours are flow crusts and darker colours are flow cores. b) Expanded model to show the full distribution of each layer. 87

Figure 5.9 The GOCAD® surface used to construct the Talisker Bay model. 88

Figure 5.10 Completed GSI3D models of the Talisker Bay case study. Animated versions available. a) Exploded view of the lava flows and sedimentary units. b) The 3D volumes cut to the present day topography. c) Transparent view of the entire model highlighting the sill, dyke and lava tubes. 89

Figure 5.11 Synthetic borehole through Ljosa quarry model. 90

Figure 5.12 Hjorleifshofði headland, a thick sequence of hyaloclastites in southern Iceland. 97

Figure 5.13 Sample photographs from the Hjorleifshofði headland. The overlap between the photographs must be around 75% for a successful reconstruction. 98

Figure 5.14 3D reconstruction of the headland. Model is 200m high, 500m long. Triangles are camera positions, circles are features tracked between photographs. The red line shows the path from the camera position to the point picked out in Figure 5.15. 99

Figure 5.15 Matlab interface for picking points on 3D reconstruction. a) The yellow triangle shows the surface between three tracked points. b) A point is selected within the triangle, as indicated by the yellow cross, and the 3D position on the model is calculated from the position within the photograph. 100

Figure 6.1 Determining Hurst number and correlation length from a power spectrum. 103

Figure 6.2 Effect of the Hurst number on surface roughness, while the standard deviation remains constant. From Saupe (1988). 104

Figure 6.3 Eldhraun branch of the Laki lava flow: location map and satellite DEM from ASTER Global Digital Elevation Model (http://www.gdem.aster.ersdac.or.jp/). Data at 30m resolution. Original data of ASTER GDEM is the property of the Ministry of Economy, Trade and Industry (Japan) and NASA. Flow directions and Laki extent from Guilbaud et al. (2005). 107

Figure 6.4 Laki surface roughness. a) Eldhraun branch near Kirkjubaejarklaustur. b) Looking south across the Eldhraun from Fjaðrárgljúfur. 108

Figure 6.5 Laser scan data from coastal quarry at Glyvursnes. Outcrop height is approximately 10m. a) Acquiring the laser scan data. b) The quarry wall with photo-interpretation of the lava flow top and base. c) The completed scan data. d) Lines interpreted from the scan data. 110

Figure 6.6 Laser scan data from Erte Ale, Ethiopia. Photos courtesy of Dougal Jerram. a) Collecting the scan data. b) Overview of the crater and surroundings. c) Complete scan data and scan positions. 112

Figure 6.7 Power spectra of data from a) Laki, b) Glyvursnes and c) Erte Ale. 114

Figure 6.8 All power spectra plotted together, only 1s.d. error bars shown. Dashed lines show other Hurst numbers for comparison. 115

Figure 6.9 Fractal models produced with the random volume building code of White (2009). a) Satellite scale. b) Laser scan scale. 117
Figure 6.10 Perspective view of satellite scale random model. Area is 10kmx10km. 118
Figure 6.11 Random models plotted against real data. 119
Figure 7.1 Histogram of flow thicknesses from the Beinisvorð Formation in the Lopra 1/1A borehole.124
Figure 7.2 Histograms of a) crust and b) core velocities from the Beinisvorð Formation in the Lopra 1/1A borehole. 125
Figure 7.3 Profiles through 20 flow crusts from the the Beinisvorð Formation in the Lopra 1/1A borehole, and trendline with equation. Distances through the flow crust have been normalised for comparison. 126
Figure 7.4 Stacked random surfaces forming the framework for the model. Model is 10km x 10km x 500m, view shows 10x vertical exaggeration. 128
Figure 7.5 Model space divided into regions. Model is 10km x 10km x 300m, view shows 10x vertical exaggeration. 129
Figure 7.6 3D model of a single flow. a) Constant velocity in flow crust and core. b) Flow crust velocity generated using Equation 7.1. c) Flow crust velocity generated using Equation 7.1, and core velocities drawn from distribution in Figure 7.2b. 130
Figure 7.7 10km x 10km x 300m model of tabular flows, with location of virtual borehole used for analysis. The complete model contains 20 flows and is 500m thick. 131
Figure 7.8 Comparison between a) histogram for tabular flow model and b) histogram for type section from Lopra 1/1A borehole. c) Part of virtual borehole. This may be compared to Figure 4.4, where an example of real data from the Lopra-1/1A borehole is shown. 132
Figure 7.9 Interaction of random surfaces leads to flows “pinching out”. a) Side view of stack of five flows. b) Plan view of one flow core. 133
Figure 7.10 GSI3D models from Chapter 5. a) Ljosa Quarry. b) Talisker Bay. 134
Figure 7.11 Histogram of velocity data from the Malinstindur Formation in the Glyvursnes-1 borehole, overlaid with simple distributions. 136
Figure 7.12 Profiles through 20 flows from the Malinstindur Formation in the Glyvursnes-1 borehole with trendline and equation. Data are normalised to allow comparison. 136
Figure 7.13 Method for adding random noise to GSI3D surfaces. Example is from the Ljosa Quarry model. Parameters for the random surface are the same as the laser scan scale surface in Chapter 6. 138
Figure 7.14 Ljosa Quarry model. a) Model with rough surfaces. b) Voxet taking in as much complexity as possible. c) Voxet divided into regions. 139
Figure 7.15 Talisker Bay model in GOCAD®. a) Model showing the rough surfaces. b) The voxet divided into regions. 140

Figure 7.16 a) Completed Ljosa Quarry model with virtual boreholes. b) Completed Talisker Bay model with virtual borehole. 141

Figure 7.17 a) Histogram of data from virtual boreholes through the Ljosa Quarry model. Three boreholes were created to obtain an adequate sample size. b) Virtual borehole through the Ljosa Quarry model. c) Histogram of data from virtual borehole through the Talisker Bay model. d) Virtual borehole through the Talisker Bay model. 142

Figure 7.18 a) Example of data from the Glyvursnes-1 borehole. b) Power spectra of Glyvursnes-1 data, produced in the same way as those in Chapter 6. 144

Figure 7.19 Random compound flow model. Model is approximately 100m x 100m x 25m. 145

Figure 7.20 a) Histogram of velocity values from the random compound model. b) Virtual borehole through the random compound model - as expected, there is no pattern to the velocity data.146

Figure 7.21 Velocity-density cross plots for a) Tabular-classic flows from the Lopra-1/1A borehole. b) Compound-braided flows from the Glyvursnes-1 borehole. See also Christie et al. (2006). 147

Figure 8.1 a) Simple layered reference model used to generate seismograms. b) Seismogram resulting from this model at offsets up to 500m. c) Zoomed in view of the target reflector at ~2s. 156

Figure 8.2 Tabular model. a) Velocity model used to generate seismograms. b) Seismogram resulting from this model at offsets up to 500m. c) Zoomed in view of the target reflector at ~2s. Note that the reflection time of the target reflector varies depending on the mean velocity of the basalt sequence. 157

Figure 8.3 Compound model from Talisker Bay. a) Velocity model used to generate seismograms. b) Seismogram resulting from this model at offsets up to 500m. c) Zoomed in view of the target reflector at ~2s. Note that the reflection time of the target reflector varies depending on the mean velocity of the basalt sequence. 158

Figure 8.4 Graphs for calculating Q by the spectral ratio method for a) the tabular model. b) the Talisker Bay compound model. 160

Figure 8.5 Synthetic seismic data from a 2D profile through the tabular model. a) Unmigrated section. b) Migrated. 163

Figure 8.6 Sy nthetic seismic data from the 3D tabular model. a) Unmigrated section. b) Migrated. 163

List of tables

Table 2.1 Summary of the seismic scale facies of Planke et al. (1999; 2000) and their probable flow scale components (e.g. equivalents of Jerram 2002). 25

Table 2.2 Rock properties affecting geophysical surveying methods. Adapted from Kearey et al. (2002) and Single (2004). 29

Table 5.1 Details of flows from Ljosa quarry model. 91

Table 5.2 Details of flows from Talisker Bay model. 93

Table 6.1 Input parameters for the random volume building code from White (2009). 116

1

1. INTRODUCTION 1

1.1 PROJECT MOTIVATION: THE PROBLEMS 1

1.1.1 Problems with seismic imaging through flood basalts 1

1.1.2 Problems with mapping flood basalt lava flows 2

1.2 3D MODELLING 5

1.2.1 Geological models from outcrop observations 5

1.3 AIMS AND GENERAL APPROACH 6

1.4 THESIS OUTLINE 8

1. Introduction

1.1 Project motivation: the problems

This work aims to construct 3D models of flood basalt provinces, to improve understanding of the effects of basalt sequences on seismic energy and provide new volcanological data. Flood basalt provinces are vast outpourings of basalt lava flows, intrusions, hyaloclastites and other associated facies, often having total volumes of millions of cubic kilometres. For references and additional information, see Chapter 2 where flood basalt provinces and associated volcanic margins are described in more detail. This chapter begins with a discussion of the project motivations, then introduces 3D modelling, and provides a summary of the thesis aims and structure.

1.1.1 Problems with seismic imaging through flood basalts

Seismic imaging of features below flood basalt provinces is difficult. The complex internal architecture of a stack of basalt lava flows causes a great deal of scattering and attenuation of a seismic wave, and as a result little energy is returned from below the basalt sequence (e.g. Maresh et al., 2006). High frequencies are preferentially attenuated, so the returned energy is predominantly at a low frequency. The reasons for this are explored further in Chapter 2, along with a review of research into methods for improving the quality of the returned image.

Research into seismic imaging below flood basalt provinces is motivated by the possible presence of hydrocarbon-bearing basins below basalt sequences. In the North Atlantic, sedimentary basins with known hydrocarbon discoveries extend below the edge of the basalt sequences of the North Atlantic Igneous Province. Additionally, one significant discovery has been made within the area covered by the basalt (Helland-Hansen, 2009), and oil has been observed within the basalt itself (Laier et al., 1997). In order to help resolve the problems of imaging beneath basalts we require a good understanding of the 3D internal architecture of a basalt sequence. The potential of 3D models to help improve seismic imaging is discussed in Chapter 2.

1.1.2 Problems with mapping flood basalt lava flows

In many geological settings, it is possible to map out significant features in onshore exposures to give information on offshore settings - channel features in sedimentary sequences, for example, which can also be identified in seismic data. The main constituents of flood basalt provinces, lava flows, are extremely difficult to map completely. The main reasons for the difficulty in mapping lava flows include:

Incomplete exposure. To map the extent of a lava flow, it is necessary to know the position of all the edges of the flow. This is easy for recent, uneroded lava flows, but extremely difficult when a lava flow is buried by many subsequent flows. Additionally, the edges of a flow may have been removed by erosion. As can be seen in Figure 1.1, large parts of a flood basalt sequence can be removed to leave only isolated occurrences, or large valleys can be carved through the middle.

Poor exposure. Basalt weathers easily and, in wet climates such as those found on the North Atlantic islands, it is often covered in vegetation. Figures 1.1a and 1.1b show typical exposures from the Faroe Islands, where thin flows especially are often completely covered by grass. Even in dry areas such as the Etendeka Flood Basalt Province (NW Namibia) scree cover reduces exposure. The slopes formed in areas of flood basalt lava flows are steep, unstable and difficult to access.

Difficulty in correlation. Lava flows within a flood basalt province can be of a similar composition, and have a similar physical appearance. If no marker horizons (such as sedimentary layers) are present it can be extremely difficult to correlate flows between outcrops - especially as they may change in thickness between two outcrops. In the Faroe Islands, there are channels several kilometres wide between islands, making correlation difficult.

However, some researchers have had success in mapping lava flows, most notably in the Columbia River flood basalt province (e.g. Thordarson and Self, 1998). Self et al. (2008) correlated lava flows across the Deccan Volcanic Province using a combination of geochemical and palaeomagnetic methods. Passey (2009) used sedimentary marker units and detailed field mapping to correlate major lava flows between islands in the Faroe Islands.

Figure 1.1 Typical exposure in flood basalt provinces. a) Eysturoy, Faroe Islands. b) Streymoy, Faroe Islands. c) Etendeka, NW Namibia.

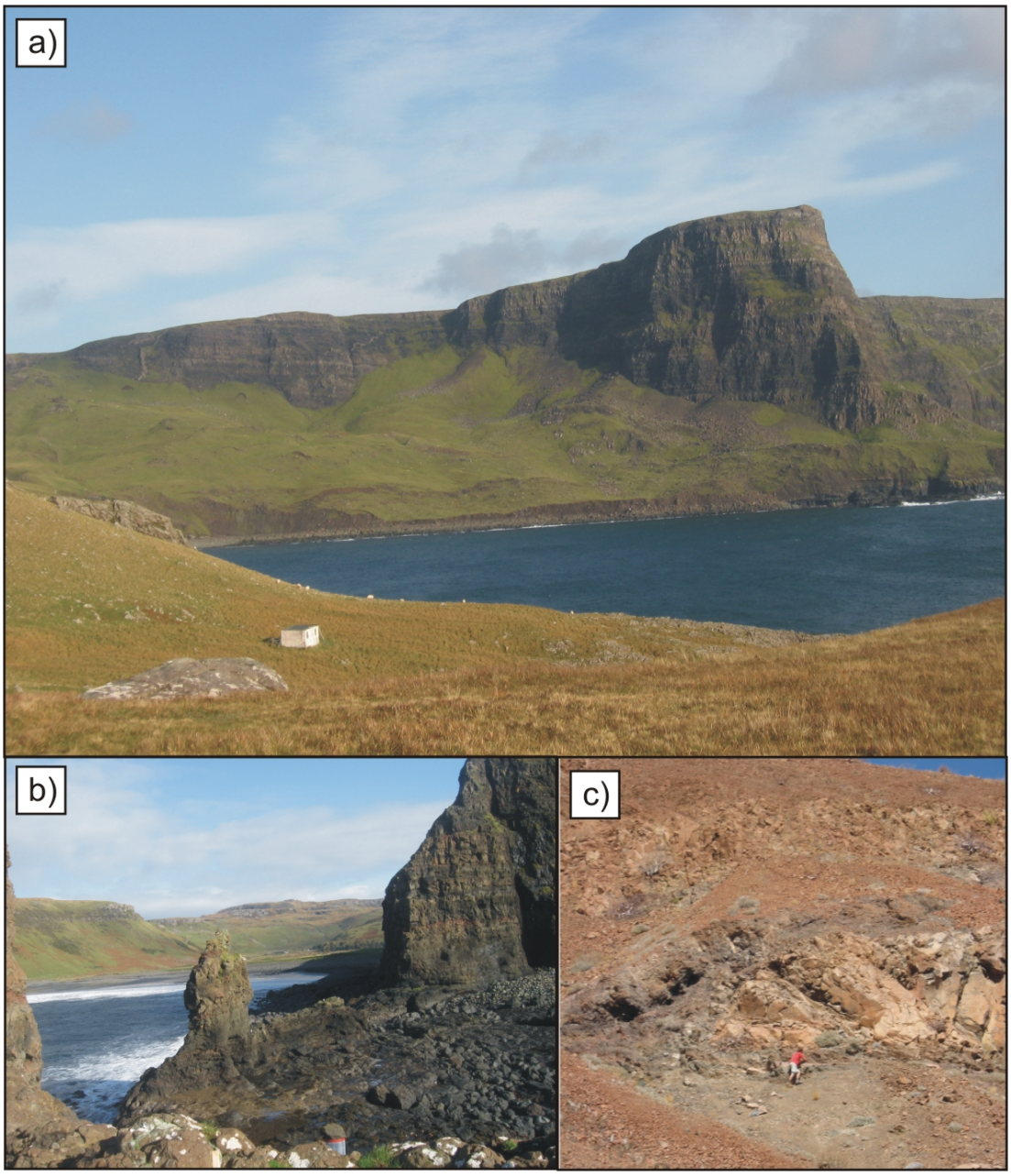

Figure 1.2 Well-exposed areas of flood basalt provinces. a) Neist sea cliffs, Skye, UK. b) Talisker Bay, Skye, UK. c) Flow termination, Etendeka, Namibia.

Ideally, 3D models would be constructed from detailed maps of lava flows (e.g. Single and Jerram, 2004); however as discussed above this is extremely time-consuming. In this work I attempt to provide methods for modelling the internal structure of a flood basalt province without detailed and lengthy traditional field mapping. This is achieved by combining datasets from different remote sensing techniques to produce well-constrained 3D models.

1.2 3D modelling

3D modelling in geology involves the representation of real-world geology, for example in a computer. Many different approaches are possible, including geological modelling (deterministic/mapping), stochastic modelling, numerical simulations and analogue modelling (using other materials such as wax or glucose). 3D modelling has received increasing amounts of attention, including a move towards systematic geological modelling by the British Geological Survey (Merritt et al., 2007; Kessler et al., 2009). Previous work on constructing 3D geological models of flood basalt provinces is summarised in Section 1.2.1.

In flood basalt provinces, stochastic modelling has been used to generate velocity models (e.g. Martini and Bean, 2002; Martini et al., 2005; White, 2009);. Attempts at numerical modelling of flood basalt lava flows have met with limited success because not all of the necessary parameters are well known, for example temperature, cooling rate, effusion rate (Harris et al., 2007), flow rate, pre-existing topography, viscosity, amount of lava available for eruption, final volume of flows, fracturing (Kattenhorn and Schaefer, 2008). The relationships between these factors also need to be well-defined for successful numerical modelling. Much work has focussed on predicting the path of a single lava flow (e.g. Young and Wadge, 1990; Miyamoto and Sasaki, 1998) but no data are available for multiple flows. Analogue modelling has also been used extensively to predict the flow of single lava flows (e.g. Blake and Bruno, 2000; Gregg and Fink, 2000), but again these do not provide data on stacking patterns.

1.2.1 Geological models from outcrop observations

Previous researchers have constructed geological models from outcrop observations in flood basalt provinces (e.g. Figure 1.2). Jerram and Robbe (2001) produced a 3D geological model in GOCAD® for the Etendeka region in Namibia (Figure 1.3), and were able to use this to map out a palaeo-shield volcanic feature in the sequence. Further detailed examples have been constructed for the Skye lavas in the British Palaeogene (e.g. Single and Jerram, 2004), and for the offshore Faroe-Shetland (Single, 2004). Passey (2009) obtained 3D triangulated surfaces for some major lava flows and sedimentary horizons from detailed mapping on the Faroe Islands. Bean

and Martini (2010) used outcrop observations from Northern Ireland to construct a 2D velocity model used for generating synthetic seismograms. This work uses improvements in mapping technology and software to build on previous efforts to produce 3D models.

1.3 Aims and general approach

The aim of this work is to construct 3D models of flood basalt lava flows from a variety of data. The models need to be geologically realistic: approaches are primarily informed by outcrop observations, rather than seismic or borehole data. The models also need to reflect recent research into lava flow emplacement processes.

Specific aims are:

- Identify volcanic facies in borehole logs.
- Obtain velocity data for different volcanic facies.
- Use laser scanning to capture outcrops in 3D.
- Add velocity data to outcrop models.
- Construct large models suitable for generating synthetic seismograms.

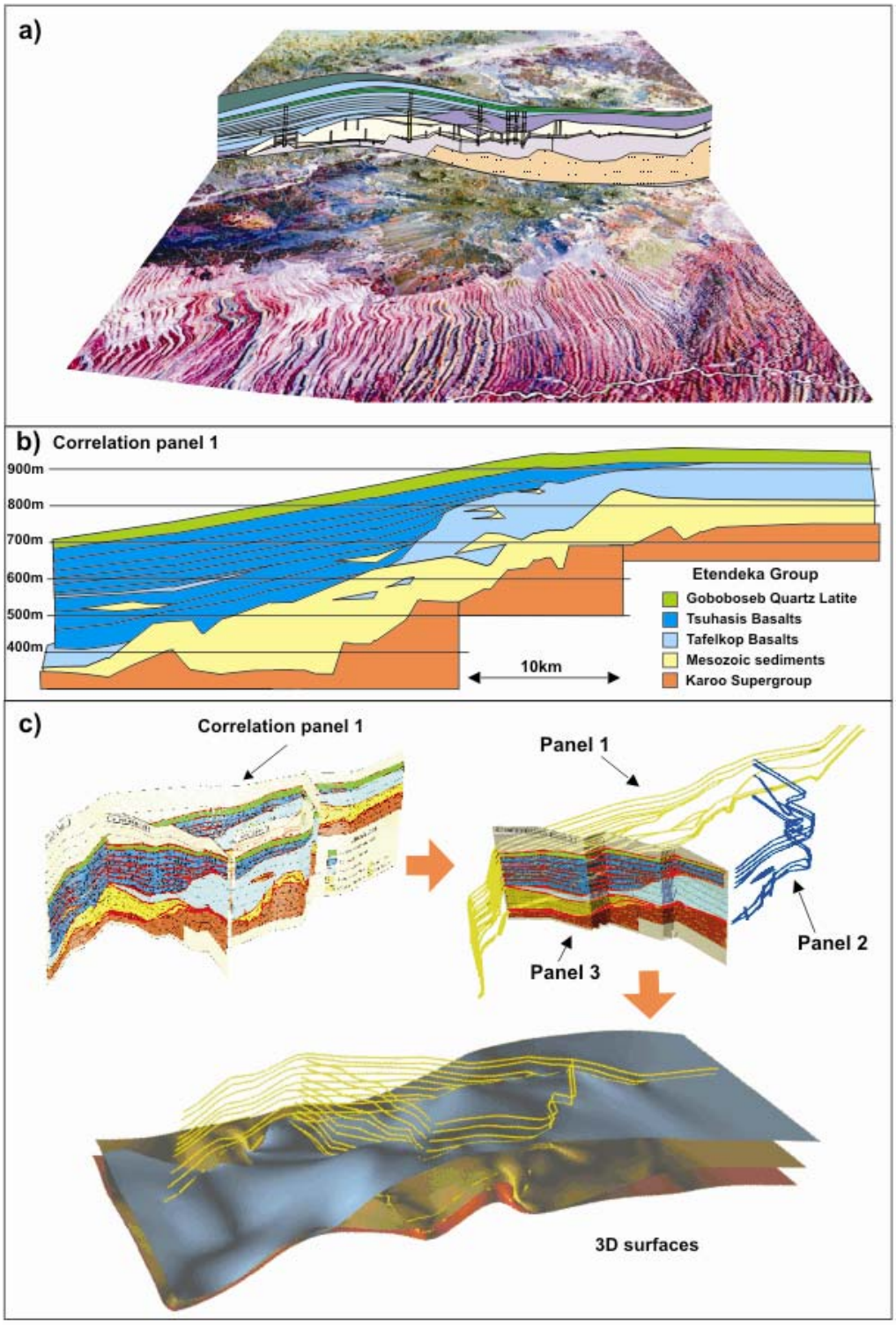

Figure 1.3 Construction of a 3-D model from surfaces identified on correlation panels. a) Fully geo-spatially constrained logs and correlation panels. Data based on detailed satellite located logs. b) A correlation panel of key surfaces is constructed through logged data (e.g. Jerram et al., 1999). c) Panels orientated into true 3-D position, key surfaces identified from the 3 correlation panels, and 3-D surfaces reconstructed as GOCAD™ interpolated surfaces (adapted from Jerram and Robbe, 2001).

1.4 Thesis outline

The thesis is structured as follows:

Chapter 1: Introduction to flood basalt provinces and 3D modelling, thesis aims, and project motivation.

Chapter 2: A review of previous work on volcanic facies, sub-basalt seismic imaging and brief geological history of the North Atlantic Igneous Province. Further discussion of the need for 3D modelling to improve seismic imaging.

Chapter 3: Overview of methods and data used in the thesis: borehole data specifics, introduction to terrestrial laser scanning, the GSI3D software and GOCAD software.

Chapter 4: Results of analysing borehole data through basalt lava flow sequences and how volcanic facies can be identified from histograms of borehole data.

Chapter 5: Methods for constructing 3D geological models from terrestrial laser scanning, using the GSI3D software developed by the BGS. Pilot study constructing 3D models from digital photographs alone.

Chapter 6: Spectral analysis of lava flow top surfaces and generation of random surfaces.

Chapter 7: Synthesis of all data into 3D geological and geophysical models.

Chapter 8: Conclusions, recommendations for future work and testing of 3D models for the computation of constrained synthetic seismic data.

Appendices: Papers published in support of the thesis; workflows for GOCAD, GSI3D, GMT and Riscan Pro; interpretations of borehole data; completed 3D models on DVD.

2

2. BACKGROUND: FACIES ARCHITECTURE OF FLOOD BASALT PROVINCES AND VOLCANIC MARGINS, AND EFFECTS ON GEOPHYSICAL PROPERTIES 10

2.1 CHAPTER SUMMARY 10

2.2 FLOOD BASALT PROVINCES AND HYDROCARBON EXPLORATION 10

2.2.1 Introduction to flood basalt provinces and volcanic rifted margins 10

2.2.2 Exploration problems in flood basalts, volcanic rifted margins and associated basins 13

2.2.3 The developing field of detailed facies analysis in flood basalt terrains 15

2.3 FLOOD BASALTS AND VOLCANIC RIFTED MARGINS – A FACIES ARCHITECTURE APPROACH 17

2.3.1 How to define key volcanic facies 17

2.3.2 Scales of heterogeneity 1 – intrafacies 17

2.3.3 Scales of heterogeneity 2 – flow facies and facies associations 19

2.3.4 Scales of heterogeneity 3 – seismic scale 23

2.4 A GEOPHYSICAL PERSPECTIVE 26

2.4.1 Relating basaltic facies to geophysical properties 27

2.4.2 How does heterogeneity affect seismic data? 29

2.5 CONCLUSIONS 31

2. Background: facies architecture of flood basalt provinces and volcanic margins, and effects on geophysical properties

2.1 Chapter summary

Chapter 2 reviews the current developments in our understanding of the facies architecture of flood basalts and volcanic rifted margins. I also give an overview of attempts to image below basalt sequences using seismic reflection surveying, and expand on the reasons for using 3D modelling from a geophysical perspective.

The main scales addressed in this chapter comprise: intrafacies – heterogeneity on a lava flow scale; facies/facies associations – variations on a lava field scale; and seismic facies – the sub-province scale. Intrafacies cover features up to 10s of metres, while facies variations are seen at the metre to kilometre scale and seismic facies can be identified at scales of kilometres to tens of kilometres. These scales of heterogeneity are important in the interpretation of flood basalt sequences from a variety of different settings. Examples from the North Atlantic Igneous Province, Paranã-Etendeka, Deccan and Ethiopia are discussed, which suggest that there are common facies elements in the generation of flood basalt provinces associated with volcanic rifted margins. Facies analysis also aids understanding of the temporal and spatial evolution of a flood basalt province.

2.2 Flood basalt provinces and hydrocarbon exploration

2.2.1 Introduction to flood basalt provinces and volcanic rifted margins

Three quarters of the Atlantic rifted margins are estimated to be volcanic, and perhaps as much as 90% of rifted margins worldwide (Menzies et al., 2002). In places along these margins, subaerial lava flows were erupted to form flood basalt provinces, especially where the positions of mantle melting anomalies were coincident with the rifted margin (e.g. North Atlantic Igneous Province, Paranã-Etendeka; White and McKenzie, 1989, Jerram and Widdowson, 2005). Substantial volumes of material were also added to the underside of the continental crust via magmatic underplating (Cox 1980; 1993).

The distribution of several of the main Cenozoic and Mesozoic flood basalt provinces is highlighted in Figure 2.1a. These provinces contain enormous volumes of lava; the Deccan Volcanic Province, for example, has an estimated maximum extrusive volume of c. $1x10^6$ km^3 (Self et al., 2006). The North Atlantic Igneous Province (NAIP) (Figure 2.1b), when its volcanic rifted margins are included, is estimated to have a volume of $1.8x10^6$ km^3 covering an area of $1.3x10^6$ km^2 (Eldholm and Grue, 1994). The NAIP covers some sedimentary basins which are thought to have a high potential for hydrocarbon discovery. This is because volcanism coincided with the deposition of Palaeocene sediments in the Faroe-Shetland Basin, which contain the Foinaven and Schiehallion fields in areas without basalt cover (Naylor et al. 1999), and the Rosebank discovery within the edge of the basalts (Helland-Hansen, 2009). Similar areas are associated with other flood basalt provinces, such as the Kudu Gas Field, offshore Namibia (Jerram et al., 1999), associated with the Paranã-Etendeka flood basalts. Areas covered by the Deccan Volcanic Province such as the Saurashtra Peninsula, western India (Sain et al., 2002) and the Kutch Basin, offshore to the west of India (Kumar et al., 2004) have also been identified as sub-basalt hydrocarbon prospects. Therefore, a major target in hydrocarbon exploration is to exploit areas with flood basalt cover, which specifically requires good seismic imaging of the structure beneath the basalt sequence, often over 1km thick.

This chapter shows how a facies architecture approach is useful in understanding the spatial and temporal development of flood basalt provinces, with specific focus on the potential problems and implications for the successful exploration of sub-basalt basins. Facies analysis provides information on the different scales of heterogeneity through the volcanic pile, which will have major effects on remote sensing techniques through such media. Figure 2.1c shows schematically how extensive these facies variations can be on a basin-wide scale.

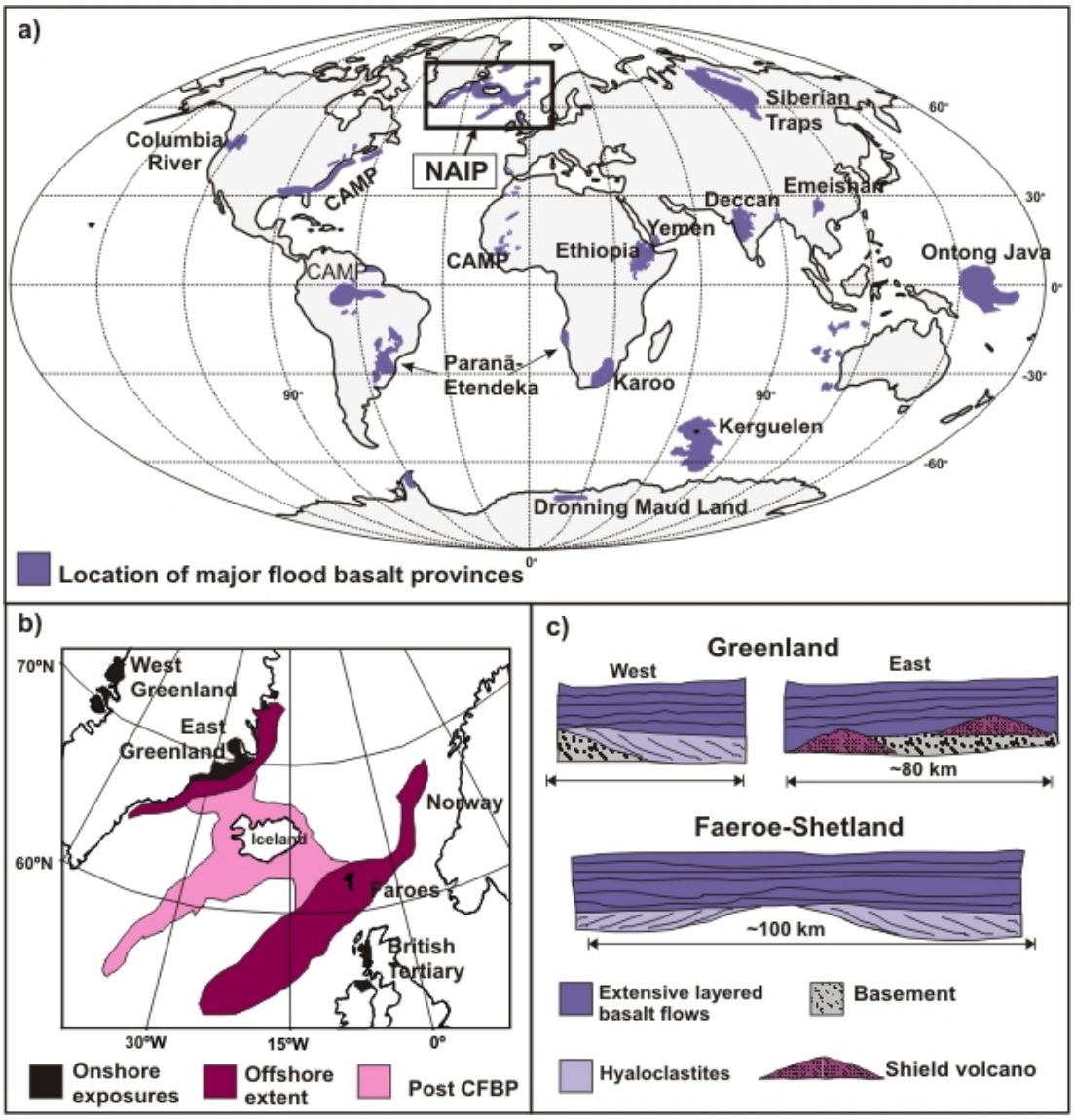

Figure 2.1 a) Location map of major flood basalt provinces, North Atlantic Igneous Province (NAIP) is highlighted. b) Schematic map of the NAIP showing location of onshore exposure. c) Schematic E-W cross-section from Greenland to Shetland, showing large scale lateral facies variations (adapted from Jerram and Widdowson, 2005).

2.2.2 Exploration problems in flood basalts, volcanic rifted margins and associated basins

Many areas in the North Atlantic have a high potential for petroleum discoveries, usually investigated by seismic reflection surveying. Unfortunately, the presence of thick, layered basalt sequences (consisting predominantly of lava flows and associated lithologies) in flood basalt provinces and volcanic rifted margins creates an environment where very few clear reflections are returned from below the basalt sequence, as demonstrated in Figure 2.2. The poor imaging below the basalt sequence is due to loss of seismic energy by scattering and attenuation. This is caused by the high impedance contrast between sediments and basaltic lava flows at the top of the basalt succession, and by energy loss within the basalt sequence from its internal heterogeneity. This internal heterogeneity causes more of a problem than the high impedance contrast (Martini and Bean, 2002), causing the production of multiples, scattering due to layering and rubbly flow tops, and transmissions and mode conversions at flow boundaries (Maresh et al., 2006). The net effect is that higher frequencies are preferentially attenuated.

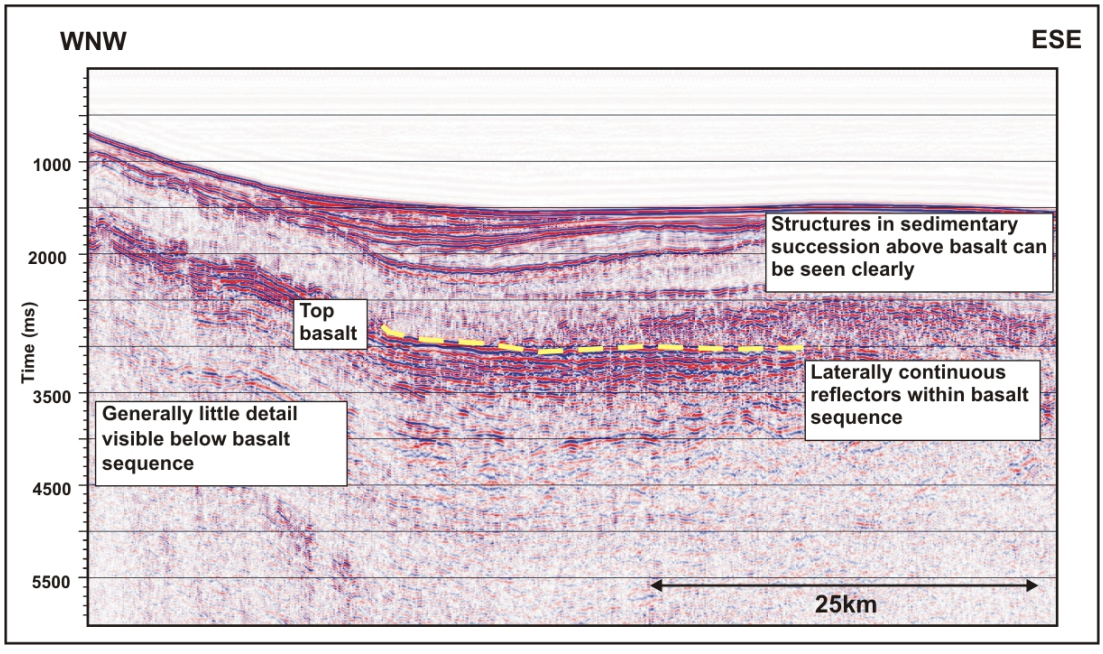

Figure 2.2 Seismic reflection data from the FAST profile, Faroe-Shetland Basin (England et al., 2005). The source was designed to maximise penetration through basalts, using large airguns to increase low-frequency energy. A long offset was used, allowing better multiple suppression by normal moveout strategies.

Research by Maresh et al. (2006) investigated the cause of the attenuation in layered basaltic lava flows, using a vertical seismic profile from Well 164/07-1. The measured attenuation was considerably higher than predicted from laboratory basalt samples, indicating that either the impedance contrasts caused by layering, or the scattering caused by the rugose interfaces between flows, contributed to the attenuation. Modelling synthetic seismograms showed that the layering caused more attenuation than the rubbly surfaces, and the layering alone could account for the observed attenuation in the borehole data. However, this study only considered the effect of one rubbly surface, and the combined effect of many such interfaces may be significant. Bean and Martini (2010) suggested that a rough basalt surface caused a significant amount of the imaging problem, and showed how to limit this effect by employing wave equation datuming.

Due to the loss of high frequencies through attenuation, strategies for imaging below basalt sequences have concentrated on the use of low frequencies. Wide-angle surveys have also had some success in imaging the base of the basalt sequence, as fewer interbed multiples are present in long-offset data (White et al. 2005). Work has also focussed on optimizing the source and receivers to obtain better low frequency data. Ziolkowski et al. (2003) argued for the use of larger airguns and for towing both the seismic source and receiver at a depth of around 20m below the sea surface. Towing the source at a greater depth allows a reflection from the sea surface, to increase constructive interference at low frequencies (Maresh and White, 2005). More recently, efforts have included using a low frequency source (Roberts et al. 2009; Eccles et al. 2009) and using paired sources and cables in a configuration known as “over/under” (e.g. Leathard et al. 2009).

An alternative approach is to concentrate on improving data processing strategies. Gallagher and Dromgoole (2008) showed that reprocessing of legacy data could lead to improved images, using improved velocity models and multiple removal strategies. Hobbs et al. (2009) discussed how low frequency reflections could best be obtained using improved multiple suppression algorithms, in addition to recommending the best data acquisition strategies.

Martini et al. (2005) highlighted the need for synthetic seismic data based on realistic 3D geology. A 3D model of a basalt succession could be used for the simulation of realistic seismic data, to test seismic acquisition and processing techniques.

2.2.3 The developing field of detailed facies analysis in flood basalt terrains

As discussed above, it is the internal heterogeneity of the flood basalt provinces and volcanic rifted margins that gives rise to imaging problems. Figure 2.3 shows three logged sections highlighting the vertical stacking of lava flows preserved in onshore examples of flood basalt sequences. Each lava flow contains internal heterogeneities and this, together with the stacking variations, would give rise to complex seismic characteristics in the offshore setting. Clearly, a simple solid block of massive basalt would present very different seismic characteristics (e.g. an intrusive sill). Characterising this internal heterogeneity gives valuable information on the effect of the basalt sequence on the passage of seismic energy. An additional problem affecting exploration of such areas is the prediction of inter- and intraflow variations. Here, a clear understanding of the volcanic facies distributions and their physical properties is of vital importance.

Although borehole data gives a vertical section, the existence of lateral variations (e.g. Passey, 2004; Jerram and Widdowson 2005) requires the use of onshore analogues where much more data is available to characterise the 3D nature. Recent studies have investigated the physical characteristics of continental flood basalt provinces, and classification schemes have been developed (see below). No onshore analogues are available for the parts of volcanic rifted margins found further offshore; facies here (such as the outer seaward dipping reflectors facies of Planke et al., 2000) have been classified based on their shape and characteristic reflections in seismic data. However, the use of 3D seismic data has led to successful imaging of the structure of sill complexes (e.g. Corfield et al., 2004; Thomson, 2005; Smallwood and Maresh, 2002).

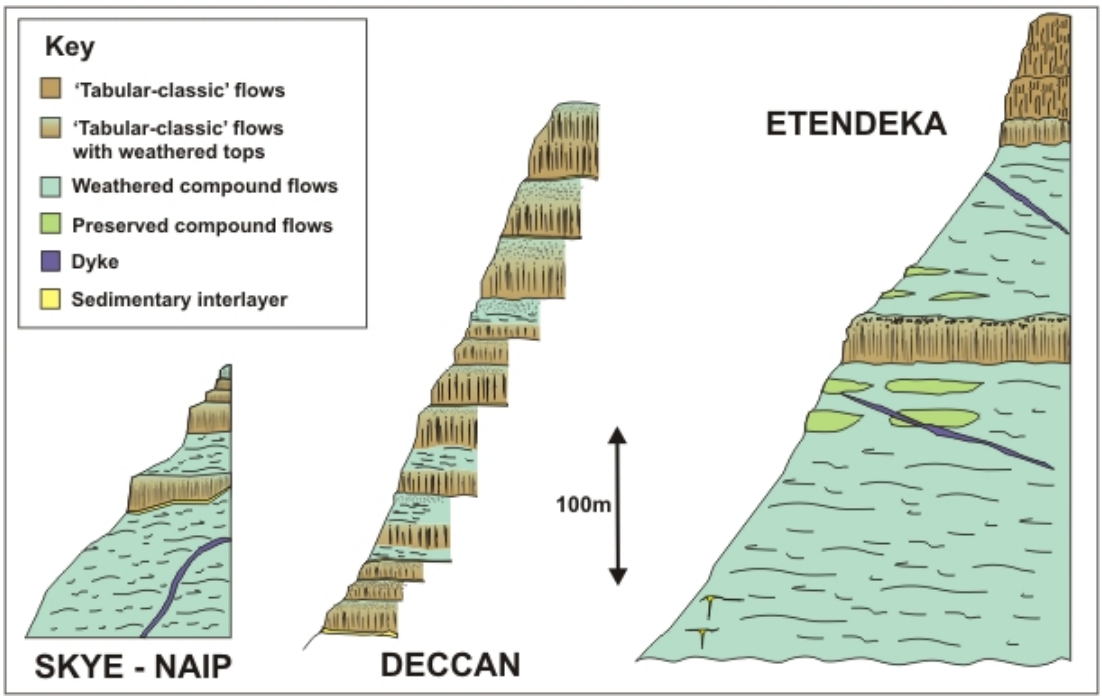

Figure 2.3 Examples of the internal heterogeneity present in flood basalt provinces. Sections were produced from field sketches made by D. Jerram. Note that the scale is the same for each example. It can be seen that there is a wide variation in the internal architecture of a flood basalt province - flow thicknesses, numbers and associations all vary within a province and between provinces. Provinces are, however, made of the same "building blocks" allowing classification schemes to be developed, as discussed in Section 2.3.

The facies concept, used extensively in describing sedimentary rocks, was first applied to volcanic rocks by Cas and Wright (1987). A facies is defined as a body of rock with specified characteristics (Reading, 1986), and these characteristics are definable and distinguish the rock from other facies. The facies is considered to be the product of a particular set of conditions (Cas and Wright 1987). In volcanic successions different styles of volcanism, different magma compositions, topographic variations or differences in rates of eruption, produce the various facies (e.g. Jerram, 2002). An understanding of the evolution of a province can thus be gained from facies analysis.

Facies variation has been observed at scales from the individual lava flow to the seismic scale. Classification schemes have been developed by Single and Jerram (2004; Figure 2.4) at the intrafacies scale (flow scale variation), at the facies scale (e.g. Jerram, 2002; Figure 2.5) and at the seismic scale (e.g. Planke et al., 2000;

Table 2.1). Although these schemes are not fully inclusive of all facies types found in flood basalt provinces, they provide a conceptual means of defining volcanic heterogeneities and comparing between different flood basalt provinces, thus providing a systematic framework for observations. In the following section I will summarise these conceptual facies models and discuss key examples from a number of onshore flood basalt provinces.

2.3 Flood basalts and volcanic rifted margins – a facies architecture approach

2.3.1 How to define key volcanic facies

Cas and Wright (1987) suggested that facies should be defined by two major groups of characteristics. Firstly, the geometry of the facies should be considered: the volume, shape, pre-existing relief and flow direction. Secondly, the lithology is equally important: the composition and the texture. The lithology is subject to later modification by processes such as erosion and alteration. Deformation may also be important as flood basalt provinces are often situated at sites of later rifting. Flood basalt provinces are massive outpourings of predominantly tholeiitic basalt, but also basaltic andesite lava which cover several thousands of square kilometres, and build to a thickness of up to a few kilometres. They are, however made up of many hundreds or thousands of individual lava flows, with associated sills and dyke facies which vary on the scale of metres and in some cases centimetres. Therefore, it is useful to consider the heterogeneities present at different scales of observation. Below, I consider scales of heterogeneity from 1) intrafacies variations, 2) facies variations and associations and 3) seismic scale variations.

2.3.2 Scales of heterogeneity 1 – intrafacies

To understand the volcanology and physical characteristics of flood basalts it is important to look beyond their geochemical variations, and quantify them from a volcanological perspective. For example, in attempting to understand lava emplacement mechanisms, Self et al. (1996; 1997) divided flows into an upper crust, core and basal zone, based on vesicle patterns, jointing style and petrographic texture. The abundance of flows with this three-part structure led to an emplacement model of inflating pahoehoe flows whereby liquid lava is injected under a solidifying

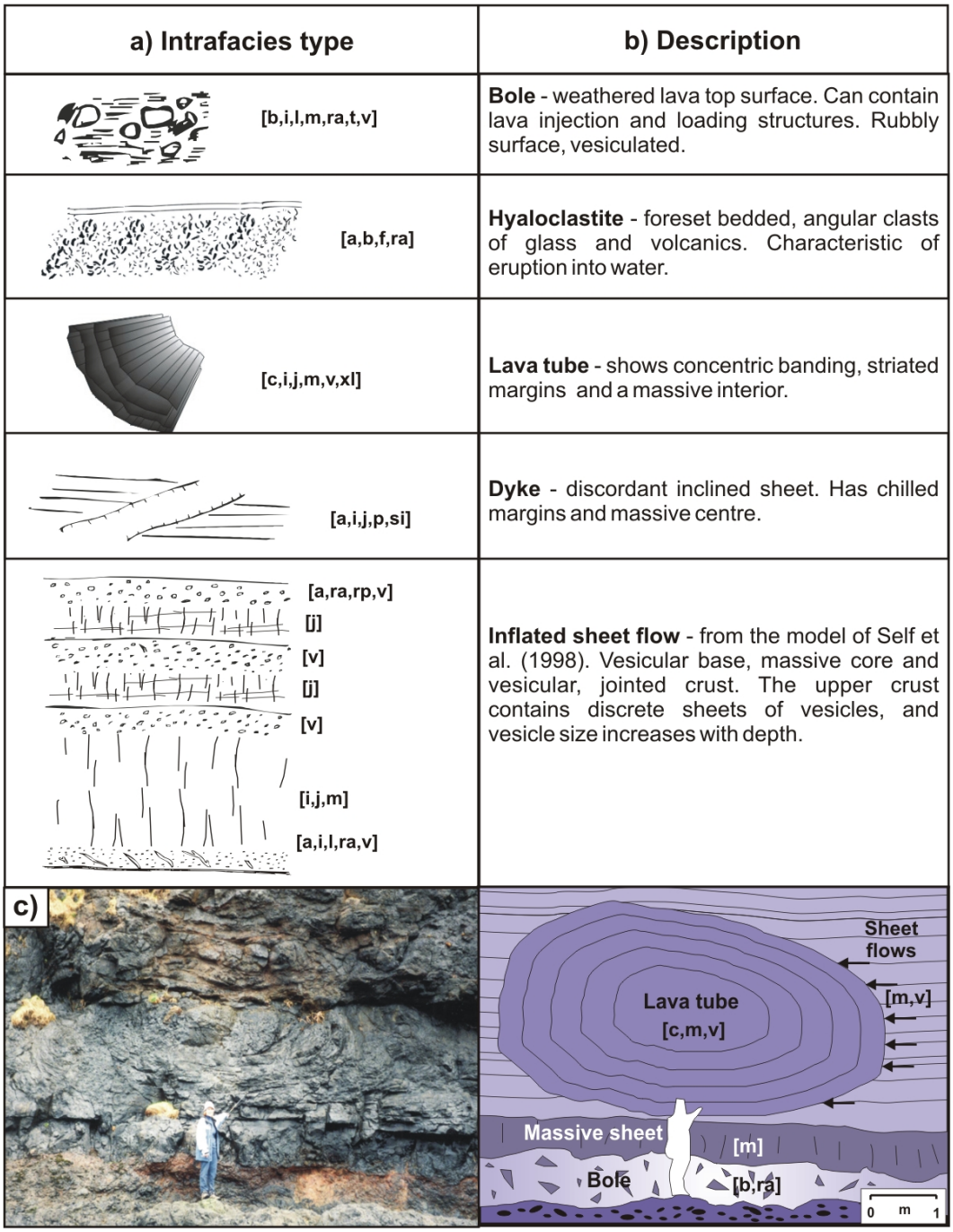

Figure 2.4 The intrafacies classification scheme. a) The components which make up the various facies are indicated next to the diagrams. The abbreviations are as follows: a aphanitic margin, b bole material, c concentric banding, f foreset bedding, i injection structure, j regular jointing, l loading structure, m massive, p porphyritic texture, ra rubbly surface, rp ropy surface, si inclined sheet, t tuffaceous material, v vesiculated, xl medium to coarsely crystalline. Other intrafacies include Flow base, Flow top (unweathered), Sill, Pillow lava and Volcaniclastic. b) Descriptions of the different intrafacies shown in a). c) An example of various intrafacies from Talisker Bay, Skye, NAIP. There is a high degree of complexity evident in this one small area. For further details on all the intrafacies and their components, see Single and Jerram, 2004.

crust. This model was proposed as the standard way of emplacing large pahoehoe lava fields (e.g. Self et al., 1996).

A similar approach was taken by Single and Jerram (2004), who developed a classification scheme for small-scale heterogeneity within lava flows, which built on the core-crust observations to include bole horizons, lava tubes, small intrusions and so on. Within this scheme, known as the 'intrafacies' scheme (Single and Jerram 2004), information on components important for geophysical modelling are also included, providing a systematic method of characterising features in lava sequences and allowing comparisons to be made between provinces. A summary of the different intrafacies components is shown in Figure 2.4.

This intrafacies classification scheme is based on field observations and covers heterogeneities visible at the smallest scale of field observation: the 0.1-10m scale. These intrafacies can provide information on the method of emplacement, for example if vesicle patterns characteristic of inflated pahoehoe flows are present (e.g. Cashman and Kauahikaua, 1997), and give information on the association of flow breakouts, inflation textures and lava feeder systems (e.g. Single and Jerram, 2004). Intrafacies components are identified by changes in properties such as fracturing, vesiculation, shape of the feature, and the presence of palaeosols. The effect of these properties on geophysical parameters such as seismic velocity, density and magnetic susceptibility is discussed further in Section 2.4.1.

2.3.3 Scales of heterogeneity 2 – flow facies and facies associations

Studies of heterogeneity at the facies scale are somewhat more common than those at the intrafacies scale, but they are still relatively few in number. Walker (1971) proposed the terms "simple" and "compound" for describing two different types of lava flow, based on observations of numerous recent and ancient lava flows. Compound flows are defined as those that are divisible into smaller flow lobes, whereas simple flows are composed of only one flow unit.

Jerram (2002) outlined the major facies types and facies associations providing a systematic way of describing heterogeneity at the metre to kilometre scale (summarised in Figure 2.5). Facies types described in this scheme include different types of lava flow (incorporating the terminology of Walker, 1971), hyaloclastites,

ponded flows, sills and dykes, based on observations made in the Etendeka, Karoo, Columbia River, Ethiopia, Deccan and British Palaeogene provinces. Sedimentary units may also be present as interbeds, and would thus be included in this classification scheme. Examples are shown in Figure 2.6 and Figure 2.7. These facies are identified by their characteristic physical properties, and are made up of the intrafacies described above. In common with facies analysis in sedimentary successions, their interpretation is based on analogues with present-day examples. The eruptions of Kilauea, Hawaii, and Laki, Iceland, are the most commonly used analogues, with preserved flood basalt lavas which range in size from examples similar to modern day occurrences to flows that are orders of magnitude larger (Jerram, 2002), with the largest flows having volumes of 1000s of km^3 (e.g. the Roza Member, Columbia River, Self et al., 1997).

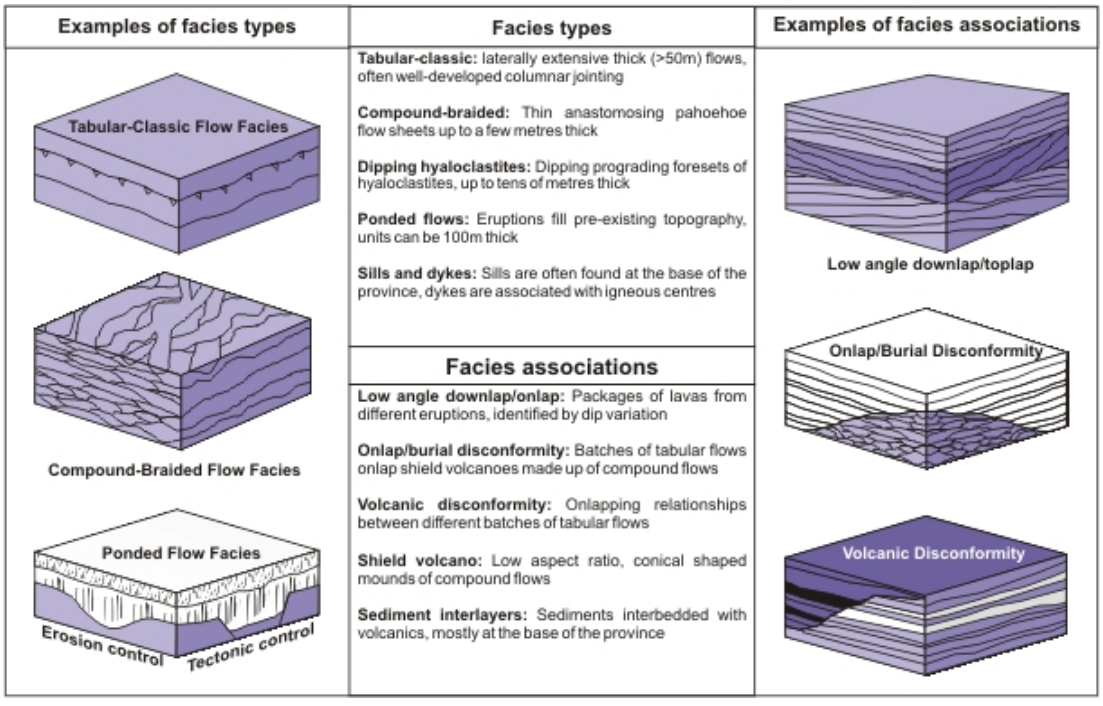

Figure 2.5 The volcanic facies classification scheme. 3D examples of different facies are shown, together with a list of the facies from the classification scheme of Jerram (2002).

The study of the relationships between these facies is particularly important when considering offshore examples. Geometrical stacking patterns may be seen on seismic scales, so if we know what causes these patterns in well-exposed onshore

examples, we can then begin to identify facies offshore. Characteristic stacking patterns include disconformities, downlap and shield volcanoes. Examples are given in Figure 2.6 and Figure 2.7.

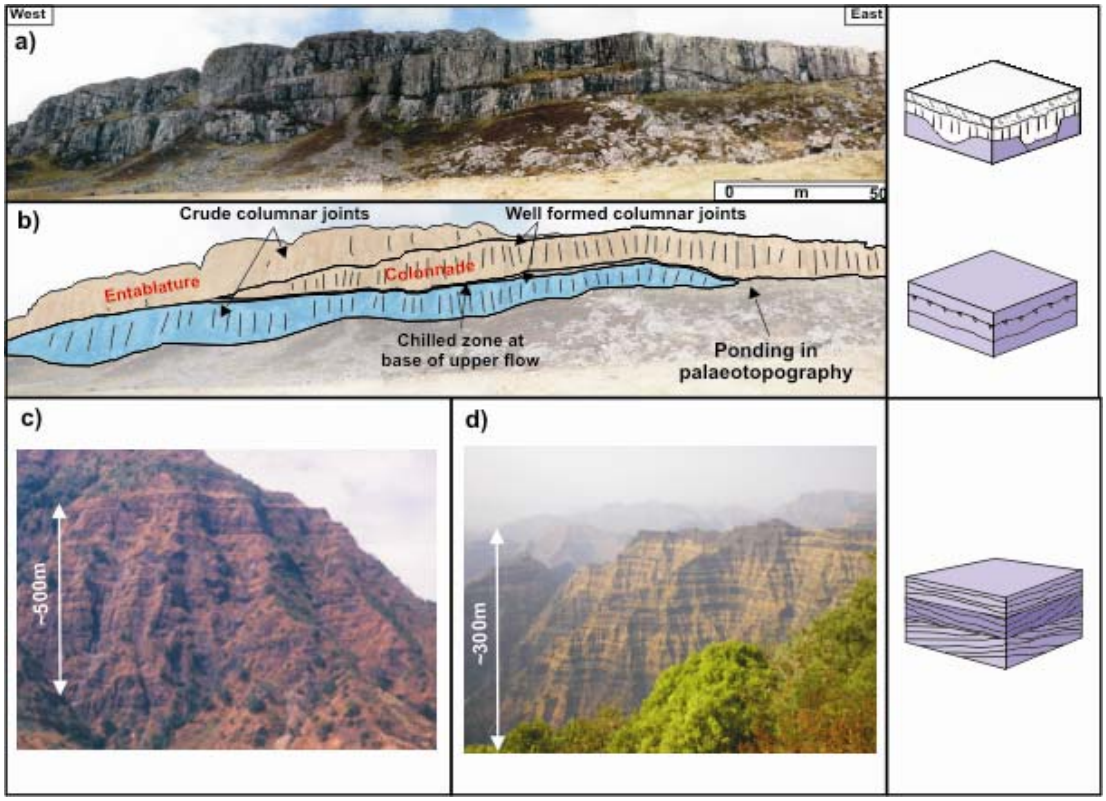

Figure 2.6 Examples of facies types. a) is a cliff section from Talisker Bay, Skye, NAIP. b) shows the interpretation. Two flows are present, both showing the tabular-classic facies type. The upper flow shows a well-developed entablature and colonnade structure. The ponded flow facies type is also present here, on the right of the photograph. Also note the onlapping relationship between the two flows. Examples of facies associations: Large scale onlap-offlap facies variations in Ethiopia and Deccan.. c) is from the Ethiopian Traps, Africa. d) is from the Deccan Traps, India. Note that the scale is similar - in both areas, this facies association is present on a scale of hundreds of metres. Modified from Jerram 2002; Jerram and Widdowson 2005.

The facies classification scheme has been applied successfully in several flood basalt provinces. In the NAIP, Passey and Bell (2007) characterised the morphologies of the Faroe Islands Basalt Group, incorporating a facies approach such as the scheme of Jerram (2002). The three main eruptive sequences (the Beinisvørð, Malinstindur and Enni formations) demonstrate a variety of different facies architectures. The

Beinisvørð Formation is dominated by a 'tabular-classic' facies architecture, which is interpreted as indicating that the flows were erupted as single continuous flows from fissure systems. In contrast, the Malinstindur formation consists mainly of 'compound-braided' flows, suggesting a different eruptive style whereby flows were not erupted continuously, but at longer time intervals from separate shield volcanoes. The Enni formation has a mixture of the two facies architectures. Hyaloclastite and sill facies are also present (Ellis et al., 2002; Rasmussen and Noe-Nygaard, 1970). Single (2004) also studied the NAIP, focussing on the facies architecture of the Talisker Bay area, Skye. A series of tabular-classic flows was found overlying compound-braided flows, with a transitional sequence in between.

Jerram (2002) describes many different facies; however the most abundant in the NAIP (in terms of volume) are the compound-braided, tabular-classic, hyaloclastite and intrusive facies. These will be the main facies considered in later chapters; however many of the principles developed in this thesis will be applicable to other facies.

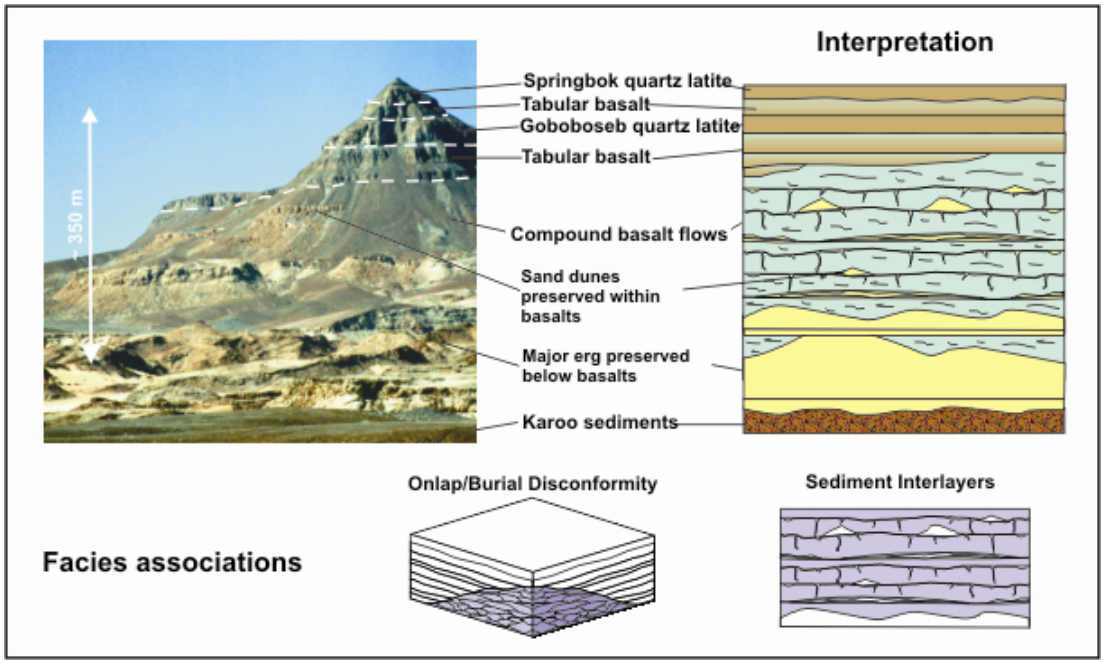

Figure 2.7 Section through the Etendeka flood basalts, NW Namibia. Compound-braided and tabular-classic flow facies can both be observed here, as well as onlap disconformity and sediment interlayer facies associations.

Jerram and Widdowson (2005) showed how facies variations may successfully be compared across different provinces. The architecture of the Deccan, the Paranã-Etendeka and the NAIP was considered; despite many differences between the provinces, there are some key similarities. All show initial low-volume eruptions followed by a main phase of relatively short duration (1-5Ma). This main phase is often characterised by large volume, extensive tabular flows.

The characteristic associations of these facies are important in developing models of the basin as a whole. In the NAIP and the Paranã-Etendeka, early shield volcanoes were buried by later large-volume flat-lying tabular flows, creating volcanic disconformities (Jerram and Widdowson, 2005). The Ethiopian flood basalt province, where the top of the flood basalt sequence is preserved, contains a series of flood basalts overlain by large shield volcanoes (Kieffer et al., 2004). Clearly the relative abundance and distribution of key facies within flood basalt sequences will help define their evolution both spatially and temporally, particularly below the resolution of geochronological markers or where these are absent.

2.3.4 Scales of heterogeneity 3 – seismic scale

Seismic imaging can generally pick out features greater than 50m thick, so individual lava flows (typically 5-30m thick) cannot be identified. A certain amount of heterogeneity is, however, still apparent within processed seismic data. This has been characterised by Planke et al. (1999; 2000) who developed a facies classification scheme at the seismic scale (1 to 10s of kilometres). Their scheme is summarised in Table 2.1, and is based on seismic reflection data from the Atlantic and Western Australia volcanic rifted margins. The different facies were identified by their gross form, and the reflection characteristics of their boundaries and internal reflections.

In order to gain a better understanding of offshore basaltic successions, the use of onshore analogues is crucial to the interpretation of seismic data. In Table 2.1 I summarise the possible flow scale components which make up the seismic scale facies described by Planke et al. (1999; 2000). In the offshore region around the Faroe Islands, it has proved possible to correlate onshore observations with offshore seismic data. Ellis et al. (2002) determined the offshore extent of the Lower, Middle and Upper Lava Formations from seismic data. Passey (2004) correlated material from 240km east of the Faroe Islands (Well 214/04-1) with the Lower Basalt

Formation, based on geochemical data, although there is also evidence of a lateral facies change. Seismic interpretation by Single (2004) identified tabular lavas, delta fans, compound braided flows and hyaloclastites, with direct analogues onshore (Figure 2.8). These facies were identified by their characteristic shapes and internal

Facies	Shape	Characteristics	Probable flow scale components
Inner flows	Sheet	High amplitude top reflector, high amplitude parallel internal reflectors	Mixture of compound and tabular facies and volcaniclastics; subaqueous.
Lava delta	Bank	Prograding clinoform internal reflectors	Hyaloclastites and volcaniclastic; coastal
Landward flows	Sheet	High amplitude top reflector, high amplitude parallel internal reflectors	Mixture of compound and tabular facies; subaerial.
Inner Seaward Dipping Reflectors (SDR)	Wedge	Divergent-arcuate internal reflectors, toplap seen on top reflector	Mixture of compound and tabular facies; subaerial.
Outer high	Mound	Strong top reflector, chaotic internal reflector	Hyaloclastites and volcaniclastics; shallow marine
Outer SDR	Wedge	Divergent-arcuate internal reflectors, weaker than Inner SDR	Deep marine compound facies, pillow lavas, sediments and sills.

Table 2.1 Summary of the seismic scale facies of Planke et al. (1999; 2000) and their probable flow scale components (e.g. equivalents of Jerram 2002).

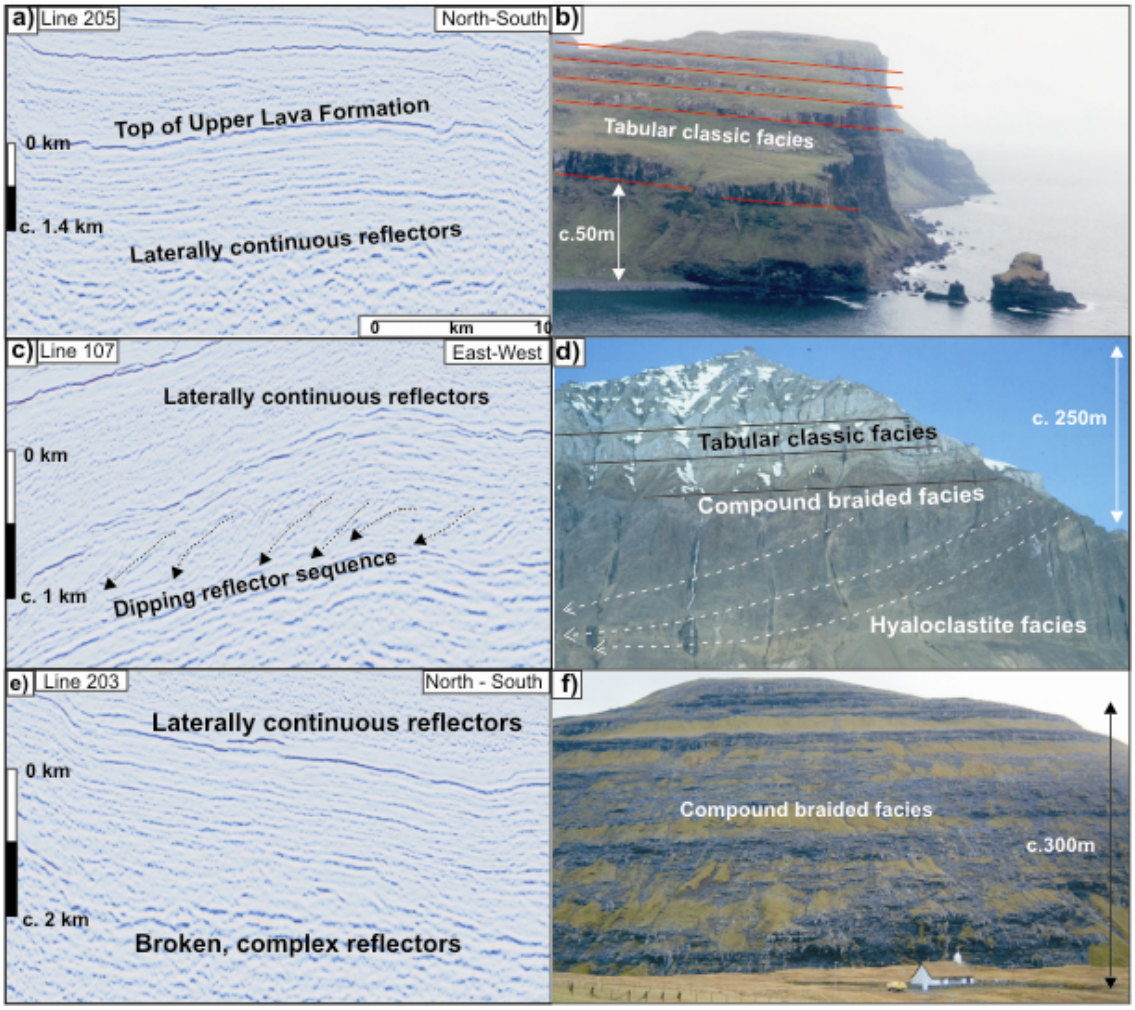

Figure 2.8 Facies observed in seismic sections and onshore analogues. a) Section of GFA-99 line 205 interpreted as showing tabular-type facies. The GFA-99 seismic data was collected approximately 60km SE of the Faroe Islands in the Faroe-Shetland Basin. b) Example of thick tabular flows from Talisker Bay, Skye. c) Section of GFA-99 line 107 showing dipping reflector sequences interpreted as hyaloclastite facies. Section changed from W-E to E-W for comparison with onshore analogue. d) Cliff section in the Nausuaq area, West Greenland shows hyaloclastites dipping and prograding eastwards onto Jurassic sediments. The hyaloclastites are covered by subaerial compound and tabular flows; this section is interpreted as filling a water-filled basin. Photograph courtesy of D.G. Pearson. e) Section of GFA-99 line 203 showing contrasting seismic signatures. f) These different seismic signatures are interpreted as compound braided facies overlain by tabular classic facies. An example of compound braided facies is shown from NW Streymoy, Faroe Islands. Seismic data courtesy of Western-Geco.

reflections, and the thickness and areal extent of these facies were also calculated.

2.4 A geophysical perspective

To improve sub-basalt imaging, it is necessary to understand the effect of a layered, heterogeneous basalt sequence on the seismic wave. This is currently poorly constrained, though it is known that a flood basalt sequence causes scattering and preferentially attenuates high frequencies (Maresh et al., 2006). Knowledge of how the heterogeneity within the basalt sequence affects the seismic wave will enable optimisation of the seismic method. Figure 2.9 schematically highlights some of the geophysical problems that a thick basalt sequence would cause. Accordingly, in the following section some of the issues related to the geophysical response of basaltic sequences will be explored.

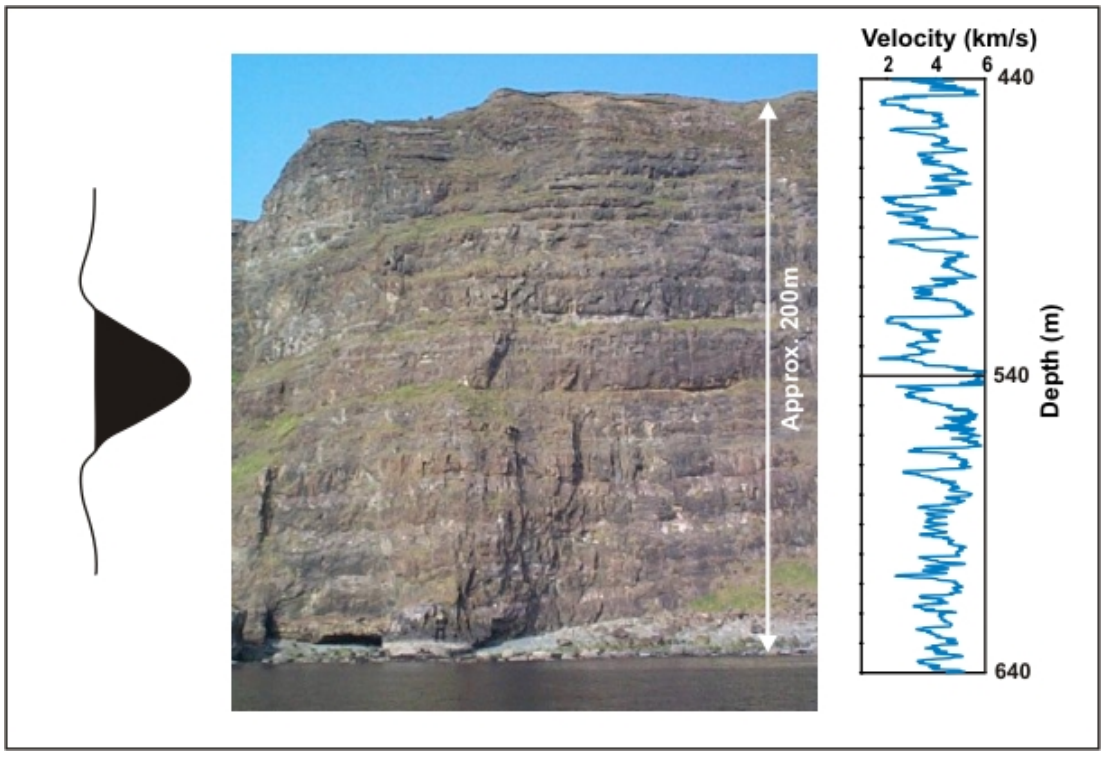

Figure 2.9 Schematic representation of the effects of basalt heterogeneity on the velocity profile through a lava pile. All elements of this diagram are on approximately the same scale. Photo from Skye Main Lava Series showing a typical layered basalt sequence. A seismic wavelet is included for comparison at a frequency of approximately 40Hz, as is commonly used in exploration. A frequency of 10Hz would be four times larger. The velocity profile is taken from ODP Hole 642E (Eldholm et al., 1987) and shows the wide and rapid variation in P-wave velocity.

2.4.1 Relating basaltic facies to geophysical properties

To ascertain how the geological heterogeneity affects geophysical data, it becomes necessary to link physical rock properties to the different facies. Methods to distinguish between facies include the amount of vesiculation, jointing, flow thickness, colour, shape of the feature, and so on. We must determine which of these also affect geophysical data. The different physical properties that affect geophysical surveying methods are summarised in Table 2.2.

We can say qualitatively that these rock properties affect the various geophysical methods, based on our knowledge of, for example, the relationship between jointing and seismic velocity. Unfortunately, no studies have yet quantified the relationship between the physical properties and the geophysical data. The rock properties are complex and change dramatically over centimetre scales.

However, the effect of the variations in rock properties can be observed in borehole data. Both commercial and academic boreholes have penetrated thick basalt sequences and wireline logs recorded include sonic, density, gamma ray and resistivity. A strong correlation is found between recovered core and wireline logs. Examples of borehole data from basalt sequences are discussed further in Chapter 4.

Geophysical method	Operative physical property	Basalt rock properties which may affect this
Seismic	Seismic velocity and density	Vesicularity, jointing, geochemistry, degree of alteration, size of flow, shape of flow
Gravity	Density	Vesicularity, geochemistry, degree of alteration
Resistivity	Electrical conductivity	Vesicularity, geochemistry, degree of alteration, jointing, pore fluid
Magnetic	Magnetic susceptibility and remanence	Geochemistry, degree of alteration

Table 2.2 Rock properties affecting geophysical surveying methods. Adapted from Kearey et al. (2002) and Single (2004).

The EU 5th Framework SIMBA (ENK6-CT-2000-00075) project collated a database from various wells in the North Atlantic (Single, 2004). From this, the range of P-wave velocities and densities present for the different intrafacies has been identified, and the results are shown in Figure 2.10. It is immediately apparent that there is a wide velocity range within a basalt succession, which must be taken into account in geophysical models involving basalt sequences. Boles, volcaniclastics, flow bases and flow tops all have a relatively low P-wave velocity (around 2.5-4.5 km s^{-1}) whereas dykes, flow cores and sills have a relatively high P-wave velocity (around 4.5-6 km s^{-1}). A similar pattern is observed for density, although boles, volcaniclastics and hyaloclastites have a wide range. It is also obvious that the range

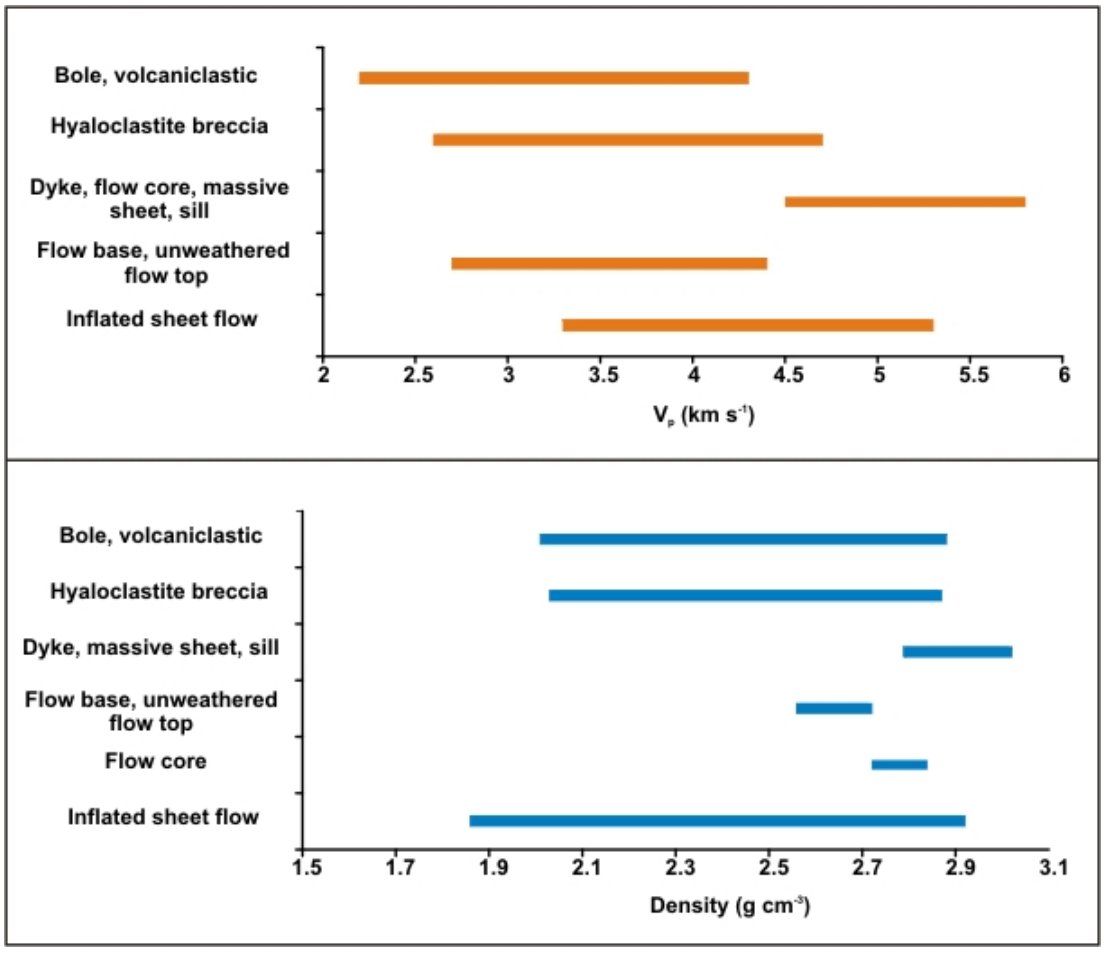

Figure 2.10 Physical properties of different intrafacies. a) P-wave velocities for the different intrafacies. It can be seen that there is a wide velocity range. Massive intrafacies such as dykes and flow cores are faster, while more vesicular intrafacies such as boles are slower. The inflated sheet flow shows a range. b) Densities for the different intrafacies. Again, there is a wide range, from high density flow cores to low density boles. Data from the SIMBA database.

of velocities and densities alone is not useful in distinguishing between the intrafacies. In Chapter 4, wireline log data are examined in more detail to identify facies based on their log responses.

2.4.2 How does heterogeneity affect seismic data?

I have discussed in previous sections how basalt sequences are heterogeneous at a variety of scales. As discussed in Section 2.2.1, a basalt sequence causes attenuation of high frequency seismic waves by scattering and the production of multiples. In this section, the theoretical basis for the effect of heterogeneity on the seismic wave is examined, focussing in particular on the different types of scattering caused by different scales of heterogeneity. A heterogeneity, as discussed in this section, is for example a lava flow crust, which is different to the flow core above and below it. A flow crust is typically of the order of one to ten metres thick, depending on the overall flow thickness, so an average heterogeneity for a lava crust could be considered as 5m.

Figure 2.11 shows the interplay between the size of the heterogeneity, the seismic wavelength of the input pulse, and the length of the travel path of the seismic wave. The labelled boxes correspond to the approximations that can be used to correct for the scattering, and thus obtain clear reflections. “Geometric optics” are the simple rules of reflection and refraction. The heterogeneity (a) is large relative to the wavelength (λ) and the travel path (L). Therefore, a coherent reflection is received from the boundary of the heterogeneity, and it can be imaged. In the “Diffraction theory” region, it is still possible to image the heterogeneity, provided that diffraction is taken into account and single scattering approximations (e.g. Born theory, Aki and Richards 1980) can be used.

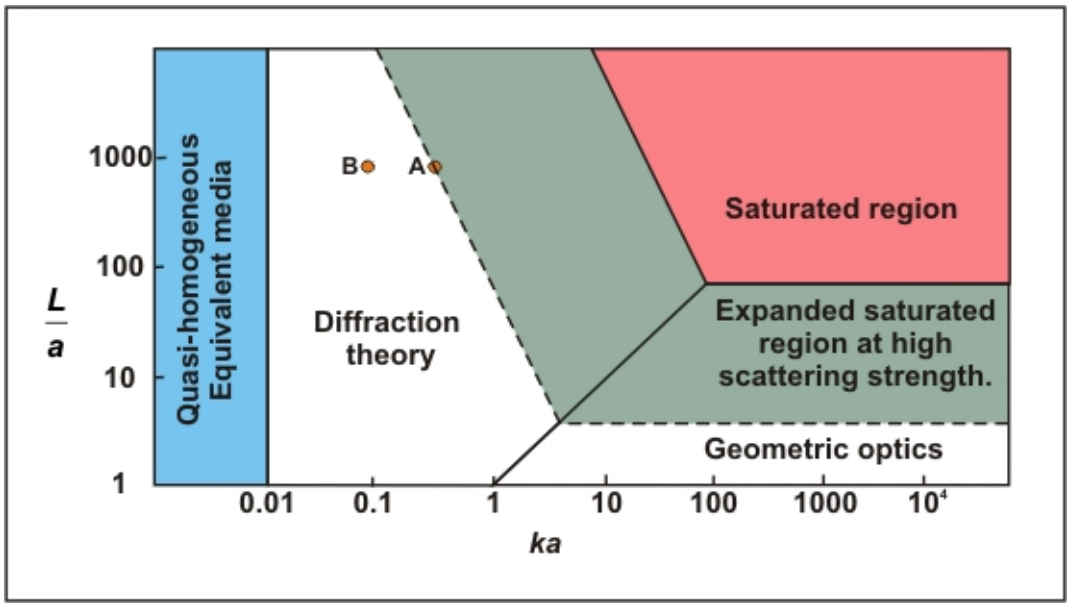

Figure 2.11 Classification of scattering problems in heterogeneous media. Regions where different methods of analysis can be used are highlighted. *L* is the extent of the heterogeneous region, or the distance the seismic wave travels (the travel path). *a* is the size of the heterogeneity. *k* (the wavenumber) is $2\pi/\lambda$ where λ is the wavelength. Adapted from Wu and Aki, 1988.

"Quasi-homogeneous" means that the seismic wave only responds to the average properties of the region it travels through – the heterogeneity is so small relative to the wavelength that it does not affect the seismic wave. No measurable reflection is received from the boundary of the heterogeneity.

In the "Saturated region", the seismic wave encounters a large number of heterogeneities that are large relative to the wavelength. The seismic energy undergoes multiple reflection events creating a complex path, which can no longer be analysed by conventional approximations. The saturated region expands or contracts depending on the scattering strength – this is greater if the heterogeneities exhibit a large velocity and density contrast. Figure 2.11 shows how the saturated region expands for a material with a high scattering strength such as a layered basalt sequence.

If we consider a layered basalt sequence with a thickness of 2000m, the two-way travel path of a seismic wave through this sequence (L) has a value of 4000m. A typical heterogeneity size (a), for example a flow crust as described above, would be

around 5m. $\frac{L}{a}$ in this case is 800, which plots on the y-axis of Figure 2.11. If a high frequency seismic wave, with a frequency of 40Hz, passes through the basalt sequence, λ is 100m if the average velocity is 4000m s^{-1}. ka (on the x-axis) is thus approximately 0.3 (Point A on Figure 2.11). If a low frequency seismic wave (10Hz) passes through this basalt sequence, ka is approximately 0.79 (Point B on Figure 2.11). It can be seen that a low frequency wave (Point B) falls within the "Diffraction regime", whereas a high frequency wave falls on the boundary of the "Saturated region". This more complex scattering at high frequencies explains why low frequency waves have produced better imaging through basalt sequences.

Figure 2.11 may also be able to predict which approximations could be used when attempting to image the different facies. It may be able to give information on which facies can be better imaged. For example, a hyaloclastite sequence has small internal impedance contrasts, so it has a weak scattering strength. The saturated region is smaller in this case, so the likelihood of clear imaging is greater. A sequence comprising compound-braided facies would contain many strong impedance contrasts between the flow crust and the flow core. Its scattering strength would therefore be stronger, and the saturated region would be larger. Later chapters will characterise the size of the heterogeneities in the different facies, the average velocity within the facies, and the thickness of the sequence. This would allow the construction of diagrams similar to Figure 2.11, with appropriately sized regions depending on the scattering strength.

2.5 Conclusions

This chapter reviews previous work on facies analysis of volcanic rocks and shows how it can be useful in geophysical exploration of areas of flood basalt cover. As discussed above, a systematic facies classification scheme has been established, and this has been applied in several flood basalt provinces worldwide. Facies can be described at scales from a few metres (intrafacies) to several kilometres (seismic scale facies). However, these facies only become useful for geophysical modelling when quantitative information is attributed to them. For example, lava flow sizes, shapes, stacking patterns and proportions of flow crust and core are necessary to fully describe the tabular-classic or compound-braided facies. It is also necessary to

attribute properties such as P-wave velocity and bulk density to the component parts of a lava flow.

Accordingly, later chapters develop methods of quantifying the facies architecture of a flood basalt province and attributing physical properties. Most of the data comes from the North Atlantic Igneous Province, and the most abundant facies are tabular-classic flows, compound-braided flows, hyaloclastites and intrusions. From a geophysical perspective, the most important factor at a smaller scale is the difference between the seismic velocity of the flow core and flow crust. The primary focus of the thesis is therefore to develop 3D models of these facies from outcrop analogues, taking into account the sharp changes in velocity within those facies containing lava flows. 3D modelling of the seismic scale facies of Planke (2000) is beyond the scope of this work, as it would require high quality 3D seismic data linked to borehole data.

3

3. METHODOLOGY AND DATASETS 35

3.1 CHAPTER SUMMARY 35

3.2 BOREHOLE DATA 35

3.3 TERRESTRIAL LASER SCANNING 36

3.3.1 Principles and equipment details 36

3.3.2 Data acquisition 38

3.3.3 Data processing 40

3.3.4 Previous work 43

3.4 THE GSI3D SOFTWARE 45

3.4.1 Background 45

3.4.2 The GSI3D methodology 46

3.4.3 Previous work 49

3.5 GOCAD 49

3.5.1 Introduction to the software 49

3.5.2 Key concepts 50

3.5.3 Model creation with GOCAD® 52

3. Methodology and datasets

3.1 Chapter summary

This chapter summarises the principal methods, datasets and computer software used in the thesis. I briefly describe some of the relevant information and background for the methods and data used in this study, which are in turn explored in more detail in each chapter. Borehole data are used in Chapters 4 and 7; terrestrial laser scanning is used in Chapters 5 and 6; the GSI3D software is used in Chapter 5; and the GOCAD® software is used in Chapters 5, 6 and 7.

3.2 Borehole data

Six boreholes are used in this thesis: three onshore boreholes from the Faroe Islands, and three offshore from the North Atlantic. The Faroe Islands boreholes are Lopra-1/1A, Glyvursnes-1 and Vestmanna-1, and data are courtesy of Jarðfeingi, the Faroese Earth and Energy Directorate. Previous publications on these boreholes include Berthelsen et al. (1984), Japsen et al. (2005) and Chalmers and Waagstein (2006). The offshore boreholes are two IODP boreholes, 642E and 917A (Eldholm et al., 1987; Larsen et al., 1994) and one commercial well, 164/07-1 (Archer et al., 2005). These data were chosen to provide a range of volcanic facies and settings, and the Faroese boreholes can easily be related to onshore analogues. The two IODP wells chosen contain the largest basalt sequences drilled by the IODP in the North Atlantic.

For each of these boreholes, different wireline logs were available, including VP (P-wave velocity) VS (S-wave velocity) AI (Acoustic Impedence), RHOB (density), NPHI (neutron porosity) and CAL (calliper). The available logs are detailed in Chapter 4. The wireline log data were obtained in digital format, and imported into Microsoft Excel. From this the data could be exported to specialist log interpretation software such as ODM (Oilfield Data Management, http://www.senergyworld.com). These data are used extensively in Chapter 4, and also in Chapter 7.

3.3 Terrestrial laser scanning

Terrestrial laser scanning is used to capture 3D digital data which are used in Chapters 5 and 6. This is a relatively new technique within the earth sciences and its basic principles are outlined below.

3.3.1 Principles and equipment details

Terrestrial laser scanning has become increasingly popular amongst geologists, as it allows 3D data to be captured which can be analysed away from a field situation. 3D point clouds thus obtained can be analysed to provide quantitative structural or geological data (e.g. McCaffrey et al. 2005, 2008). The laser scanner measures the XYZ coordinates of points on the outcrop at specified intervals by calculating the distance from the scanner based on the return time of the laser beam. These points can then be coloured from digital photos to give an accurate representation of the outcrop, which can then be viewed from any angle and features on it can be measured. This is particularly useful for inaccessible parts of outcrops. Multiple scans from different angles are obtained to minimise shadow areas where parts of the outcrop hide other areas from the scanner viewpoint. Reflectors are used to provide common points of reference between scan and photo, and between scans. Previous studies have documented in detail the standard workflow for capturing and processing TLS data (e.g. Buckley et al., 2007; Enge et al., 2007) and the basic details are summarized here.

The equipment used in this work is a Riegl LMS-Z420i terrestrial laser scanner, frequently used in geology and optimized for rapid data acquisition, a long range and usage in demanding environmental conditions. A schematic view of the equipment is given in Figure 3.1 and its usage is shown in Figure 3.2. The vertical field of view is 80° and the accuracy can be 4mm with repeated scans. The resolution depends on the settings chosen. The range varies depending on the reflectivity of the outcrop surface, angle of incidence of the laser beam, and the weather conditions (see Figure 3.3). The range is greater in clear air, when the outcrop is perpendicular to the travel path of the laser beam, and on lighter coloured outcrops. The attached camera is a Nikon D70 camera capable of 6 megapixel resolution, with 14mm, 50mm and 85mm calibrated lenses available.

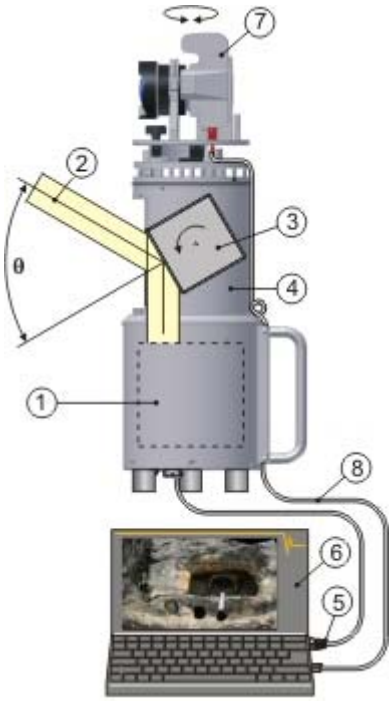

Figure 3.1 Schematic view of Riegl LMS-Z420i terrestrial laser scanner. Image from http://www.riegl.com. (1) Range finder electronics. (2) Laser beam. (3) Reflective polygon - rotates rapidly to fire and collect laser beam. (4) Rotating optical head allows 360° coverage. (5) TCP/IP Ethernet interface. (6) Ruggedized laptop. (7) Nikon D70 digital camera. (8) USB camera interface.

Figure 3.2 The LMS-Z420i equipment in action in the Faroe Islands.

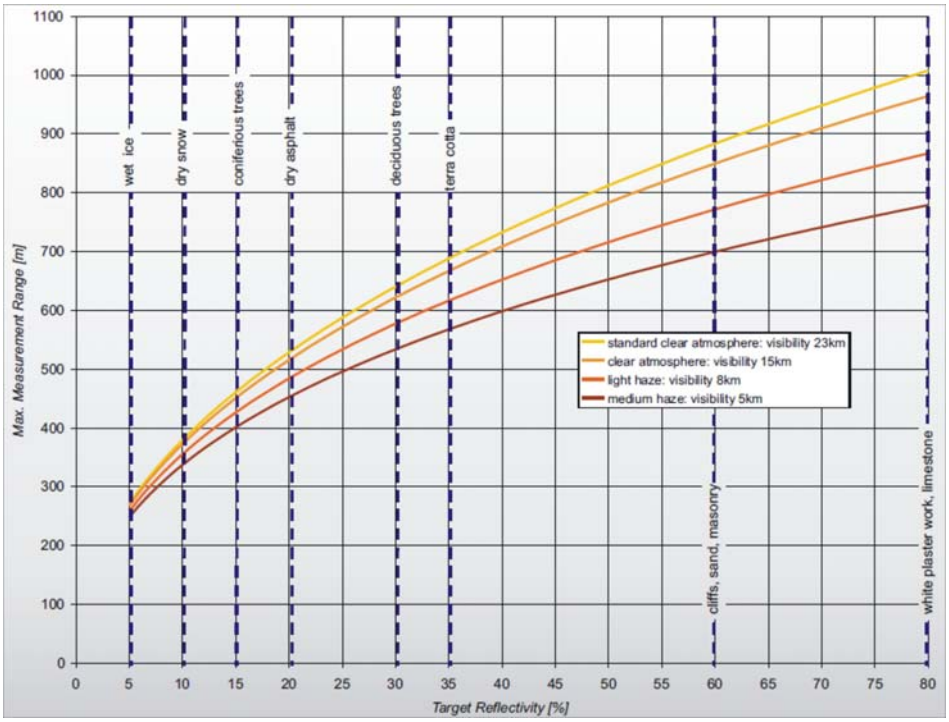

Figure 3.3 Range data for the LMS-Z420i laser scanner. From http://www.riegl.com. This graph assumes a flat target, average brightness and a perpendicular angle of incidence.

3.3.2 Data acquisition

Acquisition of TLS data can take the following steps:

1. The scan positions are located to minimise shadow areas on the outcrop. The angles of the outcrop face are considered and any areas not seen from one scan position should be visible from another. An example of this is given in Chapter 5, and also in Buckley et al. (2008).
2. The reflectors are placed around the site area so that they are visible in as many scans as possible. Larger reflectors (10cm and above) are used to tie scans together, and smaller reflectors are used to tie the camera images to the scan point cloud.
3. Scan data are acquired. The scanner must be connected to a portable battery and a laptop (see Figure 3.4b). An overview scan is taken for a 360° view, then a fine scale scan is taken of the area of interest. The resolution of the

scan is specified at this point, and generally this is dependent on the results required and the time available. A resolution of a centimetre or even finer can be obtained, but this also depends on the distance between the scanner and the outcrop.

Figure 3.4 shows the data acquisition process on Skye, along with some of the logistical challenges to acquiring TLS data. These are discussed further in Chapter 5. It should be noted that at the time of writing new laser scanning equipment is coming onto the market with built-in high resolution GPS which reduces the need for a large number of reflectors.

Figure 3.4 Data acquisition on Skye. a) Transporting the equipment. b) Setup procedures. c) Operating the equipment.

3.3.3 Data processing

Most data processing is carried out away from the field, and in this case the Riscan Pro software was used. This is proprietary software developed by Riegl for use with their laser scanning equipment (http://www.riegl.com). The major data processing steps are as follows:

- The digital photographs must be linked to the scan point cloud.
- Multiple scans must be correctly located to merge the scans.

These processes are illustrated below using an example from Brancepeth Castle, near Durham. The castle courtyard is approximately 100m across, with a wall around the outside and buildings around part of the courtyard. Scans were acquired from the centre of the courtyard and from the roof of the main building in summer 2007, and provide an easy way of illustrating the methods of data processing. A point cloud from the castle is shown in Figure 3.5a, with photographs in Figure 3.5b.

Linking photographs to the point cloud

Figure 3.6 shows screenshots from Riscan Pro of the steps required to link the photographs to the point cloud. Reflectors are spaced around the area of interest, as described in Section 3.3.2, and these can be identified in the digital photographs. The software automatically gives each reflector a rough position within the photograph, based on a pre-existing camera calibration matrix. The calibration matrix defines the rotation and translation that must be applied to the photographs to project them onto the point cloud in the correct position, and this is required because the camera is in a different location to the scanner itself. Fine-tuning the position of each reflector in each photograph is done manually, and this makes the camera calibration more accurate. A fine scan of each reflector is also carried out when scanning (Figure 3.6b) so that the position of each reflector is known very accurately. Following this step, the photographs can be accurately projected onto the point cloud, as shown in Figure 3.5c.

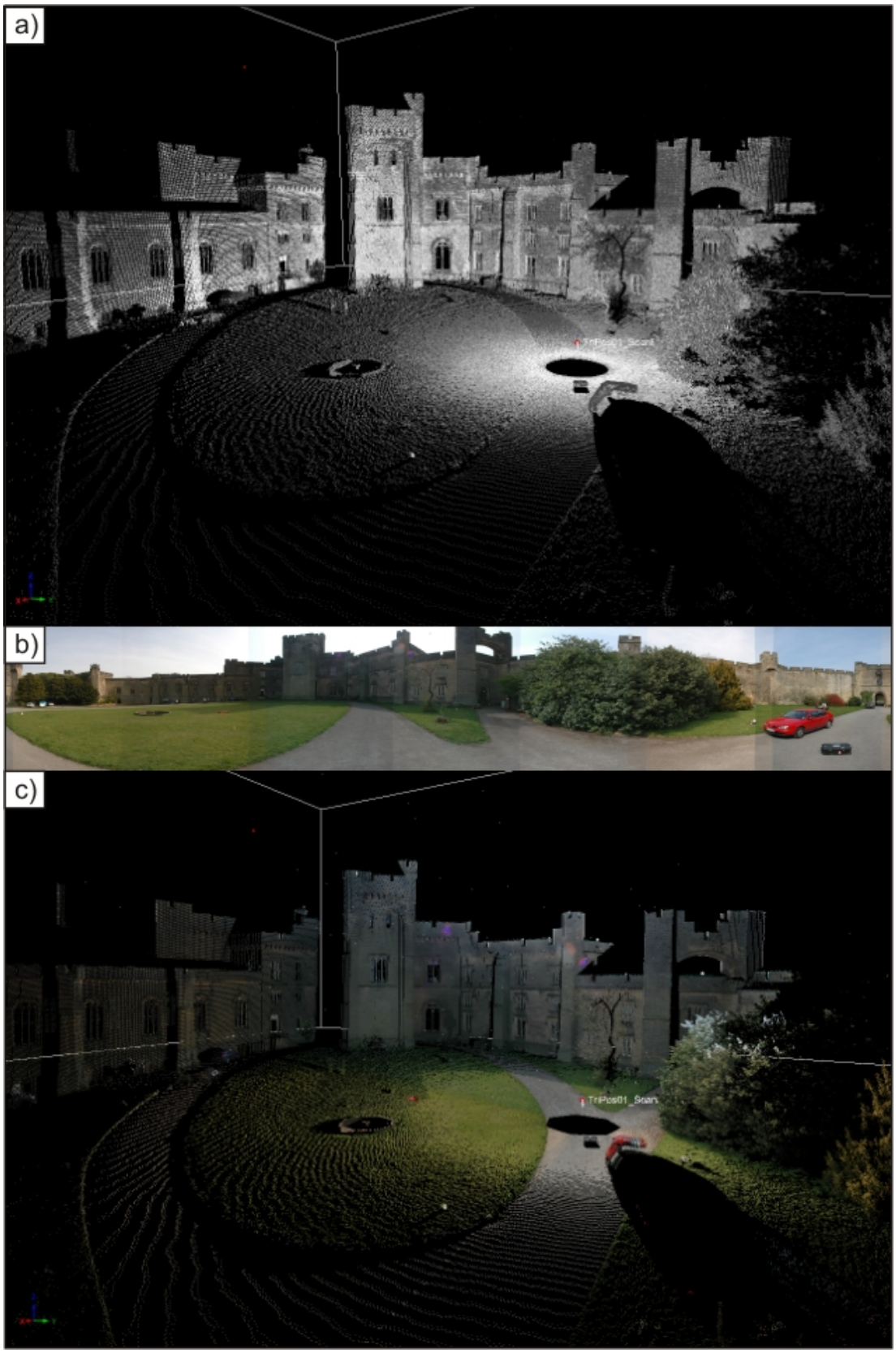

Figure 3.5 a) TLS point cloud for Brancepeth Castle. b) Panorama made from stitched photographs from one scan position. c) The point cloud coloured from the digital photographs.

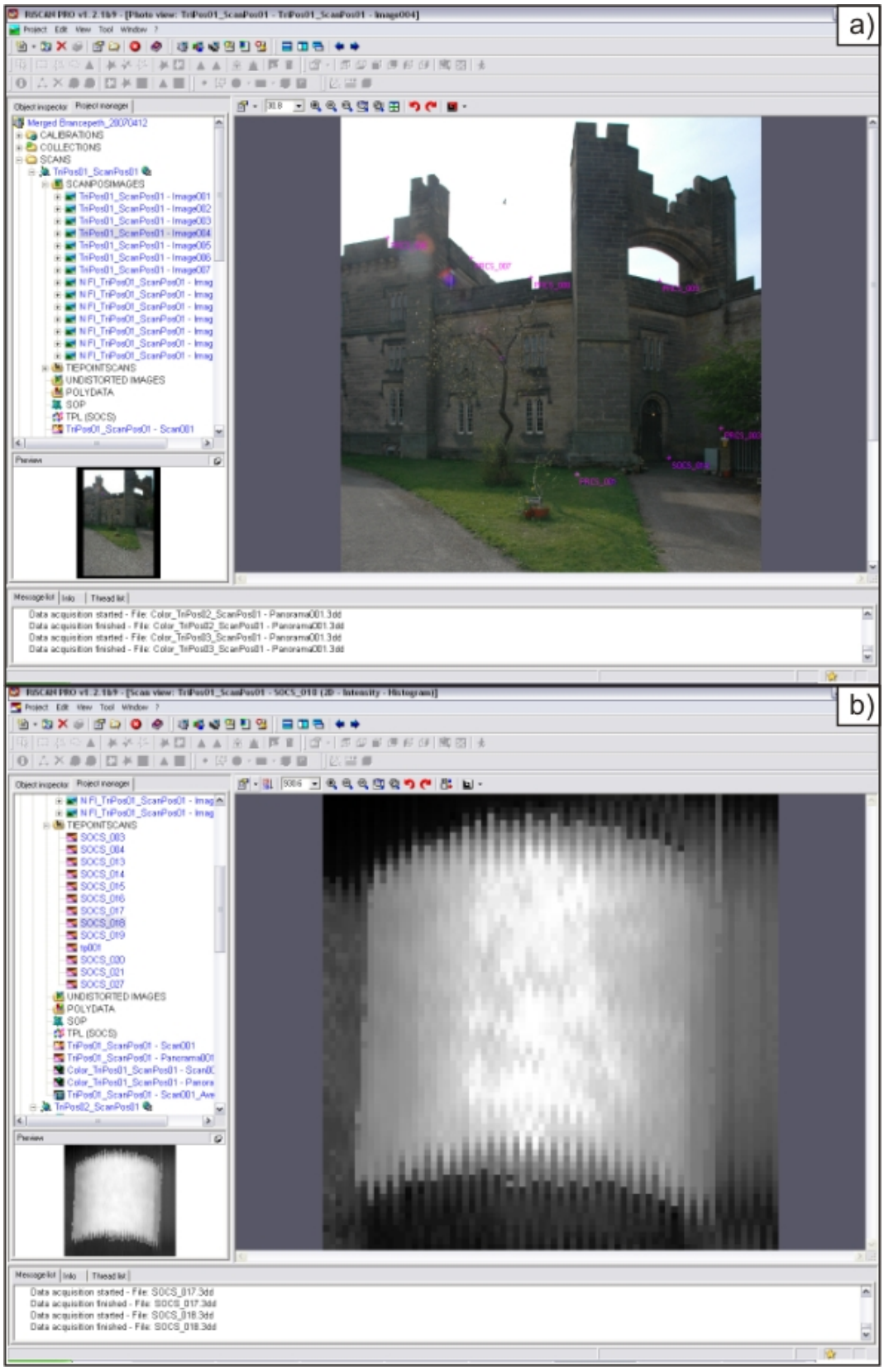

Figure 3.6 Initial data processing using Riscan Pro. a) Photograph showing positions of reflectors. b) Fine scan of a 22cm reflector.

Merging scans

In addition to the camera calibration matrix, a second matrix is required when multiple scan positions are used. This applies a rotation and translation to entire scans to bring them all into the same coordinate system. This matrix is calculated by having reflectors which are visible in more than one scan position - ideally at least five reflectors should be shared between scans. The reflectors are identified in each scan then manually linked between scans. The merging process is shown in Figure 3.7.

The completed models can then be viewed from any angle, interpretations made and features measured. The models can also be exported to other software packages, such as those described in Section 3.4 and 3.5.

3.3.4 Previous work

3D geological models created using TLS are used in areas such as fluid flow modeling (e.g. Rotevatn et al., 2009) and reservoir modeling (Pringle et al., 2004). Until recently much of the work developing and using these virtual outcrops has been aimed at sedimentary problems (e.g. Bellian et al. 2005; Labourdette and Jones, 2007), and structural problems (Wilson et al., 2009; McCaffrey et al., 2008), with few examples in the field of volcanology.

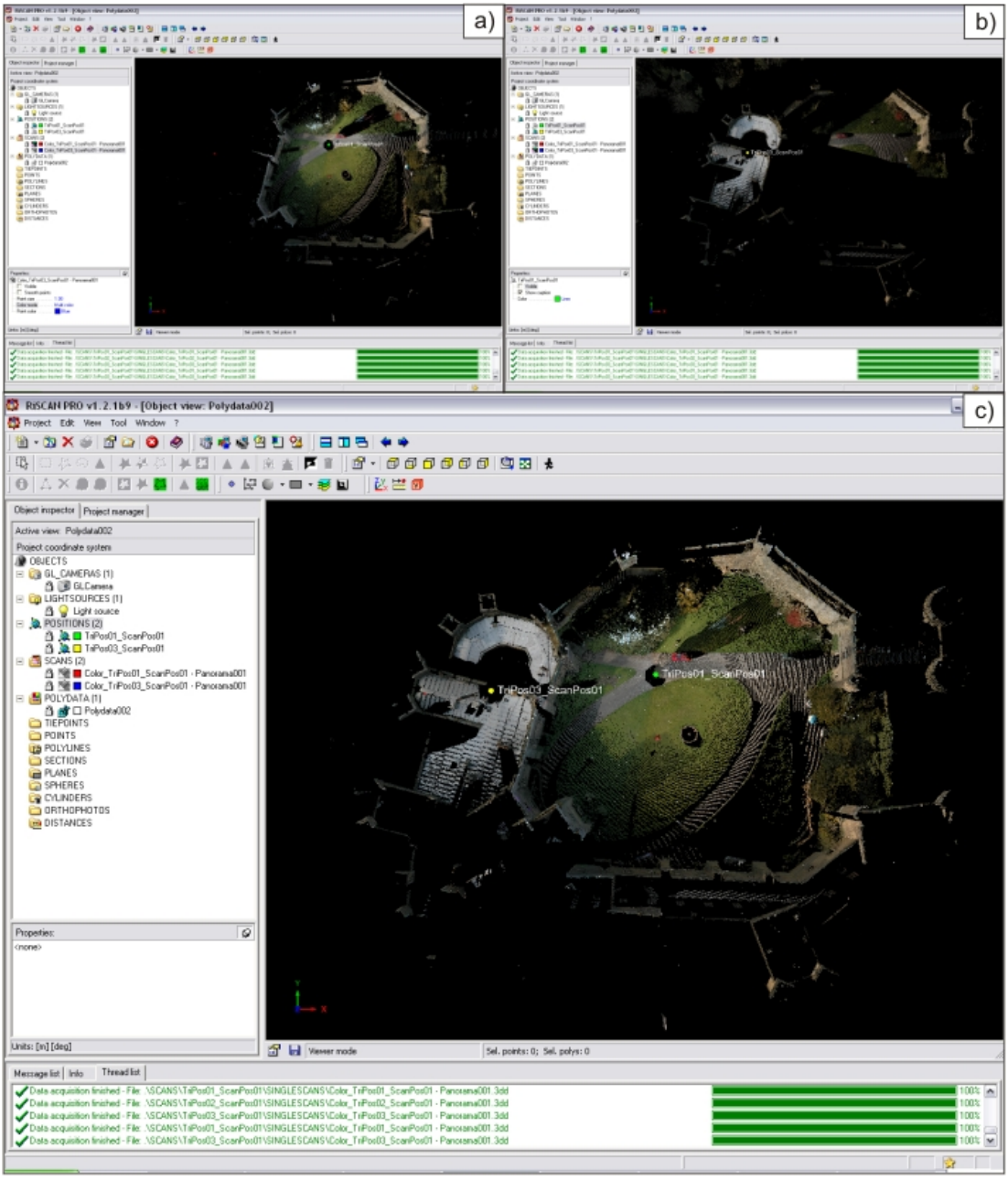

Figure 3.7 Merging scans. a) Scan from the centre of the courtyard. b) Scan from the rooftop. c) Merged scans.

3.4 The GSI3D software

This section introduces the GSI3D (Geological Surveying and Investigation in 3 Dimensions) software, used extensively in Chapter 5. Here, I cover previous work using the software and its theoretical basis. The details of incorporating laser scanning data and building 3D models of flood basalt lava flows using GSI3D can be found in Chapter 5.

3.4.1 Background

GSI3D is a software package for the construction of 3D geological models. It is designed to be intuitive for a geologist to use, as models are constructed from cross-sections, geological maps and boreholes, all of which are familiar forms of data. It also allows the user to manipulate the final model to fit their geological understanding.

Initially, GSI3D was developed by Hans-Georg Sobisch at INSIGHT GmbH in collaboration with the Geological Survey of Lower Saxony (Germany). The British Geological Survey (BGS) has been using and developing the software since 2001, building systematic 3D models using its extensive map and borehole data (e.g. Figure 3.8). The software was originally designed for modelling superficial deposits, however since 2007 the BGS have been further developing the software and methodology to allow the construction of faulted bedrock models. For further information on the development of GSI3D, see Kessler et al. (2009).

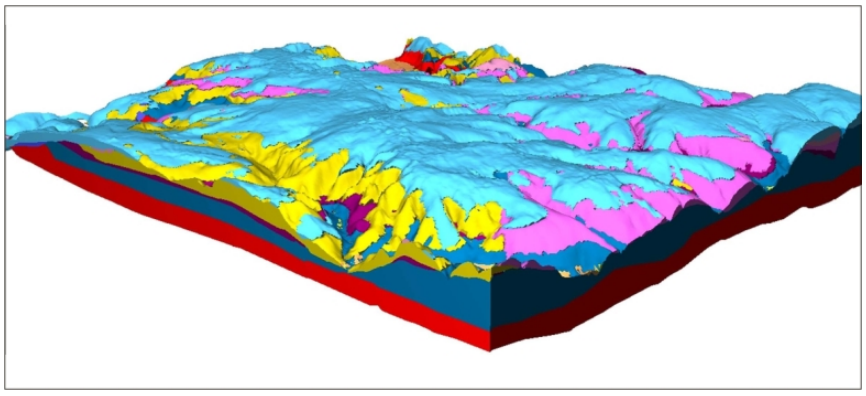

Figure 3.8 Example of a complete GSI3D model from the BGS. Sudbury area, Suffolk, UK. From Kessler et al., 2009.

3.4.2 The GSI3D methodology

For further information, the manual for GSI3D version 2.6 is available to download from http://nora.nerc.ac.uk/4903/1/GSI3D_manual_V2_6_OR08064.pdf .

GSI3D can import the following data formats:

- Digital terrain models (ASCII grid files)
- Digital borehole data (tab-separated ASCII files)
- Geological map data (ESRI shape files)
- Geo-registered sections (.jpg)
- GOCAD triangulated surfacse (.ts)
- Raster maps (.jpg)

Data are imported into a project (saved as .gmxl format). Each project requires a Generalised Vertical Section (GVS) and legend (.gleg) file. The GVS contains the stratigraphic order of the geological units within a project in a tab-separated ASCII file. It defines the "stack" of units which is calculated to construct the 3D geological model. The legend file describes the colours and textures assigned to the geological units, again as a tab-separated ASCII file. Examples of the GVS and legend files are available in the manual (Mathers and Kessler, 2008).

The GSI3D interface consists of four windows: the map, cross-section, 3D and borehole windows (see screenshot below). All of these are dynamically linked - changes in the map or cross-section window update the other windows. A typical workflow for the construction of a 3D model would be as follows (also see Figure 3.10):

1. Set up GVS and legend files.
2. Import map linework, borehole data and/or rough 3D surfaces.
3. Define a cross-section network covering the area of interest (see Figure 3.9).
4. Draw cross-sections including all the geological units, honouring their mapped locations and borehole occurrences.
5. Define the plan-view extent of the units (envelopes).

6. "Calculate" - interpolate 3D volumes between cross-sections (see Figure 3.9).
7. Refine cross-sections until the correct 3D model is achieved.

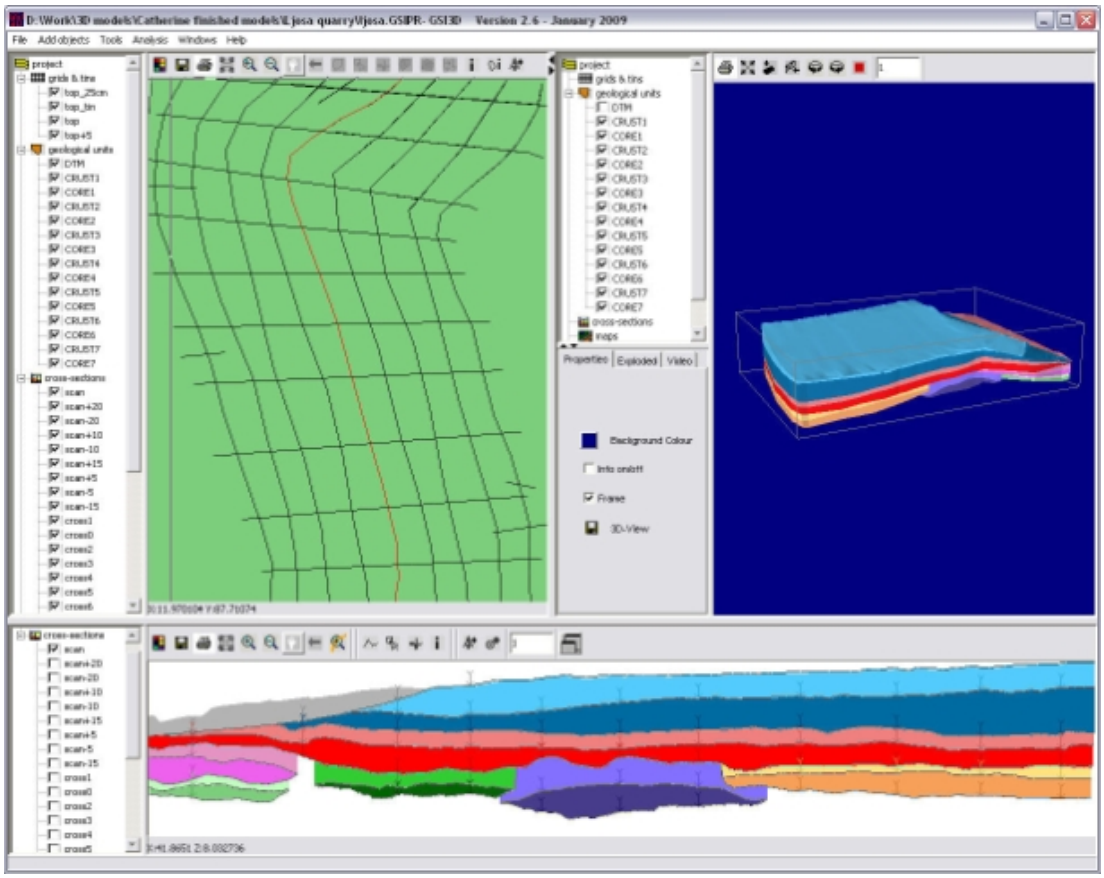

Figure 3.9 Screenshot of GSI3D version 2.6, showing the map, 3D and cross-section windows.

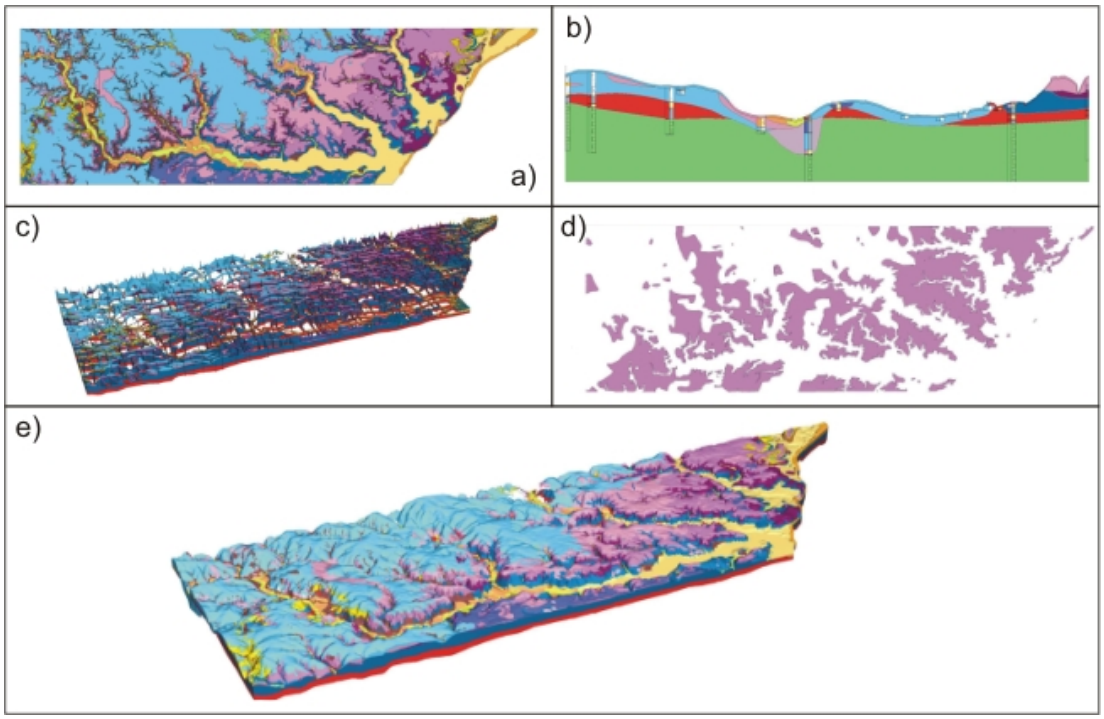

Figure 3.10 1200 km^2 model of the Sudbury – Ipswich – Felixstowe area, East Anglia. From Kessler et al., 2009. a) Imported geological map. b) Correlated cross-section. c) Fence diagram. d) Unit distribution. e) Completed block model.

The interpolation of 3D volumes in GSI3D requires further explanation. First, a basal surface for each geological unit is constructed. Nodes are supplied by the cross-sections and the limits of the envelope for each unit. Next, a triangulated irregular network (TIN) is interpolated between the nodes, following a bespoke Delaunay-triangulation algorithm (Kessler et al., 2009). 3D objects are then created by capturing the base of the overlying unit (according to the GVS) or the DTM at the top of the model, and vertical side walls inserted at the edge of the project. This results in a triangulated, topologically sound 3D object for each geological unit (see Figure 3.10). The process of triangulation results in smoothing between the nodes, however it is possible to insert further cross-sections as required and recalculate the model. Cross-sections can also be inserted in any areas of the model that do not fit with the interpreted geology of the project area.

The GSI3D methodology has a few drawbacks: surfaces are smoothed between nodes, though this is common to most packages using TINs. It is difficult to model vertical or steeply dipping intrusions. This can partly be resolved by modelling the

intrusions as lenses, independent from the stratigraphy. At present, the GSI3D software cannot model faults or repeated stratigraphy (e.g. recumbent folds) though work is in progress on a new version which will handle these scenarios.

3.4.3 Previous work

Most previous work using the GSI3D software has been carried out by the BGS. A major use has been for Environment Agency projects, using the software to model superficial deposits to investigate groundwater flow and aquifer vulnerability. For example, Lelliott et al. (2006) give an overview of the construction of a 3D model of the Manchester and Salford area to investigate aquifer recharge. Recently, the BGS has begun to construct systematic 3D models of British geology at a variety of scales, providing a 3D version of traditional geological maps (Kessler et al., 2009). GSI3D has also been used with geophysical data including ground-penetrating radar (Rogers et al., 2009), and for urban landuse planning (Royse et al., 2008).

3.5 GOCAD

3.5.1 Introduction to the software

GOCAD® (Geological Object Computer Aided Design) is a software package used to model complex 3D volumes in geology. It was developed in the 1990s by a group at the University of Nancy, France, and conceived as an alternative to CAD packages used in the manufacturing industry (http://www.gocad.org). The current version of the software is used primarily in the oil industry for 3D subsurface modelling, but has also found many academic applications. It is now developed and distributed by Paradigm™, and the versions used in this work were 2.1.4 and 2009.2. Single (2004) reviews the object types and methodologies for an earlier version of GOCAD®. The basic principles remain the same, but the user interface is much improved and many extra functions have been added. GOCAD® requires a large amount of memory when working with datasets such as those used in this work, and at least 4GB of memory is recommended by Paradigm™.

Applications of GOCAD® include:

- Structural geology - constructing fault surfaces, fault modelling
- Reservoir modelling - geostatistics, flow simulation

- Geophysical modelling - 3D velocity modelling, 3D seismic interpretation

More information is available from the Paradigm™ website (http://www.pdgm.com) and the Gocad consortium website (http://www.gocad.org).

3.5.2 Key concepts

GOCAD® has many functions and data types, which are described fully in the user manual. Here, I introduce two key concepts from the GOCAD® methodology which are used extensively in this work: surface creation from points and curves; and 3D modelling using Voxets.

Surface creation

A GOCAD® surface is made up of interconnected triangles, with nodes at the corner of each triangle. The nodes can be imported into GOCAD® as a PointsSet (Figure 3.11a) and the surface created from the PointsSet (Figure 3.11b).

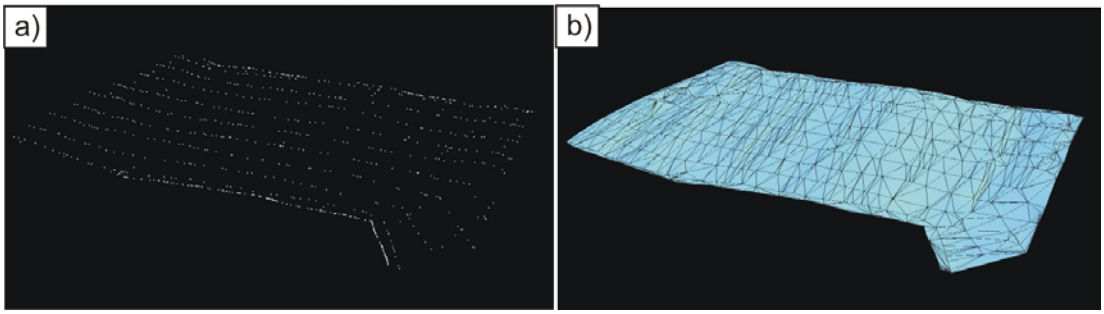

Figure 3.11 Creating a GOCAD® surface from points. a) Imported points from GSI3D. b) Completed GOCAD® surface.

GOCAD® uses a Delaunay triangulation algorithm to build the surface from the points. For a 3D grid of points, there are a number of different ways that the points may be connected, especially when points have the same x,y position but a different z coordinate. Figure 3.12 shows how GOCAD® builds a surface in such a case. Different configurations are possible if a "normal" to the surface is specified. A Discrete Smooth Interpolation (DSI) algorithm is used to build a surface in areas of little data. For more information see Royer (2004).

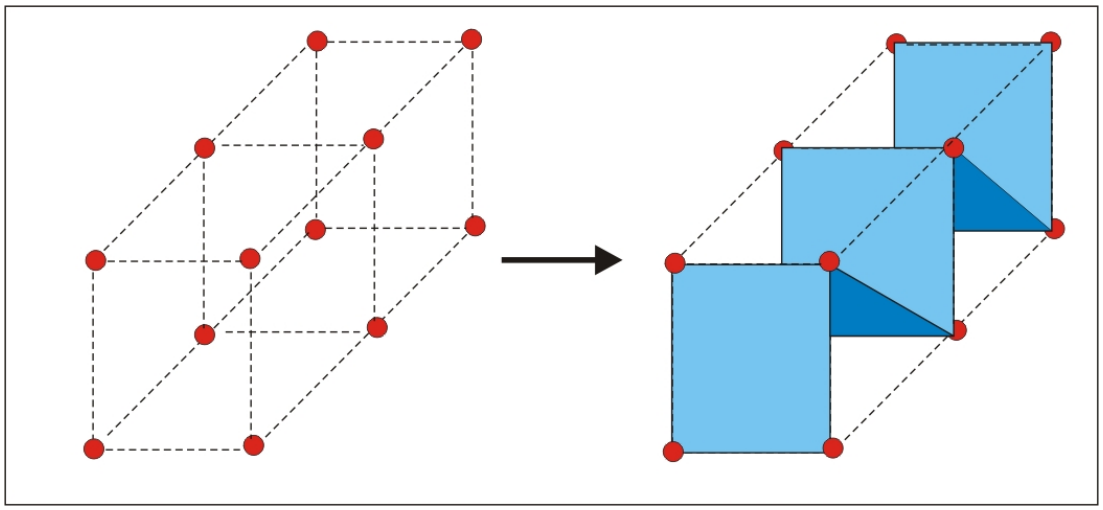

Figure 3.12 The default configuration for creating a surface from a grid of points in GOCAD®

Voxet modelling

In GOCAD®, 3D modelling can be carried out using a Voxet, or volume object. The Voxet is a regular 3D grid consisting of a set of points at a fixed spacing. The axes can be in any orientation. Each cell has eight corner points, and the data point for each cell is at the centre point of the cell. Properties can be attributed to each cell, such as position, seismic velocity, density and so on.

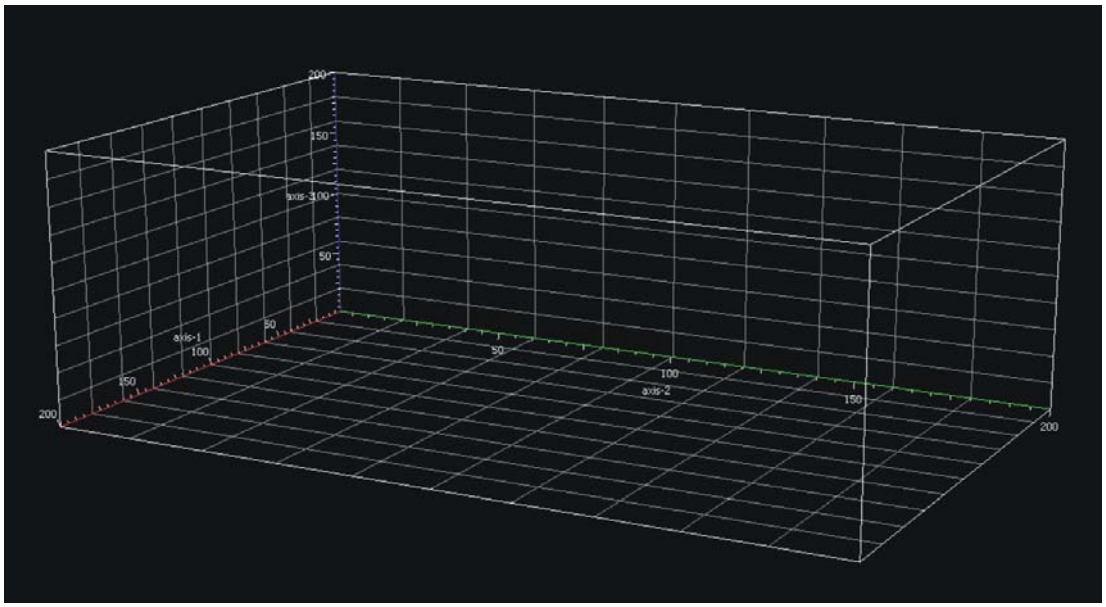

Figure 3.13 Example of an empty voxet showing cells, with grid lines every 40 cells.

Voxets can be divided into sub-volumes, called “regions”. These can be created by dividing the Voxet using surfaces, and for this to be successful the surfaces must not have borders within the Voxet. The surfaces can either have a greater extent than the Voxet, or be an entirely closed volume. Once regions have been created, a property may be given a different value for cells within different regions.

3.5.3 Model creation with GOCAD®

The voxet modelling and surface creation capabilities of GOCAD® can be used in a number of geological applications (e.g. Jerram and Robbe, 2001; Bellian et al., 2005). Figure 3.14 below shows an example of building surfaces to correlate stratigraphic logs from a basalt sequence on Skye.

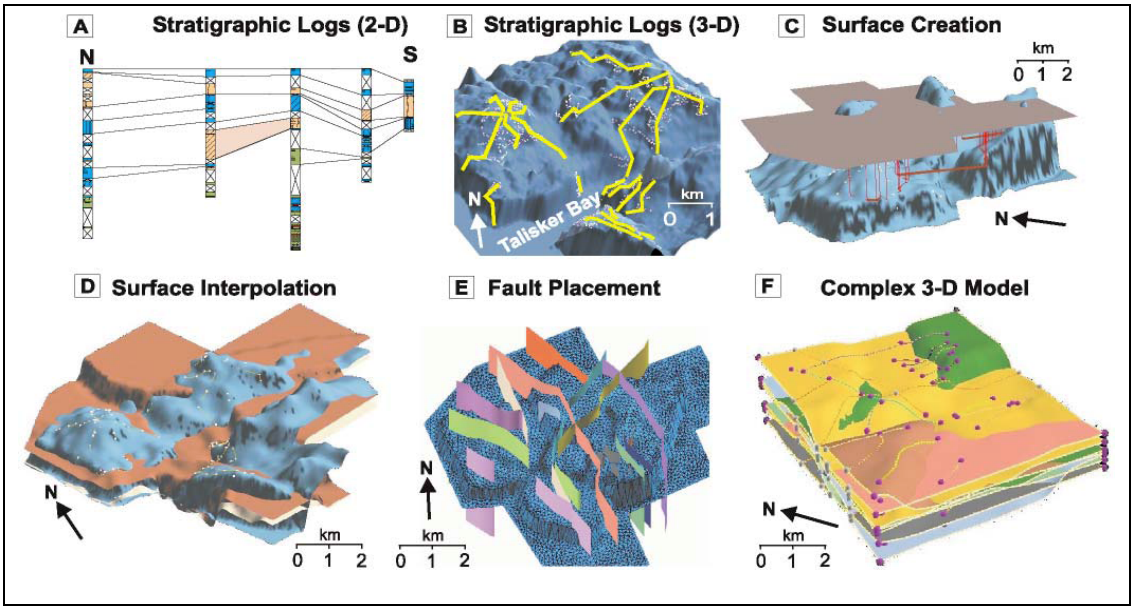

Figure 3.14 Model creation in GOCAD® from stratigraphic log data. From Single and Jerram, 2004.

4

4. FLOOD BASALT FACIES FROM BOREHOLE DATA 54

4.1 CHAPTER SUMMARY 54

4.2 INTRODUCTION 54

4.2.1 The internal structure of flood basalt lava flows 54

4.2.2 Terminology 56

4.2.3 Interpreting wireline log data in flood basalt provinces 56

4.3 FAROESE CASE STUDY 58

4.3.1 Analysis of the Lopra-1/1A, Vestmanna-1, and Glyvursnes-1 borehole data 58

4.3.2 Methodology 60

4.3.3 Results of data analysis 64

4.3.4 Understanding the lava flow signature: Comparing tabular-classic and compound-braided facies 66

4.4 IDENTIFYING FACIES DISTRIBUTIONS IN UNCONSTRAINED DATA 69

4.4.1 Velocity distributions for the unconstrained boreholes 70

4.5 DISCUSSION AND CONCLUSIONS 73

4. Flood basalt facies from borehole data

4.1 Chapter summary

In this chapter I present an effective method of obtaining information from borehole data on the different volcanic facies within a flood basalt succession. The aims of this chapter are: 1) to provide a means of determining proportions of different volcanic facies without detailed examination of borehole data or where borehole data is limited; and 2) to explore the relationship between onshore and offshore observations. Data are used from three different basalt formations in the Faroe Islands, displaying a range of facies onshore. Boreholes have been drilled through these, and several kilometres' depth of log data collected. The proximity of these boreholes to onshore observations allows the identification of different facies within the wireline log data. The wireline log responses for tabular-classic and compound-braided flows, hyaloclastites and intrusions are investigated using boreholes from the Faroe Islands to assess whether these facies can be identified by the statistical distribution of their rock properties.

This chapter demonstrates that histograms of P-wave velocities provide an efficient method of identifying the different facies, and I also explore why these distributions display such variation. The Faroese boreholes (Lopra-1/1A, Glyvursnes-1 and Vestmanna-1) also provide "type sections" for the different facies, and provide useful datasets for later chapters. Published ODP/IODP boreholes which have encountered significant flood volcanic sequences are used to further constrain the relationships. When applied to borehole data from the ODP wells (642E and 917A) and one commercial well (164/07-1), it is possible to estimate proportions of the different volcanic facies using the velocity distributions alone.

4.2 Introduction

4.2.1 The internal structure of flood basalt lava flows

The large-scale facies architecture of flood basalt provinces is discussed in Chapter 2; however on a smaller scale, individual lava flow lobes can also be divided into their component parts. Aubele et al. (1988) recognised a three-part vertical structure consisting of an upper vesicular zone, a middle non-vesicular zone and a lower

vesicular zone. Self et al. (1997) developed this for continental flood basalts based on observations in the Columbia River Basalt Group and divided flows into a crust, core and basal zone. This three-part zonation is observed in other flood basalt provinces including the NAIP (Passey & Bell, 2007) and the Deccan Volcanic Province (Self et al., 2007) (Figure 4.1), as well as in sections from offshore boreholes (e.g. Planke, 1994). As discussed in Chapter 2, Single and Jerram (2004) developed a classification scheme for variations at the scale of individual flow lobes These intrafacies included flow cores, crusts, boles, and small intrusions. These intrafacies can be identified from field observations, and were applied to the characterisation of lava flows in Talisker Bay, Skye (Single & Jerram, 2004). Andersen et al. (2009) characterised the basalt succession in eight wells in the Faroe-Shetland channel and the Rockall Trough, describing five classes of units. Helm-Clark et al. (2004) provide a detailed study of the uses and limitations of various wireline logging tools, using data from the Deccan Traps and Columbia River flood basalt provinces amongst others.

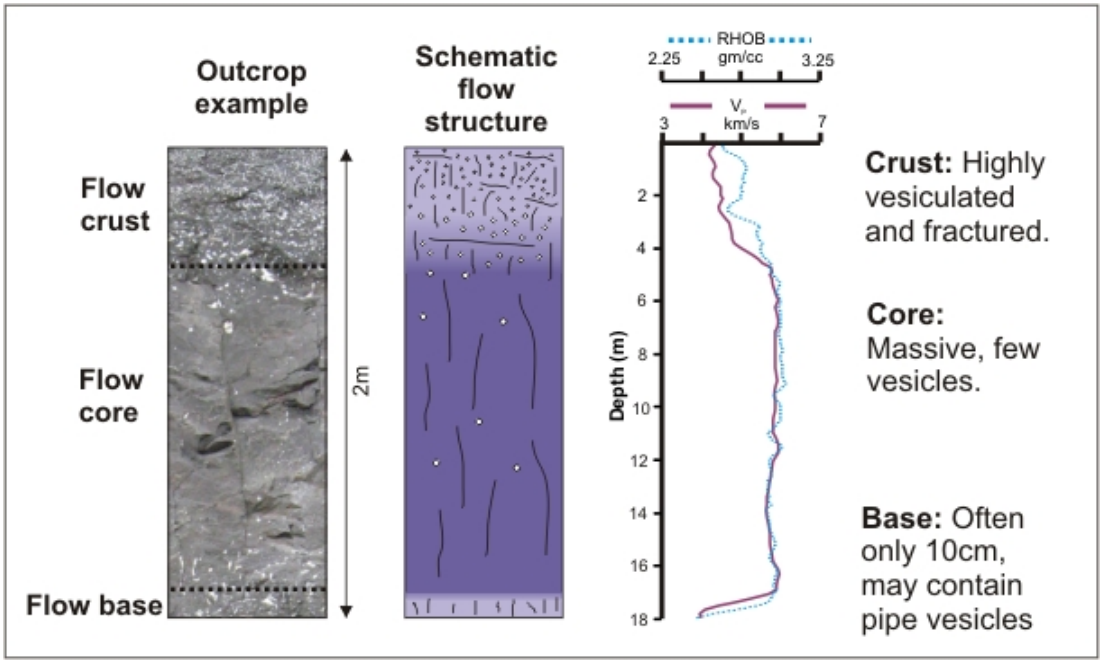

Figure 4.1 Principles of interpreting wireline log data. As discussed in the text, variation in velocity and density can be used to subdivide lava flows into their crust, core and base regions. Photo from Ljosa quarry, Eysturoy, Faroe Islands. This is at a different scale to the log data, but this three-part division has been shown to be independent of scale (e.g. Self et al., 1997). Schematic flow structure from Self et al. (1997). Log data from the Lopra-1/1A borehole.

While this thesis is mainly concerned with subaerial and near-shore environments in this work, many flood basalt provinces were emplaced into deeper water. Bartetzko et al. (2001; 2002) defined facies such as pillow basalts in wireline log data from ODP holes in oceanic crust. This is of use when considering oceanic large igneous provinces such as the Wrangellia oceanic plateau, Canada, where significant submarine pillow sequences exist (Greene et al., 2009) and the approaches taken in this chapter could be extended to these provinces as additional datasets become available.

4.2.2 Terminology

A **flow lobe** is "an individual package of lava that is surrounded by a chilled crust" (Self et al., 1997). Flow lobes can be easily identified in the field by the presence of this chilled crust. Most flow lobes in CFBPs show a three-part vertical division into an upper **crust**, a **core** and a lower crust or **base** (Self et al., 1998). This is illustrated in Figure 4.1. The crust is highly vesicular and extensively fractured, while the core is massive with few vesicles. This three part structure is largely independent of flow thickness, though the upper crust may be fully or partially eroded if the lobe top is exposed at the surface for a significant amount of time. The smallest lobes (below 50cm) may have vesicular cores. A **lava flow** is defined as "the product of a single continuous outpouring of lava" (Self et al., 1997). This may be very difficult to recognise in ancient flood basalt provinces, as a lava flow can be made up of one or more flow lobes.

4.2.3 Interpreting wireline log data in flood basalt provinces

Several Ocean Drilling Program (ODP) boreholes have penetrated flood basalt lava flows in the North Atlantic. The first to have its log data fully analysed was Hole 642E (Leg 104) on the Vøring margin (Planke, 1994). Its location is shown in Figure 4.2. The data from Hole 642E showed wide variations in the sonic, density, neutron porosity and resistivity logs. Planke (1994) recognised a cyclic response in these logs related to the internal structure of the flow lobes – the velocity and density are low at the flow top, gradually increase to a maximum in the flow core and decrease sharply at the flow base. This within lobe variation maps onto the crust-core-base sequences often observed in flood basalt facies described above (Figure 4.1). This cyclic pattern

is caused by the vertical variations in vesicularity and fracturing that characterise a flood basalt flow lobe. In the crust, vesicle density and fracturing are high, thus reducing sonic velocity and bulk density. The crust often shows a greater degree of alteration than the rest of the lobe, resulting in a high gamma ray value. The flow core has a low degree of fracturing and vesicularity is also low, so velocity and density are high. The thin flow bases generally show a return to high values of fracturing and vesicularity.

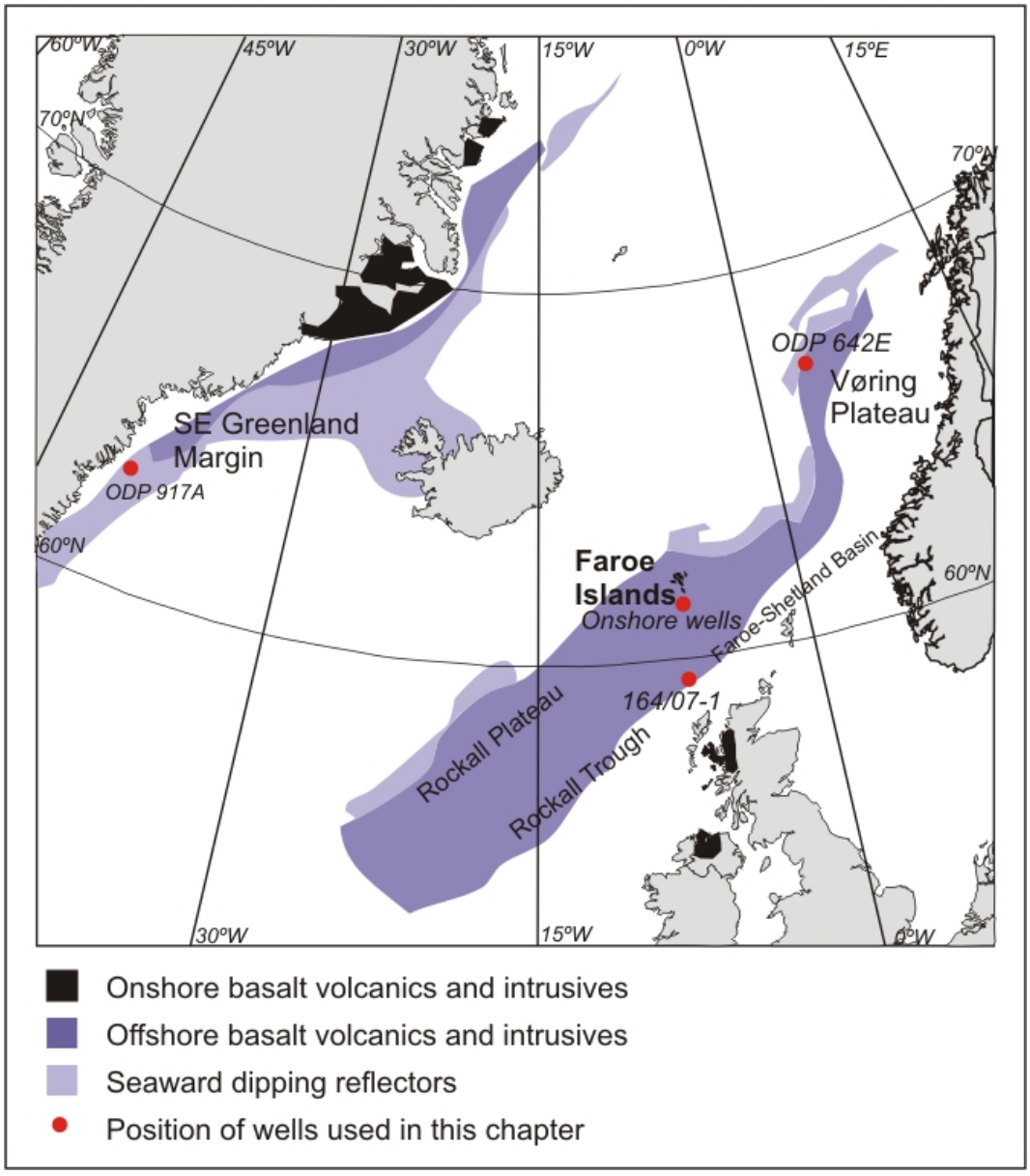

Figure 4.2 Location map of boreholes used in this chapter.

As ODP boreholes have a full set of cores as well as wireline log data, they are invaluable for linking geophysical data to geological observations. Bücker et al. (1998) confirmed the link between the cyclic pattern in log data and the internal flow structure, using data from ODP Holes 553A (Leg 81), 642E (Leg 104) and 917A (Leg 152). It was also shown that geographically distant boreholes demonstrated the same cyclic pattern, which was also unaffected by core size (Bücker et al., 1998). This suggests that this pattern in wireline log data is common to all areas of the NAIP, and possibly to other flood basalt provinces, and may be used to identify intraflow structures in areas of no core recovery.

Several more recent studies have used this cyclic pattern to identify flow lobes where no core has been recovered. Archer et al. (2005) identified individual flow lobes in Well 164/07-1, in the Rockall Trough, using the cyclic pattern present in sonic and density logs. Boldreel (2006) used this technique to construct a detailed stratigraphy for the Lopra 1/1A borehole, Faroe Islands. “Flow units”, minor compound flows, intrusions and a hyaloclastite sequence were observed in this borehole, aided by the lithological analysis of Hald and Waagstein (1984).

4.3 Faroese case study

A set of key borehole data from the Faroe Islands provides a vital case study for this work. The proximity of the boreholes to the onshore basalt equivalents allows a full investigation into the use of the borehole signatures to identify key flood basalt facies. In turn, it helps us determine a strategy for the interpretation of boreholes from areas where no close onshore analogues exist. Facies relationships found in the Faroe Islands will be described, and then the borehole data used in this chapter and its analysis will be introduced.

4.3.1 Analysis of the Lopra-1/1A, Vestmanna-1, and Glyvursnes-1 borehole data

The purpose of this chapter is to investigate the link between wireline log data and volcanic facies observed onshore. In order to do this, three recently released onshore boreholes in the Faroe Islands (Lopra-1/1A, Vestmanna-1 and Glyvursnes-1) were selected for this work, and their locations are shown in Figure 4.2. These boreholes are ideally suited for studying the wireline log responses of altered flood basalt lava flows, as they are in close proximity to well-exposed onshore flows. The facies

architecture of the flows penetrated by the boreholes is therefore well-constrained. The Faroe Islands exhibit a variety of facies architectures in onshore exposures, as discussed in Chapter 2: the EF is a mixture of tabular-classic and compound-braided flows; the MF is dominated by compound-braided flows; the BF is dominated by tabular-classic flows; and the LF by hyaloclastites.

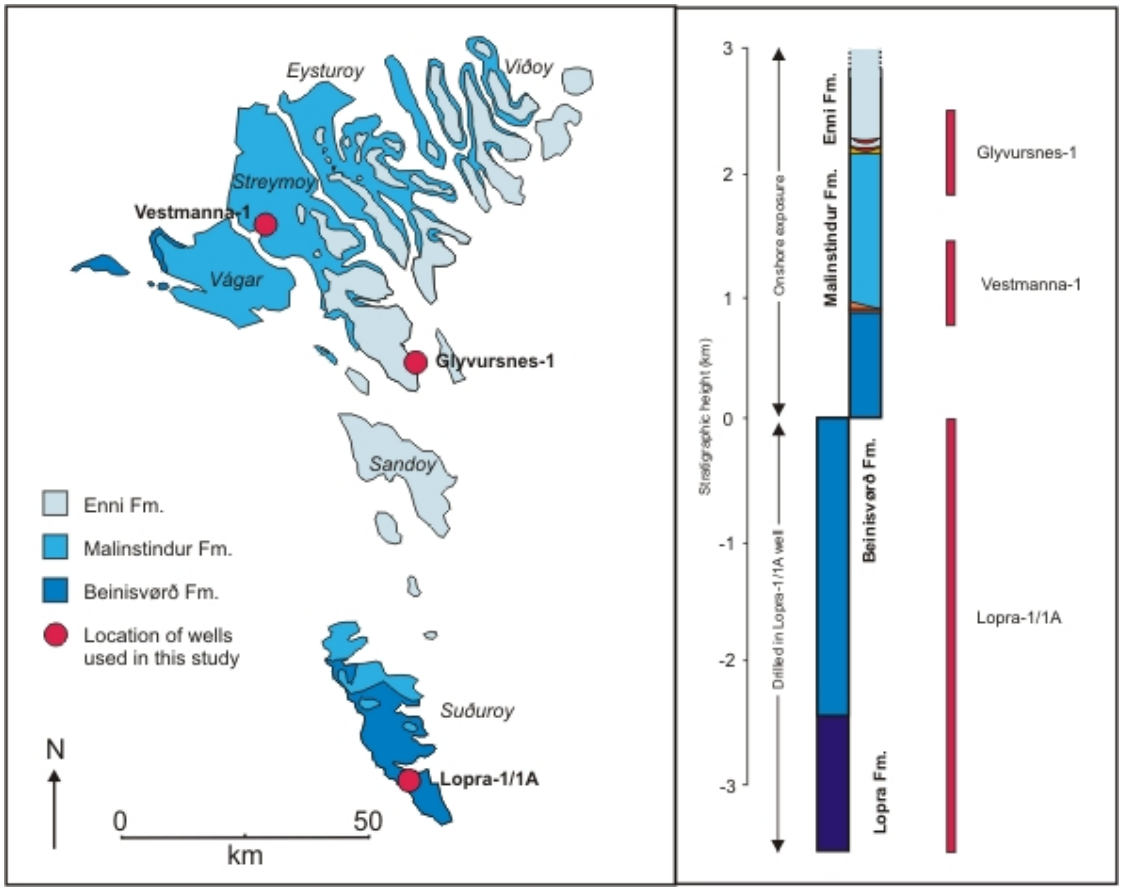

Figure 4.3 Location map of Faroese onshore boreholes and their stratigraphic positions. After Passey and Bell (2007). Borehole depths from Japsen et al. (2005).

The Lopra-1/1A borehole was drilled to a depth of 2.2km on the island of Suðuroy, Faroe Islands, in 1981 and deepened to 3.6km in 1996 (Hald & Waagstein, 1984). The entire depth of this borehole was within the Faroe Island Basalt Group, and two formations were encountered: the subaerial Beinisvørð Formation, and the near-shore Lopra Formation. The BF is dominated by tabular flows, and the LF by hyaloclastites (Passey & Bell, 2007). The entire borehole was logged in 1996, and data between 180m and 3550m depth are used in this chapter. The approximate depths of all three boreholes within the FIBG stratigraphy are shown in Figure 4.3.

The Vestmanna-1 borehole was drilled in 1980 on the island of Streymoy (Berthelsen, 1984). Its original total depth was 660m, but in 2002 it was reamed and logged to 590m as part of the SeiFaBa project (Japsen et al., 2005). It encountered the bottom 550m of the MF and the top 100m of the BF. The MF mainly consists of compound-braided flows.

The Glyvursnes-1 borehole was also drilled as part of the SeiFaBa project in 2002. It reached a total depth of 700m and sampled the bottom 250m of the EF and the top 450m of the MF (Japsen et al., 2005).

4.3.2 Methodology

Velocity distributions are useful in geophysical analysis and modelling, as they are a primary “parameter” that determines the seismic response of the medium (Holliger, 1996). As wireline log data is sampled at constant intervals (usually 15.24cm), a histogram is representative of the velocity structure of the borehole. A histogram can thus be easily constructed by counting the frequency of measurements for the desired intervals. This is shown in Figure 4.4.

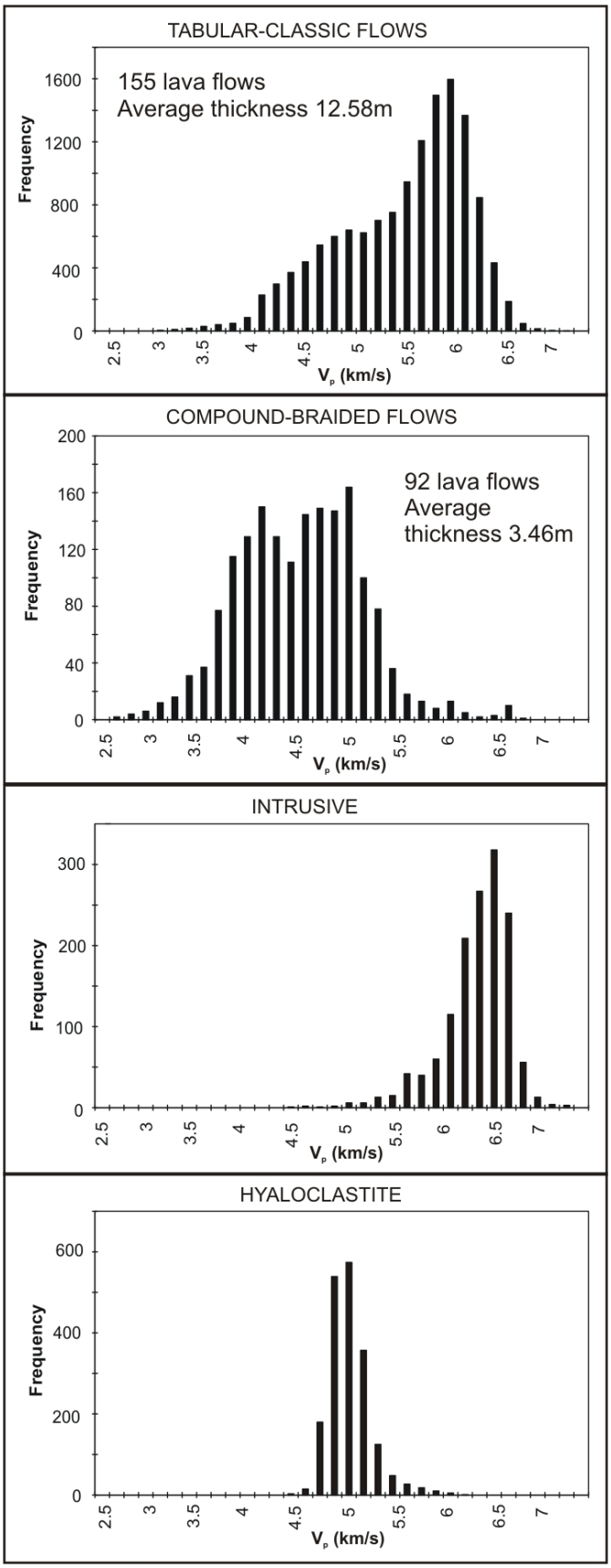

Figure 4.4 Velocity histograms of various volcanic facies. Tabular-classic, hyaloclastite and dyke data from the Lopra-1/1A borehole; compound-braided data from the Glyvursnes-1 borehole.

The shape of a histogram is known to be sensitive to the bin size. Larger bins produce more robust shapes but may mask finer details of the data. Accordingly, I use the method of Freedman and Diaconis (1981, summarized in Izenman, 1991). This gives bin sizes based on the number of samples and their inter-quartile range (IQR). I selected the largest bin size calculated for the various facies (0.8km/s), and used this in all histograms, to allow us to compare the histograms easily. Choosing a smaller bin size would either mean that the shapes of some histograms were not robust, or that the histograms were difficult to compare.

The relevant data for each facies were identified by combining previous work on the boreholes with interpretations of the data. Data were filtered to remove caved intervals identified in the calliper log, where available. Flow lobes can be identified by the cyclic velocity pattern described in the introduction and Figure 4.1 (Planke, 1994). Boldreel (2006) identified the transition between the BF (known to be dominated by tabular-classic flows) and the LF (composed of hyaloclastites) in the Lopra 1/1A borehole. Boldreel (2006) also identified two dykes which provide the data for the dyke facies shown in Figure 4.4. Logging data characteristics for tabular-classic flows, intrusions and hyaloclastites were identified from the Lopra-1/1A borehole and are summarised below. From previous studies, the boundary between the EF and MF in the Glyvursnes-1 borehole, and the boundary between the MF and BF in the Vestmanna-1 borehole, can be identified. These were used, along with the known facies from outcrop examples, to divide the boreholes into the appropriate facies. Examples of logs from the different facies are given in Figure 4.5. The exact details of the data used are given in Table 4.1.

Facies	Well	Depth range (MD)	Number of samples	Logs available
Tabular-classic	Lopra-1/1A	184-2467, omitting the intrusive intervals below	13573	V_p, V_s, RHOB, SGR, CAL
Compound-braided	Glyvursnes-1	354-697	1715	V_p, V_s, RHOB, SGR, CAL, NPHI, RES, TEMP
Intrusive	Lopra-1/1A	494-610; 724-823	1413	V_p, V_s, RHOB, SGR, CAL
Hyaloclastite	Lopra-1/1A	2596-2886	1902	V_p, V_s, RHOB, SGR, CAL
Mixed	164/07-1	2242-2952	4660	V_p, RHOB, GR, CAL, RMLL
Mixed	917A	238-546	2020	V_p, RHOB, SGR, CAL, SFLU
Mixed	642E	416-1068	4255	V_p, RHOB, SGR, CGR, GR, CAL, NPHI, SFLU, ILD, ILM

Table 4.1 Data used in this chapter

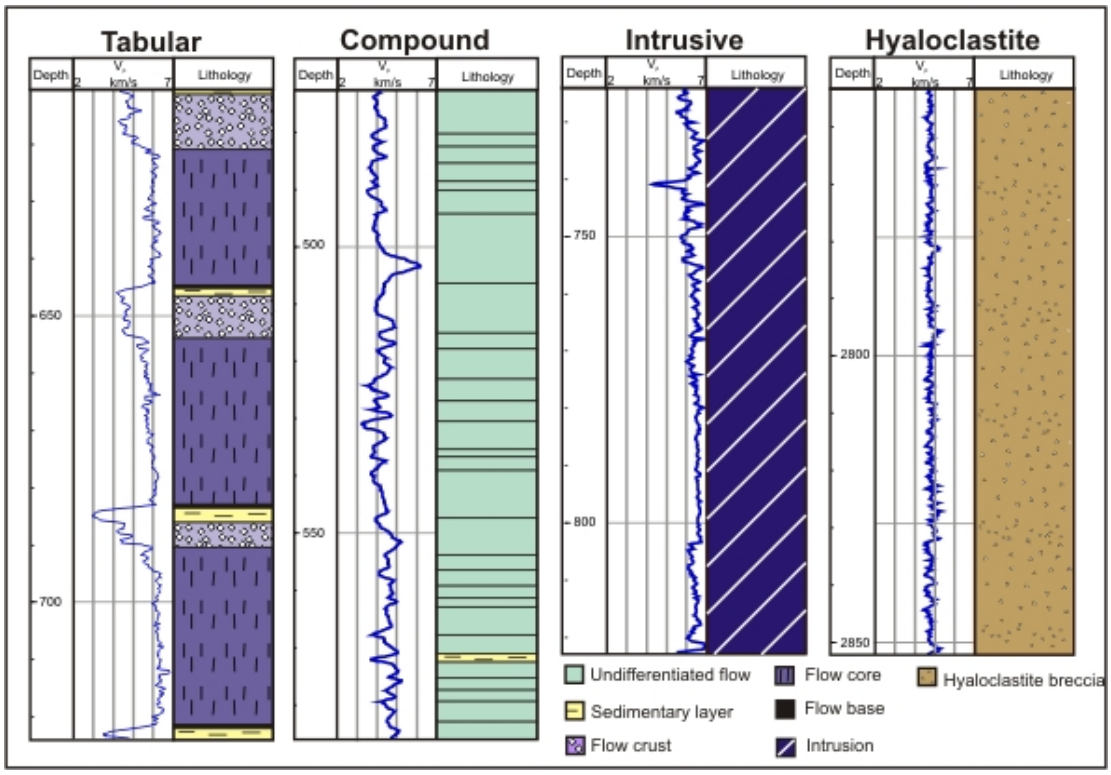

Figure 4.5 Examples of P-wave velocity (V_p) data from different volcanic facies, divided into individual lava flows and showing intraflow variations where appropriate. Compound data from the Glyvursnes-1 borehole, other data from the Lopra-1/1A borehole.

4.3.3 Results of data analysis

Investigations of the wireline logging data from the three Faroese boreholes showed that each volcanic facies has a characteristic velocity histogram. This allows a link to be made between onshore observations and logging data from boreholes. The velocity distributions for the various volcanic facies are shown in Figure 4.4. Table 4.2 gives a mathematical description of the shape of these distributions in terms of their mean, modality and skewness.

It can be seen from Figure 4.4 that the volcanic facies show very different velocity distributions. Intrusions show a high peak, with a very small spread of data. Hyaloclastites surprisingly also have a small spread, but a lower peak velocity. Both lava flow facies (tabular-classic and compound-braided) have a large spread of data; however the shapes of their distributions are very different. Tabular-classic flows produce a negatively-skewed distribution with a high single mode, whereas

compound-braided flows produce a largely symmetrical distribution with two modes. Data from compound-braided flows in the Vestmanna-1 borehole gave a similar histogram to those from the Glyvursnes-1 borehole.

Intrusive sills and dykes have a high mode and narrow distribution because of their homogeneous nature, low porosity and low fracture density. Hyaloclastites show a high level of heterogeneity, sometimes including lava flows (e.g. Ellis et al., 2002). In other places, the V_p is relatively constant, probably responding to zones of hyaloclastite breccia. I use a section of hyaloclastite breccia for this type example. This has a low spread because of its homogeneity, and the inclusion of the lava flows would have increased the spread of the data.

Sedimentary units are found in all boreholes used; however their data is not separated from the facies in which they occur. Their velocity distribution is not shown in Figure 4.4 because they make up only a small proportion of the data analysed. When taken separately, their velocity distribution is symmetrical with a peak at 3.25 km/s. The sedimentary layers account for the slower velocity "tails" of the compound and tabular distributions. In the next section, I explore the reasons for the difference between the tabular-classic and compound-braided distributions.

	Facies			
	Tabular-classic	**Compound-braided**	**Dyke**	**Hyaloclastite**
Number of modes	1	2	1	1
Modal value(s)	5.9-6.05	3.95-4.1; 4.4-4.55	6.35-6.5	4.85-5.0
IQR (spread)	0.991	0.934	0.381	0.259
Fisher skewness	-0.689	0.212	-1.342	1.339

Table 4.2 Statistics for the velocity distributions for the various facies. Tabular-classic, hyaloclastite and dyke data from the Lopra-1/1A borehole; compound-braided data from the Glyvursnes-1 borehole. IQR is inter-quartile range. Fisher skewness is a measure of the asymmetry of the distribution. A positive number indicates an asymmetric tail extending towards larger values, while a negative number indicates that the asymmetric tail extends towards smaller values.

4.3.4 Understanding the lava flow signature: Comparing tabular-classic and compound-braided facies

For each of the major subaerial formations in the Faroe Islands, flow thicknesses and core proportions were calculated, to identify the causes of the different velocity distributions. Recalling from Figure 4.4, tabular-classic flows have a negatively-skewed distribution with a high mode. Compound-braided flows have a more symmetrical distribution. The peak at 5.75-6km/s in the tabular-classic distribution is due to the many measurements recorded in the fully degassed core of the tabular flows. If the core proportion varies between tabular-classic and compound-braided flows, this would explain the difference between the distributions. Another contributing factor may be that the cores of tabular-classic flows are fully degassed, resulting in a higher velocity, while the cores of compound-braided flows are slightly more vesicular.

In order to investigate the flow lobe thickness and core to crust ratio, the Glyvursnes-1, Vestmanna-1 and Lopra-1/1A borehole data were subdivided into individual flow lobes, then into lobe crusts and cores, and an example is shown in Figure 4.6. Boldreel (2006) plotted individual flow lobes and flow crusts for the Lopra 1/1A borehole, and I repeat this work to obtain core to crust ratios. This work uses a modified version of the zones identified by Bücker (1998) and Planke (1994) to divide this stratigraphy into lava flows and their component parts. The transition zone identified by Planke (1994) is not used in this work for simplicity and because it is not often observed in the density log, and it may be an “edge effect” of the deep penetrating sonic logging tool (Rider, 1996). The transition zone is not generally observed in the field, where a relatively sharp divide is commonly observed between the crust and core. This zone is included in the crust. Sonic, density and gamma ray logs have proved most useful for interpreting log data and were available for all datasets used in this work. Available data are summarised in Table 4.1. The lack of neutron porosity data for some wells meant I was unable to use the “cross over technique” of Boldreel (2006). The criteria I used for identifying the zones are summarised in Table 4.3.

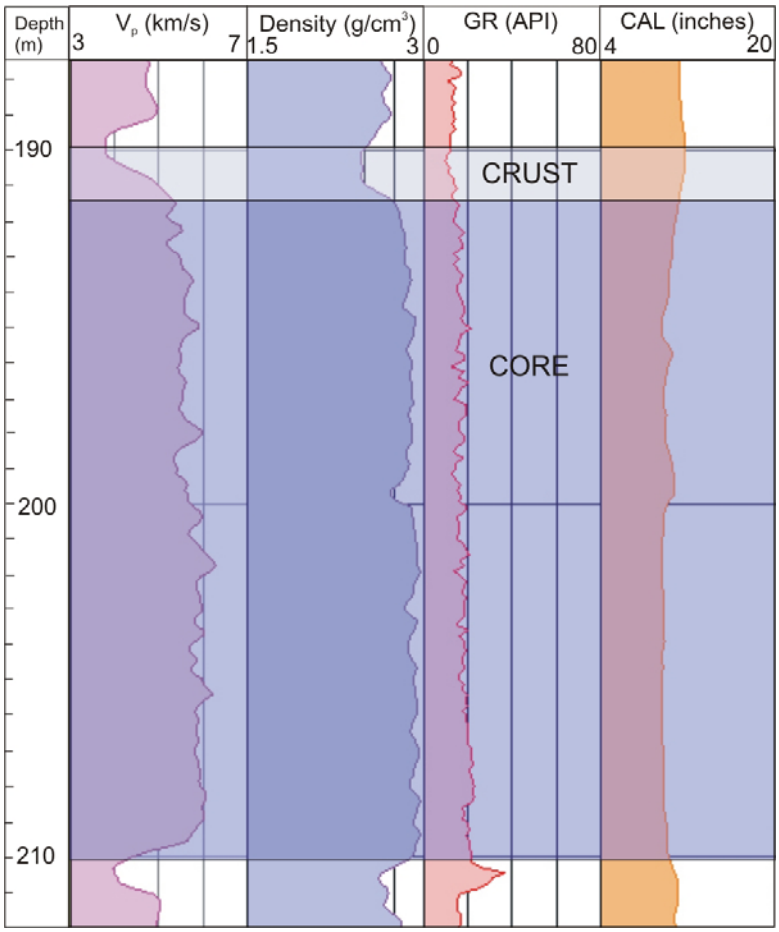

Figure 4.6 Example of log data divided into core and crust. Core has high velocity, high density, and low gamma ray. Crust has decreasing velocity and density, and often a high spike in the gamma ray. Data from the Lopra-1/1A borehole.

The interpreted boreholes also form an extremely useful dataset for examining general properties of lava flows such as average core and crust velocities and the distribution of flow thicknesses. These are used and discussed further in Chapter 7. Full interpretations of the Faroese Boreholes following the methods of Planke (1994) are included in Appendix B.

The proportion of core in each flow is plotted against flow thickness for all the formations in Figure 4.7, and data are summarised in Table 4.4. This displays a trend in the minimum value of the core proportion: thick flows do not have a low core proportion, whereas thin flows display a wide range of core proportions. When combined with data on flow thicknesses in Table 4.4, it is predicted that core

proportions in the MF are low compared to the BF. The EF shows intermediate flow thickness values, as expected for a mixture of compound and tabular flows.

In summary, I suggest that the significant differences between tabular-classic and compound-braided velocity distributions are due to the differences in flow thickness and thus core proportion. In tabular-classic flows, relatively more measurements are recorded in the massive, faster flow core, whereas in compound-braided flows relatively more measurements come from the vesicular, slower crust. In compound-braided flows, the flow core may also be less well degassed than that of tabular flows, resulting in a lower velocity peak for core values. This is a feature of the inflation model (Self et al., 1996), where the thicker tabular flows develop a much more prominent flow core.

Flow lobe component	V_p	Density	GR
Crust	Relatively low. Below ~4km/s	Relatively low. Below ~2600kg/m^3	Often shows a peak of 10-20 API at flow top.
Core	Relatively high. Above ~5km/s	Relatively high. Above ~2600kg/m^3	Low, <10 API.
Base	Decreasing	Decreasing	Increasing

Table 4.3 Criteria for dividing flow lobes into separate zones. After Planke (1994); Bücker et al. (1998); Boldreel (2006).

Formation	Mean flow thickness (m)	Standard deviation (m)	Percentage of total core thickness made up of flows >5m thick
BF	12.6	12.6	91%
MF	3.46	2.24	36%
EF	6.39	6.55	73%

Table 4.4 Flow thickness statistics from the BF, MF and EF. Mean and standard deviation accurate to 3sf; percentages to 2sf.

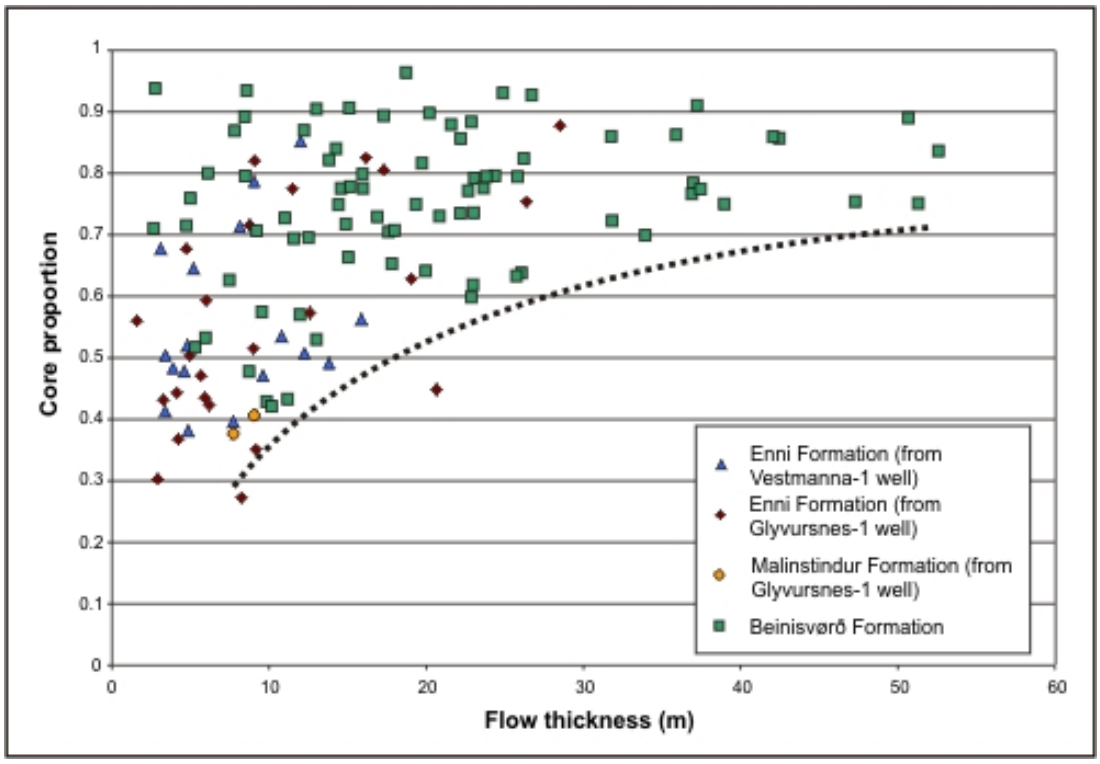

Figure 4.7 Plot of core proportion (core thickness divided by total flow thickness) versus flow thickness. Beinisvørð Formation data from the Lopra-1/1A borehole.

4.4 Identifying facies distributions in unconstrained data

This chapter has shown that the key flood volcanic facies (tabular-classic, compound-braided, hyaloclastites and intrusions) have characteristic velocity distributions, for examples where the facies is well known. The next step is to investigate whether these distributions can be used to identify volcanic facies in areas with no nearby onshore exposure, or where data is limited (e.g. little or no core data). Three offshore boreholes were available: ODP Hole 642E, ODP Hole 917A and the commercial borehole 164/07-1 (Figure 4.2). These are described in detail below.

ODP Hole 642E (Leg 104) was drilled in 1985 through a sequence of seaward dipping reflectors (SDR) on the Vøring margin (Eldholm, 1987). This work uses approximately 700m of logging data from a layered terrestrial tholeiitic basalt sequence, which was also cored. ODP Hole 917A (Leg 152) was also drilled through a SDR sequence, this time on the SE Greenland margin (Duncan et al., 1996). The basalt sequence was terrestrial, and 370m of wireline logging data were obtained.

Well 164/07-1 was drilled in the UK sector of the Rockall Trough, penetrating a 1.2km sequence of lava flows (Archer et al., 2005). Approximately 300m of this was interpreted as subaqueous, the rest being subaerial. As I wish to test my methods on data that has not previously been interpreted, I attempt to identify the volcanic facies within the subaerial data only. The geological history is similar to the Faroe-Shetland basin – the lavas are a subaerial flood basalt sequence. The borehole also contained approximately 70 dolerite sills, although data for these were not available.

4.4.1 Velocity distributions for the unconstrained boreholes

Velocity frequency distributions for Well 164/07-1 and ODP Holes 917A and 642E are plotted in Figure 4.8, and statistics for these distributions are given in Table 4.5. The distributions do not correspond to any single distribution in Figure 4.3, as they contain multiple modes and show a high spread of data. A possible hypothesis from these features is that these boreholes penetrate a mixture of compound-braided and tabular-classic flows. Based on the relative heights of the modal velocities, it is suggested that ODP Hole 642E has mainly compound flows, while ODP Hole 917A has around 25% tabular flows. The data from Well 164/07-1 are taken as an example to test the hypothesis.

	Borehole		
	164/07-1	**917A**	**642E**
Number of modes	2	2	2
Modal values	4.4-4.55; 5.45-5.6	3.65-3.8; 5-5.15	3.65-3.8; 4.4-4.55
IQR (spread)	1.326	1.356	1.215
Fisher skewness	-0.317	0.255	-0.064

Table 5 Statistics for the borehole s unconstrained by nearby onshore analogues.

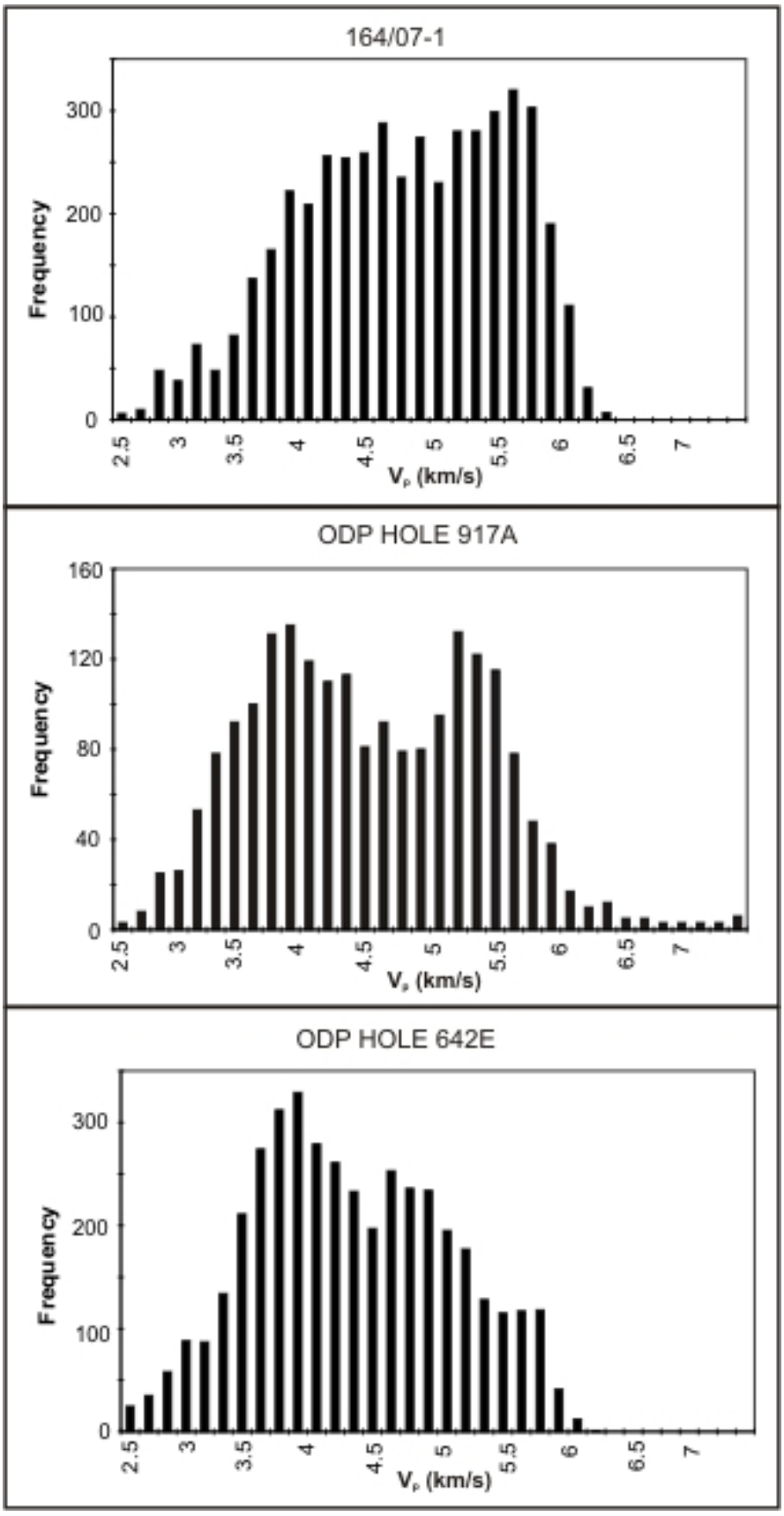

Figure 4.8 Velocity histograms for the boreholes with no nearby onshore analogues, as described in the text.

Histograms were constructed from the Faroe Islands data showing tabular and compound data combined in different proportions (Figure 4.9). Data from Well 164/07-1 are plotted, in an attempt to derive proportions of tabular and compound flows by fitting the borehole data to the closest constructed histograms. It was found that the peak corresponding to the lava flow cores from the Lopra-1/1A data was at a higher velocity than the interpreted core peak from the 164/07-1 data, resulting in a poor fit between the modes of the datasets, but with a similar overall range. Such differences in absolute velocity between different data sets would be expected if the composition of the basalt were different between boreholes. Composition data from Hald and Waagstein (1984), Waagstein (1988) (Lopra-1/1A borehole) and Archer et al. (2005) (164/07-1 data) were used to calculate a theoretical density following the method of Hall (1987). The calculated density was significantly higher than other boreholes for data from the Lopra-1/1A borehole, indicating that the rock composition variation is responsible for the slightly higher velocity values in the Lopra-1/1A borehole. Other possible causes of a high flow core velocity would include a lower level of fracturing in the borehole or a lower proportion of vesicles in the core (i.e. a more degassed core). A more degassed core is unlikely, because the same increase in average velocity is found in data from the flow crust, suggesting a mechanism that affects both crust and core.

To account for the higher overall velocity in the Lopra-1/1A data, I can overlay the velocity distributions by matching their flow core peaks. In Figure 4.9 the combination of different mixes of tabular-classic vs. compound-braided facies is presented, representing the distributions expected from lava stratigraphy which would contain different amounts of each facies (normalised to the core peak values). An overlay of the natural distribution from the 164/07-1 data (Figure 4.9) shows that the best fit to the 164/07-1 data is a mixture of 50% compound flows and 50% tabular flows.

As a further test of this result a detailed (flow by flow) volcanological interpretation of the 164/07-1 wireline logging data found that compound flows totalled 361m out of the 710m analysed, or 51%. The velocity distributions of key facies and their relative abundances can be used as a way of estimating proportions of the different

facies in wireline data sets, and has the potential to be developed further when used to map out the distributions of these facies in 2D or 3D.

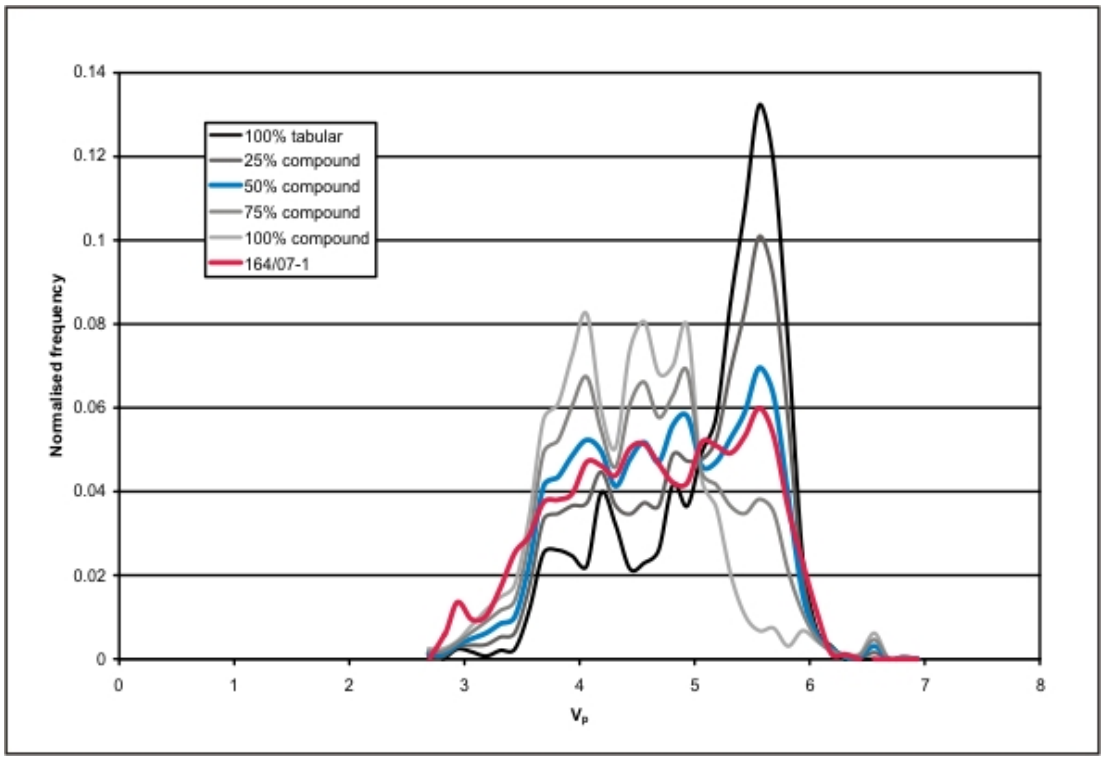

Figure 4.9 Well 164/07-1 histogram plotted with synthetic histograms constructed from tabular-classic and compound-braided data. The tabular data is a 300m selection from the Lopra-1/1A borehole of almost entirely tabular flows, while the compound data is a 150m selection from the Glyvursnes-1 borehole. These are normalised to the number of sample points.

4.5 Discussion and conclusions

It can be demonstrated that the key facies used in this work are found in a wide selection of known sections through flood basalt provinces worldwide (e.g. Figure 4.10a). In each example there is a wide variation in the amounts and distributions of these facies. Where good onshore analogues and field data allow, such facies variations and facies architectures can be mapped (e.g. Jerram and Widdowson 2005). In this chapter I have provided a means to detect such facies variations from limited data such as borehole signatures. With improved coverage, and linked with additional information (such as seismic data), this method may allow a better

understanding of the facies variations and associations in the sequences now preserved offshore.

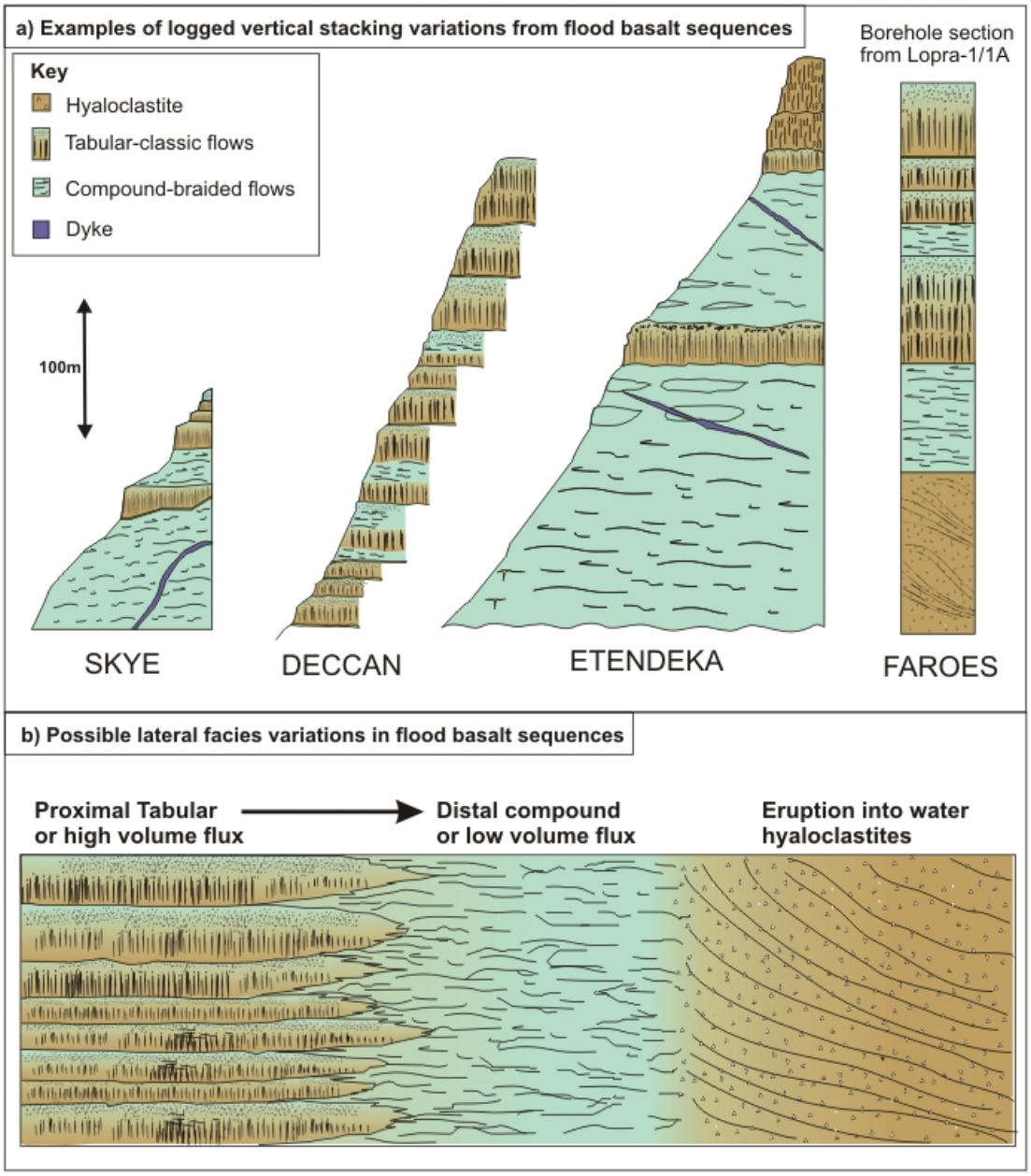

Figure 4.10 a) Comparison between the borehole data in this chapter and cross-sections through a variety of flood basalt provinces from Chapter 2. b) Possible lateral variations.

There are also implications for research into the physical volcanology of flood basalt provinces. If the key facies types I describe can be identified over a wide area, it is possible to begin to build up a picture of the 3D architecture of the province, and

characterise its lateral heterogeneity (e.g. Figure 4.10b). We might expect thick tabular flows proximal to the vent to develop into thinner compound facies in distal areas (Figure 4.10b). The presence of different facies types could also be linked to the original volumes of magma flux in the system. Mapping the hyaloclastite distribution within the volcanic system is also of vital importance. This can highlight palaeo-shorelines and the transition from lava flows to volcaniclastic dominated parts of the basin (e.g. Jerram et al., 2009). One of the limitations of the method, however, is that I cannot classify flows into a'a and pahoehoe. To date, these have not been identified by log data alone; it has been necessary to identify the characteristic vesicle shapes from core sections (e.g. Keszthelyi 2002; Garcia et al. 2007).

I have demonstrated that the key volcanic facies (intrusions, hyaloclastites, tabular-classic flows, and compound-braided flows) have characteristic velocity histograms. These type distributions have also been used to interpret data from areas without nearby onshore analogues. While the same interpretations could be made by subdividing each borehole into individual lava flows, using the velocity distributions is far quicker and more efficient. This method will be useful to those involved in hydrocarbon exploration in understanding the structure of a flood basalt sequence. There are also implications for the process of drilling through a flood basalt sequence: the rock properties of tabular and compound flows are very different and will require drilling strategies to take this into account. If these key facies can be defined, the occurrences of significant thick 'hard' basalt sections interspersed with softer basalt sections can be better predicted when drilling exploration wells. It is hoped that future work will use these velocity distributions as a tool in the interpretation of wireline logs in flood basalt terrains. This work could also be extended by looking at a smaller "window" of, say, several hundred metres' thickness within a borehole and investigating the change in facies throughout the borehole.

Data from the boreholes described in this chapter also provides a "type section" through the various facies. The detailed breakdown into flow components is used to build 3D velocity models in Chapter 7.

5

5. CAPTURING 3D DATA IN FLOOD BASALT PROVINCES 77

5.1 CHAPTER SUMMARY 77

5.2 CASE STUDIES 77

5.2.1 Ljosa Quarry, Faroe Islands 79

5.2.2 Talisker Bay, Skye 80

5.3 COLLECTION AND PROCESSING THE LASER SCAN DATA 80

5.3.1 Ljosa quarry 80

5.3.2 Talisker Bay 81

5.3.3 Data processing 83

5.4 BUILDING 3D MODELS FROM THE LASER SCAN DATA 85

5.4.1 Picking key horizons 85

5.4.2 Extending the horizons laterally 86

5.4.3 Interrogating the block models 89

5.5 EVALUATION OF TERRESTRIAL LASER SCANNING 93

5.6 AN ALTERNATIVE APPROACH: STRUCTURE FROM MOTION 94

5.6.1 Theoretical principles 94

5.6.2 Pilot study: Hyaloclastites in Iceland 95

5.7 DISCUSSION 100

5. Capturing 3D data in flood basalt provinces

5.1 Chapter summary

This chapter presents a new method for reconstructing flood basalt lava flows from outcrop data, using terrestrial laser scanning (TLS) to generate 3D models. Case studies are from the Faroe Islands and the Isle of Skye, both part of the NAIP. These were analysed to pick out lava flow tops and bases, as well as dykes, lava tubes and sedimentary layers. 3D surfaces were then generated using the GSI3D software, a modelling package developed by the BGS and INSIGHT GmbH, and 3D geological models constructed. The models were interrogated to give data on flow thickness and crust to core ratio.

This chapter also examines alternative approaches to capturing 3D data, using digital photography and advanced software. A pilot study on hyaloclastite outcrops in Iceland is presented, along with a discussion on the benefits and drawbacks of both approaches.

5.2 Case studies

Previous studies have documented in detail the workflow used to capture and process TLS data (e.g. Enge et al., 2007; Buckley et al., 2008; Hodgetts, 2009; McCaffrey et al., 2008). The workflow in this thesis mostly follows that of previous studies with slight site-specific variations highlighted in the text. Previous work using terrestrial laser scanning is discussed in Chapter 3.

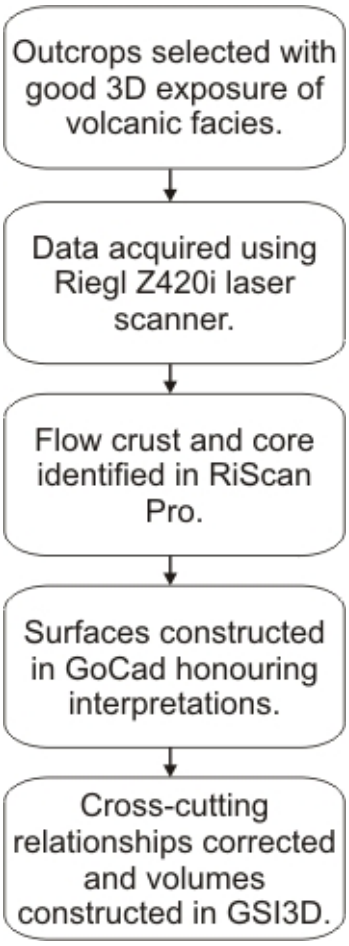

Figure 5.1 Summary of the workflow used in this study. The data collection and processing steps follow standard procedures (e.g. Buckley et al., 2008). Enge et al. (2007) provide a similar workflow for model building.

In order to test the applicability of TLS to the study of flood basalt facies, and the potential for successful reconstruction of lava sequences, two case studies were selected. Both are located within the North Atlantic Igneous Province, and are taken to be representative of compound-braided flows both onshore and offshore in this province. It was important that the case study areas met certain criteria to make a successful 3D model, including:

- Detailed facies architecture in 3D.
- Composed of typical flood basalt facies.
- Being of a scale that our equipment could cope with, and having good accessibility to enable the heavy laser scanning equipment to be relatively easily deployed.

5.2.1 Ljosa Quarry, Faroe Islands

The first case study, located near Ljosa, Eysturoy, Faroe Islands, is a quarried outcrop approximately 75m by 20m. Its location is shown in Figure 5.1. It is an extremely well-exposed section through compound-braided lava flows, comprising two flows which extend across the entire outcrop and several more which pinch out within the exposure. It is not a true 3D exposure as the two faces are at right angles, but a 3D model can be built by extending the interpretations laterally. The relative simplicity of the flow geometries and the small number of flows made this an excellent case study for developing the methods used in this work.

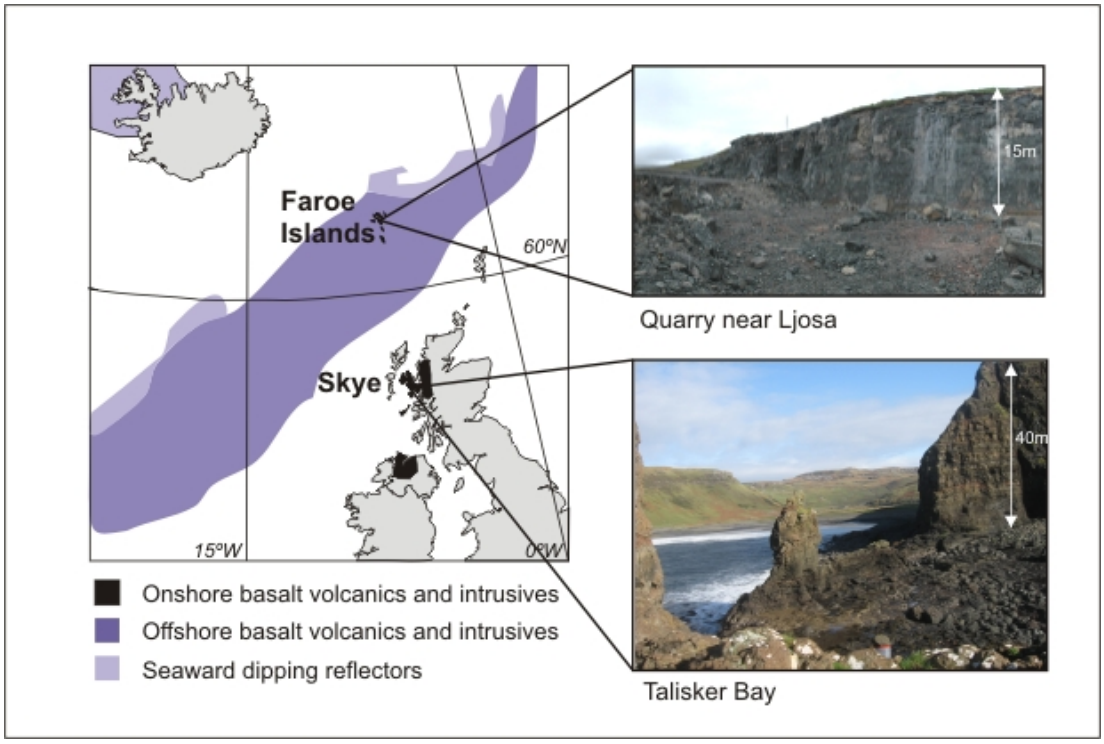

Figure 5.2 Map of part of the NAIP and locations of case studies used in this chapter.

The first case study is located within the Malinstindur Formation. As discussed in Chapter 2, this formation is predominantly composed of compound-braided lava flows. The quarry near Ljosa cuts through a sequence of thin (up to 3m) compound-braided basaltic lava flows, giving excellent exposure. The flow cores and crusts are easily identified, and the location is an excellent example of the complex flow architecture of the compound-braided facies.

5.2.2 Talisker Bay, Skye

The Isle of Skye, located off the west coast of Scotland, contains excellent exposures of flood basalt lava flows forming part of the NAIP. The Skye Lava Field covers much of the island, with the main sequence erupted between ~61-59 Ma, and in the west of Skye this can be divided into three sequences based on facies types (Single and Jerram, 2004). These are: lower compound-braided lavas; transitional lavas; and upper tabular lavas.

The Talisker Bay case study is located in the Minginish district on the west coast of Skye, within the lower compound-braided lavas. This area has been mapped in detail by Single (2004) and it is also the basis for a fine-scale facies classification scheme for flood basalt lava flows (Single and Jerram, 2004). In this study, we incorporate these detailed observations into a 3D reconstruction.

5.3 Collection and processing the laser scan data

Data for this study were collected during fieldwork in June 2007 (Faroe Islands) and September 2008 (Skye) using a Riegl LMS-Z420i terrestrial laser scanner combined with a calibrated Nikon D70 digital camera (6MP resolution). The Z420i equipment is described in detail in Chapter 3. As discussed in Chapter 3, the scanning range can be up to 1000m for highly reflective objects, however the maximum range falls as the reflectivity of the target decreases. We found that the dark colour of weathered basalt and the often wet nature of the outcrops reduced the range to less than 200m, suggesting the reflectivity is likely to be 10% or less based on Figure 3.3.

5.3.1 Ljosa quarry

At this location, three scans were required to collect all the required data. The quarry is extremely well-exposed, and the surfaces are relatively smooth. This means there are few shadow areas to cause problems, and the three scans were required primarily to obtain good photos for interpretation. Figure 5.3 shows the quarry layout and the scan setup. The three scans collected a total of approximately 8,600,000 points, at an angular resolution of 0.03°, giving a spacing of approximately 10mm between points on the quarry wall. Points were duplicated between scans. A total of 60 digital photos

were taken, at focal lengths of either 14mm or 50mm depending on the distance from the scanner to the quarry walls.

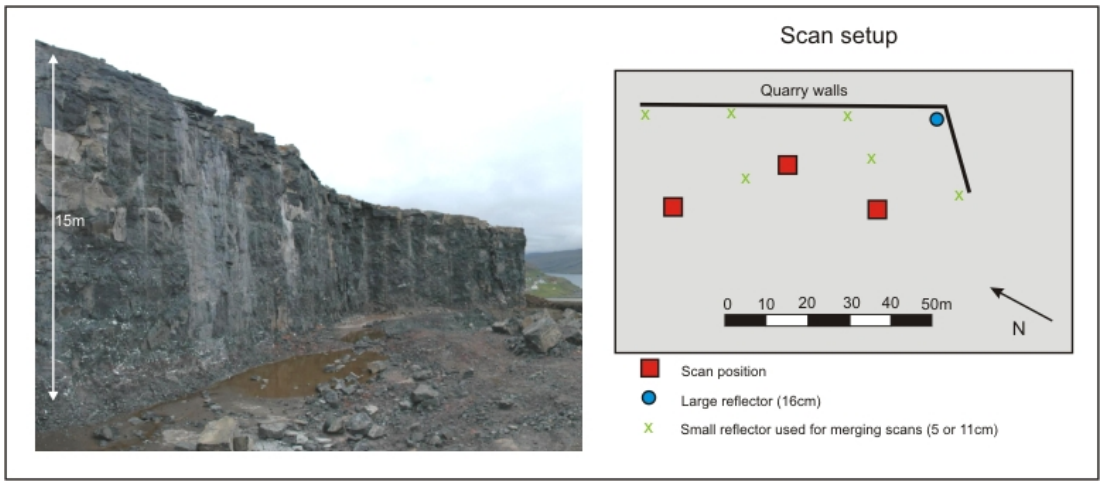

Figure 5.3 Overview photo of Ljosa quarry and map of the scanning setup, showing the scan positions and the reflector positions.

5.3.2 Talisker Bay

Five laser scans were acquired here, however many more could have been acquired to provide a more complete coverage of the outcrops. Unfortunately the other locations were inaccessible due to the tidal nature of the site. The five scans obtained provided a good coverage of the outcrops and allowed us to correlate flows between the outcrops. In total, approximately 10,020,000 points were collected at an angular resolution of 0.05-0.06°. 84 digital photos were taken, again using either the 14mm or 50mm lenses. Figure 5.4 gives an overview of the Talisker Bay site and the scanning fieldwork, and Figure 5.5 shows the layout of the scans.

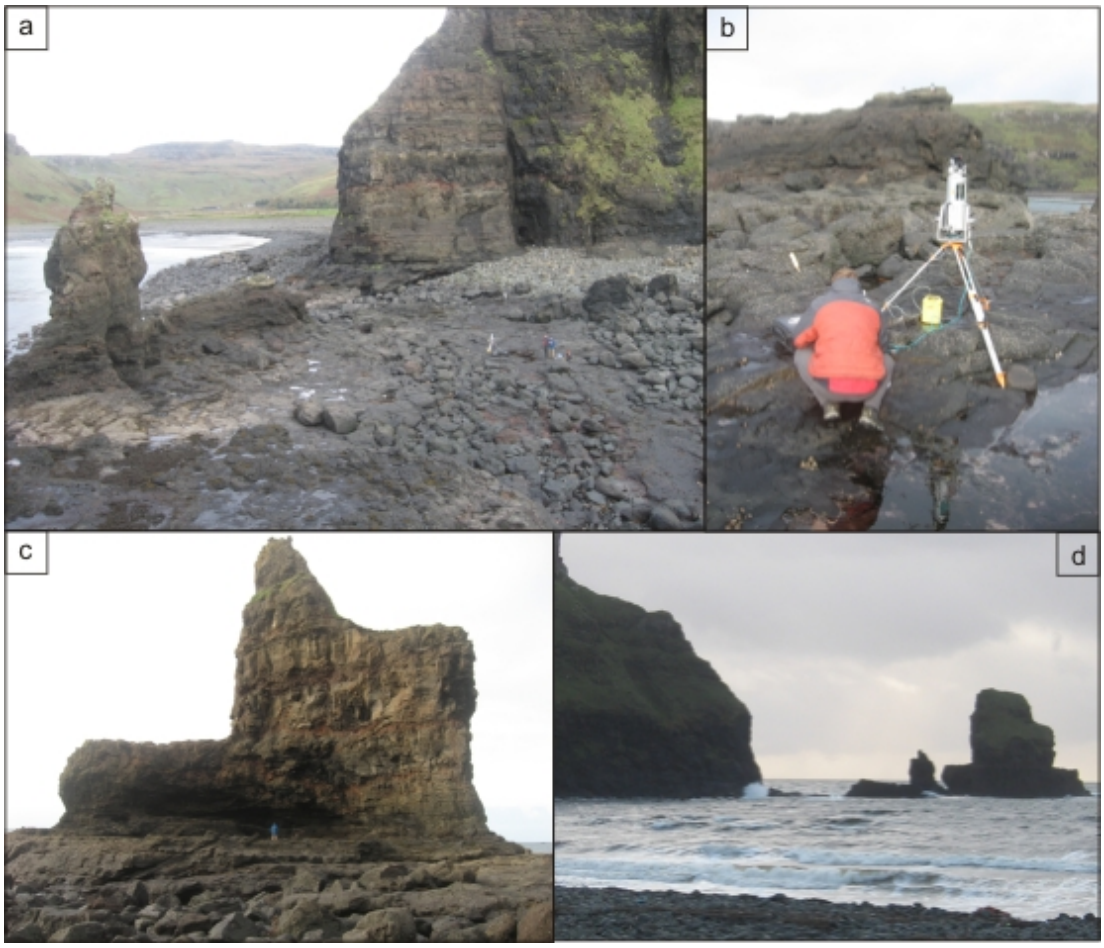

Figure 5.4 a) Overview photo of the Talisker Bay case study, showing the small sea stack, cliff section and wave-cut platform. b) The TLS equipment in action. c) The large sea stack. d) The case study area at high tide, showing the cliff section and both sea stacks.

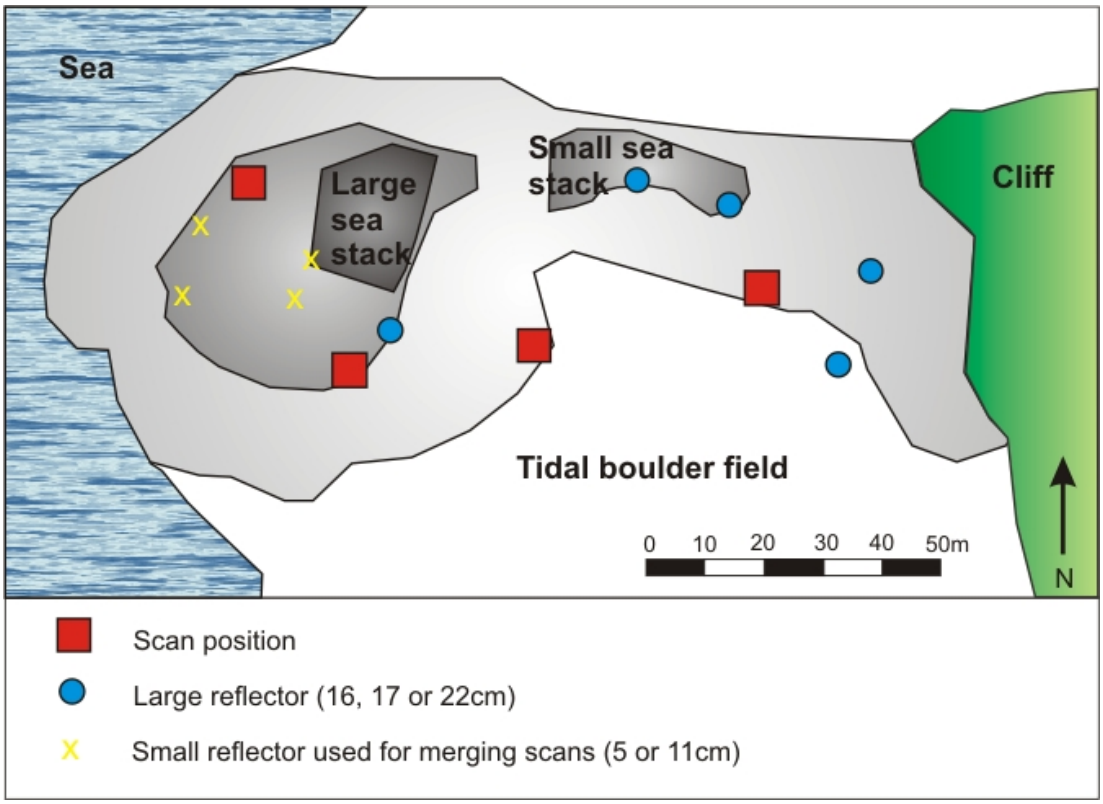

Figure 5.5 Map of the scan setup at Talisker Bay. The complex layout meant several scans were carried out; two on the platform halfway up the large sea stack. Two scans were carried out at one position, one of which was tilted at an angle of 30° to the horizontal, in order to capture the top of the sea stack.

5.3.3 Data processing

The steps required to produce a coloured 3D point cloud are now well-documented (e.g. Buckley et al., 2008; Hodgetts, 2009) and are described only briefly here. Once the point clouds and digital photos were collected at each site, a common frame of reference was needed. This was provided by the reflectors, as shown in Figures 5.3 and 5.5. These were identified in both the scans and the photos, and an adjustment carried out to establish the relative locations of the scanner and camera, and the relative locations of the various scan positions. A common coordinate system was thus established for the whole project. The point clouds could then be coloured from the images, and the scans merged to give one point cloud, as shown in Figure 5.6.

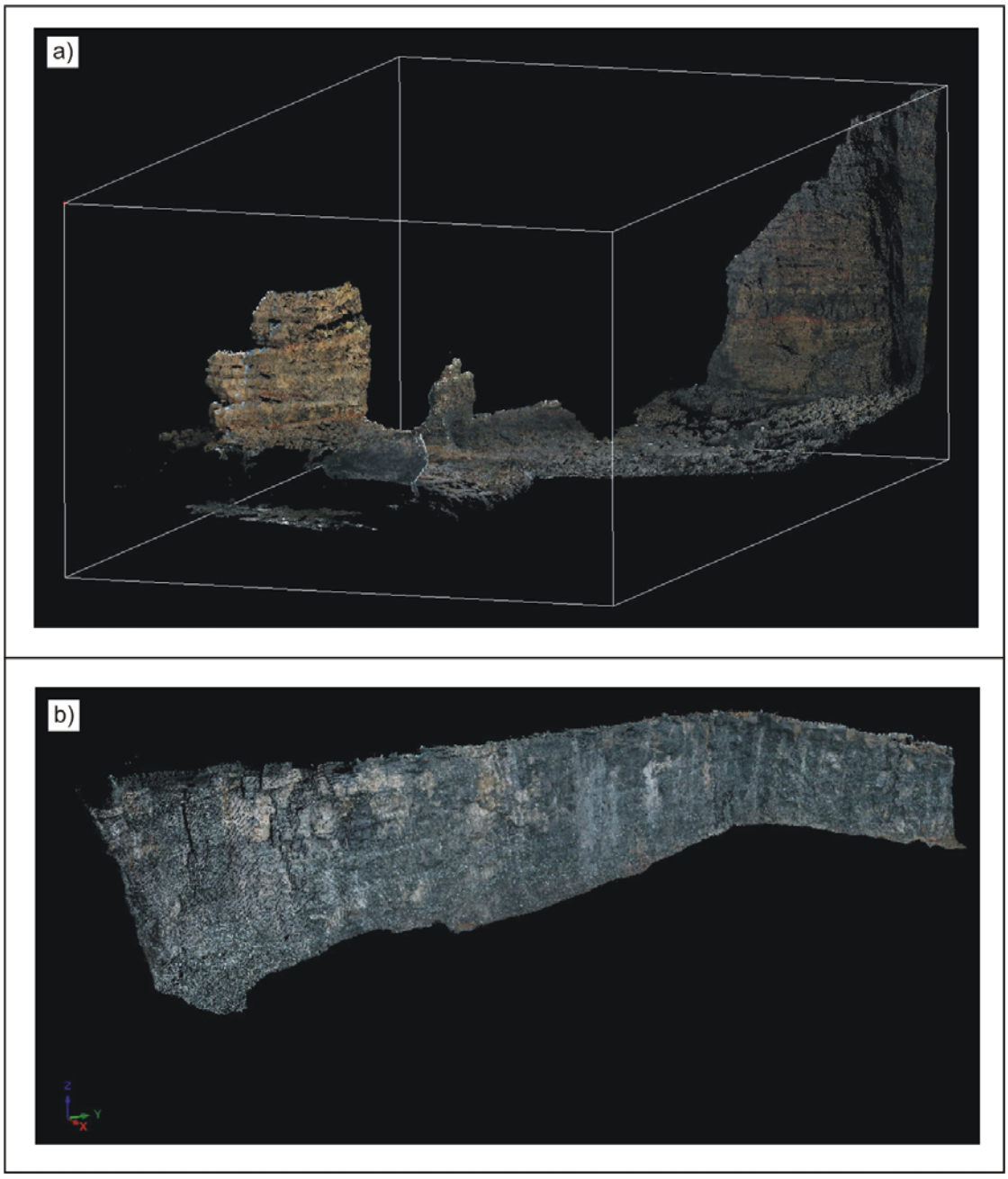

Figure 5.6 The completed laser scan point clouds, coloured from the digital photos. a) Talisker Bay data. b) Ljosa Quarry data.

The 3D point clouds at this stage are made up of millions of points, making it difficult for software to handle. Unwanted areas of the outcrop were removed to leave only the areas of interest. The data were then filtered using an Octree filter (e.g. McCaffrey et al., 2008) to leave around 10,000 points, suitable for importing into GOCAD®. In the case of the Ljosa quarry data this was achieved by giving the

resulting points a spacing of 20cm; whereas the point spacing for the Talisker Bay data was 50cm.

5.4 Building 3D models from the laser scan data

5.4.1 Picking key horizons

At this point, our workflow differs slightly from that of Buckley et al. (2008) and Enge et al. (2007). In their workflows, a triangulated mesh is formed from the point cloud, and the photographs are draped onto this. This allows detailed interpretation not possible on the point cloud itself, as the photograph is at a higher resolution than the point cloud. Enge et al. (2007) show the difficulty of making detailed interpretations directly onto the point cloud. The process of meshing the point data is extremely time-consuming, and becomes more so when the geometry of the site is complex. The Talisker Bay case study is extremely complex, and attempts to build a triangulated mesh were hampered by the high level of computing power required. Accordingly, a simpler method for interpreting the data was devised.

It was decided to draw interpretations directly onto the digital photographs, and then project the altered photographs onto the point cloud. The point clouds generated are at a resolution of around 50 points/metre, whereas the photographs have 300 or more pixels/metre, so much more detailed interpretation is possible. Lines drawn on the photograph had a width of approximately 10cm when projected onto the point cloud, covering 4 or 5 points. The lines from the photos are projected into the correct position on the point cloud, and can easily be seen, so 3D lines could be drawn directly onto the point cloud then exported.

The purpose of our 3D geological models is to show the different volcanic facies present in the outcrops, and provide data on flow thicknesses and crust to core ratios. The high quality digital photographs, accompanied by detailed field observations, allowed us to identify flow tops, bases and crust/core boundaries, as well as dykes, sills, lava tubes and boles. The loss of 10cm of accuracy is acceptable in this situation, as very high accuracy is not required, but this workflow would not be suitable for other uses.

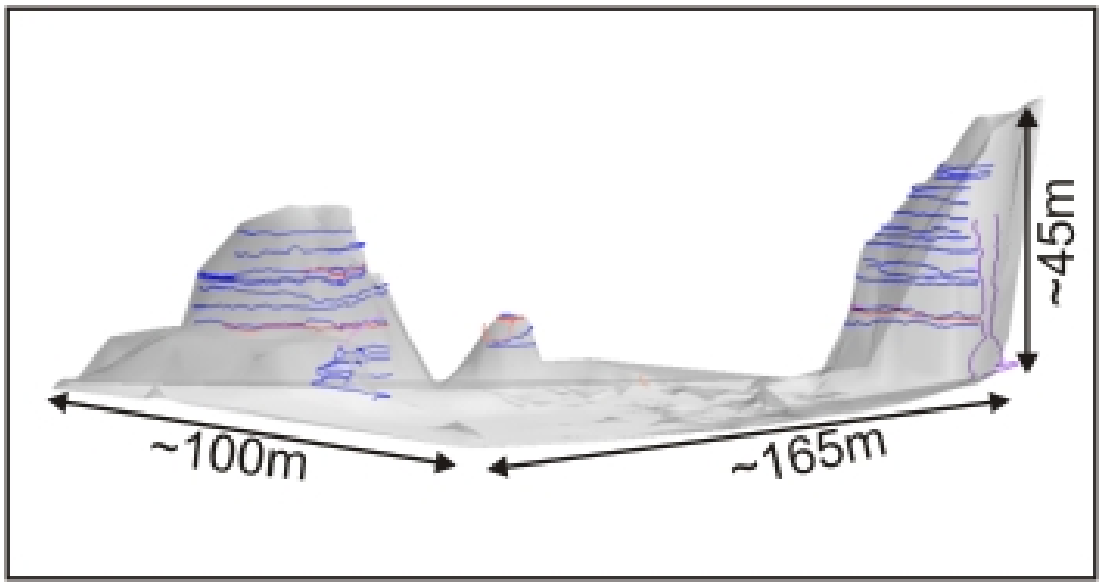

Figure 5.7 Interpreted 3D lines from the Talisker Bay case study

5.4.2 Extending the horizons laterally

The GSI3D software, described in Chapter 3, uses cross-sections, mapped outlines and a digital terrain model to produce a solid model made up of triangulated objects. Its main function is to produce 3D geological models from existing geological maps and borehole data (e.g. Kessler et al., 2009). For example, detailed models of quaternary sediments have been constructed to give information on groundwater flow (Lelliott et al., 2006).

To produce a 3D geological model in GSI3D, the user must first construct cross-sections through the units of interest. Then, the outline extents must be defined in a map view. Once these have been defined, the software triangulates surfaces satisfying the cross-sections and map extents, and the DTM forms the top of the model. All these steps are fully controlled by the user, allowing the user to apply their geological knowledge to construct a realistic final model. This level of control makes the software potentially ideal for use with TLS data, and one of the additional goals of this study is to test the use of TLS data within the GSI3D environment. The process of constructing the models is described in detail below.

The .dxf files produced in the previous step were imported into GOCAD®, and the fault modelling package used to produce preliminary surfaces. In the case of the

Talisker Bay data, flows from different outcrops had already been correlated, and their top surfaces were constructed using the interpreted lines as edges. Where each horizon only had one interpreted line, this was extended laterally by treating the line as a fault centre line. The triangulated surfaces were then exported to GSI3D. GSI3D, unlike GOCAD®, places no limitations on where surfaces are constructed. This allowed us to extend surfaces to where no data was available, and to use our geological experience to determine where the surfaces should go. While this introduced a much higher level of uncertainty, it allowed us to extend the surfaces and construct a useful block model. The finished model of Ljosa quarry is shown in Figure 5.8. Lighter colours are flow crusts and darker colours are flow cores.

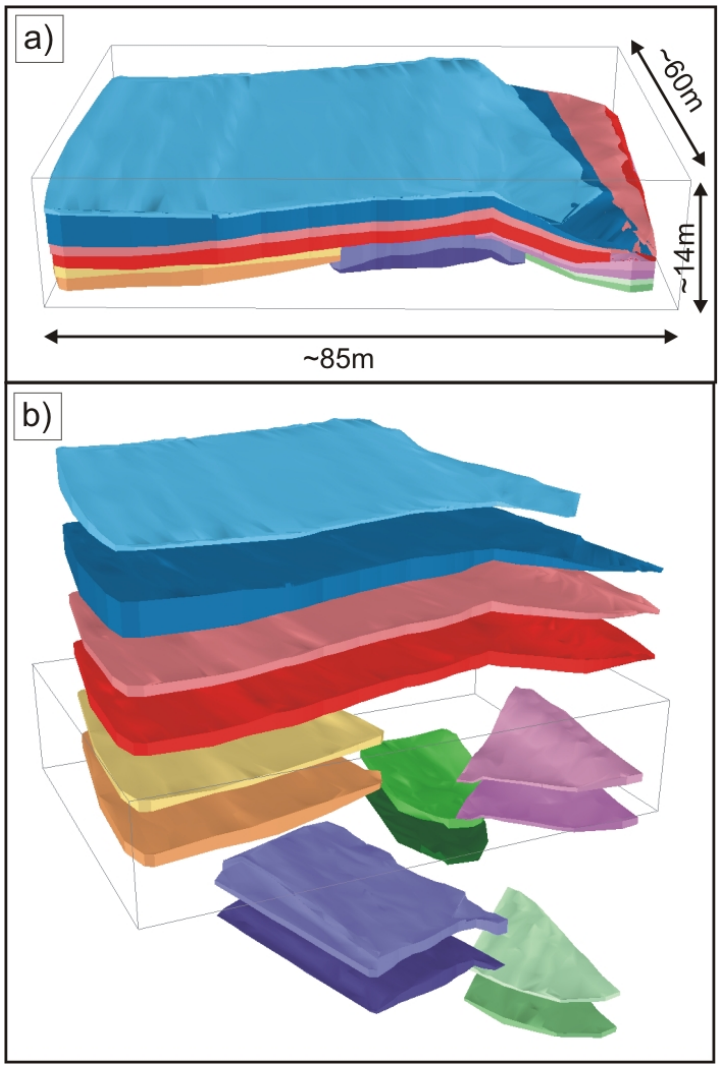

Figure 5.8 The completed 3D model of the Ljosa Quarry case study constructed in GSI3D. a) Final model - lighter colours are flow crusts and darker colours are flow cores. b) Expanded model to show the full distribution of each layer.

For the Talisker Bay case study, two final models were constructed. The first is a palaeoreconstruction of the lava flows between the sea stacks and cliff section, constructed as detailed above. The second uses a GOCAD® surface of the topography, generated from the filtered laser scan point cloud, to display only the present-day flows. The GOCAD® surface is shown in Figure 5.9. All overhanging areas have been replaced by vertical sections to make it compatible with the GSI3D software. The final models are shown in Figure 5.10. It has also been possible to include lava tubes, a sill and a dyke in this model, making it possible to determine what proportion of the total volume is made up of these features.

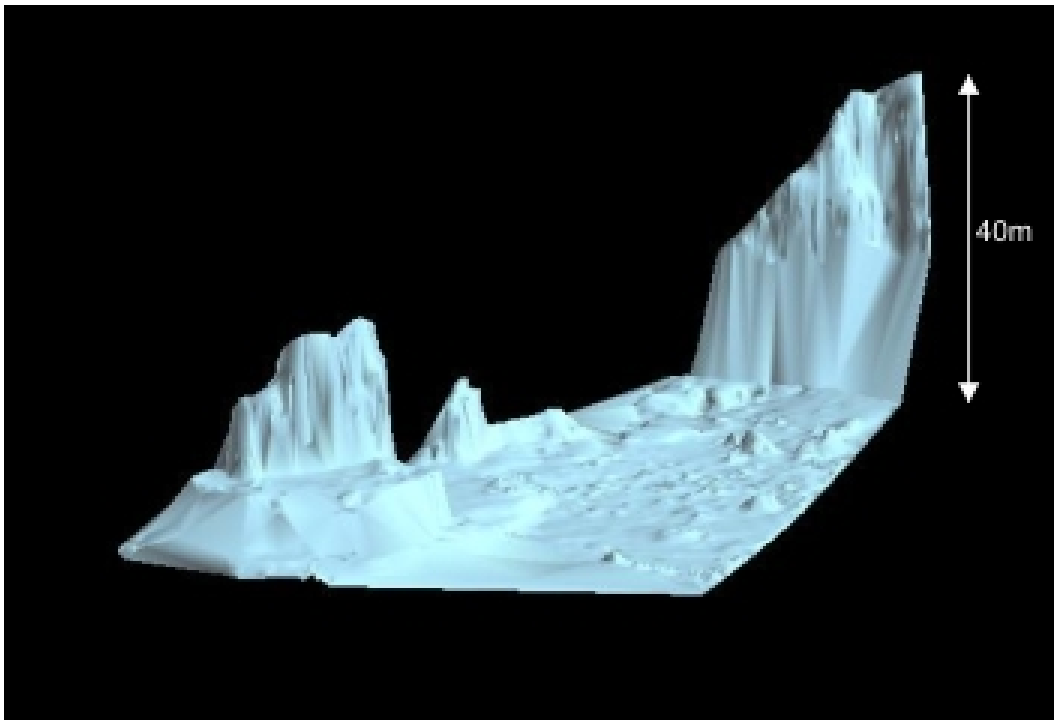

Figure 5.9 The GOCAD® surface used to construct the Talisker Bay model.

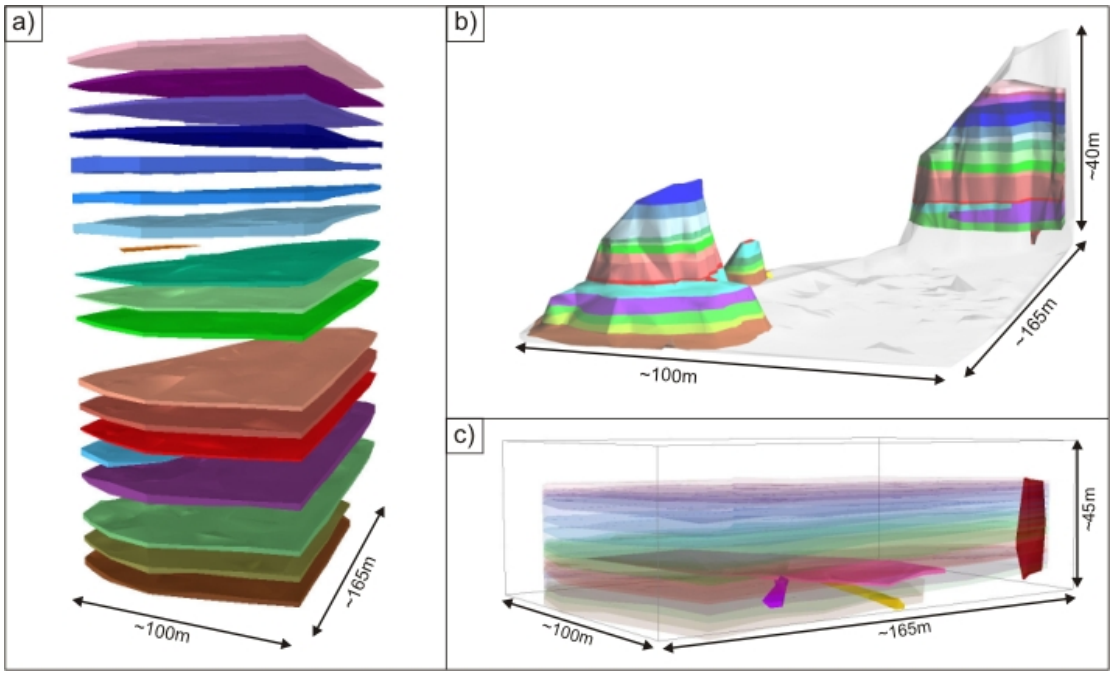

Figure 5.10 Completed GSI3D models of the Talisker Bay case study. Animated versions available. a) Exploded view of the lava flows and sedimentary units. b) The 3D volumes cut to the present day topography. c) Transparent view of the entire model highlighting the sill, dyke and lava tubes.

5.4.3 Interrogating the block models

The completed geological models can be analysed in a number of ways. Virtual boreholes and cross-sections can be obtained for any area of the model to give an idea of the heterogeneity, which is useful in showing how complex the stacking patterns of lava flows may be. An example of a synthetic borehole is given in Figure 5.11.

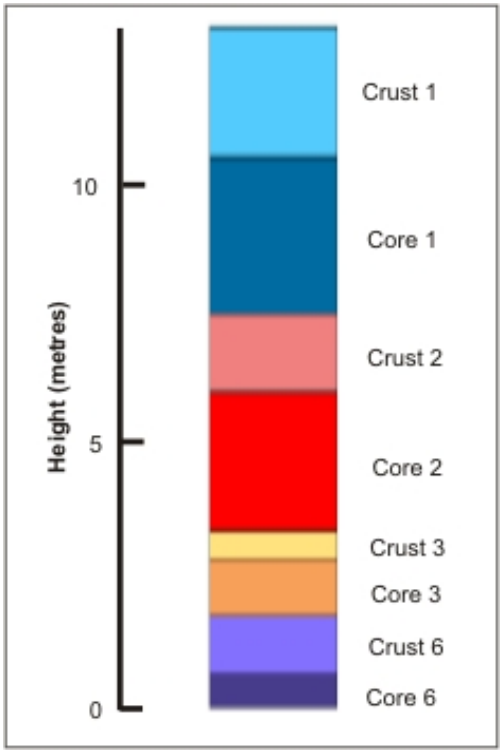

Figure 5.11 Synthetic borehole through Ljosa quarry model.

It is also easy to obtain volumes and map areas for each unit. While the volume is a function of the size of the model, and therefore not useful in determining the original flow volume, it can be used with the flow area to calculate an average thickness. We have calculated average flow thicknesses and crust to core ratios for the Ljosa quarry model, and these are given in Table 5.1. In the case of the Talisker Bay model, it was not possible to identify crusts for the majority of flows; however volumes and average thicknesses were calculated. These are given in Table 5.2. The use of these data is described in the next section.

	Area (m^2)	Volume (m^3)	Average thickness (m)	Core proportion
Crust1	3050	7575	2.483	
Core1	3303	9336	2.826	0.532
Crust2	3621	4907	1.355	
Core2	3656	6890	1.884	0.582
Crust3	1441	1107	0.768	
Core3	1434	2725	1.900	0.712
Crust4	554	529	0.955	
Core4	551	745	1.353	0.586
Crust5	544	827	1.521	
Core5	538	478	0.888	0.369
Crust6	1091	2305	2.113	
Core6	1085	2219	2.045	0.492
Crust7	483	357	0.739	
Core7	478	487	1.020	0.580

Table 5.1 Details of flows from Ljosa quarry model.

	Area (m^2)	Volume (m^3)	Average thickness (m)	Core proportion
Flow 17	11140	20419	1.83	
Flow 16	11140	13714	1.23	
Flow 15	11140	18809	1.67	
Flow 14	11140	22996	2.06	
Flow 13	11140	45107	4.05	
Flow 12	11140	31387	2.82	
Flow 11	11140	31915	2.86	
Red Bole 2	397.54	127.64	0.32	
Flow 10	11140	16998	1.53	
Crust 9	11140	19605	1.76	0.554
Core 9	11140	24368	2.19	
Crust 7	11140	19390	1.74	0.672
Core 7	11140	39761	3.57	
Red Bole 1	11140	8599.6	0.77	
Flow 6	6047.4	13383	2.21	
Flow 5	9620.5	28832	3.00	
Flow 4	1613.7	2243.4	1.39	
Flow 3	11140	20655	1.85	
Flow 2	8381.7	9848.4	1.17	
Flow 1	8723.3	22517	2.58	
Sill	2111.7	2365.1	1.12	

Table 5.2 Details of flows from Talisker Bay model.

5.5 Evaluation of terrestrial laser scanning

The general benefits and drawbacks to the use of TLS technology are summarised in Buckley et al. (2008), Enge et al. (2007), and McCaffrey et al. (2005), amongst others. Those most relevant to the work presented here are outlined below:

Benefits:

- 3D data can be captured rapidly from a large area.
- Data are captured in a digital format suitable for analysis away from a field situation.
- Data can be viewed from any angle and at a wide range of scales, limited only by the resolution of the scan.
- Inaccessible parts of outcrops can be viewed in detail.
- Accurate sizes, shapes and angles can easily be obtained.

Drawbacks:

- The equipment weighs 70kg in total, limiting possible scanning sites to those relatively near the road. Logistics of reaching the field area become more complicated.
- Data processing is time-consuming and involves a slight loss of data accuracy.
- Setup procedures are complex.
- The equipment does not function in poor weather, an important factor on the west coast of Scotland.
- The range of the equipment used in this work is limited to around 200m on basalt. This is reduced further if the outcrop is wet.

In summary, TLS provides an efficient, accurate way of capturing 3D data at a limited range of flood basalt outcrops. Problems arise when outcrops are far from a road or extremely large (though the size depends on the exact equipment used). As discussed in Chapter 1, the outcrop exposure of flood basalts is often quite limited, and finding suitable outcrops near a road can be problematic.

5.6 An alternative approach: structure from motion

As discussed in Section 5.5, TLS has a number of limitations. One of the most relevant to this work is that the choice of outcrops that may be captured is limited, both in size and location. Many features in flood basalt provinces, for example tabular lava flows, are larger than may be captured by the Z420i laser scanner, with lateral extents of several kilometres. The cost of laser scanning equipment meant that purchasing a scanner with a longer range was not possible - additionally, long-range scanners are many times slower than the Z420i scanner.

Another potential approach is to construct a 3D virtual outcrop from photographs alone, without using a laser scanner. Over recent years, many improvements have been made in computing power and computer science research, and the feasibility of this approach is discussed below.

5.6.1 Theoretical principles

In computer science, reconstructing 3D geometry from images is an important area of research in computer vision. Reconstruction techniques rely on one of the following (Dellaert et al., 2000):

Known cameras: given calibrated images from known camera viewpoints, solve for the 3D scene shape. This is the basis of most digital photogrammetry used in geology (e.g. Gaich et al., 2006).

Known shape: given a 3D model and images, determine the camera position for each image. This is not useful for our purposes.

Known correspondence: This relies on features being recognised in multiple images. The trajectories of these features can be measured, and the 3D positions of the features can then be solved, along with the camera position when the images were obtained.

In digital photogrammetry, improvements have been made that allow realistic 3D models to be generated automatically (Gaich et al., 2006). However, if a spatially correct 3D model is required, the location of control points must be measured (e.g. with GPS) and the camera must be calibrated. Camera calibration involves measuring the precise focal length, image distortion and pixel size of a camera,

amongst other parameters. While calibration is now possible with a handheld digital camera, it is time-consuming and requires specialist equipment. Using this approach, it is possible to produce virtual outcrops accurate to within 1cm of a TLS dataset (Birch, 2006).

Solutions using known correspondence do not require camera calibration or control points. One area using known correspondence is “structure from motion” (SFM). This works in a similar way to kinetic depth perception in human vision - as a person moves relative to objects, they can tell which is closer to them by the perceived movements of the objects. In software based on SFM, features are extracted from images and matched between images, and then a solution is found for the structure of the scene and the positions of the cameras. A key point with this method is that large numbers of images of the target area from different locations are required. This is commonly achieved with a video camera but can be done with a conventional digital camera, as described below. The mathematical basis for SFM is beyond the scope of this thesis, but is described in detail by Hartley and Zisserman (2004).

The main benefit to a geologist of using SFM is that a reconstruction can be obtained solely from taking photographs of an outcrop with an uncalibrated camera. To be spatially accurate, all that is required is a GPS position for the first and last photographs. A large number of photographs are required; however these can be obtained in under an hour. The equipment is highly portable and does not require a stable surface, so data can be obtained from remote locations or from a boat. Software capable of reconstructing outcrops using SFM has been developed by Vicon Motion Systems Ltd., based on an algorithm by Fitzgibbon and Zisserman (1998), but this is not yet widely used in geology. In Section 2.6.2 I present a pilot study reconstructing outcrops using SFM, and explore the feasibility of this approach.

5.6.2 Pilot study: Hyaloclastites in Iceland

A case study was selected to test the approach described in the previous section. Hjorleifshofði, a headland on the South coast of Iceland, is a remnant of an emergent submarine volcano (Thordarson and Hoskuldsson, 2002) and has a well-exposed sequence of hyaloclastites up to 200m high. The outcrop at the south end of the

headland is 200m high with a lateral extent of around 700m (Figure 5.12). As discussed earlier in this chapter, an outcrop this size would be difficult to capture with the Z420i laser scanner. The outcrop is of interest because the facies architecture of hyaloclastites has so far received little attention, but thick sequences exist offshore in the North Atlantic.

Figure 5.12 Hjorleifshofði headland, a thick sequence of hyaloclastites in southern Iceland.

Data required were a series of digital photographs covering the extent of the outcrop, taken while walking along the outcrop base, and GPS positions from the locations of the first and last photographs. There had to be a large overlap (75% or more) between successive photographs to allow features to be tracked, and examples are shown in Figure 5.13. For this location, 50 photographs were taken in a distance of 500m, following a roughly straight line along the base of the outcrop. The same focal length had to be used for each photograph but the shutter speed and aperture were allowed to vary.

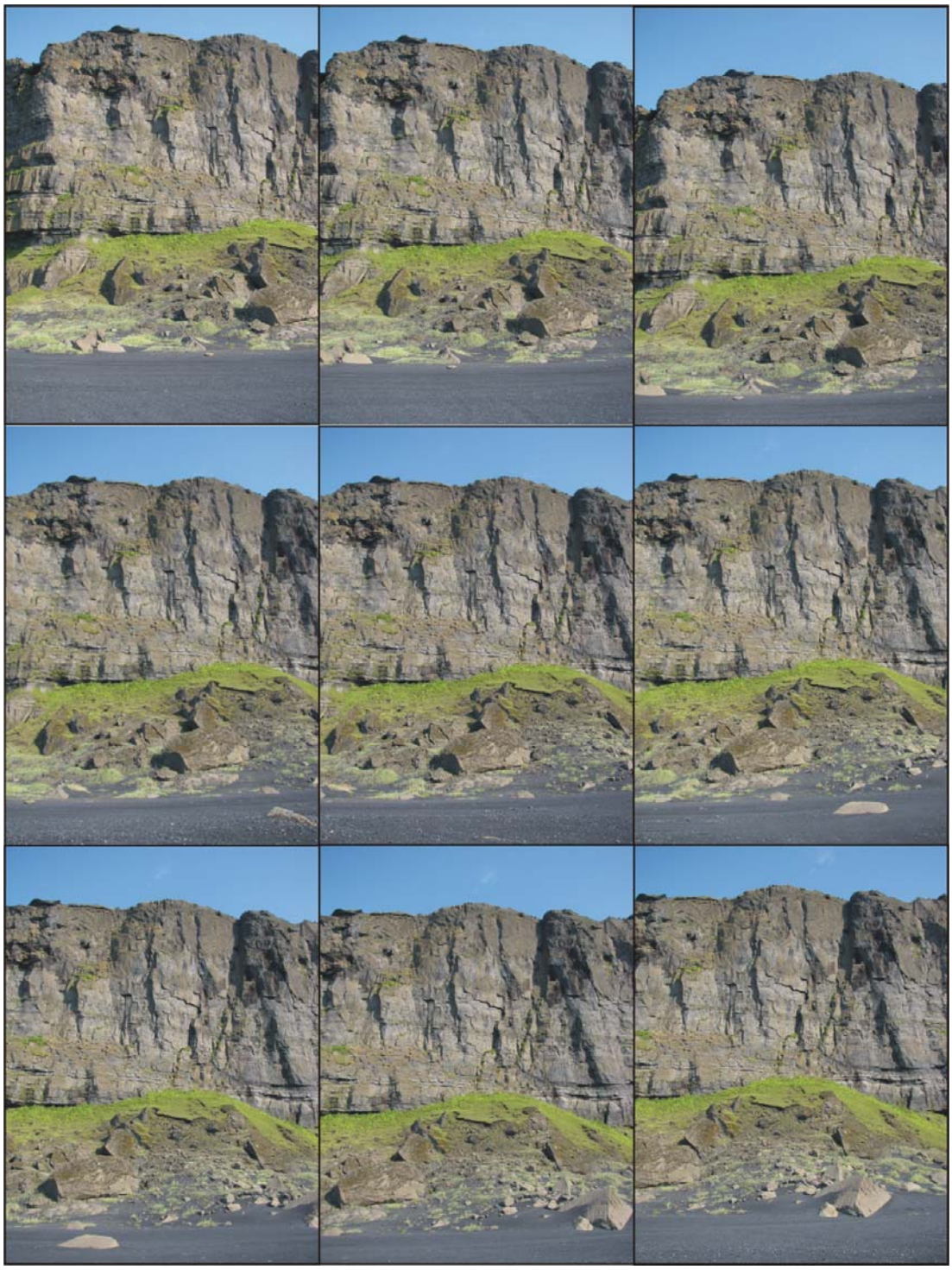

Figure 5.13 Sample photographs from the Hjorleifshofði headland. The overlap between the photographs must be around 75% for a successful reconstruction.

No processing of the images was required prior to performing the reconstruction. The 3D reconstruction was carried out using the Boujou software developed by Vicon Motion Systems Ltd. (http://www.vicon.com/boujou). This produced a series of matrices describing the transformations required to project each photograph onto the 3D model, and the positions of the camera when each photograph was taken. A Matlab frontend was developed by Aeron Buchanan (pers. comm.) to take these matrices and the GPS positions and produce a 3D reconstruction, as shown in Figure 5.14. This also allows a user to pick relevant points on each photograph (for example the boundary between two units) and 3D coordinates of each point are returned, as shown in Figure 5.15. The coordinates are in metres from an arbitrarily chosen origin, and are derived by interpolating between the corner nodes of the triangle shown in Figure 5.15a. Further developments in this frontend could produce a draped surface or, if this approach is pursued, commercially available software could be used to produce a virtual outcrop. Increased accuracy could also be obtained from increasing the number of tracked points.

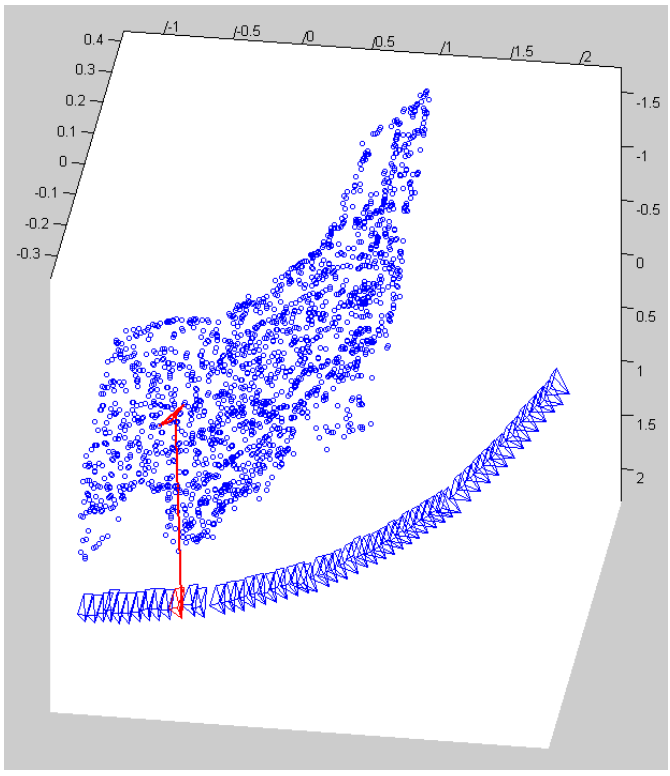

Figure 5.14 3D reconstruction of the headland. Model is 200m high, 500m long. Triangles are camera positions, circles are features tracked between photographs. The red line shows the path from the camera position to the point picked out in Figure 5.15.

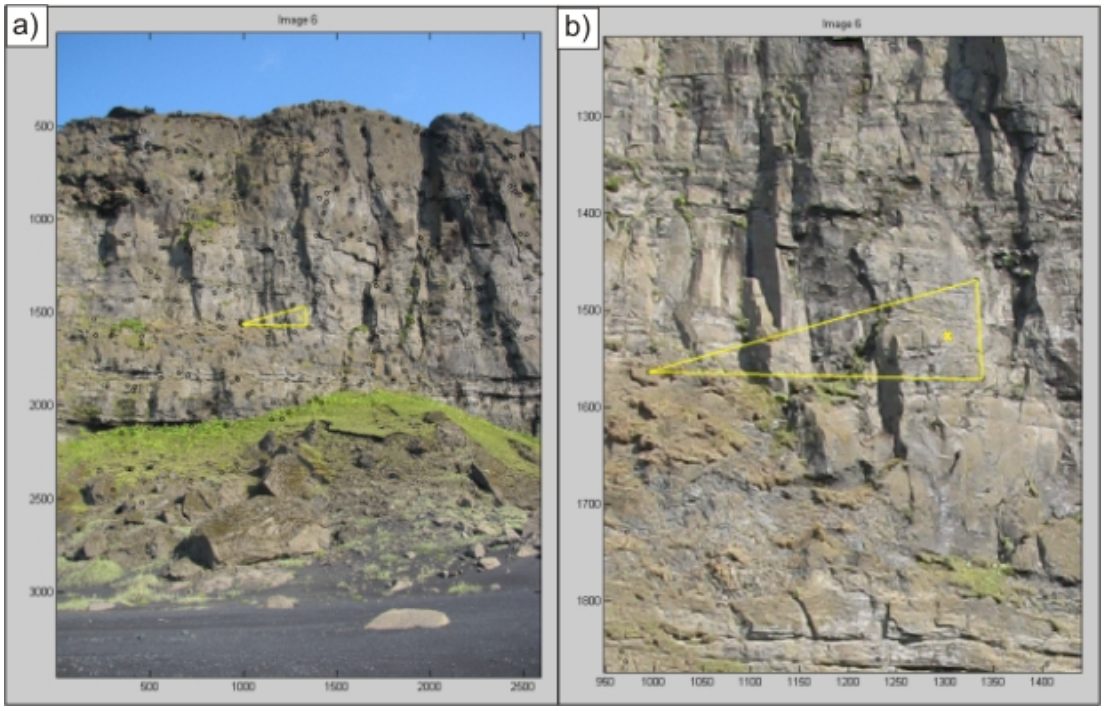

Figure 5.15 Matlab interface for picking points on 3D reconstruction. a) The yellow triangle shows the surface between three tracked points. b) A point is selected within the triangle, as indicated by the yellow cross, and the 3D position on the model is calculated from the position within the photograph.

The interpreted points could form the basis for construction of models following the methods described for the TLS data earlier in this chapter, but time constraints prevented this. However, more needs to be known about the accuracy of this method before 3D models can be built. It is likely that the major source of error is from the GPS coordinates: a hand-held unit was used, and its accuracy was given by the unit as ±10m at this location (or approximately 0.2% of the total distance). This could be significantly reduced by using differential GPS equipment, with an accuracy of a few centimetres. There will also be errors in the 3D reconstruction within the body of the image, and these need to be quantified using accurate calibration points.

This approach has only become possible very recently following developments in software and computing power; however it may have potential for future use. The principal advantages are the lack of specialist equipment and ease of transportation of equipment.

5.7 Discussion

The 3D geological models presented in this chapter accurately capture the heterogeneity present in a complex sequence of compound-braided lava flows. The internal flow structure can be identified, and irregular features such as dykes, sills and lava tubes can be visualized. Quantitative data on lava flow thicknesses, volumes and crust to core ratios can be easily obtained from the final models, and virtual boreholes constructed in any location.

This work builds on previous detailed facies analysis of flood basalt sequences (e.g. Single & Jerram 2004; Passey and Bell 2007). The use of TLS technology and associated software packages provides many advantages over traditional "paper-based" methods, as summarised by Buckley et al. (2008). For our purposes, it is useful to capture 3D data quickly and accurately, allowing for lab-based analysis. The fine-scale modelling is required to capture all the heterogeneity present in a flood basalt sequence, and the models also need to include lateral variations. Additionally, the level of detail and accuracy provided by TLS makes it possible to correlate lava flows between inaccessible parts of outcrops.

The TLS workflow presented here provides a relatively simple way to construct 3D models, albeit with a slight loss in accuracy. It reduces the computer memory and processing power required compared to workflows such as that of Buckley et al. (2008). The loss of accuracy may make the workflow unsuitable for detailed structural analysis, but the interpretations have an uncertainty of around 10cm, making them suitable for facies analysis.

However, TLS is not suitable for capturing data from all flood basalt outcrops. Often, outcrops are remote or features are extremely large - tabular lava flows may be several kilometres long. The level of accuracy of TLS is not required to map out these flows, but advances in digital photogrammetric techniques may provide a method for mapping lava flows in the future.

6

6. DEFINING AND MODELLING LAVA FLOW SURFACE ROUGHNESS.....102

CHAPTER SUMMARY 102

6.1 INTRODUCTION TO RANDOM MODELS AND PREVIOUS WORK 102

6.1.1 Spectral analysis and basalts as fractals 102

6.1.2 Previous work 104

6.1.3 Requirement for new data 105

6.2 DATASETS.....105

6.2.1 Remote sensing data from Iceland.....105

6.2.2 Laser scan data from the Faroe Islands.....108

6.2.3 Laser scan data from Ethiopia.....110

6.2.4 Data preparation.....110

6.3 DATA ANALYSIS.....112

6.4 BUILDING RANDOM SURFACES 115

6.5 DISCUSSION 119

6. Defining and modelling lava flow surface roughness

Chapter summary

In this chapter, I explore ways of constructing synthetic lava flow top surfaces. Data were obtained from terrestrial laser scanning in the Faroe Islands and Ethiopia, and remote sensing data from Iceland. In all of these datasets it was possible to identify the top surface of a single lava flow, and profiles were taken across the flows. By plotting power spectra of these data, we observe that surface roughness displays a power-law relationship, so we assume they have fractal behaviour. From these power spectra, the fractal parameters of the Hurst number and correlation length were calculated. These describe a fractal distribution and are defined in detail below. The fractal parameters were then used to generate synthetic surfaces which will be used further in Chapter 7.

6.1 Introduction to random models and previous work

Random models are introduced here for two reasons. Firstly, they provide a means to generate 3D models than can be created from most outcrops, as discussed in Chapter 1. Secondly, they provide a means of reintroducing small-scale topography not captured in triangulated surfaces with sparse data points, as discussed in Chapter 5. Accordingly, surfaces are generated at two scales: a 10km x 10km surface is larger than most outcrops and is suitable for generating synthetic seismic data; and a 100m x 100m surface is similar to the models from Chapter 5. This chapter describes the theoretical basis for the random modelling, the source data and the outputs.

6.1.1 Spectral analysis and basalts as fractals

Many geological and topographic features are scale-invariant, meaning they can be described by a fractal dimension, D (Turcotte, 1989). It is possible to test whether a medium is fractal by taking the Fourier transform of a profile across it to generate a power spectrum. A fractal medium displays a relationship between the power spectrum and wave number given by the following equation (Huang and Turcotte, 1989):

$$P(k)=Ak^{-\beta}$$

where $P(k)$ is the power spectrum, k is the wavenumber and A is a constant. If the power spectral density is plotted against the wavenumber on a log-log scale (Figure 6.1), β is given by the slope of the straight line part. The fractal dimension D can be calculated from the slope as follows:

$$D = \frac{5-\beta}{2}$$

This equation holds for the one-dimensional case (i.e. a cross-section of a surface) (Huang and Turcotte, 1989; Dolan and Bean, 1997). The upper limit of the straight line in Figure 6.1 is the correlation length a, and beyond this the medium is no longer fractal (Frenje, 2000). If a 1D profile across a basalt lava flow surface shows this type of plot we know it is fractal at scales up to the correlation length.

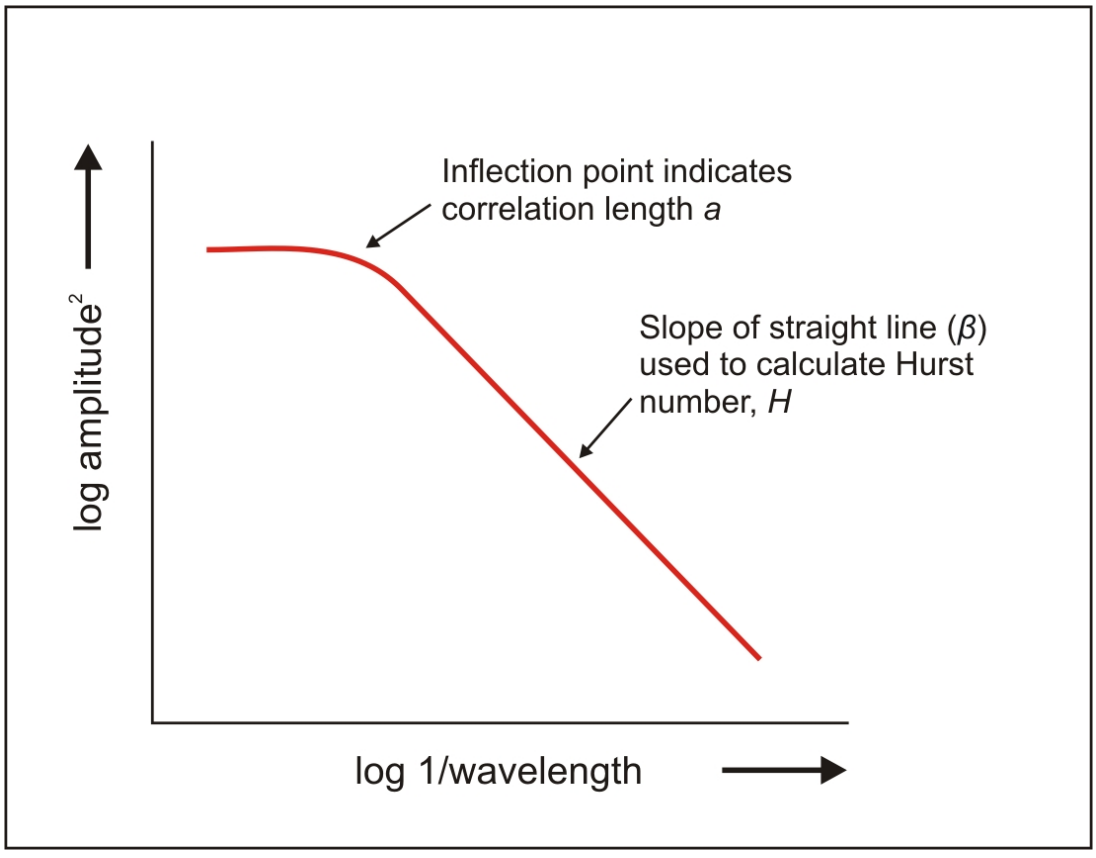

Figure 6.1 Determining Hurst number and correlation length from a power spectrum.

The Hurst number is also used to quantify the fractal properties of a medium, and is useful for comparison between 1D and 2D fractal parameters. The Hurst number, H (or ν) is related to D by the following equation in the one-dimensional case (Dolan and Bean, 1997):

$$D = E + 1 - H$$

where E is the Euclidean dimension. For a profile, $E = 1$, for a surface $E = 2$, and so on. The effect on surface roughness of altering the Hurst number is shown in Figure 6.2.

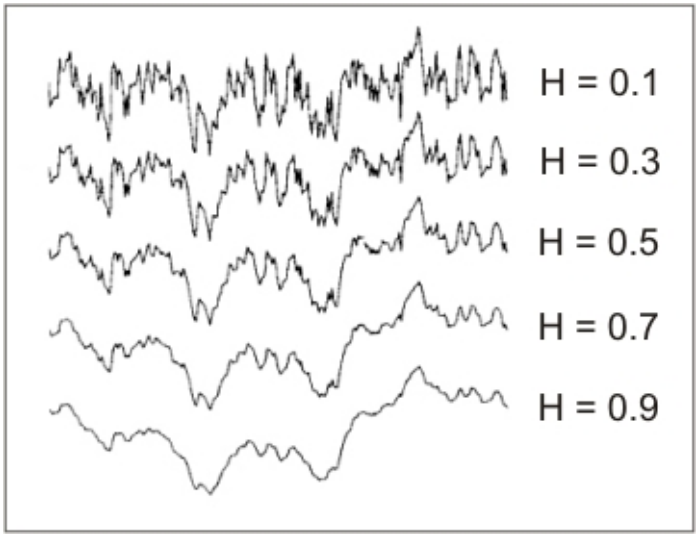

Figure 6.2 Effect of the Hurst number on surface roughness, while the standard deviation remains constant. From Saupe (1988).

6.1.2 Previous work

Previous studies have also considered basalt lava flows as fractal surfaces. Walia and Bull (1997) analysed seismic data from the Rockall Trough, using spectral analysis to obtain a fractal dimension of 1.36 for the top of the lava sequence. Martini et al. (2005) used this value to construct 3D velocity models, along with a fractal dimension for the vertical velocity distribution obtained from a large dataset of Ocean Drilling Program wells. Maresh (2004) analysed 3D seismic data from the Rockall Trough, obtaining a 2D fractal dimension of 2.49. White (2009) built a random basalt volume using data from Well 164/07-1 in the northern Rockall Trough

(see Chapter 4). Bean and Martini (2010) used digital photographs to obtain a fractal dimension, discussed in Section 6.5.

Much of this work stems from analysis of borehole data to produce stochastic models (e.g. Bean, 1996; Holliger, 1996; Dolan and Bean, 1997; Dolan et al., 1998; Frenje and Juhlin, 1998) and analysis of topography both on land (Huang and Turcotte, 1989) and on the seafloor (Goff and Jordan, 1988). Similar approaches have been used in a number of different fields including the analysis of sedimentary cycles (Browaeys and Fomel, 2009) and in seismic oceanography (Buffett et al., 2010).

6.1.3 Requirement for new data

Whilst several analyses exist of seismic data of basalt surfaces, few outcrop data are used (e.g. Bean and Martini 2010). Seismic data offers a wide area of coverage; however because of the resolution limit (first Fresnel zone) of band-limited seismic data it is impossible to know whether the top surface of the basalt sequence is one flow or many. Field data is much better constrained but harder to obtain. Here, we present high resolution data that are known to be from single lava flows, at scales covering 10cm to 10km. The datasets are described in the next section.

6.2 Datasets

In this section, I introduce the datasets used to provide inputs for the random models and summarise their geological setting. No one dataset covers all scales at a suitable resolution, so a combination of laser scans and satellite data is used.

6.2.1 Remote sensing data from Iceland

The first data set was obtained from the Laki lava flow, Iceland. This was emplaced in 1783-84 and is regarded as the closest modern analogue to a flood basalt lava flow (Self et al., 1998). It has been used to model the environmental impact of flood basalt eruptions (Self et al., 2006) and has also been used as an analogue to Martian lavas (Keszthelyi et al., 2004). Thordarson and Self (1993) and Guilbaud et al. (2005) provide a full description of the flow morphology and its eruption. Cross-sections through the Laki lava flow and the Roza Member of the Columbia River flood basalt province reveal the same three-part internal structure (Self et al., 1998).

The Laki lava field totals approximately 14.7km^3 of basaltic lava, covering an area of approximately 599km^2 (Thordarson and Self, 1993). The lava erupted from fissures in the Sída highlands of southern Iceland, part of the Grimsvotn volcanic system, and flowed south down the gorges of two rivers: the Skaftá and the Hverfisfljót. It then spread out onto the flat coastal plain formed by the earlier Eldgja lava flow (934AD). The area of interest for this study, shown in Figure 6.3, is the branch that flowed out of the Skaftá gorge onto the coastal plain - the Eldhraun branch. This comprises ~5km^3 of lava that was emplaced directly onto the Eldgja lava, into an unconfined area. This area is therefore a useful analogue for a flood basalt lava flow.

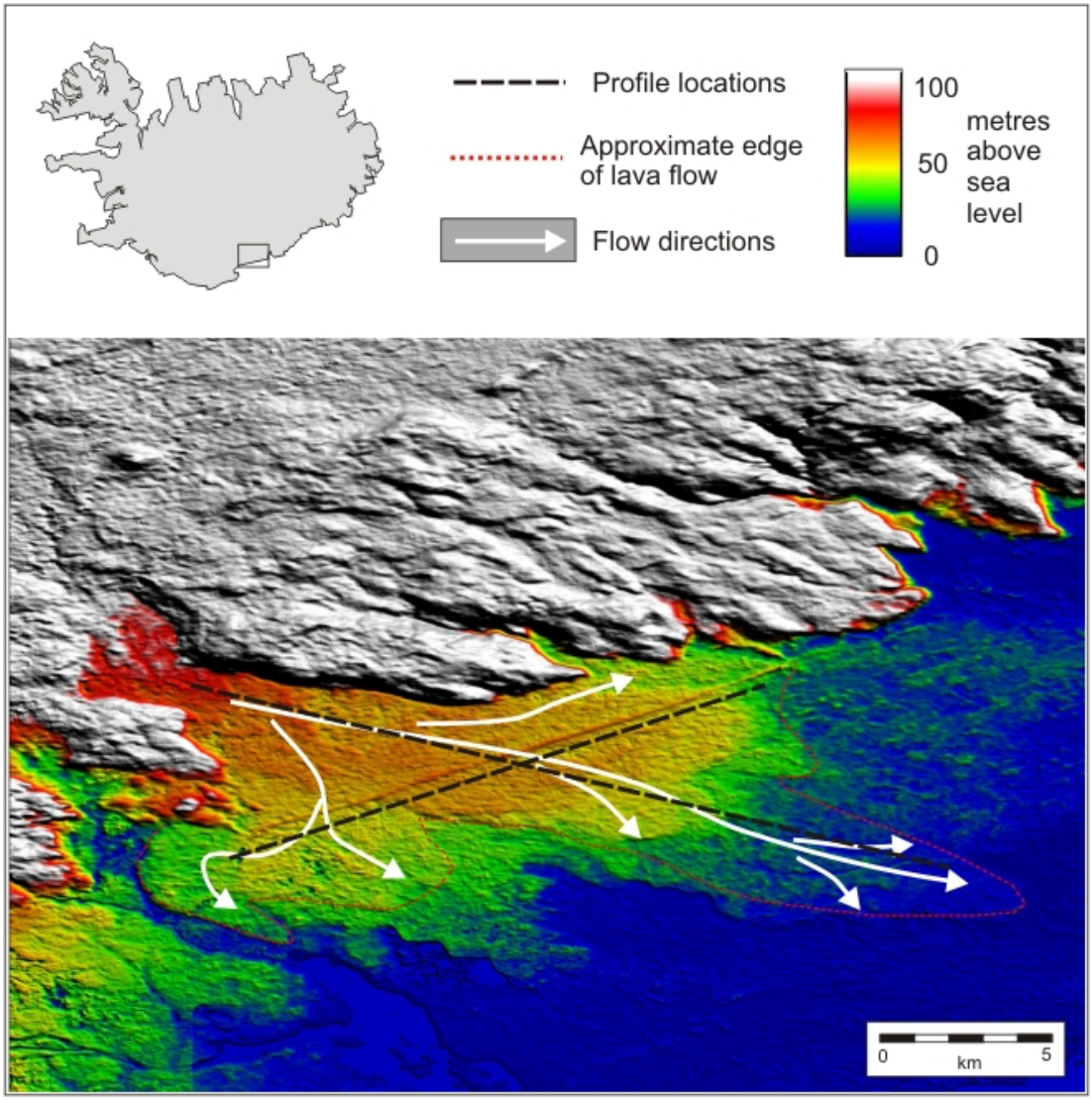

Figure 6.3 Eldhraun branch of the Laki lava flow: location map and satellite DEM from ASTER Global Digital Elevation Model (http://www.gdem.aster.ersdac.or.jp/). Data at 30m resolution. Original data of ASTER GDEM is the property of the Ministry of Economy, Trade and Industry (Japan) and NASA. Flow directions and Laki extent from Guilbaud et al. (2005).

The Eldhraun branch is also useful because it offers a very large distance to analyse – approximately 15km profiles can be made as shown in Figure 6.3. As it is so young, and remains uncovered by any later lava flows, it preserves its surface morphology very well, as shown in Figure 6.4.

Two cross-sections were taken from this dataset, one across the flow direction and one along the flow direction, as shown in Figure 6.3. The data were exported from the Global Mapper program (http://www.globalmapper.com) as x-z sections with 1024 data points. The along-flow section has a length of 23.7km, giving a point spacing of approximately 23m, and the across-flow section has a length of 15.1km, giving a point spacing of approximately 15m.

Figure 6.4 Laki surface roughness. a) Eldhraun branch near Kirkjubaejarklaustur. b) Looking south across the Eldhraun from Fjaðrárgljúfur.

6.2.2 Laser scan data from the Faroe Islands

Laser scan data were acquired in June 2007 during field work in the Faroe Islands, in the same period as the data from Ljosa Quarry used extensively in Chapter 5. The data used here come from a quarried exposure near Glyvursnes, the location of one of the boreholes described in Chapter 4. Data were collected following the methods described in Chapter 3.

This outcrop, shown in Figure 6.5 below, was chosen because it offered a very clear top surface of one lava flow and a base surface of another, with a bole horizon in the middle. It is within the Enni Formation of the Faroe Islands Basalt Group (see Chapters 2 and 4 for further details) which contains a mixture of compound-braided and tabular-classic flows. The two flows at this outcrop are probably compound-braided flows; however this is not certain because neither flow shows its entire thickness or extent. The top and base are very well-preserved and offer an excellent 2D section for analysing the surface roughness.

Two scans were required for complete coverage of this outcrop because its geometry was relatively simple. A total of approximately 8,200,000 points were collected, and 14 digital photographs in two panoramic sequences. The flow top and base were identified on the digital photographs, and 3D lines were drawn on the scan surface following the methods described in Chapter 5. The total length of the outcrop is approximately 130m. Approximately 700 points were digitized for the base of the upper flow, giving an average point spacing of around 17cm. Approximately 900 points were digitized for the top of the lower flow, giving an average point spacing of around 15cm. These were exported as two column x-z ASCII files and analysed as described in Section 6.3.

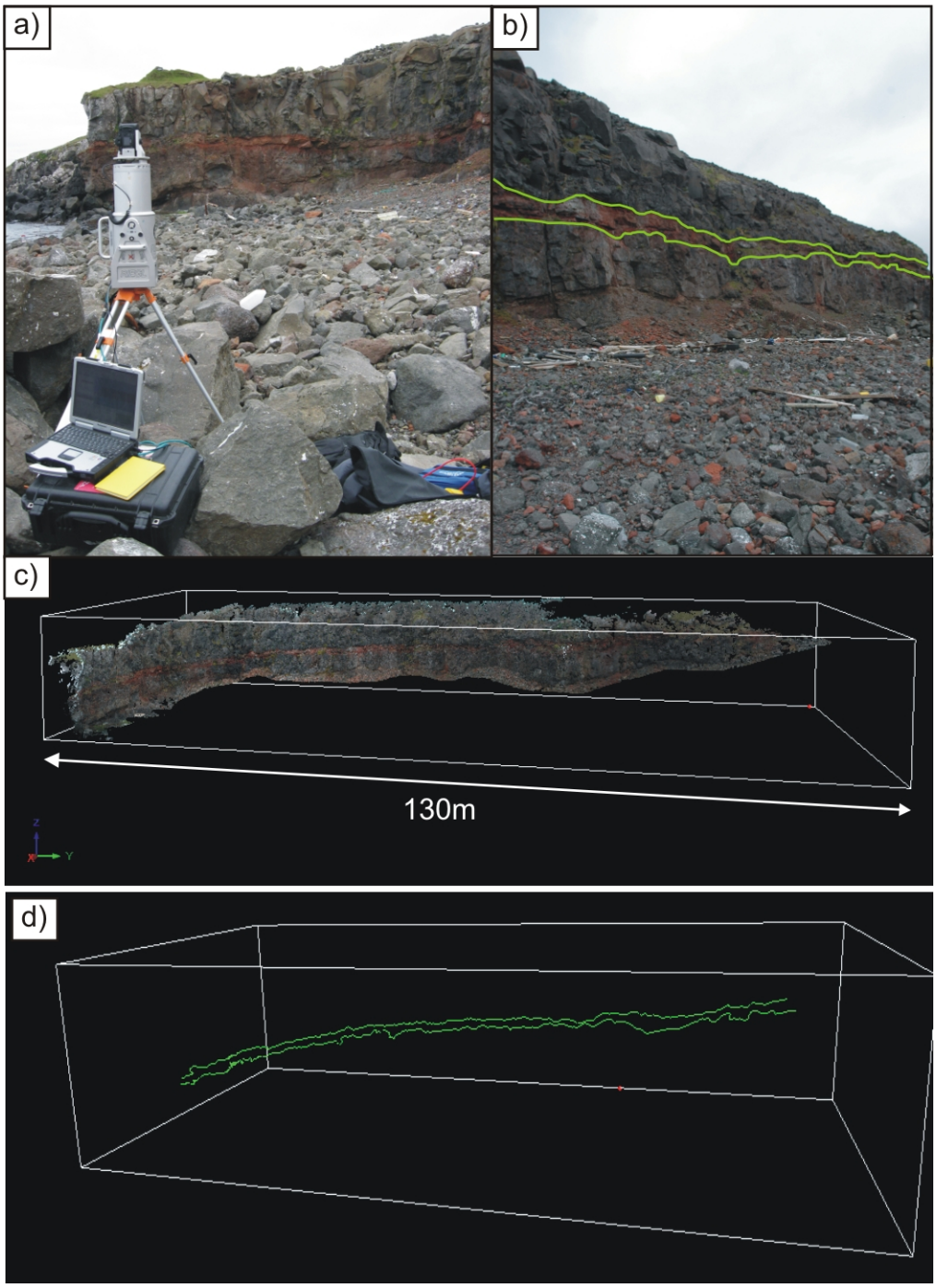

Figure 6.5 Laser scan data from coastal quarry at Glyvursnes. Outcrop height is approximately 10m. a) Acquiring the laser scan data. b) The quarry wall with photo-interpretation of the lava flow top and base. c) The completed scan data. d) Lines interpreted from the scan data.

6.2.3 Laser scan data from Ethiopia

An additional dataset was available for this work: laser scanning data from Erte Ale volcano, Ethiopia. This is a remote and rarely visited active basaltic volcano, with a lava lake and surrounding crater. The lava lake is one of the oldest known, having persisted for over 90 years (Oppenheimer and Francis, 1998). Data used here are taken from the crater floor surrounding the lava lake. The crater floor is covered by pahoehoe lava flows formed when the lava lake overflows. This provides a large fresh surface with the opportunity of taking many profiles in any direction. The area of interest is approximately 80 by 125m.

Data were collected by Dougal Jerram and Steve Smith as part of filming for the BBC1 television series "The Hottest Place on Earth" (Jerram and Smith, 2010). A total of 6 scans were required to completely capture the crater, and approximately 24,000,000 points and 42 digital photographs were collected. Data were processed following the methods described in Chapter 3, and the coloured 3D point cloud is shown in Figure 6.6.

X-z profiles were captured directly from the scan data, using the "Sections" tool in Riscan Pro. The resulting two-column files have a length of 70-125m and a point spacing of approximately 10cm. Two sections were chosen for further analysis: the longest possible sections in orthogonal directions, along and across the crater floor. Their analysis is discussed in Section 6.3.

6.2.4 Data preparation

All data were prepared in the following way:

- Cross-sections were chosen to have the longest length available from the data.
- Cross-sections were converted to x-z profiles by converting x-y coordinates to a distance in x.
- X values were altered to start at 0.
- Any linear structural trend (e.g. dip) was removed to prevent long wavelength spikes in the data.

1D profiles were used to allow comparison between the datasets as 2D surfaces were not available for Glyvursnes.

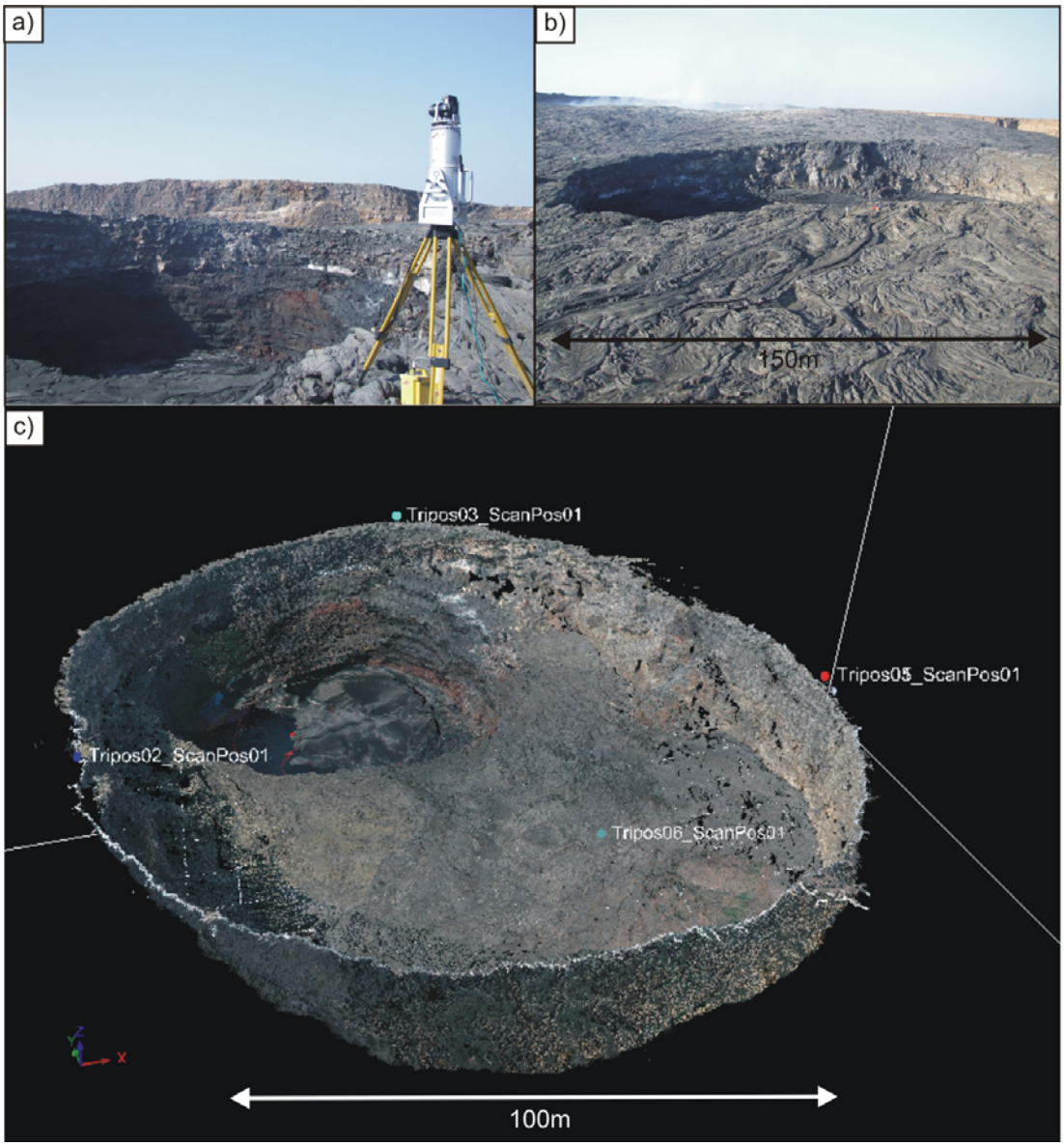

Figure 6.6 Laser scan data from Erte Ale, Ethiopia. Photos courtesy of Dougal Jerram. a) Collecting the scan data. b) Overview of the crater and surroundings. c) Complete scan data and scan positions.

6.3 Data analysis

The Generic Mapping Tools (GMT) software was used to analyse the data described in Section 6.2, (Wessel and Smith, 2009). This is an open source set of tools for manipulating x,y and x,y,z data, available to download from http://gmt.soest.hawaii.edu/ . The power spectra were generated using the `spectrum1d` command. This reads in a two column ASCII file containing x and z values, and outputs a three column file containing the frequency, power spectral density estimate and one standard deviation error bar size. Spectral density estimates follow the method of Welch (1967) and error bars are produced following the method of Bendat and Piersol (1986).

The resulting files were plotted using the `psxy` command in GMT and the power spectra are shown in Figure 6.7 below. There is a good agreement between datasets at each location. The Laki power spectra (Figure 6.7a) show a very close agreement between the section along and across the flow, suggesting that the roughness is approximately isotropic and the same fractal properties can be used in both directions. This spectrum also displays a clear roll-over point, indicating that the surface can be treated as fractal up to around 2000m (the correlation length).

The data from Glyvursnes indicate that there is no significant difference between the roughness of a flow top and flow base. For values below approximately 20cm (2 on the x axis) the wavelength is equal to the spacing of the data points, so the results are not useful. The same applies to the results from Erta Ale. Again, there is no significant anisotropy apparent in the surface roughness.

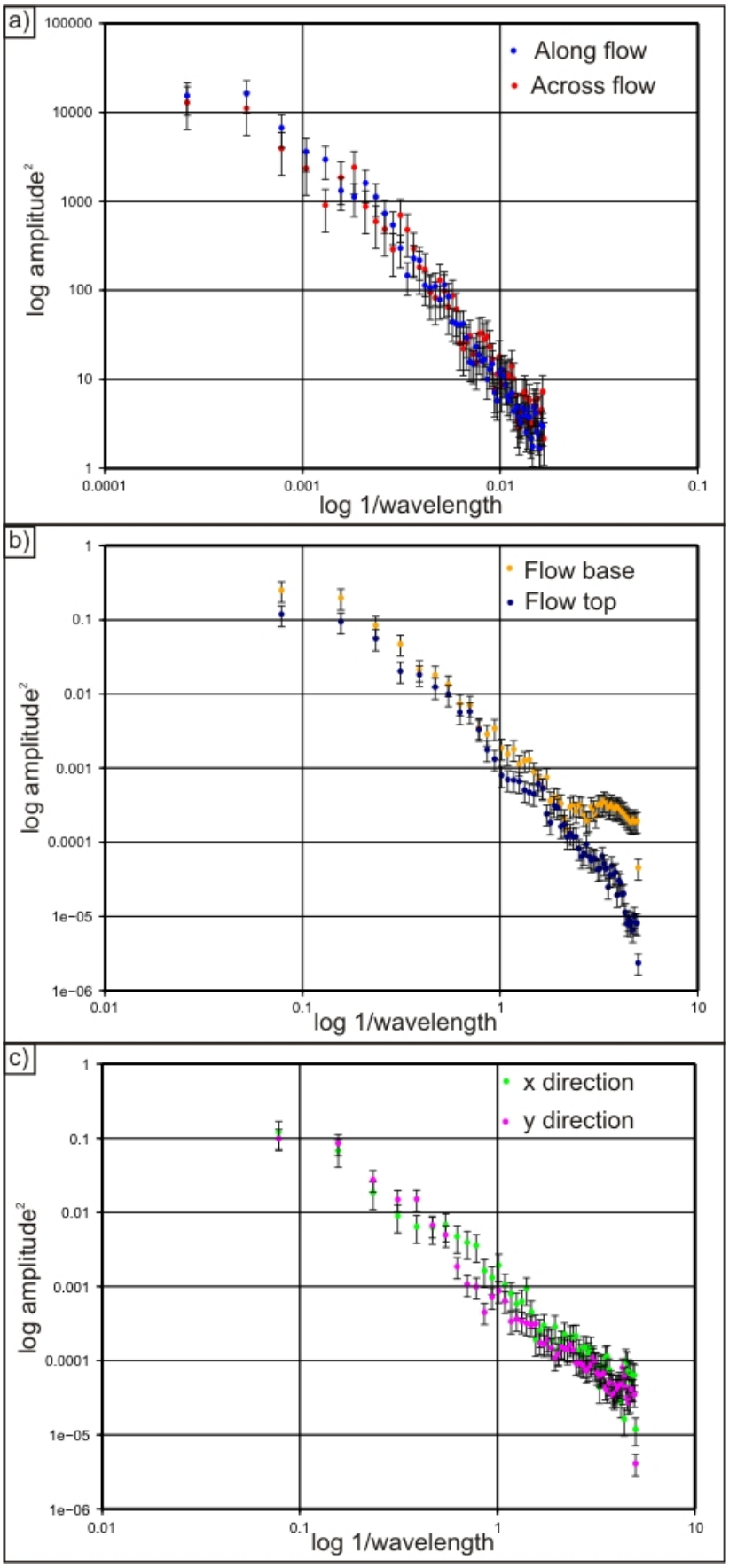

Figure 6.7 Power spectra of data from a) Laki, b) Glyvursnes and c) Erte Ale.

In Figure 6.8 below, the data from Laki, Glyvursnes and Erta Ale are plotted together. A best fit line can be drawn within the uncertainties of the data. From this, a β value (slope) of 2.1 is measured. Using the equations in Section 6.1, a Hurst number of 0.55 is obtained. As discussed above, the correlation length is approximately 2000m.

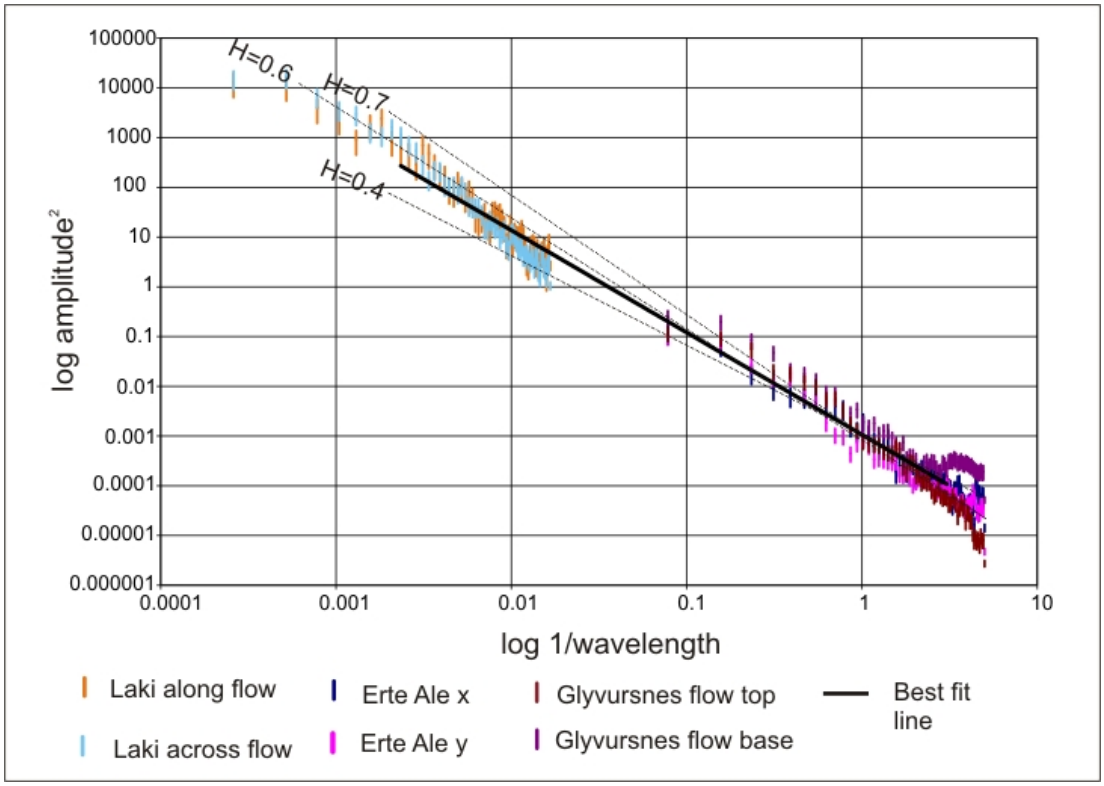

Figure 6.8 All power spectra plotted together, only 1s.d. error bars shown. Dashed lines show other Hurst numbers for comparison.

The dashed lines in Figure 6.8 give an estimate of the error on the Hurst number: the likely range is around 0.5-0.65. It can be seen that there is a slight step between the data from Laki and the laser scan data, and this is likely to be due to the change in instrumentation. However, this is within the errors of the data, so a simple single slope was chosen to describe the surface, consistent with the individual slopes from each dataset and previous work. Data at scales in between the satellite data and the laser scan data would help to verify this.

6.4 Building random surfaces

Thus far, I have analysed data from a variety of sources to obtain the Hurst number and correlation length for the top surface of a flood basalt lava flow. Armed with these, the next step was to generate synthetic surfaces with the same statistical properties as the real surfaces. These were used to add random noise to the models constructed in Chapter 5, and develop further models as described in Chapter 7.

White (2009) provides a random volume building code suitable for producing a random surface with the desired parameters. This code was originally developed for producing velocity models of basalt sequences, but works equally well for producing surface topography. Input parameters are given in Table 6.1 below.

The grid spacing is altered to produce one model comparable to the Laki remote sensing data and one comparable to the laser scan data. In the satellite scale model, the grid spacing is 20m giving an overall size of 10.22km x 10.22km. In the laser scan scale model, the grid spacing is 20cm giving an overall size of 102.2m x 102.2m. In all cases, the mean of all z values is zero.

Input parameter	Value used	Description
x nodes	512	Number of nodes in x direction
y nodes	512	Powers of 2 make the code run much faster.
z nodes	1	Creates single surface rather than random volume.
grid spacing	20 for satellite scale, 0.2 for scan scale	In metres.
correlation length in x	2000	From Section 6.3.
correlation length in y	2000	From Section 6.3.
correlation length in z	1	Nominal value.
standard deviation	1	Nominal value as scaling correction applied to the model.
Hurst number	0.55	From Section 6.3.

Table 6.1 Input parameters for the random volume building code from White (2009).

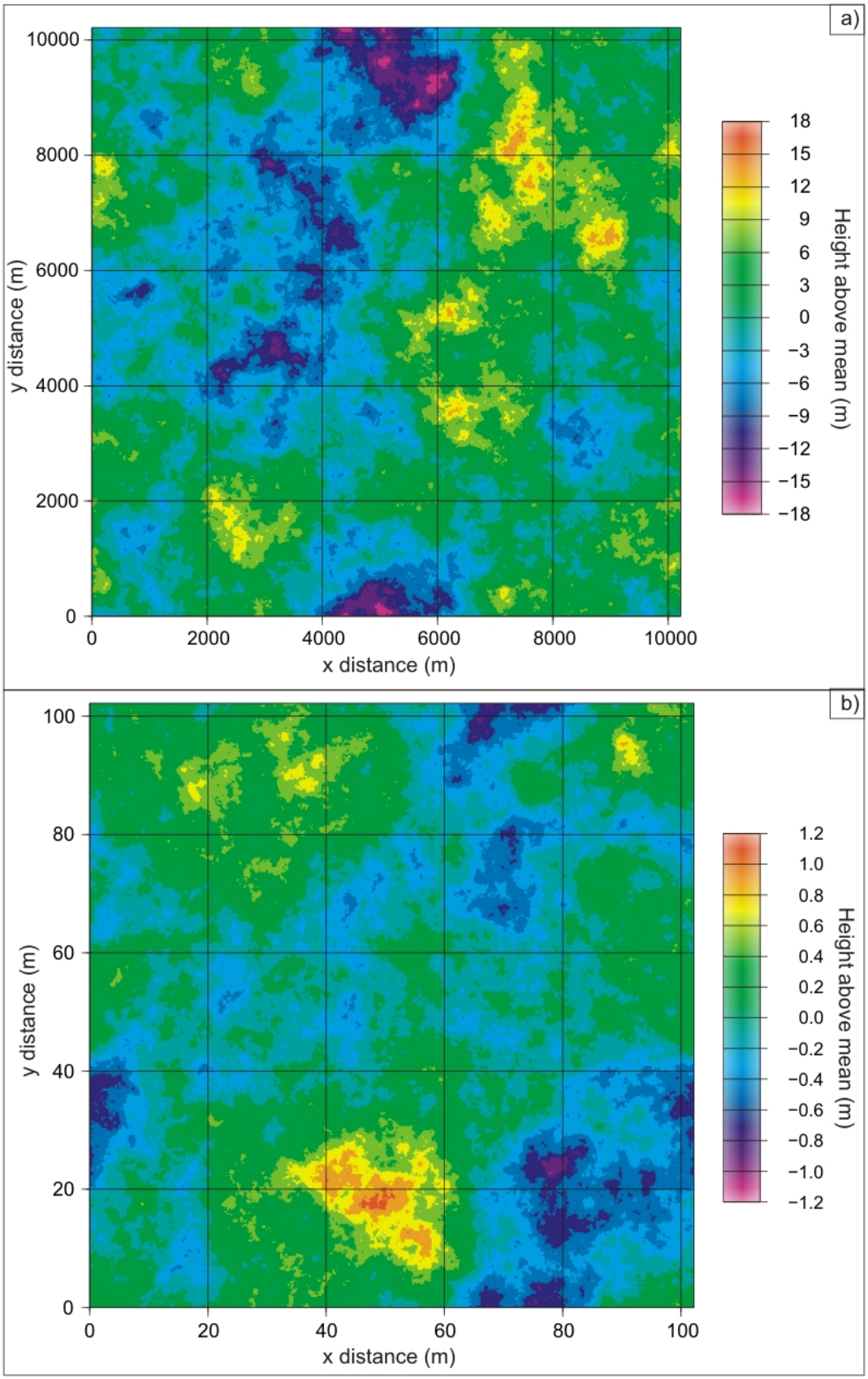

Figure 6.9 Fractal models produced with the random volume building code of White (2009). a) Satellite scale. b) Laser scan scale.

The output file is a random model with a zero mean which can then be scaled to match the observed surfaces. Standard deviations of the z values were compared to obtain a scaling parameter. The resulting models at two scales are shown in Figure 6.9 below, and a perspective view of the scan scale model is shown in Figure 6.10.

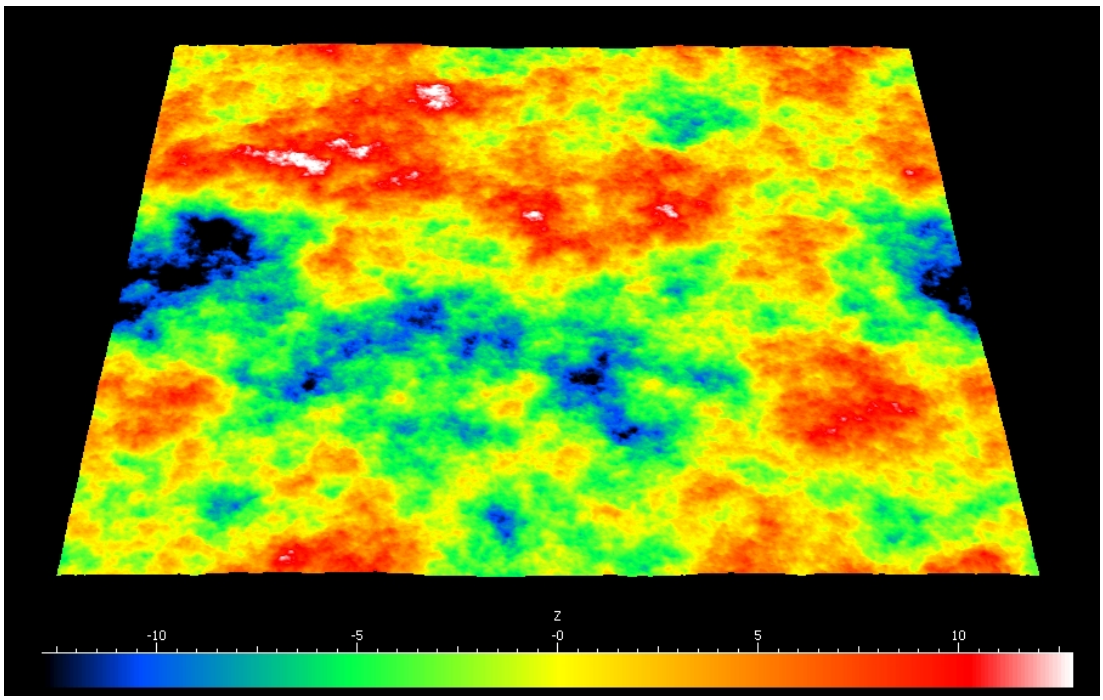

Figure 6.10 Perspective view of satellite scale random model. Area is 10kmx10km.

In order to check that the model building code is producing sensible results, power spectra were produced for each of the models in Figure 6.9, and the results are shown in Figure 6.11. There is a good agreement between the random models and the real data, indicating that the model is a good representation of the real surface. The random surfaces will be used extensively in Chapter 7.

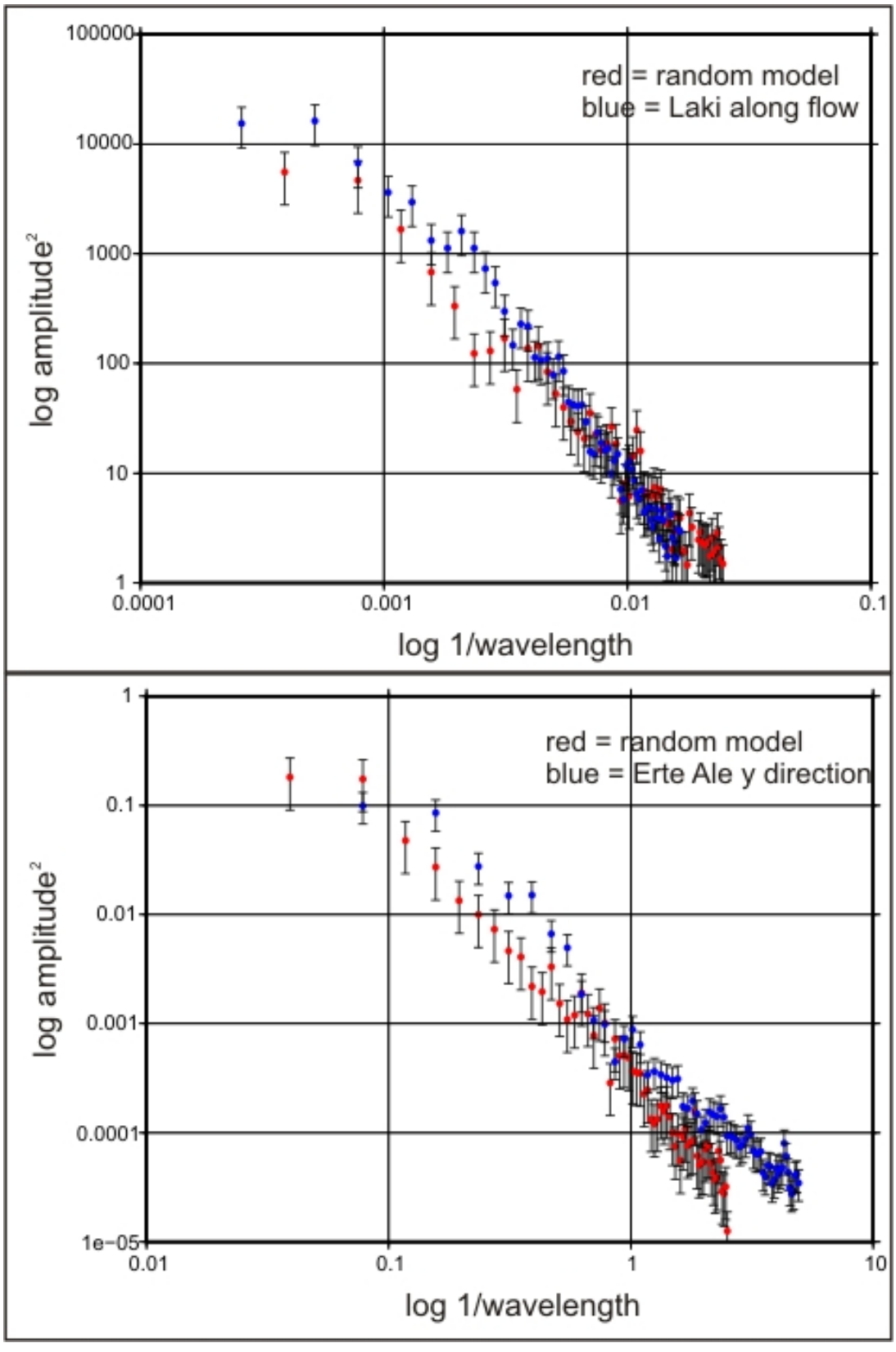

Figure 6.11 Random models plotted against real data.

6.5 Discussion

This chapter has shown that spectral analysis is a valid method for understanding the properties of a basalt lava flow surface, and that the surface can be considered as fractal up to the correlation length of 2000m. Having obtained the correlation length and Hurst number (0.55) it is possible to construct random surfaces with the same statistical properties as the real surfaces. These will be used extensively in the next chapter.

Other authors have applied similar methods to the characterisation of basalt lava flows. My result of 0.55 for the Hurst number is similar to that of Walia and Bull (1997) who obtained a value of 0.6 (D = 1.4) for the base basalt and 0.7 (D=1.3) for their top basalt surface. My result is also in good agreement with Maresh (2004) who obtained a Hurst number of 0.51 (2-dimensional D = 2.49). Bean and Martini (2010) obtain a β of 1.3-1.4, giving a Hurst number of 0.2. I suggest that the difference is due to the character of the basalt surface used by Bean and Martini: it is the interface between limestone and the base of a basalt horizon. This is likely to be controlled by the pre-existing erosional roughness on the top of the limestone. The datasets presented here are known to be from fresh, unaltered top surfaces of lava flows. The result of Bean and Martini would be of use in modelling the basal surface of a flood basalt province; however the data presented here are useful for modelling internal reflectors and the top surface.

Another issue for discussion is the correlation length. Here, I use the same value of 2000m for both along flow and across flow directions. White (2009) used a correlation length 10x larger in one direction than the other, citing Thomson (2005). Martini et al. (2005), working along similar lines, used a correlation length 5x greater in one horizontal direction than the other. This is appropriate for lava flows emplaced onto dipping surfaces, however Thomson (2005) also described flat-lying flows of roughly equant x-y dimensions, similar to our results from Laki. The dip of the required flows should be taken into account when developing a model of a flood basalt province, as lava flows emplaced onto a dipping surface will display longer correlation lengths in the down-dip direction. The correlation length can easily be altered in the random volume code of White (2009) to reflect the desired geometry.

The methods presented here for constructing random surfaces are useful in situations where the entire scale length of a feature cannot easily be captured. It is relatively easy to characterize the surface of a lava flow at the outcrop scale (10s of metres) and satellite data allows features to be measured at 100s of metres to kilometre scales; however in between this it becomes more difficult. Satellite data is not easily obtained at a resolution of below 30-50m, and outcrops larger than 100-200m are rare and difficult to measure. The use of fractal modelling covers this scale gap.

One problem with studying flood basalt provinces is that exposure is often incomplete, and it is impossible to tell the extent of a single lava flow as the edges are not preserved or are difficult to correlate. By bringing together these diverse datasets it is possible to build realistic models of lava flow surfaces without the need for correlation between outcrops or time-consuming mapping.

7

7. INTEGRATED GEOLOGICAL AND GEOPHYSICAL MODELS 122

7.1 CHAPTER SUMMARY 122

7.2 3D GEOLOGICAL AND GEOPHYSICAL MODELLING 122

7.3 TABULAR-CLASSIC FLOW MODEL 122

7.3.1 Approach and source data 122

7.3.2 Methods 127

7.3.3 Analysis 131

7.4 COMPOUND-BRAIDED FLOW MODELS: COMBINED DETERMINISTIC AND RANDOM MODELS 134

7.4.1 Approach 134

7.4.2 Methods 137

7.4.3 Analysis 142

7.5 COMPOUND-BRAIDED FLOW MODELS: FULLY RANDOM MODELS 143

7.5.1 Approach, source data and methods 143

7.5.2 Analysis 145

7.6 DENSITY 146

7.7 DISCUSSION AND CONCLUSIONS 148

7.7.1 Tabular-classic flow model 148

7.7.2 Compound-braided flow models 148

7.7.3 Conclusions 149

7. Integrated geological and geophysical models

7.1 Chapter summary

The work presented in this chapter brings together component parts from the previous three chapters. 3D geological and geophysical models are constructed for tabular-classic and compound-braided lava flows, and these are used to generate synthetic seismic data. The approaches behind these models are discussed along with the methods used for their construction. For compound-braided lava flows, models based on outcrop data are compared with entirely random models to determine which technique is most suitable.

7.2 3D geological and geophysical modelling

In Chapters 1 and 2, I discussed the need for 3D models of flood basalt provinces which combine geological and geophysical data. Chapters 4, 5 and 6 provide the component parts for these models (surfaces and velocity data), and in this chapter I bring together these data into true 3D models which contain velocity data.

I concentrate in this chapter on the two facies for which substantial outcrop observations are available: tabular-classic and compound-braided lava flows. The tabular-classic model is based on the rough surfaces generated in Chapter 6, with velocity information from the wells used in Chapter 4. For the compound-braided facies, two approaches are taken: firstly, the models from Chapter 5 are given rough surfaces and velocity data; secondly, a fully random model is generated. These two approaches are compared to test which offers the best combination of realism and ease of production.

7.3 Tabular-classic flow model

7.3.1 Approach and source data

As discussed in previous chapters, tabular-classic lava flows are thick, laterally continuous flows probably representing a high volume flux of lava. These form successive sheets of lava with thick core horizons, interspersed with variable thickness crusts, providing a media which is asymmetrically heterogeneous. Outcrop exposures rarely preserve flow terminations (e.g. Jerram and Widdowson 2005),

making it extremely difficult to determine the extents of individual flows. This does, however, mean that flow terminations make up very little of the complete volume of a stack of tabular flows, and they can be approximated for modelling purposes by a simple series of flow top surfaces. Top surfaces are generated by running the random volume building code of White (2009) as discussed in Chapter 6, and a different surface is used for each flow.

In this model, I have chosen to keep the flows horizontal. This is a good approximation for a large part of a flood basalt province, after early flows have filled in any pre-existing topography. It could easily be adapted to include dipping flows, though the correlation lengths of the rough surface would need to be changed to reflect this.

Flow thicknesses were chosen at random from the flow thicknesses in the Beinisvorð Formation in the Lopra 1/1A well. A histogram of these flow thicknesses is given in Figure 7.1. It was assumed that the flow thicknesses show no trend; a larger sample would be required to test whether this is in fact the case. Flow crust to core ratios were chosen from Figure 4.6 (plot of flow thickness against proportion of flow core). It was also assumed that the topography of the core-crust boundary would be the same as that of the flow top surface. This is a reasonable assumption as the topography of both the top surface and the core-crust boundary are the result of cooling processes from the top surface down. It is difficult to test this as few outcrops display clear core-crust boundaries at an adequate scale in 3D - certainly there is nothing like the exposure of the top surface of the Laki lava flow in ancient flood basalt examples. However, it can be seen from ancient outcrops that vesicle patterns, which are trapped by the cooling fronts, closely match the surface topography (as seen in Talisker Bay, for example).

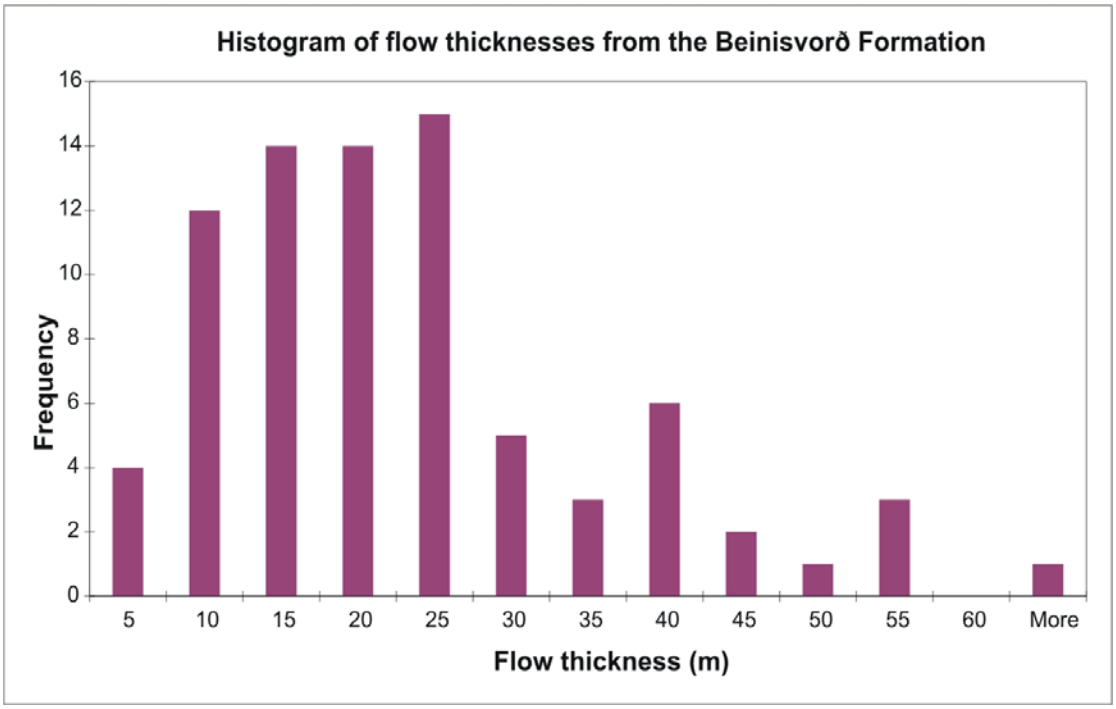

Figure 7.1 Histogram of flow thicknesses from the Beinisvorð Formation in the Lopra 1/1A borehole.

Velocity data within each flow was based on the work of Planke (1994) as discussed in Chapter 4. Flood basalt lava flows display a characteristic velocity profile with a high, relatively constant velocity within the flow core, and a decreasing velocity through the flow crust. Detailed interpretation of the Lopra 1/1A borehole, as discussed in Chapter 4 and included in Appendix 2, allows the velocity data to be divided into flow core and flow crust. Histograms for the flow core and crust are given in Figure 7.2.

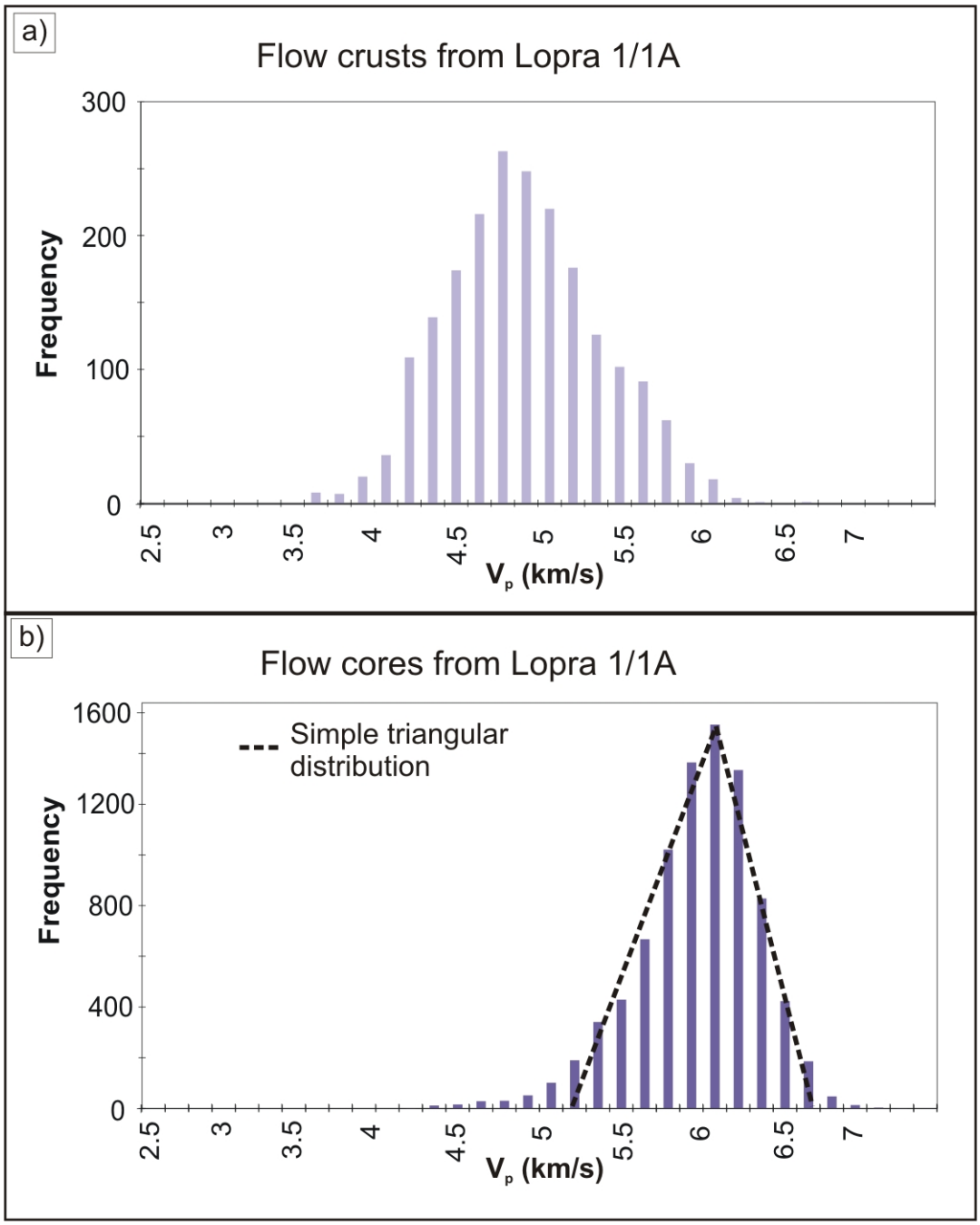

Figure 7.2 Histograms of a) crust and b) core velocities from the Beinisvorð Formation in the Lopra 1/1A borehole.

It was decided to take random values for P-wave velocity from the core distribution for the flow core, as this would reflect the observed data with a reasonable degree of accuracy. A limitation of the GOCAD® software meant the histogram was approximated by a triangular distribution, as shown in Figure 7.2b. Other distributions available in the software are a normal distribution and a uniform

distribution; however the triangular distribution captures the skewness in the data where a normal distribution would not.

Picking velocity values at random would not accurately reflect the trend within a flow crust, so a more sophisticated method was required. This is because flow crusts show a trend from higher velocity near the core to lower velocity at the flow top. Accordingly, profiles through 20 tabular flows were selected and a trendline fitted, as shown in Figure 7.3. The trendline is described by the following equation:

$$y=-4.123x^3 + 7.516x^2 - 4.616x +5.412 \quad \text{(Equation 7.1)}$$

where y is the velocity, and x is the normalised distance from the crust-core boundary. x can be calculated in the GOCAD® software using an in-built function: `Compute distance from surfaces`. Full details of the workflow are given in Appendix 3.

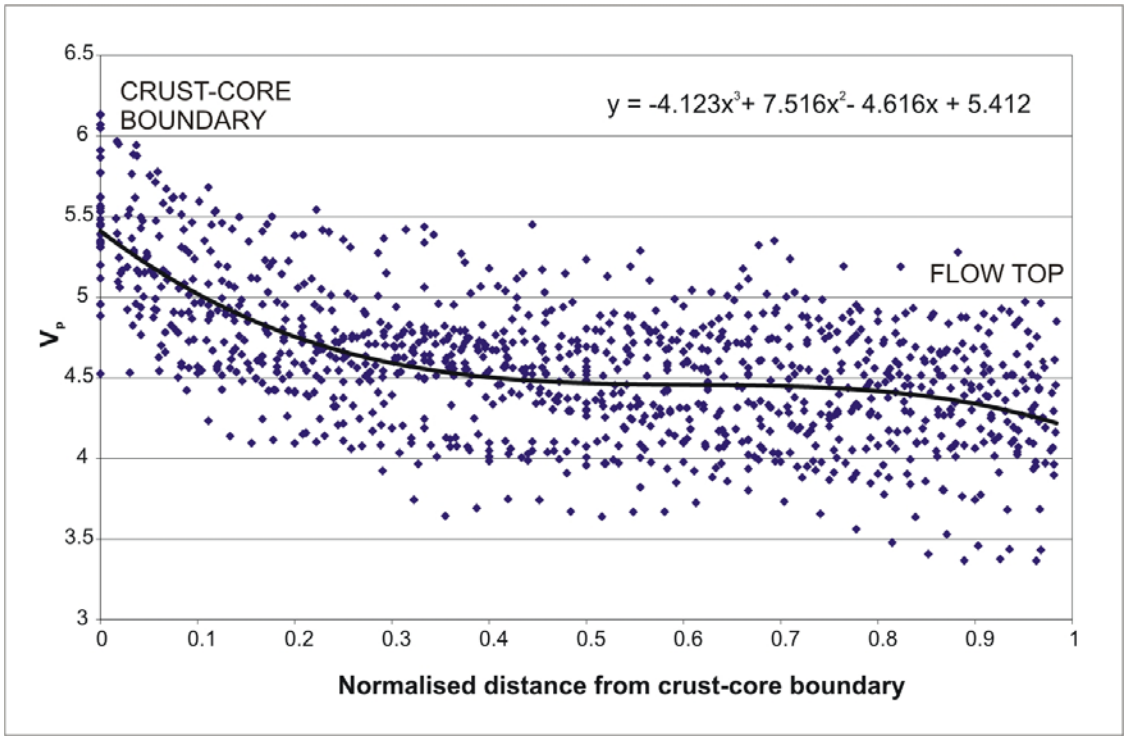

Figure 7.3 Profiles through 20 flow crusts from the the Beinisvorð Formation in the Lopra 1/1A borehole, and trendline with equation. Distances through the flow crust have been normalised for comparison.

To recap, the following assumptions were used to generate the tabular-classic model:

- The Beinisvorð Formation is representative of tabular-classic flows in the NAIP.
- Flows are flat-lying.
- Flow thicknesses do not follow any trend, and can be drawn at random from flow thicknesses of the Beinisvorð Formation.
- The flow top surface can be approximated by a random surface.
- The crust-core boundary has the same surface topography as the flow top.
- The flow core shows no trend in velocity and velocity values can be drawn at random from the appropriate distribution.
- The flow crust displays a distinct trend which can be approximated by Equation 7.1.

7.3.2 Methods

The method used to generate the tabular flow model is outlined below. Details of the GOCAD® commands are available in Appendix 3.

1. 20 random surfaces were generated using the random volume building code of White (2009) following the methods outlined in Chapter 6. The random parameters used are given in the table below. The surfaces were scaled to have the same standard deviation of their heights as the Laki lava flow.
2. The 20 surfaces were imported into GOCAD® and Z values altered to give a spacing based on the Lopra data, as described above. For each flow, the top surface was copied to produce the crust-core boundary, and moved to the correct position. The 20 flows are shown in Figure 7.4 below:

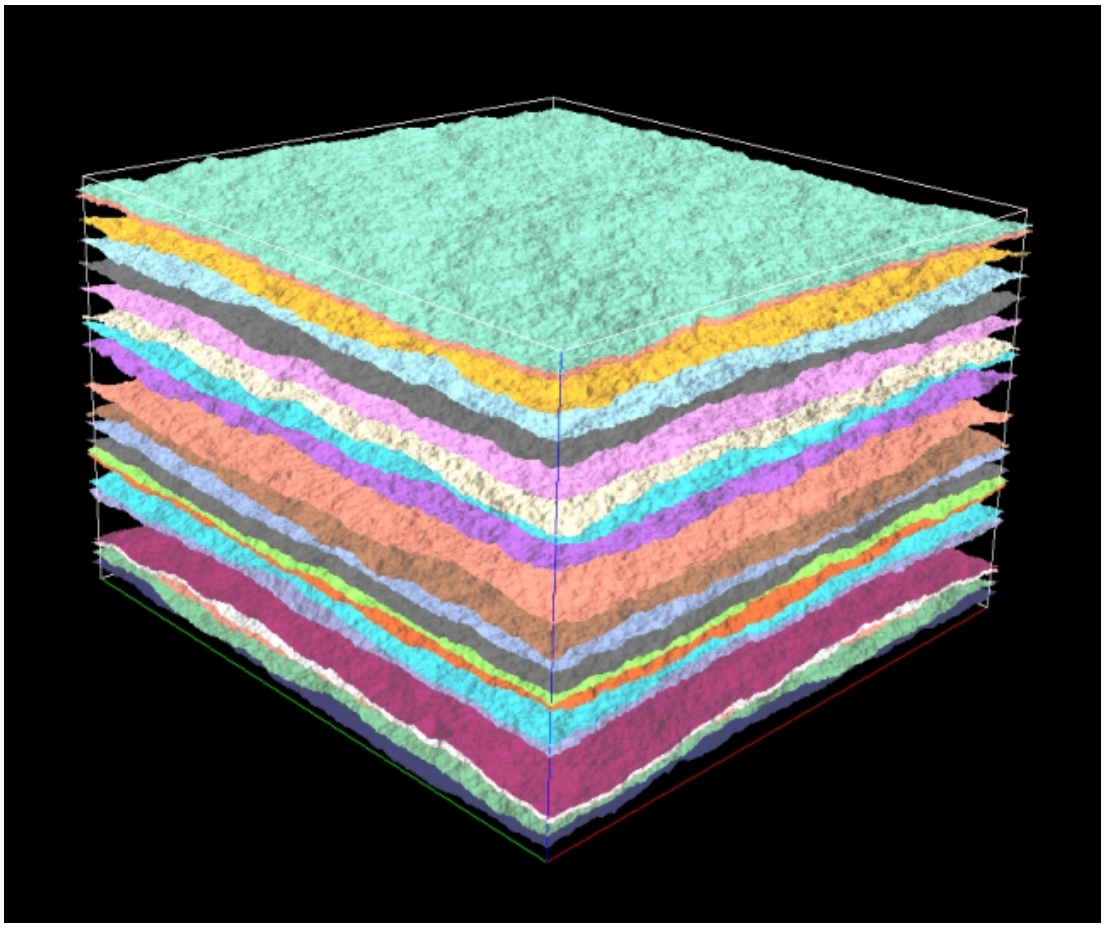

Figure 7.4 Stacked random surfaces forming the framework for the model. Model is 10km x 10km x 500m, view shows 10x vertical exaggeration.

3. A Voxet space of 10km by 10km by 500m was defined around the surfaces, divided into cells of 30m x 30m x 1m, or approximately 55 million cells. See Chapter 3 for details of Voxets. This size is designed to take in as much complexity as possible while remaining within the computing capacity available. It is also of the required size to be able to generate synthetic seismic data following the methods described in Chapter 8, and gives the vertical resolution of 1m required by Maresh (2006).
4. The Voxet space was divided into regions based on the surfaces. This step used an extremely large amount of memory and computer processing power, making it necessary to divide the 20 surface model into three smaller models. The regions are shown in Figure 7.5

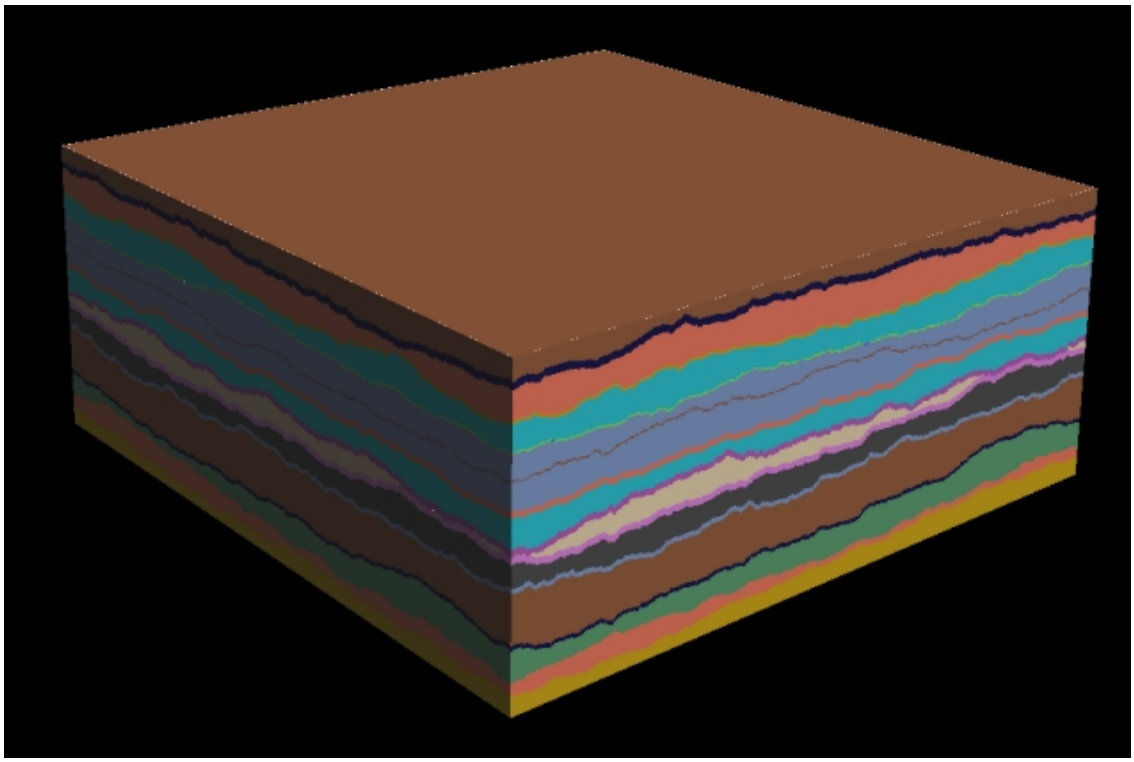

Figure 7.5 Model space divided into regions. Model is 10km x 10km x 300m, view shows 10x vertical exaggeration.

5. The next step was to give each cell a velocity value, and this process is outlined in Figure 7.6. Figure 7.6a shows a single flow in which the crust and core have been given constant velocity values. This does not accurately reflect the velocity structure within a flow, so a more complex approach was devised as discussed in Section 7.3.1. Firstly, the distance from the core-crust boundary was calculated for each crust region, then Equation 7.1 was applied to generate the crust velocity. These steps were also very expensive in both computer processing speed and memory usage. An example crust is shown in Figure 7.6b. Secondly, a random value was selected from the distribution in Figure 7.2b for each cell in each core region.
6. The finished model is shown in Figure 7.7. A “virtual borehole” can then be created at any position.

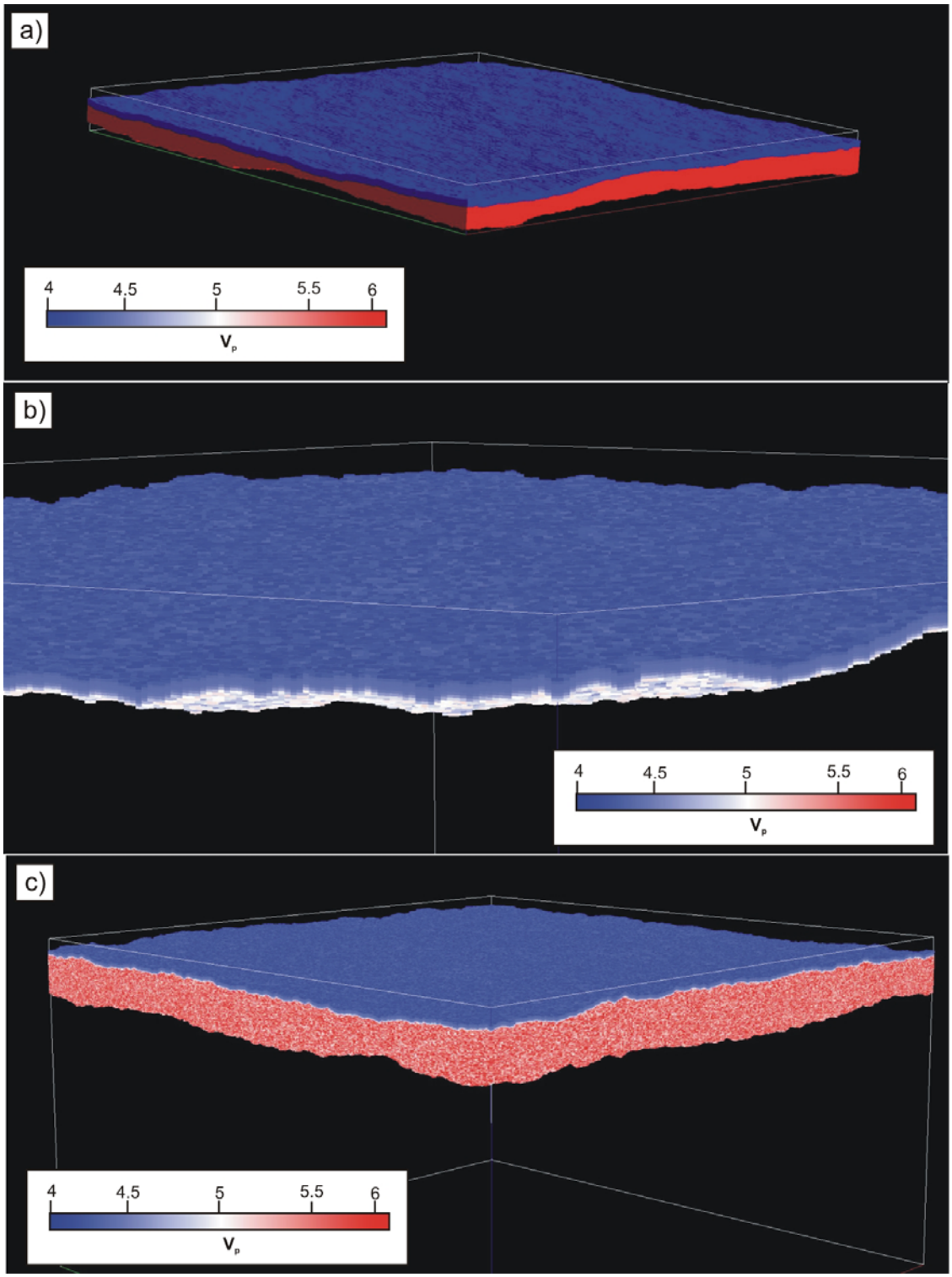

Figure 7.6 3D model of a single flow. a) Constant velocity in flow crust and core. b) Flow crust velocity generated using Equation 7.1. c) Flow crust velocity generated using Equation 7.1, and core velocities drawn from distribution in Figure 7.2b.

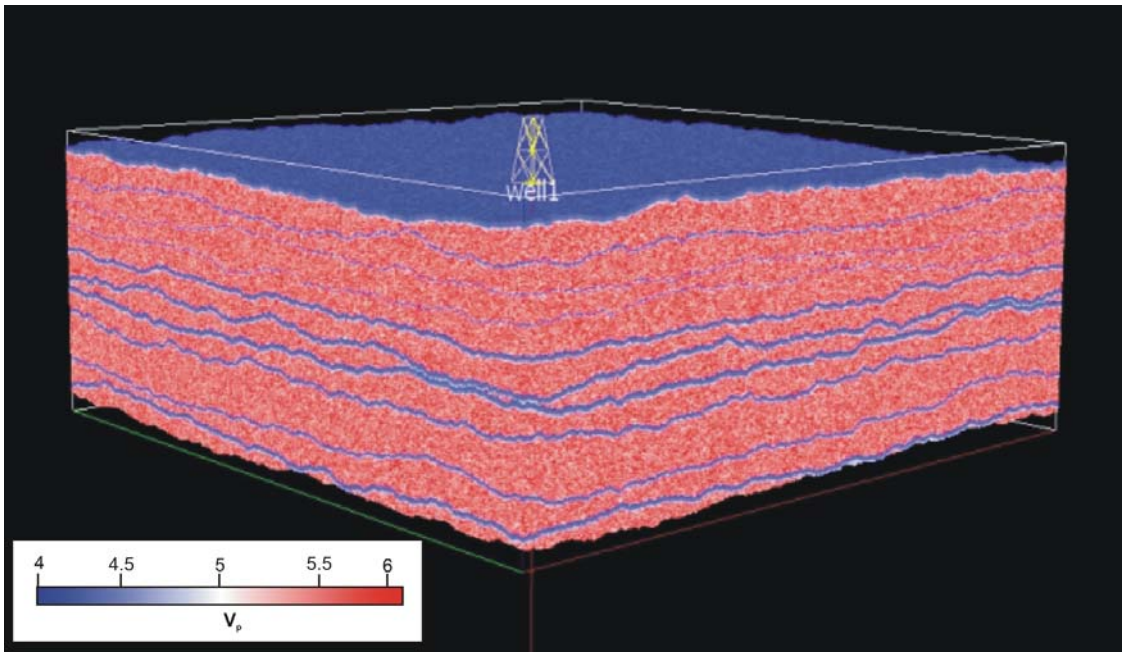

Figure 7.7 10km x 10km x 300m model of tabular flows, with location of virtual borehole used for analysis. The complete model contains 20 flows and is 500m thick.

7.3.3 Analysis

Histograms of both the completed tabular model and tabular-classic flows from the Lopra 1/1A borehole (from Chapter 4) are shown in Figure 7.8. The data from the tabular model are 500m at a spacing of 1m; whereas the Lopra data comprise 1800m at a spacing of 0.15m. The shapes of the histograms are somewhat different, as the crust equation does not give the random variation found in the real data. This may lead to a slightly higher velocity contrast between the crust and core than that found in the real data. However, the mode, range and skewness are very similar. The values for the crust are concentrated into a narrower range than the real data, and do not include any sedimentary layers that may be responsible for the lowest velocities in Figure 7.8a. Figure 7.8b gives power spectra of a profile through the tabular model and data from the Lopra 1/1A borehole. It can be seen that there is a good agreement between the data at longer wavelengths; however the agreement becomes less good at wavelengths of a few metres or less. This suggests that more work is needed to capture the fine-scale variations within the lava flow core, rather than picking random values. The virtual borehole in Figure 7.8c shows a cyclic pattern similar to that of the real data in Chapter 4.

There is scope for much more sophisticated ways of generating the velocity trend within each lava flow. The addition of a random variation in the crust equation would move the model closer to the real data. The model represents a good first step and is suitable for generating synthetic seismic data. Further work could explore the effect

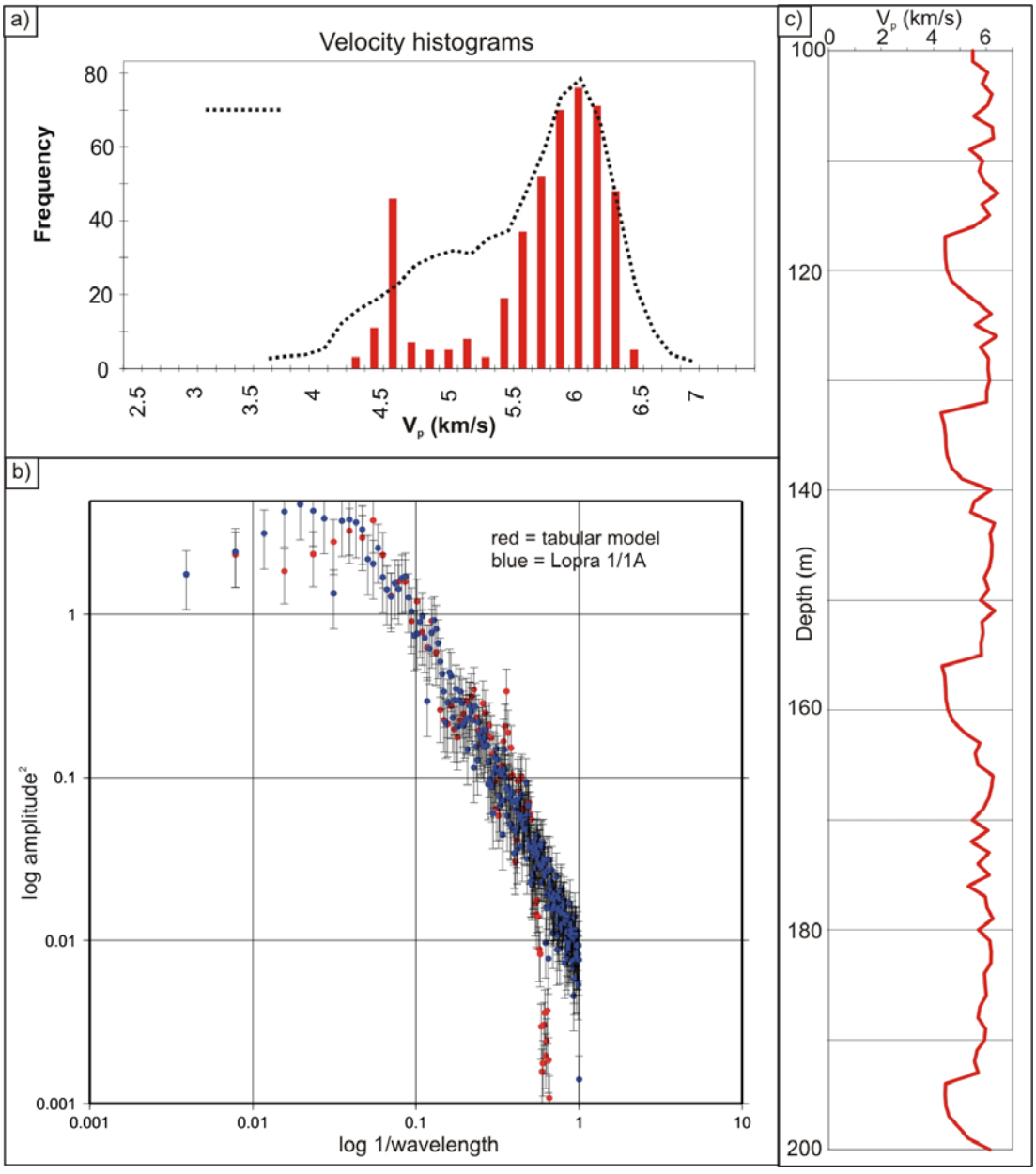

Figure 7.8 a) Comparison between histogram for tabular flow model and histogram for type section from Lopra 1/1A borehole. b) Power spectra of profile through tabular model and Lopra 1/1A data, produced in the same way as those in Chapter 6. c) Part of virtual borehole. This may be compared to Figure 4.4, where an example of real data from the Lopra-1/1A borehole is shown.

on synthetic seismic data when the method of attributing velocity data is changed, and add more realistic variation within the flow core.

One surprising outcome of the use of random surfaces is a very realistic pattern of flows pinching out, as shown in Figure 7.9. When surfaces crossed, it was decided to revise crust-core boundaries upwards to give a realistic model of flows filling in low points. This also meant that in some areas crusts are present without core, and this is realistic as very thin flows do not display a fully degassed core. The presence of isolated regions of core, as shown in Figure 7.9b, is probably reflected in real flows which pool in regions of lower topography. More field data would be useful to establish whether the number of flow terminations is realistic over this area; however such data is extremely difficult to obtain due to incomplete 3D outcrop exposure.

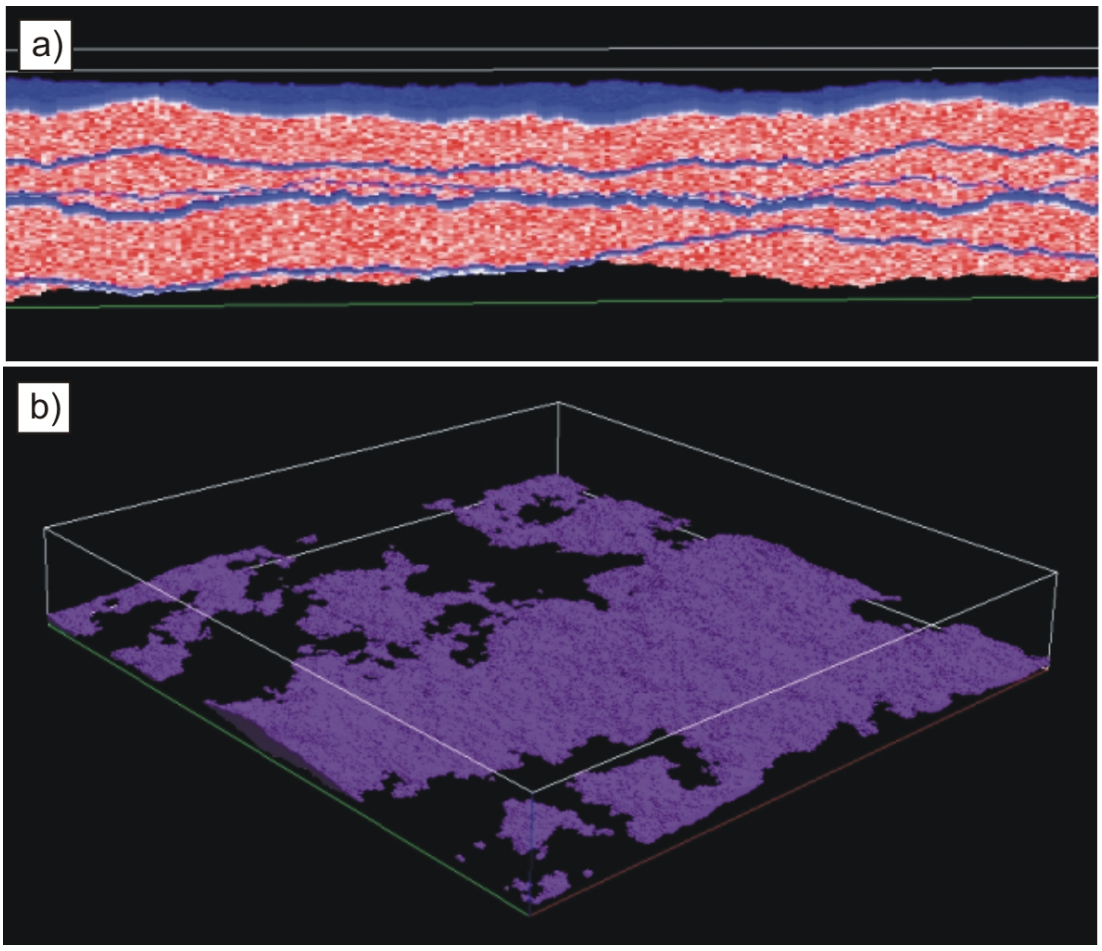

Figure 7.9 Interaction of random surfaces leads to flows "pinching out". a) Side view of stack of five flows. b) Plan view of one flow core.

7.4 Compound-braided flow models: combined deterministic and random models

7.4.1 Approach

These models are constructed by adding random topographic noise and velocity data to the models from Chapter 5 - Ljosa Quarry and Talisker Bay, shown in Figure 7.10. It is assumed that these are good examples of compound-braided flows, as they contain thin flows and many flow terminations, along with sedimentary horizons and intrusive features.

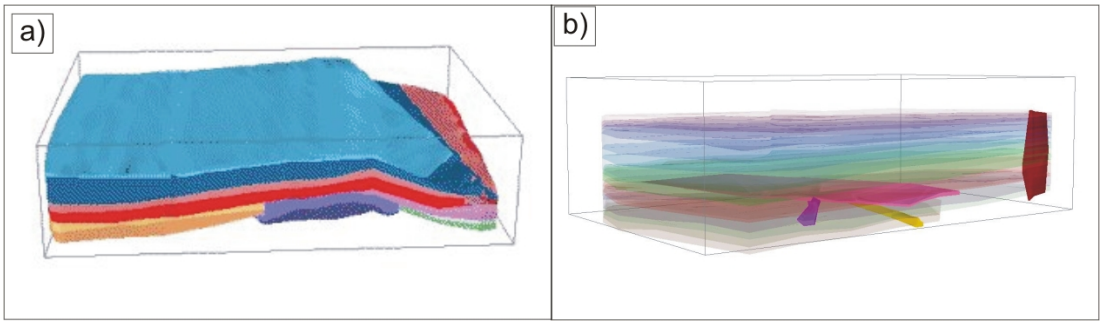

Figure 7.10 GSI3D models from Chapter 5. a) Ljosa Quarry. b) Talisker Bay.

The surfaces constructed in GSI3D honour the interpretations of the laser scans, but interpolation between the data points leads to large areas where the fine-scale roughness is smoothed out. This is a consequence of discrete smooth interpolation (DSI), as discussed in Chapter 3. To add this fine detail between the data points, the surfaces generated in Chapter 6 are used. 20 surfaces were generated using the random volume building code, as before, with a grid spacing of 20cm. As these surfaces have a mean of zero, the z values of the random surface can simply be added to those of the GSI3D surface to produce a realistic rough surface.

The next step, as with the tabular model, was to add velocity data. In the Ljosa Quarry model, crust and core were identified for each flow, and it was decided to take values at random for the crust and core for simplicity. The velocity histogram for compound flows from the Glyvursnes-1 well is shown in Figure 7.11. It is assumed that the higher mode corresponds to the flow core, and the lower to the flow

crust. Two triangular distributions were chosen to model the flow crust and core, as shown in Figure 7.11.

In the Talisker Bay model, few crusts and cores can be identified, so velocity values are obtained for each flow from a trendline. Profiles were taken through 20 flows from the Glyvursnes-1 well, and a trendline was fitted up to 70% of the distance through the flow, as shown in Figure 7.12. The equation for the trendline is given below:

$$y = 1.196x + 3.387 \qquad \text{(Equation 7.2)}$$

where y is the velocity, and x is the normalised distance from the crust-core boundary.

The method used for the tabular model was unsuitable for this model. As the top and bottom surfaces of each flow are different shapes, the distance between the surfaces varies within the flow. This meant that it was not possible to simply normalise the distance through the flow when the `Compute distance from surfaces` function was used in GOCAD®. The distance from the flow top was calculated for each cell, and divided by the average flow thickness (from Chapter 5). The trendline in Figure 7.12 was used to add a velocity value up to 80% of the average distance from the flow top, and below this a random value was taken from the "core" part of the distribution in Figure 7.11, as for the Ljosa Quarry model. A script was applied as follows:

```
if(x<=0.8){Vp=1.196*x+3.387;}else{Vp=trand(4.2,5.1,5.4;)
Formatted for GOCAD Script language
```

where Vp is the velocity, and x is the normalised distance from the crust-core boundary.

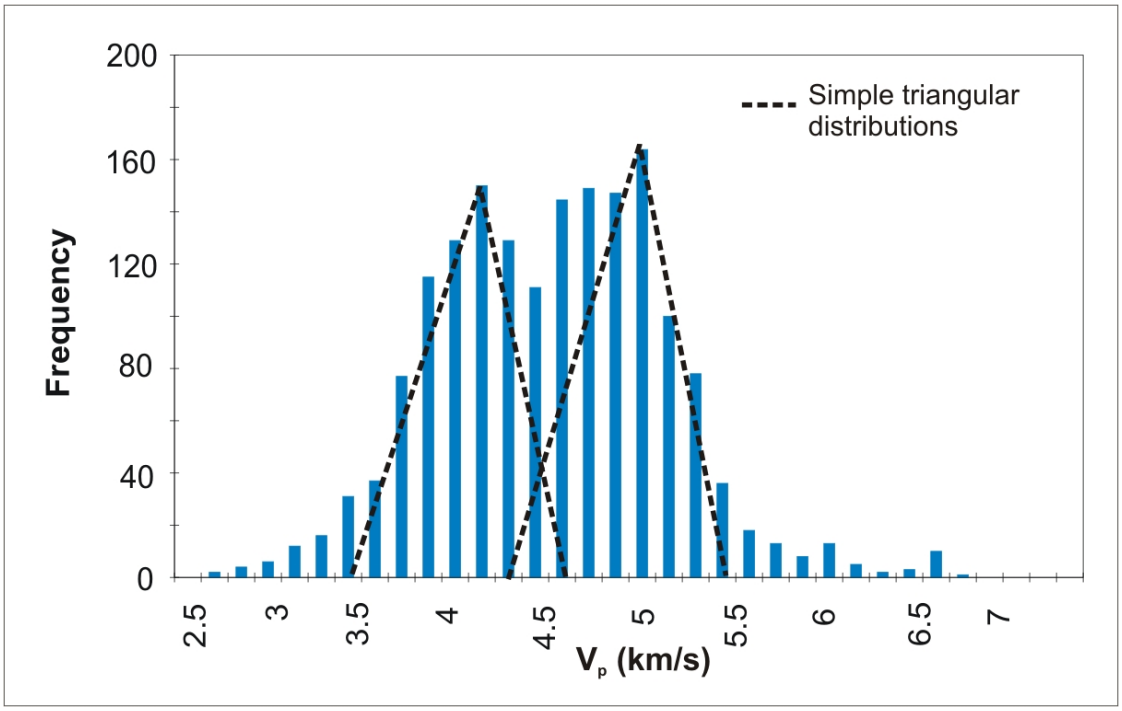

Figure 7.11 Histogram of velocity data from the Malinstindur Formation in the Glyvursnes-1 borehole, overlaid with simple distributions.

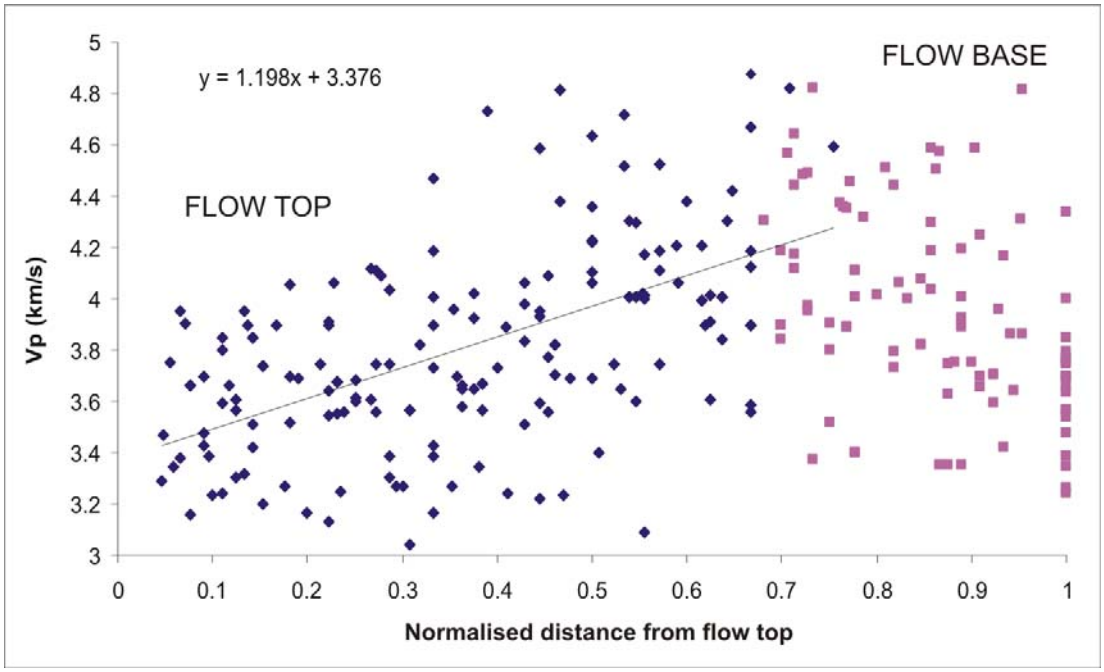

Figure 7.12 Profiles through 20 flows from the Malinstindur Formation in the Glyvursnes-1 borehole with trendline and equation. Data are normalised to allow comparison.

So to recap, the following assumptions are used to construct these compound-braided flow models:

- The selected locations are representative of compound-braided flows.

- Small-scale topography is not represented on the GSI3D surfaces and can be added from random surfaces.
- Where the core and crust can be identified, random velocity values provide a good approximation as the flows are very thin.
- Where the core and crust cannot be identified, the flow displays a distinct trend which can be approximated by Equation 7.2 and a random value.

7.4.2 Methods

1. Surfaces from the models generated in Chapter 5 were exported from GSI3D and imported into GOCAD®. In the case of smaller units which did not cover the entire extent of the model, it was necessary to export the entire "shell" of the unit. These had to be redrawn to become closed surfaces, following a workflow published by Paradigm® (the distributers of GOCAD®).

2. Random noise below the resolution of the laser scanners was added following the workflow described in Figure 7.13. The results are shown in Figure 7.14 (for the Ljosa Quarry model) and Figure 7.15 (for the Talisker Bay model).

3. Voxets were constructed around the rough surfaces, as shown for the Ljosa model in Figure 7.14b. Cell sizes for both models are 1m x 1m x 0.2m, to give a high enough resolution to accurately display velocity variations while remaining within the memory and processing capacity of the computer. The Talisker Bay voxet is 55m x 100m x 50m, giving a total of 1,375,000 cells.

4. In the same way as the tabular model, the voxets were divided into regions, as shown in Figure 7.14c and Figure 7.15b.

5. The next step, as with the tabular model, was to add velocity data to each cell. In the Ljosa model, the core and crust had been identified for each flow, so velocities were added at random based on the distributions described in Section 7.4.1. In the Talisker Bay model, some core-crust boundaries could not be identified in the field, so velocities were added using Equation 7.2.

6. The finished models are shown in Figure 7.16, and virtual boreholes can be created anywhere within the model.

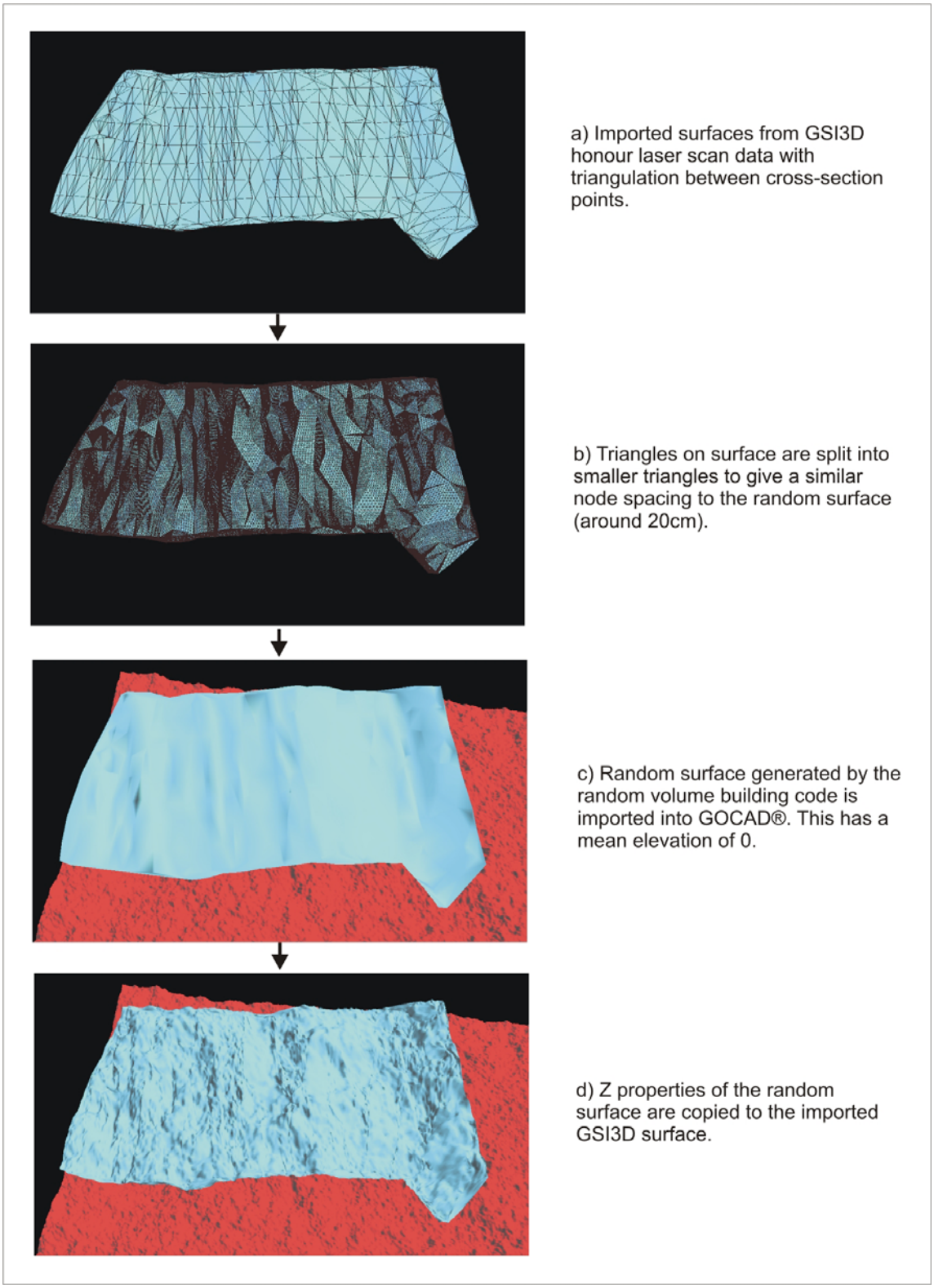

Figure 7.13 Method for adding random noise to GSI3D surfaces. Example is from the Ljosa Quarry model. Parameters for the random surface are the same as the laser scan scale surface in Chapter 6.

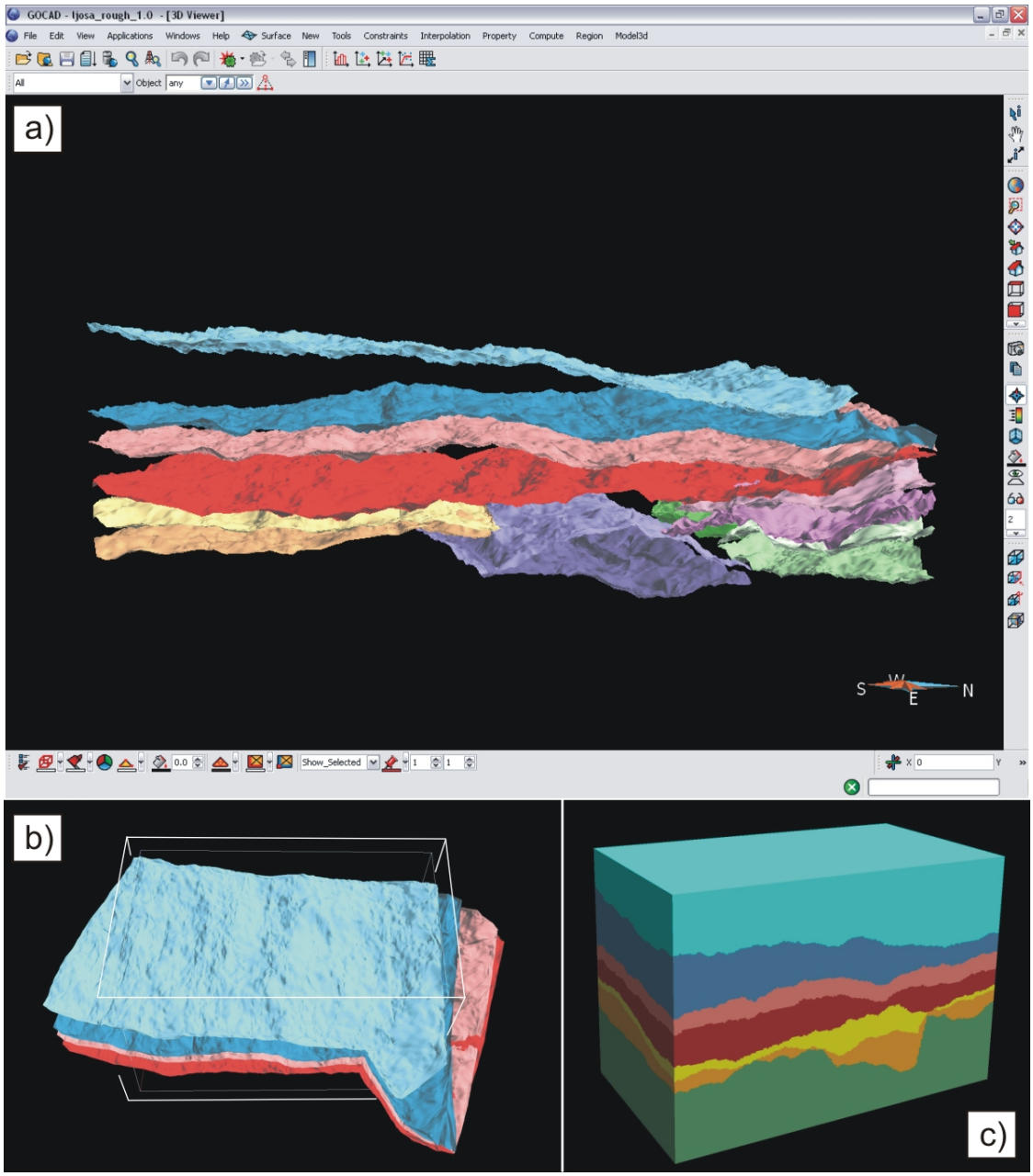

Figure 7.14 Ljosa Quarry model. a) Model with rough surfaces. b) Voxet taking in as much complexity as possible. c) Voxet divided into regions.

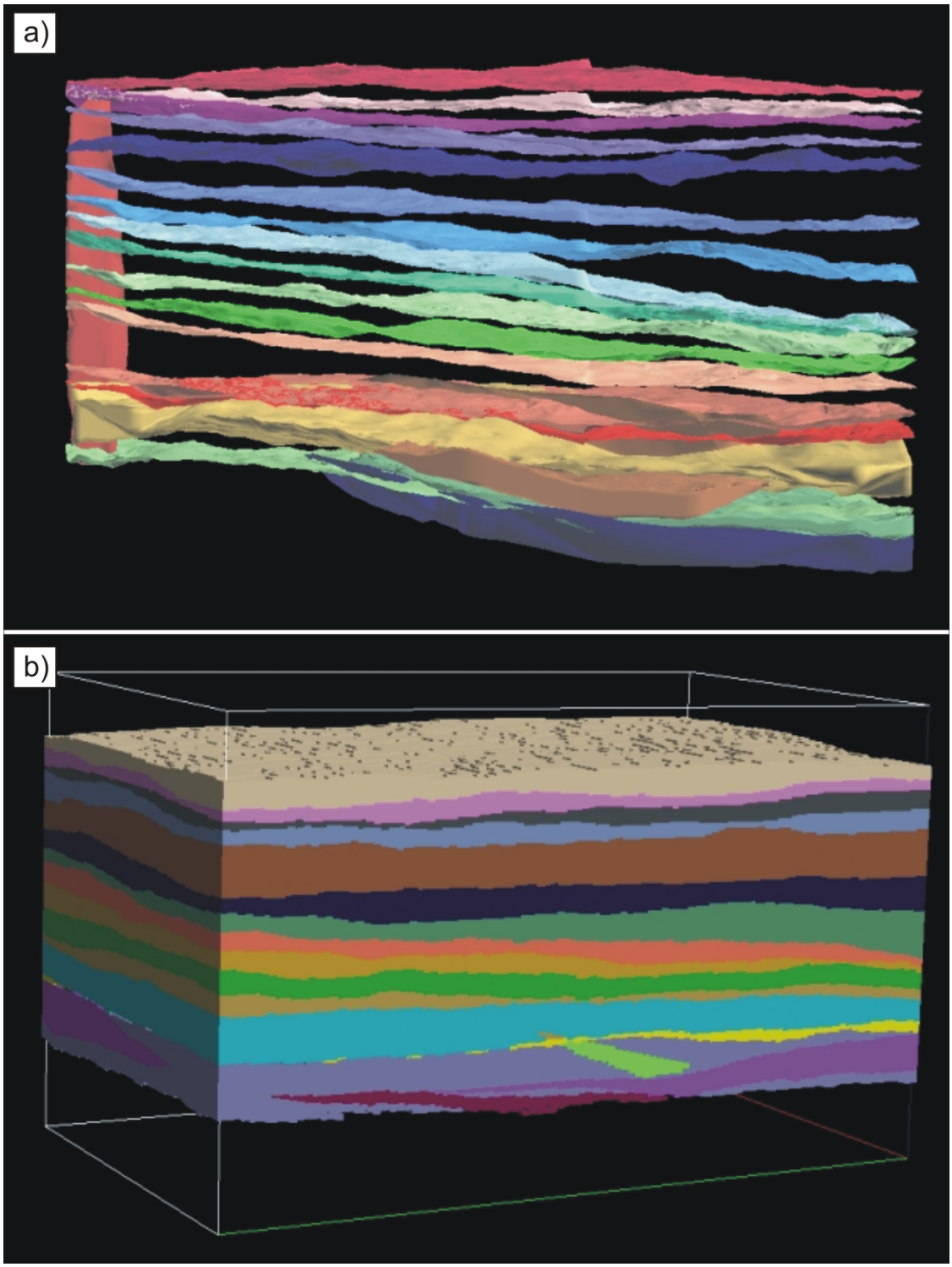

Figure 7.15 Talisker Bay model in GOCAD®. a) Model showing the rough surfaces. b) The voxet divided into regions.

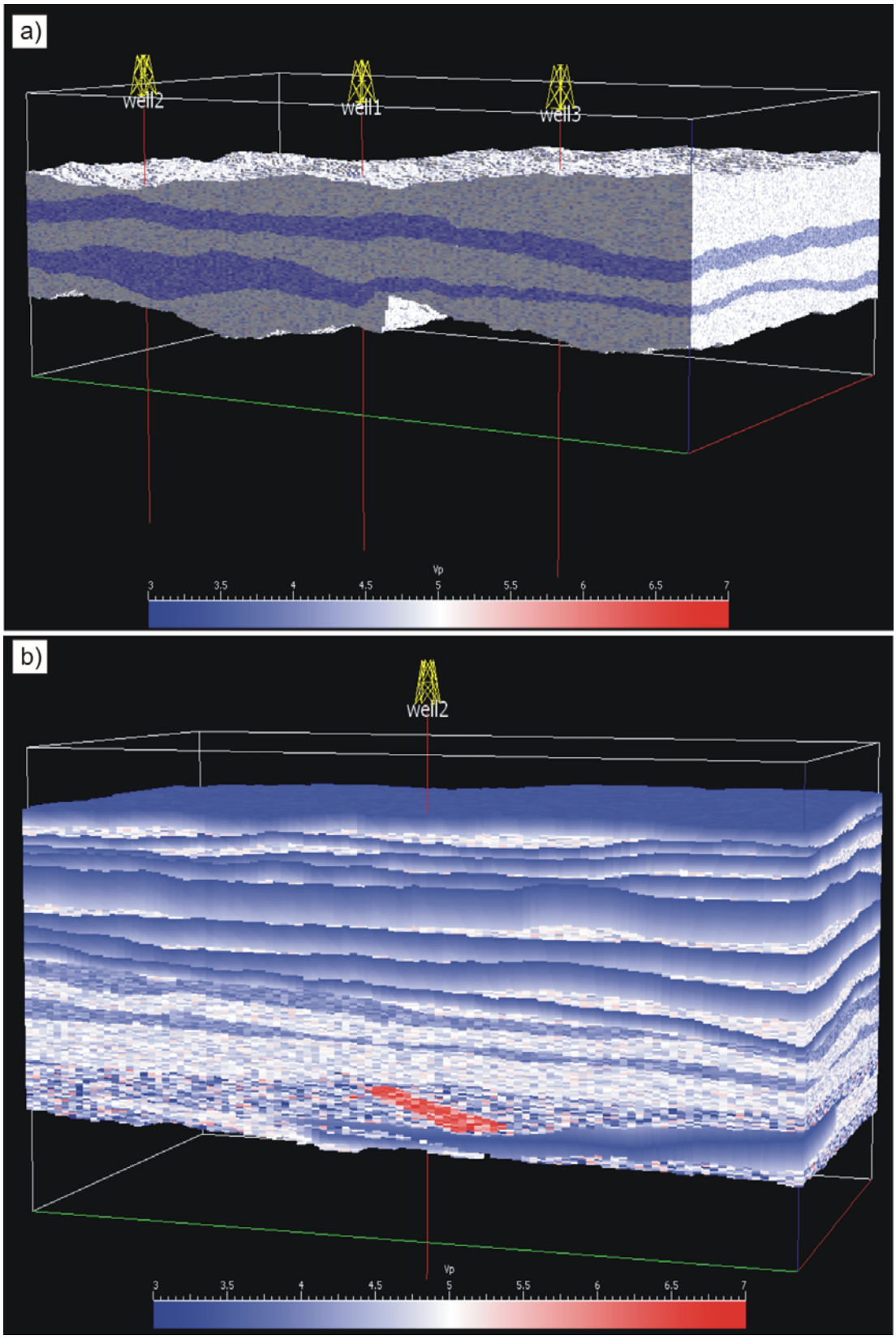

Figure 7.16 a) Completed Ljosa Quarry model with virtual boreholes. b) Completed Talisker Bay model with virtual borehole.

7.4.3 Analysis

Figure 7.17 shows histograms and virtual boreholes from both models. From the histograms, it can be seen that the models are reasonably close to the real data (data from the Glyvursnes-1 borehole are plotted in Figure 7.11). The modes are in the correct place, but the range is smaller than in the real data. The methods for attributing velocity data could be improved to better approximate the borehole data. The virtual boreholes both display the cyclic pattern seen in the real data.

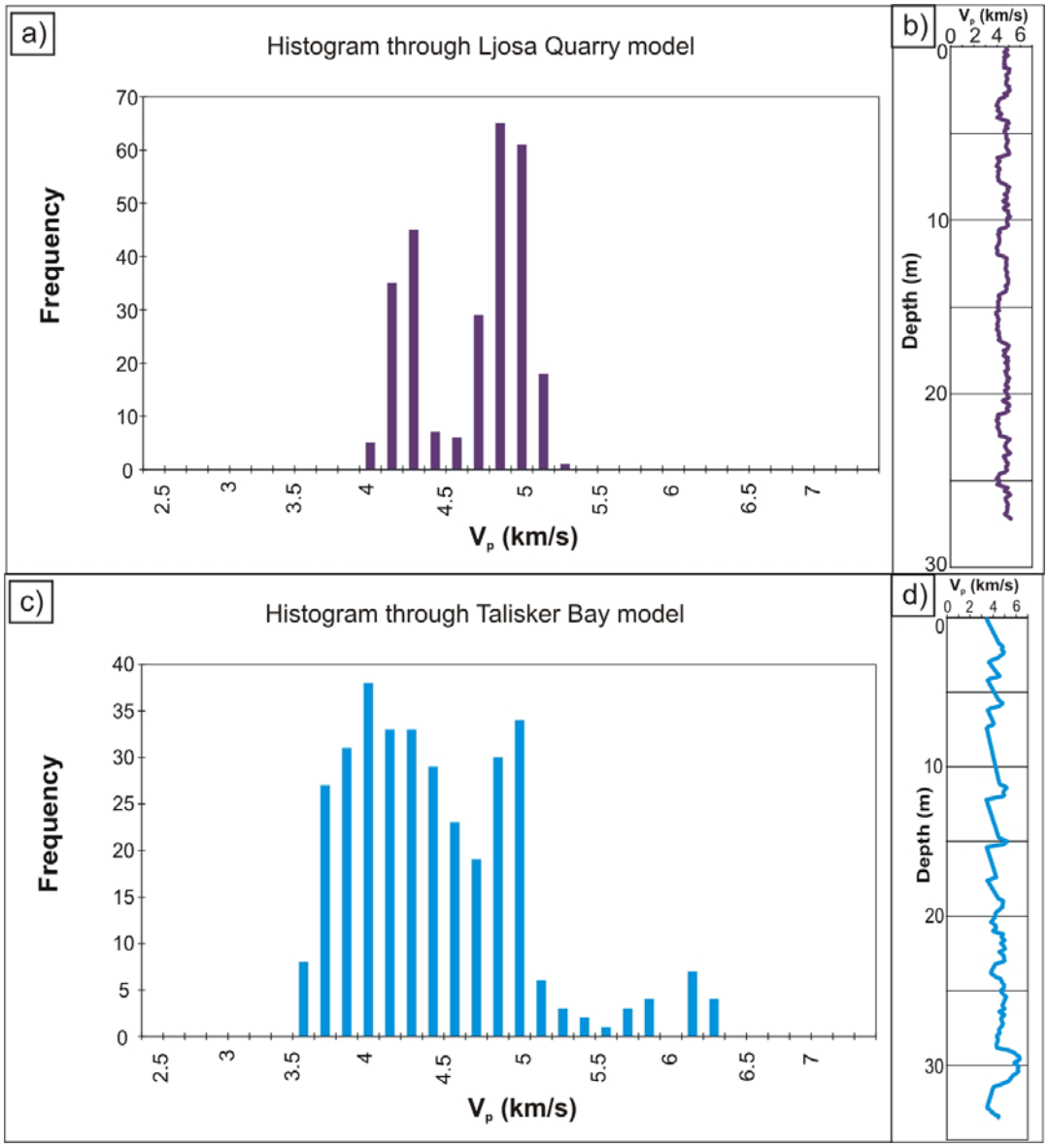

Figure 7.17 a) Histogram of data from virtual boreholes through the Ljosa Quarry model. Three boreholes were created to obtain an adequate sample size. b) Virtual borehole through the Ljosa Quarry model. c) Histogram of data from virtual borehole through the Talisker Bay model. d) Virtual borehole through the Talisker Bay model.

One limitation of these models is that the cell size is too big for the voxet to accurately be divided into all the flows - in some places they are less than one cell in thickness. This means that the flow becomes divided into many smaller regions, and velocity values cannot be added correctly. This is only a problem for the lowest flow in the study area, and this is omitted in the final model. Cell size could be decreased; however this causes a corresponding increase in computer memory usage and time required for model construction. Additionally, when used for generation of synthetic seismic data, cells this small will cause the total data volume to become too large.

7.5 Compound-braided flow models: fully random models

7.5.1 Approach, source data and methods

Another approach to building models of compound-braided lava flows is to use a fully random model. These are much simpler and quicker to produce than the models described in Section 7.4, and it is easier to produce larger volumes. Due to the highly heterogeneous nature of the compound-braided system, we investigate whether it may be possible to approximate it to a random model. Comparing the two approaches tests whether it is useful to spend the extra time constructing the models of the previous section.

Accordingly, a model was generated using the random building code of White (2009), but this time a volume was created rather than just a surface. White (2009) used velocity data from Well 164/7-1 to generate a similar model; here we use data from only one volcanic facies and combine it with the fractal properties of a lava flow top surface discussed in Chapter 6. The data used are compound flows from the Malinstindur Formation in the Glyvursnes-1 well, and an example is shown in Figure 7.18a. It can be seen that the data can be described by a power spectrum, making them suitable for fractal analysis. A 300m thickness was used, containing 90 flows with an average thickness of 3.3m. This contains more than 10 cycles, so the power spectra should be representative (e.g. Li, 1999). Figure 7.18b shows a power spectrum of these data, generated in the same way as those in Chapter 6.

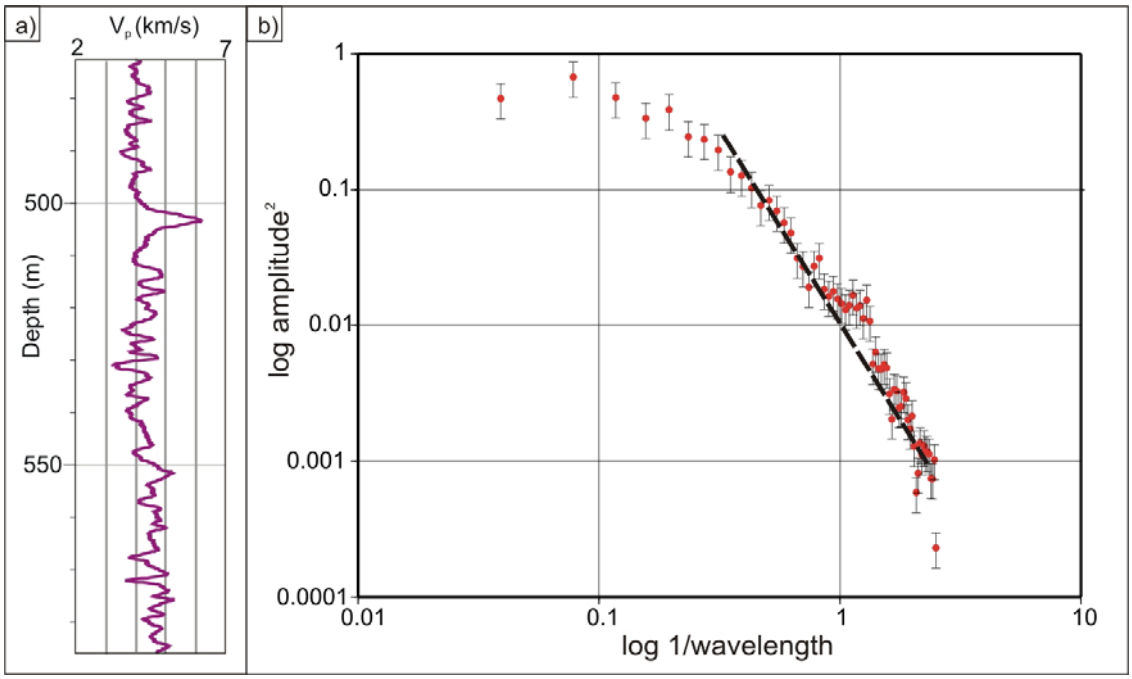

Figure 7.18 a) Example of data from the Glyvursnes-1 borehole. b) Power spectra of Glyvursnes-1 data, produced in the same way as those in Chapter 6.

Fractal parameters for the vertical velocity variation were obtained from the power spectrum in Figure 7.18b. This gives a correlation length of approximately 3m, and a Hurst number of approximately 0.85. The input parameters for the random volume building code are given in Table 7.1 below. The correlation lengths in the x and y direction are unknown - more outcrop data at a larger scale would be needed to obtain these. I assume that the flows are longer in one direction than another and use lengths of 10m and 100m. This is one area where the model could be greatly improved. Another assumption is that the Hurst number is the same in the x and y directions. It is not currently possible to prove or disprove this, as no horizontal velocity profiles exist through basalt sequences. The parameters will probably not be the same as those used to generate the random surface topography, as the periodic velocity changes will likely be due to edges of flows rather than lateral variations.

This may seem inconsistent when compared to the rough surfaces generated in Chapter 5, so further explanation is required. While the surface roughness on a flow top appears to be isotropic, based on the data from Chapter 6, a compound-braided flow itself is likely to be longer in one direction than the other. This is based on field observations by Jerram (2002).

Input parameter	Value used
x nodes	256
y nodes	256
z nodes	128
grid spacing	0.2m
correlation length in x	100
correlation length in y	10
correlation length in z	3
standard deviation	0.62
Hurst number	0.85

The finished model, imported into GOCAD®, is shown in Figure 7.19 below.

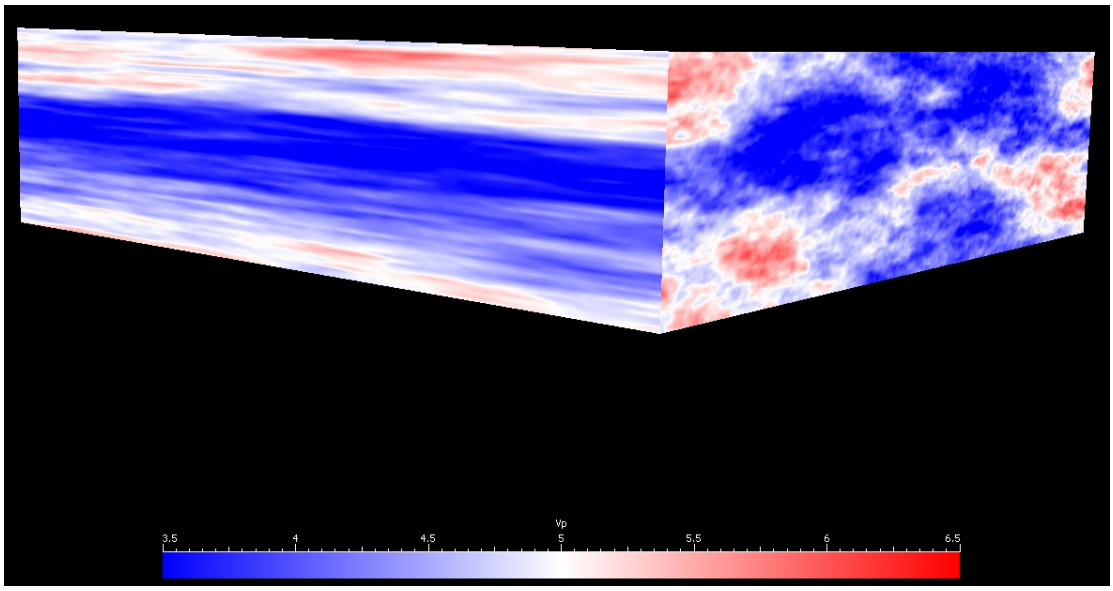

Figure 7.19 Random compound flow model. Model is approximately 100m x 100m x 25m.

7.5.2 Analysis

Figure 7.20a is a histogram of all values from the random compound model, and Figure 7.20b shows a "virtual borehole" through the model. The histogram of values is extremely similar to the real borehole data, with modes in the same place and the same range. However, as expected with this type of model, the virtual borehole is very different to the real data, as there is no cyclic pattern to the velocity values.

Compared to the models in Section 7.4, the histogram is closer to the real data but the borehole is much further from the cyclic pattern shown in boreholes such as Glyvursnes-1.

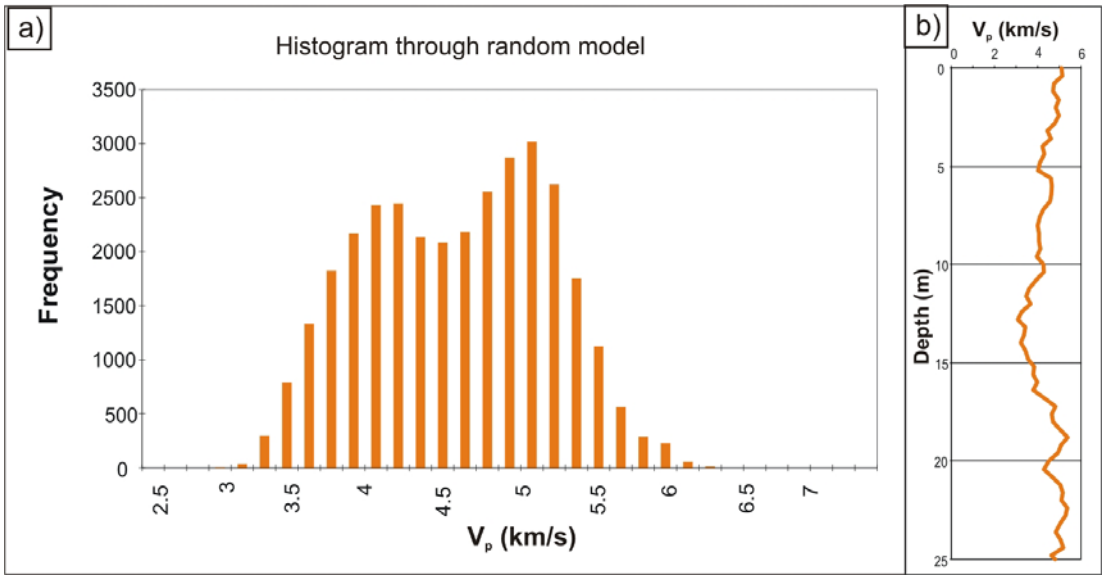

Figure 7.20 a) Histogram of velocity values from the random compound model. b) Virtual borehole through the random compound model - as expected, there is no pattern to the velocity data.

Advantages of this type of model are that it is very quick and easy to produce; however it does not replicate the layered structure found in a real sequence of lava flows. Additionally, the velocity variations in x and y are unknown, so the correlation lengths can only be estimated; however this could be resolved in the future by detailed mapping of lava flows at a larger scale than the models in Section 7.4. The principle advantage of this approach is that models of any size can easily be generated, as long as the input parameters are known accurately. Future work could be carried out to incorporate a layered structure, following the methods of Goff and Levander (1996).

7.6 Density

So far, I have only been considering P-wave velocity; however density data is also required to generate synthetic seismic data. Accordingly, cross-plots of velocity and

density data for both tabular-classic and compound-braided flows are shown in Figure 7.21.

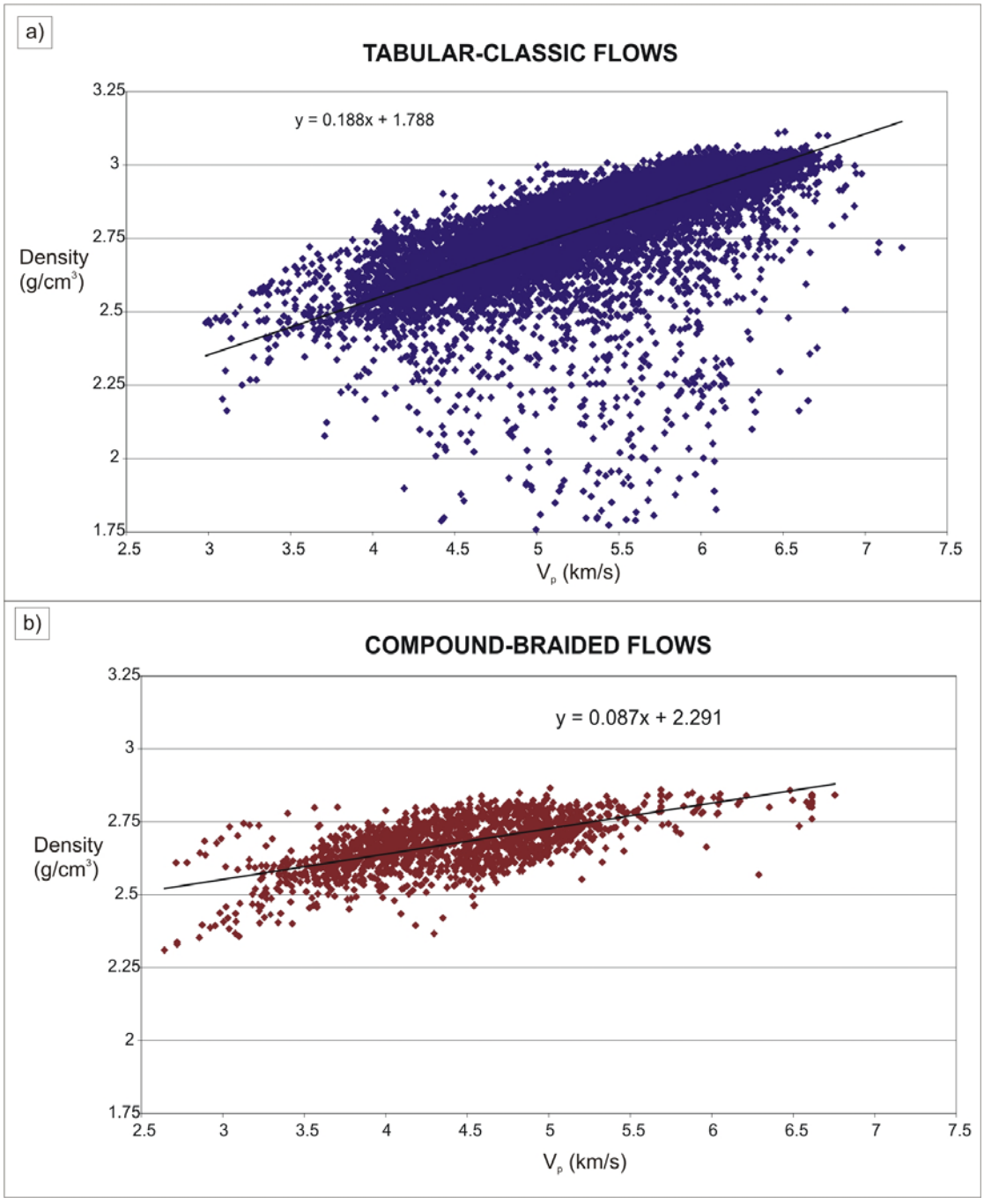

Figure 7.21 Velocity-density cross plots for a) Tabular-classic flows from the Lopra-1/1A borehole. b) Compound-braided flows from the Glyvursnes-1 borehole. See also Christie et al. (2006).

Velocity and density show a very strong correlation in both cases, though the relationship is different for the compound-braided and tabular-classic flows. This

may be due to a difference in the vesicle proportion or a geochemical difference; further investigation would be required to establish the cause. These relationships are used in Chapter 8 to generate synthetic seismic data.

7.7 Discussion and conclusions

7.7.1 Tabular-classic flow model

The workflow provided forms a relatively rapid way of creating a model of a sequence of tabular-classic flows. It is possible to generate a model of 10km x 10km x 500m at a horizontal resolution of 30m and a vertical resolution of 1m, though this was at the limits of available computing power. The model displays many features found in outcrops, and displays some features of borehole data, but as yet the model is not well constrained by outcrop data. Further work would be required to check that tabular flows have the same surface parameters as the Laki lava flow, and also to determine whether any lateral velocity variations exist. As yet, it has proved difficult to find a way of mapping out the lateral extent of tabular flows, as there are few well-exposed areas which are kilometres in length. Correlation of flows along distances this size is extremely difficult. Further work could also determine whether the crust-core boundary displays the same topography as the flow top.

7.7.2 Compound-braided flow models

The compound-braided flow models developed from the laser scanning data (Ljosa Quarry and Talisker Bay) give a good representation of the true geology, incorporating small-scale surface roughness. Velocity data can be attributed to the models at a very fine scale. However, these models have a couple of important limitations: their size and the velocity distribution. Size is a function of the available outcrop and the limitations of the laser scanning equipment, and different methods would be required to build larger models. These models are still useful, as they capture accurately the complex heterogeneity present in a sequence of compound flows, and an example of their use is introduced in Chapter 8. It is also important to consider whether these models are representative of the flow geometry found in all compound-braided sequences - additional fieldwork would help to resolve this.

In contrast, it is much easier to build a random model of any size with a velocity distribution reflecting the real data; however this type of model also has limitations. Maresh (2006) shows that a great deal of scattering of a seismic wave is due to the internal layering of a basalt sequence, and random models do not contain this. Additionally, parameters required for the random models are not well known in the x and y directions, so it is difficult to test whether the models are realistic. Random models may be useful in some circumstances, but they are probably not suitable for generating synthetic seismic data.

7.7.3 Conclusions

The models presented in this chapter are a preliminary attempt at constructing accurate 3D velocity models, and roughly agree with the borehole data from the Faroe Islands. The tabular model has been successfully constructed at a scale appropriate for generating synthetic seismic data, and is used for this purpose in Chapter 8. It incorporates outcrop data on surface roughness and thickness data from the Lopra-1/1A borehole. Velocity data have been successfully added, but agreement with observed velocities could be improved. The Ljosa Quarry and Talisker Bay models successfully incorporate laser scanning data and small-scale roughness; however again the agreement with observed borehole velocities could be improved. The random compound model contains the correct velocity data, but without the cyclic pattern observed in outcrop and borehole data.

The work in this chapter could be extended and improved by returning to outcrop observations and testing how well the models approximate the real data. This would also allow some quantification of the errors involved in the workflow presented here. The models are not exact replicas of the studied outcrops; rather, as much real data as possible is incorporated in order to obtain a “typical” facies model. The use of these models is discussed in the next chapter.

Another area where this work could be extended would be to consider other facies, in particular intrusives and hyaloclastites. The best data on intrusive geometry would be from 3D seismic data, and attributing velocities would be comparatively simple as there is little internal structure. Other researchers are investigating sill geometry (e.g. Thomson and Schofield, 2008; Planke et al., 2005). At present, comparatively little is

known about the internal structure and seismic velocity of hyaloclastite sequences, and more outcrop observations and seismic interpretation are required, which are beyond the scope of this thesis.

8

8. CONCLUSIONS, FURTHER WORK AND SYNTHETIC SEISMIC DATA 152

8.1 CONCLUSIONS 152

8.1.1 3D data in flood basalt provinces 152

8.1.2 Borehole analysis and velocity data 152

8.1.3 Methods for 3D modelling 152

8.1.4 Applications to synthetic seismograms 153

8.2 FURTHER WORK 153

8.3 AN INITIAL LOOK AT SYNTHETIC SEISMIC DATA 155

8.3.1 1D reflectivity modelling 155

8.3.2 3D synthetic seismic data 161

8. Conclusions, further work and synthetic seismic data

8.1 Conclusions

In this thesis I have combined a variety of datasets and observations with a diverse range of techniques to explore the 3D facies variations that are found in flood basalts and volcanic margins. Before some general comments about future research, I summarise the main conclusions of the thesis.

8.1.1 3D data in flood basalt provinces

This thesis provides quantitative data on lava flow sizes, shapes, stacking patterns and surface roughness. These data were collected by terrestrial laser scanning, field observations and satellite remote sensing, from outcrops mainly in the North Atlantic Igneous Province. The data form the basis for the 3D geological models presented in Chapters 5, 6 and 7.

8.1.2 Borehole analysis and velocity data

The methods presented in Chapter 4 provide a successful way to identify volcanic facies in borehole data. The different facies have a characteristic signature, easily identified by plotting histograms of the raw borehole data. These histograms can be used to identify volcanic facies in areas without nearby onshore analogues, as shown by application to Well 164/07-1 in the Rockall Trough. The borehole data from the Faroe Islands also provide a “type example” for different facies and, when analysed in detail, provide useful velocity and density data for constructing 3D models.

8.1.3 Methods for 3D modelling

The workflows presented in this thesis provide a method for constructing realistic 3D models of flood basalt lava flows. These models incorporate small-scale roughness and velocity data, drawing on previous work on fractal surfaces. The limitations of the models in Chapter 7 are that the final models have not been compared to outcrop observations and the velocity distributions do not exactly correspond to the observed

borehole distributions. The uncertainties of these models need to be quantified by further field observations.

This work also provides a valuable test of terrestrial laser scanning in flood basalt provinces. It is possible to gather extremely detailed data and extend this into full 3D models via the workflows developed in Chapters 5, 6 and 7, and terrestrial laser scanning is an extremely good way of gathering data on lava flow surface roughness. However, other parameters such as lava flow lateral extent are larger than the scales possible from conventional laser scanning, so digital photogrammetry may provide a better solution.

8.1.4 Applications to synthetic seismograms

Section 8.3 shows that the models produced in Chapter 7 are useful for generating synthetic seismograms. Using these, we can start to find out which component of a basalt sequence is actually causing the scattering and attenuation, though much more work is needed to fully explore the effects of adding different velocity data to the models, as well as combining the different facies. The models should prove useful for developing new migration strategies.

8.2 Further work

The conclusions of this thesis suggest several areas for future research. Firstly I will summarise the main areas where future work is required before taking a more detailed look at the future of synthetic seismic modelling in flood basalt provinces. The following points outline key areas where further research should be directed:

1. Improving knowledge of the link between features seen in outcrops and in wireline log data, leading to a properly quantified relationship. For example, the link between seismic velocity and vesiculation/fracturing could be quantified by a study of wireline log data and recovered core. The effects of other factors such as chemical composition could also be quantified. This would improve the way velocity data is attributed to 3D models such as those in Chapter 7, and could be carried out on IODP cores and logs.
2. Construction of larger 3D outcrop models would result in an improvement to the work presented here. The small size of the outcrops used to build

compound flow models limits their usefulness in generating synthetic seismograms, and this is partly due to the restrictions imposed by the laser scanning equipment. Digital photogrammetric techniques may prove useful, and the west coast of Skye, with extensive outcrops only accessible by boat, would be an excellent place to test this. Closer links with computer sciences may prove useful in developing new techniques, both in constructing 3D outcrops and in interpreting digital photographs.

3. More fieldwork could also be carried out to get more data on lava flow surface roughness, to check that the Laki lava flow is representative of ancient lava flows. It would also be useful to check whether tabular and compound flows display the same surface roughness, in both along and across flow directions.

4. There is a great deal of scope for further work using the models in Chapter 7 to generate synthetic seismograms, and I begin to explore this in Section 8.3. The effects of varying the methods for attributing velocity could be investigated, for example adding random noise to the tabular flow crusts. Attenuation could be further investigated using combined tabular and compound models.

5. The methods presented in this thesis could be extended to other facies and provinces where large, good-quality outcrops are present.

6. Another area for future work is the correlation of lava flows between outcrops, which is difficult by conventional methods. One possibility could be to examine the patterns of flow thicknesses and try to match these in a similar way to palaeomagnetic correlation.

8.3 An initial look at synthetic seismic data

In this section, I start to explore the possible future uses for the models constructed in Chapter 7. Synthetic seismograms are generated in two ways: reflectivity modelling and phase-screen modelling. Modelling was carried out by Richard Hobbs, and I discuss the results here. I also obtain an estimate of the attenuation caused by a sequence of tabular flows, and a sequence of compound flows. The 1D modelling does not require the full 3D models presented in this thesis, but tests that realistic values of attenuation are being produced. The synthetic seismic data is generated using the same methods as Maresh et al. (2006) to allow the comparison of results.

8.3.1 1D reflectivity modelling

Synthetic seismograms can be generated from 1D profiles using the reflectivity method (Fuchs and Müller, 1971; Kennett, 1983). This method has been used to determine the effect of a basalt sequence on a seismic wave (Maresh et al., 2006; Zielkowski et al., 2003) and the results can be used to obtain an estimate of attenuation in terms of the quality factor, Q. Here, we use the tabular model and Talisker Bay compound model from Chapter 7 for comparison with the borehole data from Well 164/07-1 used by Maresh et al. (2006). A reference model with constant velocity values was also used, identical to that used by Maresh et al. (2006).

The models are shown in Figure 8.1a, Figure 8.2a and Figure 8.3a, and were set up as follows:

Layer 1 (0-903m depth): constant velocity, 2km/s, representing a sedimentary sequence.

Layer 2 (903-1903m): basalt sequence. Constant velocity or profile through model. Sampled at 1m for the tabular model; 0.2m for the compound model.

Layer 3 (1903-3400m): constant velocity, 4km/s, representing sub-basalt sediments.

Layer 4 (3400-3600m): constant velocity, 6km/s, representing target reflector.

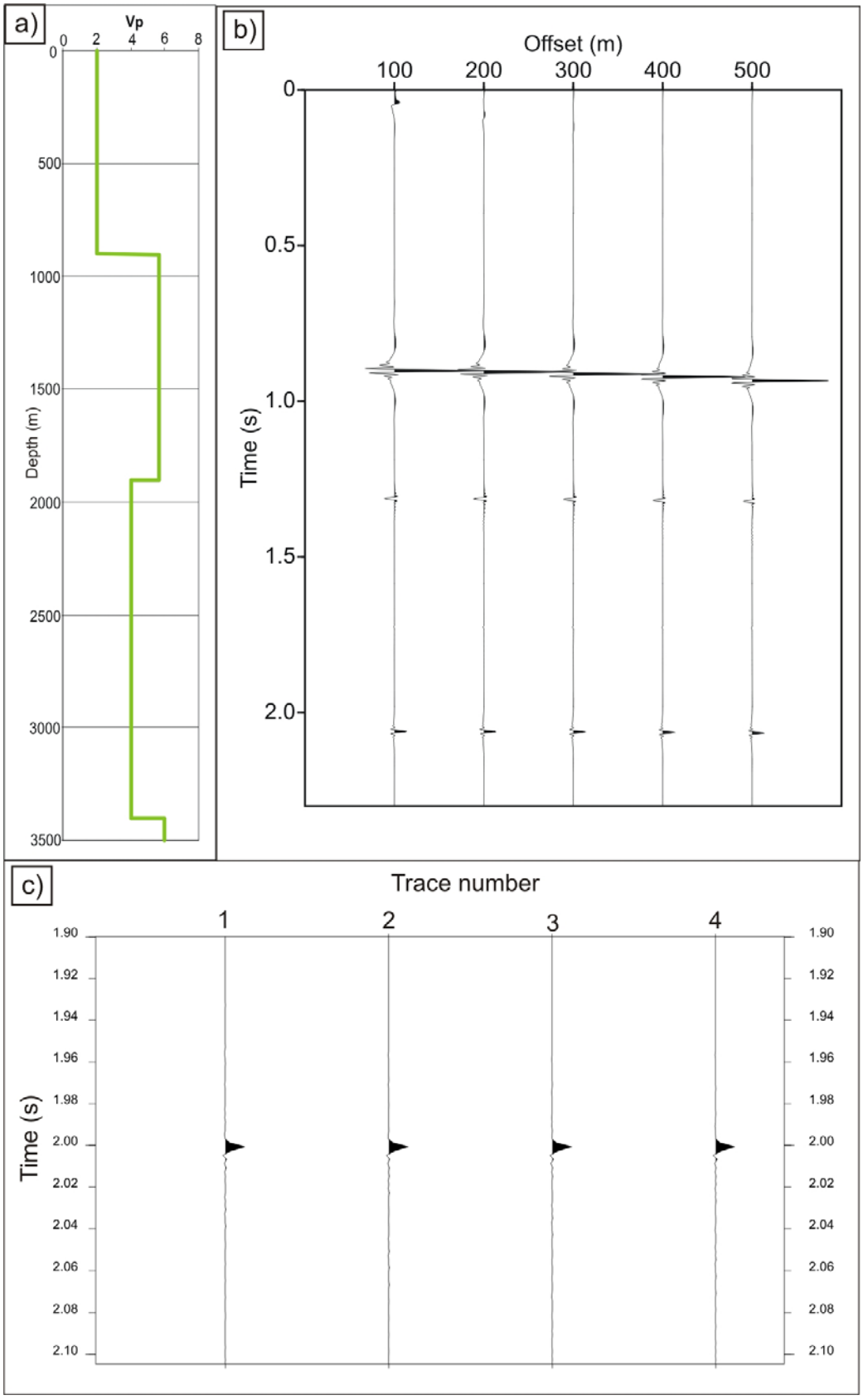

Figure 8.1 a) Simple layered reference model used to generate seismograms. b) Seismogram resulting from this model at offsets up to 500m. c) Zoomed in view of the target reflector at ~2s.

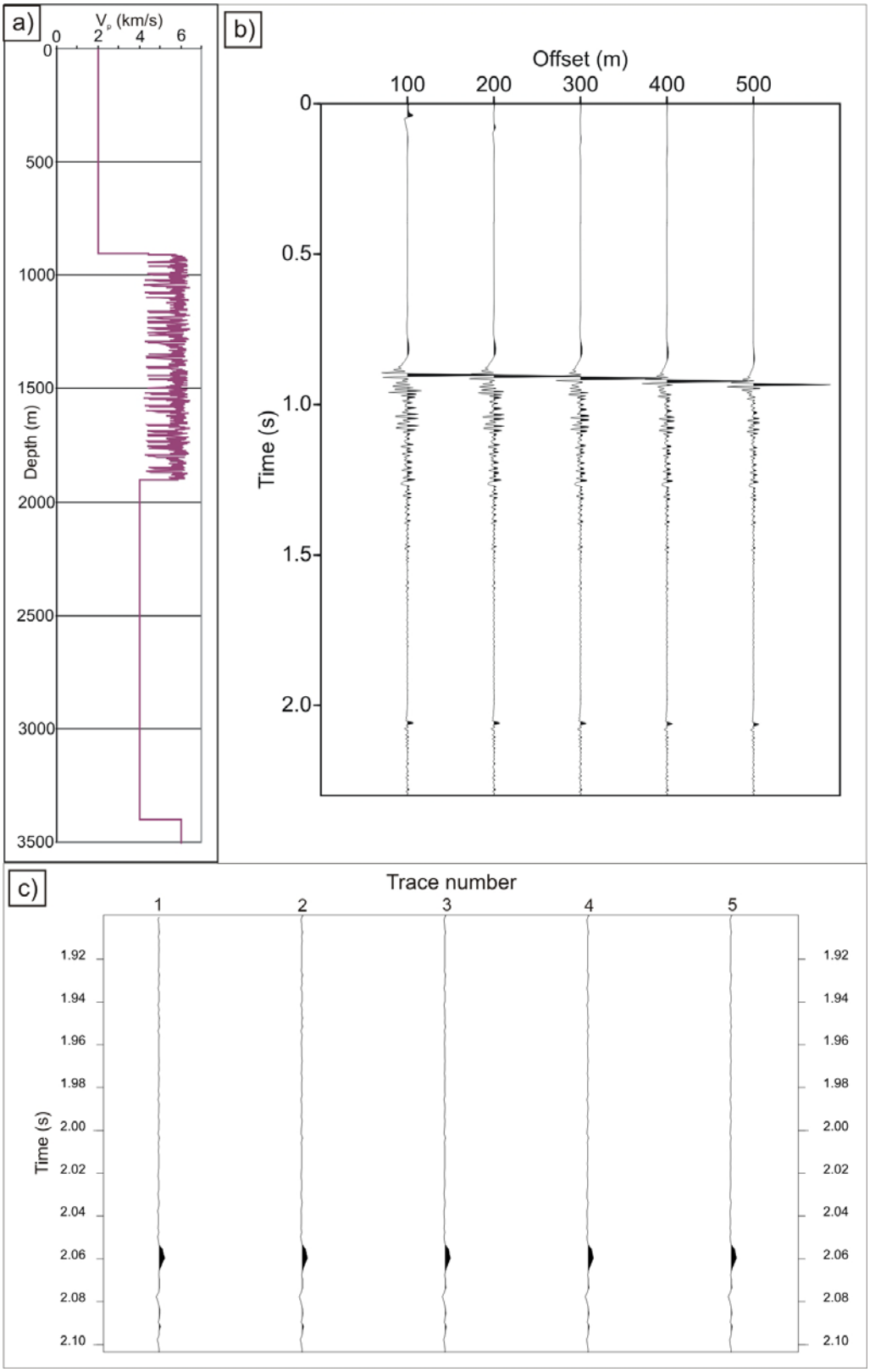

Figure 8.2 Tabular model. a) Velocity model used to generate seismograms. b) Seismogram resulting from this model at offsets up to 500m. c) Zoomed in view of the target reflector at ~2s. Note that the reflection time of the target reflector varies depending on the mean velocity of the basalt sequence.

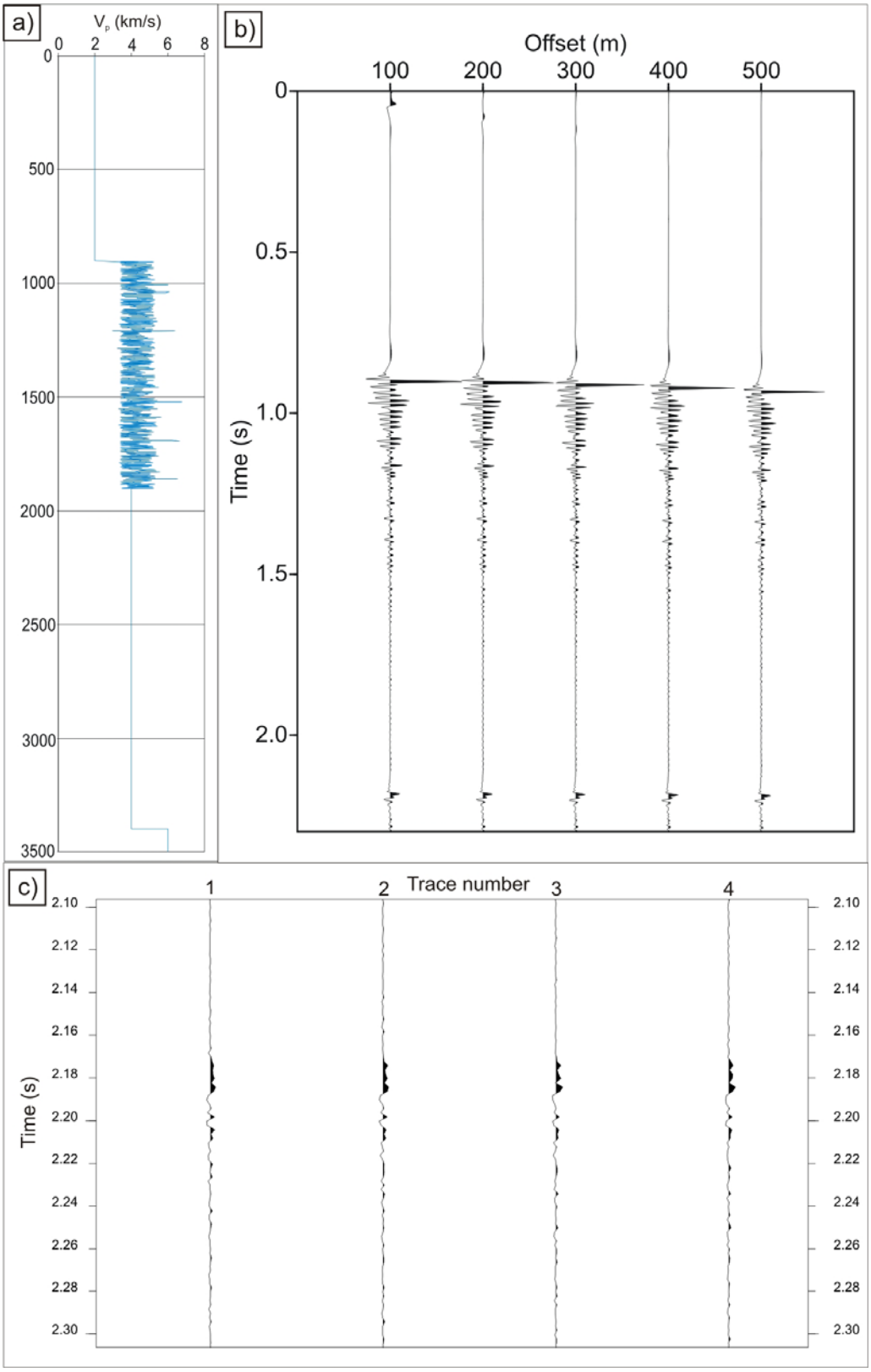

Figure 8.3 Compound model from Talisker Bay. a) Velocity model used to generate seismograms. b) Seismogram resulting from this model at offsets up to 500m. c) Zoomed in view of the target reflector at ~2s. Note that the reflection time of the target reflector varies depending on the mean velocity of the basalt sequence.

The code was implemented in the PGS Nucleus package, using the same experiment geometry as Maresh et al. The results are shown in Figure 8.1 and Figure 8.2. It can be seen that the target reflector has a much higher amplitude in the simple model (Figure 8.1c) than the tabular model (Figure 8.2c), suggesting that the seismic wave has been significantly attenuated. This attenuation can be quantified using the spectral ratio method (Aki and Richards, 2002) using the following equation (Maresh, 2004):

$$ln\left(\frac{A_2(f)}{A_1(f)}\right) = -\pi \frac{\delta t}{Q} f + c$$

where Q is the quality factor, f is frequency, c is a constant, A_1 and A_2 are the amplitudes of an upper and lower wavelet in the frequency domain, and δt is the time difference between the two wavelets (Maresh, 2004). If $ln(A_2/A_1)$ is plotted against frequency, the slope of a straight line through the data allows Q to be calculated using the following equation:

$$m = -\pi \frac{\delta t}{Q}$$

where m is the slope of the straight line. Figure 8.4 shows graphs of $ln(A_2/A_1)$ against frequency for the tabular and compound models. The data are somewhat noisy, lacking the clear trend shown by the data of Maresh et al. (2006). In the tabular model, this is likely to be caused by the range of flow thicknesses being narrow, so the energy is only attenuated at certain frequencies. The compound model was repeated around 30 times to give a sufficient thickness, and this repetition caused spikes in the data. This could be improved by obtaining more outcrop data and constructing larger models.

However, it is still possible to derive an estimate of Q from these graphs, and trendlines are plotted to show the range of possible values. A Q of around 31 is obtained for the tabular model, with a possible range from ~24 to ~114. The value for the compound model is around 120, with a range from ~55 to ~220. Even allowing for the data quality, this suggests that tabular flows display much stronger attenuation than compound flows.

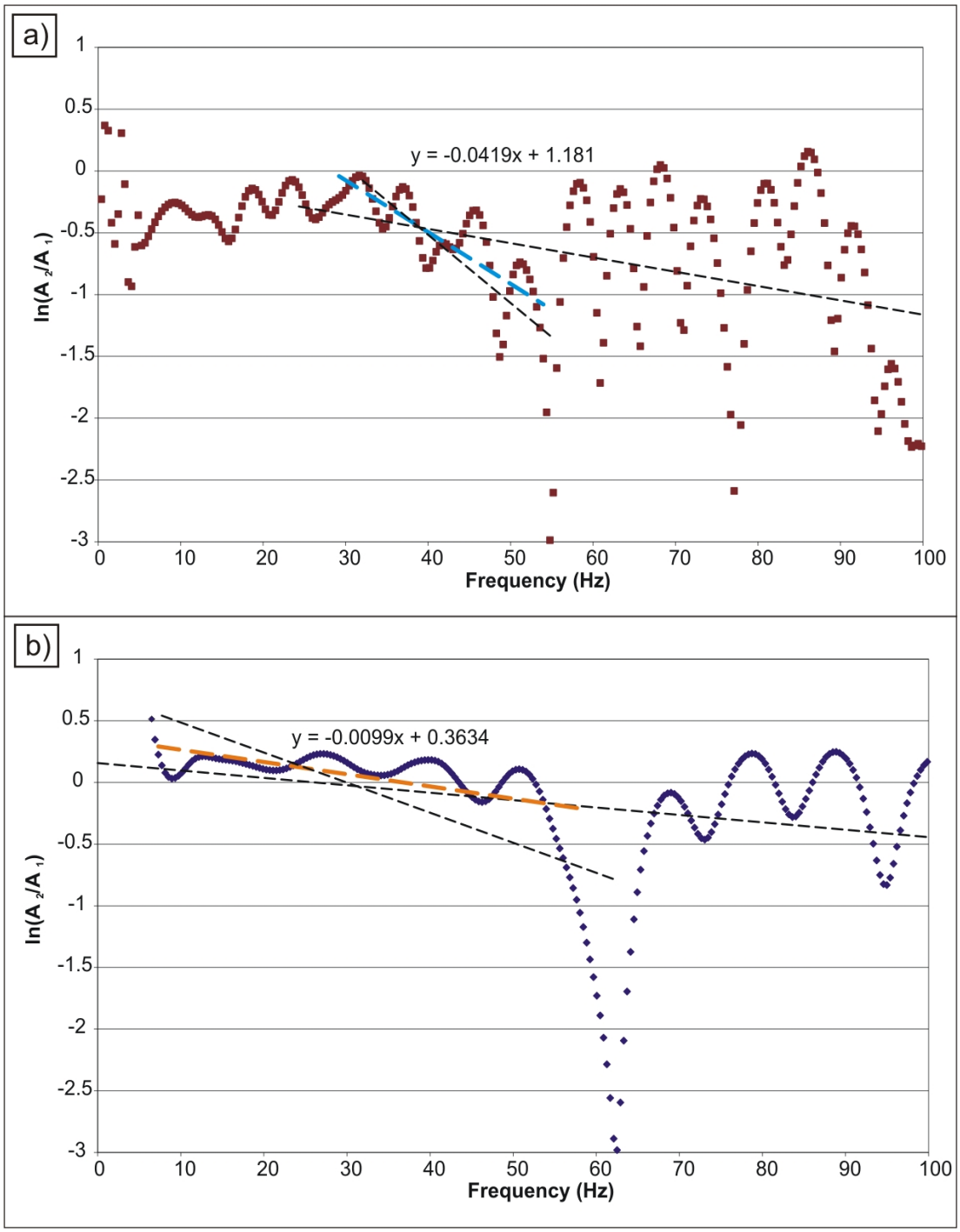

Figure 8.4 Graphs for calculating Q by the spectral ratio method for a) the tabular model. b) the Talisker Bay compound model.

These values can be compared to previous work. Christie et al. (2006) obtained a Q of 35 for the subaerial part of the Lopra-1/1A borehole, which is made up mostly of tabular flows. Shaw et al. (2008) obtained a mean Q of 24 for the Glyvursnes-1 borehole, though they noted that the Q increased with depth. The Glyvursnes-1 borehole includes the Enni Formation (tabular and compound flows) in its upper half

and the Malinstindur Formation (compound flows) in its lower half. Shaw et al. also obtained a value of Q of 84 for the compound flows in the Vestmanna-1 borehole. Maresh et al. (2006) obtained a Q of 15-35 for the 164/07-1 well, which as shown in Chapter 4 contains a mixture of tabular and compound flows. Maresh et al. also showed that a sampling distance of 1m or less was required to accurately estimate Q.

Results from these models show that we can start to determine how the different volcanic facies affect 1D attenuation; however this is only a preliminary investigation. There is still much to be done to investigate how sensitive the reflectivity modelling is to factors such as the velocity distribution and flow thickness. Maresh et al. (2006) showed that decreasing the range of velocity values increased Q, as did increasing the size of the heterogeneities, and now that we have fully constrained 3D models we can start to further investigate these factors. The modelling in this section does not require full 3D models; however it serves to test that realistic results are being produced.

8.3.2 3D synthetic seismic data

Synthetic seismic data were also generated from the full 3D tabular model from Chapter 7. The model was copied and stacked on top of the original to give a 1km thickness, consisting of 40 lava flows, and the total size is 10km x 10km x1km. The synthetic seismograms are generated by phase-screen modelling (Wild et al., 2000) in the exploding reflector mode. This is a relatively rapid way of dealing with large model sizes. The modelling was carried out by Richard Hobbs, and the results are shown in Figure 8.5 and Figure 8.6. The models were set up as follows:

Layer 1 (0-903m depth): constant velocity, 2km/s, representing a sedimentary sequence.

Layer 2 (903-1903m): basalt sequence. 2D or 3D model, with a horizontal resolution of 10m and a vertical resolution of 1m.

Layer 3 (1903-3400m): constant velocity, 4km/s, representing sub-basalt sediments.

Layer 4 (3400-3600m): constant velocity, 6km/s, representing target reflector.

No water layer was used, and the target reflector is at approximately 2s two-way travel time.

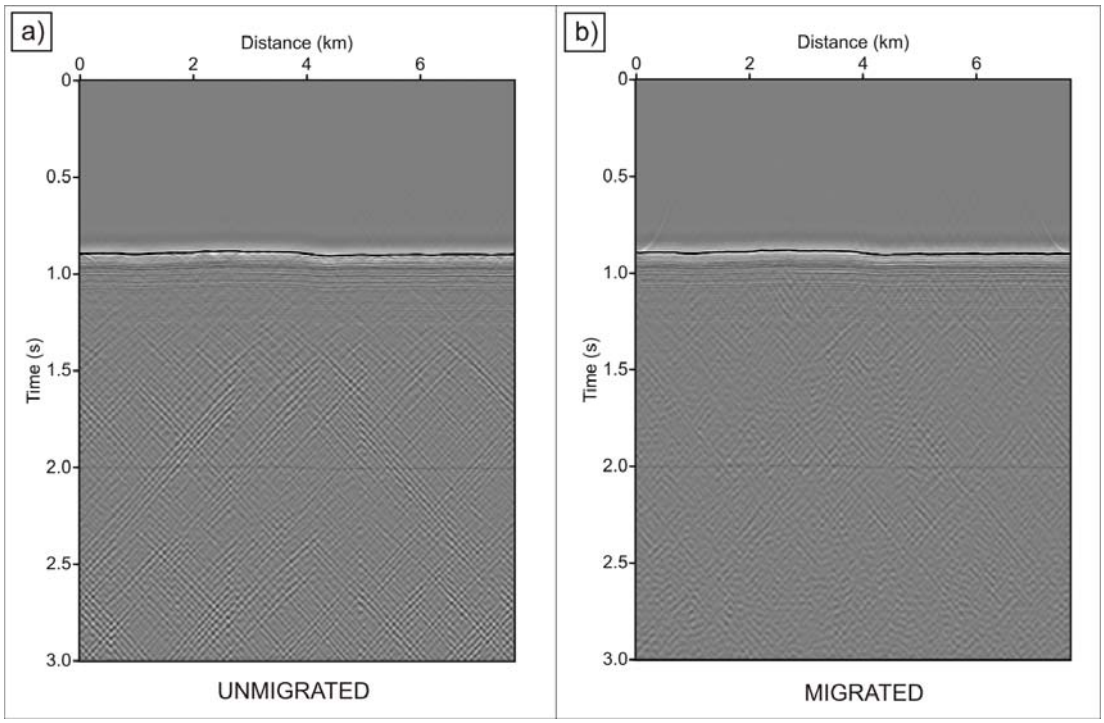

Figure 8.5 Synthetic seismic data produced using the exploding reflector mode of phase-screen seismic modelling (Wild et al., 2000) from a 2D profile through the tabular model. a) Unmigrated section. b) Migrated.

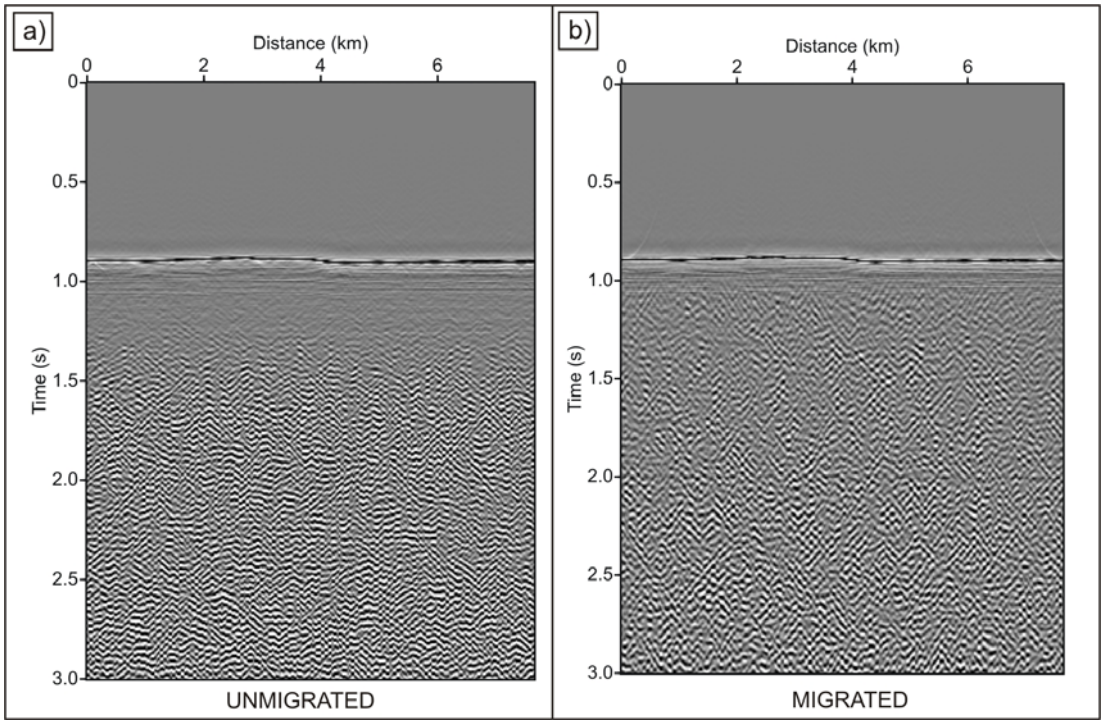

Figure 8.6 Synthetic seismic data produced using the exploding reflector mode of phase-screen seismic modelling (Wild et al., 2000) using the entire 3D tabular model. a) Unmigrated section. b) Migrated.

In Figure 8.5, the seismic line is produced from a 2D model (a single section through the tabular model). In a 2D model, scattered energy can only come from within the plane of the model. The target reflector can be clearly seen at a travel time of 2s, and when the data are migrated very little scattering remains. Figure 8.6 shows the results from the whole 3D tabular model. In this case, scattering from out of the plane of the seismogram is also included. The scattering is much more intense and the target reflector is much more difficult to distinguish. This suggests that 2D modelling does not fully capture the attenuation and scattering produced by a basalt sequence, and 3D modelling is required.

As before, this work builds on that of Maresh et al. (2006), who modelled a single rough surface using the phase-screen method. Their results showed that a single surface was not enough to produce all the observed scattering and attenuation. Advances in computing power now allow multiple rough surfaces to be modelled, and it can be seen that this produces a much greater level of scattering. The preliminary results agree with Maresh et al., in that the attenuation is probably dominated by reverberation due to layering in the model. However, the image beneath the basalt is further degraded by the high levels of scattered noise from the 3D rough surfaces. Further investigation would provide a clearer picture. This is only a starting point for the possible work using the models in this thesis to generate synthetic seismograms, and it is hoped that future work will go on to investigate further.

References

Aki, K., and Richards, P.G., 1980, Quantitative seismology: theory and methods. Volume II: San Francisco, W.H. Freeman and Company.

Andersen, M.S., and Boldreel, L.O., 2009, Log responses in basalt successions in 8 wells from the Faroe-Shetland Channel - a classification scheme for interpretation of geophysical logs and case studies.: Faroe Islands Exploration Conference: Proceedings of the 2nd Conference, Annales Societatis Scientarium Faroensis.

Archer, S.G., Bergman, S.C., Iliffe, J., Murphy, C.M., and Thornton, M., 2005, Palaeogene igneous rocks reveal new insights into the geodynamic evolution and petroleum potential of the Rockall Trough, NE Atlantic Margin: Basin Research, v. 17, p. 171-201.

Aubele, J.C., Crumpler, L.S., and Elston, W.E., 1988, Vesicle zonation and vertical structure of basalt flows: Journal of Volcanology and Geothermal Research, v. 35, p. 349-374.

Bartetzko, A., Pechnig, R., and Wohlenberg, J., 2002, Interpretation of well-logging data to study lateral variations in young oceanic crust: DSDP/ODP Holes 504B and 896A, Costa Rica Rift., in Lovell, M., and Parkinson, N., eds., Geological applications of well logs: AAPG Methods in Exploration No. 13, p. 213-228.

Bartetzko, A., Pezard, P., Goldberg, D., Sun, Y.F., and Becker, K., 2001, Volcanic stratigraphy of DSDP/ODP Hole 395A: An interpretation using well-logging data: Marine Geophysical Researches, v. 22, p. 111-127.

Bean, C.J., 1996, On the cause of 1/f-power spectral scaling in borehole sonic logs: Geophysical Research Letters, v. 23, p. 3119-3122.

Bean, C.J., and Martini, F., 2010, Sub-basalt seismic imaging using optical-to-acoustic model building and wave equation datuming processing: Marine and Petroleum Geology, v. 27, p. 555-562.

Bellian, J.A., Kerans, C., and Jennette, D.C., 2005, Digital outcrop models: Applications of terrestrial scanning lidar technology in stratigraphic modeling: Journal of Sedimentary Research, v. 75, p. 166-176.

Bendat, J.S., and Piersol, A.G., 1986, Random data: Analysis and measurement procedures: New York, John Wiley, 566 p.

Berthelsen, O., Noe-Nygaard, A. & Rasmussen, J. (eds), 1984, The deep drilling project 1980-1981 in the Faeroe Islands.: Annales Societatis Scientarium Faeroensis, Supplementum, v. IX, p. 158pp.

Birch, J., 2006, Using 3DM Analyst mine mapping suite for rock face characterization, in Tonon, F., and Kottenstette, J., eds., Laser and Photogrammetric Methods for Rock Face Characterization, p. 13–32.

Blake, S., and Bruno, B.C., 2000, Modelling the emplacement of compound lava flows: Earth and Planetary Science Letters, v. 184, p. 181-197.

Boldreel, L.O., 2006, Wire-line log-based stratigraphy of flood basalts from the Lopra-1/1A well, Faroe Islands, in Chalmers, J.A., and Waagstein, R., eds., Scientific results from the deepened Lopra-1 borehole, Faroe Islands. Geological Survey of Denmark and Greenland Bulletin, Volume 9, p. 7–22.

Browaeys, T.J., and Fomel, S., 2009, Fractal heterogeneities in sonic logs and low-frequency scattering attenuation: Geophysics, v. 74, p. WA77-WA92.

Bücker, C.J., Delius, H., Wohlenberg, J., and Leg 163 Shipboard Scientific Party, 1998, Physical signature of basaltic volcanics drilled on the northeast Atlantic volcanic rifted margins, in Harvey, P.K., and Lovell, M.A., eds., Core-Log Integration, Volume 136, Geological Society London, Special Publications, p. 363-374.

Buckley, S.J., Howell, J.A., Enge, H.D., and Kurz, T.H., 2008, Terrestrial laser scanning in geology: data acquisition, processing and accuracy considerations: Journal of the Geological Society, v. 165, p. 625-638.

Buffett, G.G., Hurich, C.A., Vsemirnova, E.A., Hobbs, R.W., Sallares, V., Carbonell, R., Klaeschen, D., and Biescas, B., 2010, Stochastic heterogeneity mapping around a Mediterranean salt lens: Ocean Science, v. 6, p. 423-429.

Cas, R.A.F., and Wright, J.V., 1987, Volcanic Successions: Modern and Ancient: London, Allen & Unwin.

Cashman, K.V., and Kauahikaua, J.P., 1997, Reevaluation of vesicle distributions in basaltic lava flows: Geology, v. 25, p. 419-422.

Chalmers, J.A., and Waagstein, R. (eds), 2006, Scientific results from the deepened Lopra-1 borehole, Faroe Islands: Geological Survey of Denmark and Greenland Bulletin, v. 9.

Christie, P.A.F., Gollifer, I., and Cowper, D., 2006, Borehole seismic studies of a volcanic succession from the Lopra-1/1A borehole in the Faroe Islands, northern North Atlantic: Geological Survey of Denmark and Greenland Bulletin, v. 9, p. 23–40.

Corfield, S.M., Wheeler, W., Karpuz, R., Wilson, M., and Helland, R., 2004, Exploration 3D seismic over the Gjallar Ridge, Mid-Norway: visualization of structures on the Norwegian volcanic margin from Moho to seafloor, in Davies, R.J., Cartwright, J.A., Stewart, S.A., Lappin, M., and Underhill, J.R., eds., 3D Seismic Technology: Application to the Exploration of Sedimentary Basins, Volume 29, Geological Society London Memoirs, p. 177.

Cox, K.G., 1980, A model for flood basalt volcanism: Journal of Petrology, v. 21, p. 629-650.

—, 1993, Continental Magmatic Underplating: Philosophical Transactions: Physical Sciences and Engineering, v. 342, p. 155-166.

Dellaert, F., Seitz, S.M., Thorpe, C.E., and Thrun, S., 2000, Structure from motion without correspondence: 2000 IEEE Computer Society Conference on Computer Vision and Pattern Recognition (CVPR'00), v. 2, p. 2557.

Dolan, S.S., and Bean, C.J., 1997, Some remarks on the estimation of fractal scaling parameters from borehole wire-line logs: Geophysical Research Letters, v. 24, p. 1271-1274.

Dolan, S.S., Bean, C.J., and Riollet, B., 1998, The broad-band fractal nature of heterogeneity in the upper crust from petrophysical logs: Geophysical Journal International, v. 132, p. 489-507.

Duncan, R.A., Larsen, H.C., Allan, J.F., et al. , 1996, Proceedings of the Ocean Drilling Program, Initial Reports.

Eccles, J.D., White, R.S., Christie, P.A.F., and Roberts, A.W., 2009, Insight into sub-basalt lithology from wide-angle converted shear wave analysis., in Varming, T., and Ziska, H., eds., Faroe Islands Exploration Conference: Proceedings of the 2nd Conference, Annales Societatis Scientarium Faroensis, supplementum, Volume 50, p. 43-60.

Eldholm, O., Thiede, J., Taylor, E., and Shipboard Scientific Party, 1987, Proceedings of the Ocean Drilling Program, Initial Reports, College Station, TX (Ocean Drilling Program).

Eldholm, O., and Grue, K., 1994, North Atlantic volcanic margins: Dimensions and production rates: Journal of Geophysical Research, v. 99, p. 2955-2968.

Ellis, D., Bell, B.R., Jolley, D.W., and O'Callaghan, M., 2002, The stratigraphy, environment of eruption and age of the Faroes Lava Group, NE Atlantic Ocean, in Jolley, D.W., and Bell, B.R., eds., The North Atlantic Igneous Province: Stratigraphy, Tectonic, Volcanic and Magmatic Processes, Volume 197, Geological Society, London, Special Publications, p. 253-269.

Enge, H.D., Buckley, S.J., Rotevatn, A., and Howell, J.A., 2007, From outcrop to reservoir simulation model: Workflow and procedures: Geosphere, v. 3, p. 469.

England, R.W., McBride, J.H., and Hobbs, R.W., 2005, The role of Mesozoic rifting in the opening of the NE Atlantic: evidence from deep seismic profiling across the Faroe-Shetland Trough: Journal of the Geological Society, v. 162, p. 661-673.

Fitzgibbon, A.W., and Zisserman, A., 1998, Automatic Camera Recovery for Closed or Open Image Sequences, Proceedings of the European Conference on Computer Vision, p. 311-326.

Freedman, D., and Diaconis, P., 1981, On the histogram as a density estimator: L2 theory: Probability Theory and Related Fields, v. 57, p. 453-476.

Frenje, L., 2000, Scattering of Seismic Waves in Random Velocity Models [PhD thesis], Uppsala University.

Frenje, L., and Juhlin, C., 1998, Scattering of seismic waves simulated by finite difference modelling in random media: application to the Gravberg-1 well, Sweden: Tectonophysics, v. 293, p. 61-68.

Fuchs, K., and Miller, G., 1971, Computation of synthetic seismograms with the reflectivity method and comparison with observations: Geophysical Journal of the Royal Astronomical Society, v. 23, p. 417-433.

Gaich, A., Pötsch, M., and Schubert, W., 2006, Basics, principles and application of 3D imaging systems with conventional and high-resolution cameras, in Tonon, F., and Kottenstette, J., eds., Laser and Photogrammetric Methods for Rock Face Characterization, p. 33-48.

Gallagher, J.W., and Dromgoole, P.W., 2008, Seeing below the basalt-offshore Faroes: Geophysical Prospecting, v. 56, p. 33-45.

Garcia, M.O., Haskins, E.H., Stolper, E.M., and Baker, M., 2007, Stratigraphy of the Hawai‘i Scientific Drilling Project core (HSDP2): Anatomy of a Hawaiian shield volcano: Geochemistry, Geophysics, Geosystems, v. 8, p. doi:10.1029/2006GC001379.

Goff, J.A., and Jordan, T.H., 1988, Stochastic modeling of seafloor morphology - inversion of sea beam data for 2nd-order statistics: Journal of Geophysical Research-Solid Earth and Planets, v. 93, p. 13589-13608.

Greene, A.R., Scoates, J.S., Weis, D., Nixon, G.T., and Kieffer, B., 2009, Melting history and magmatic evolution of basalts and picrites from the accreted Wrangellia oceanic plateau, Vancouver Island, Canada: Journal of Petrology, v. 50, p. 467-505.

Gregg, T.K.P., and Fink, J.H., 2000, A laboratory investigation into the effects of slope on lava flow morphology: Journal of Volcanology and Geothermal Research, v. 96, p. 145-159.

Guilbaud, M., Self, S., Thordarson, T., and Blake, S., 2005, Morphology, surface structures, and emplacement of lavas produced by Laki, AD 1783-1784: Special paper- Geological Society of America, v. 396, p. 81.

Hald, N., and Waagstein, R., 1984, Lithology and chemistry of a 2-km sequence of Lower Tertiary tholeiitic lavas drilled on Suðuroy, Faeroe Islands (Lopra-1), in Berthelsen, O., Noe-Nygaard, A., and Rasmussen, J., eds., The Deep Drilling Project 1980-1981 in the Faeroe Islands. Annales Societatis Scientiarum Faeroensis, Supplementum, Volume IX, p. 15-38.

Hall, A., 1987, Igneous Petrology, Longman Scientific & Technical.

Harris, A.J.L., Dehn, J., and Calvari, S., 2007, Lava effusion rate definition and measurement: a review: Bulletin of Volcanology, v. 70, p. 1-22.

Hartley, R., and Zisserman, A., 2004, Multiple view geometry in computer vision, 2nd Edition, Cambridge University Press.

Helland-Hansen, D., 2009, Rosebank - Challenges to development from a subsurface perspective, in Varming, T., and Ziska, H., eds., Faroe Islands Exploration Conference: Proceedings of the 2nd Conference, Annales Societatis Scientarium Faroensis, supplementum, Volume 50, p. 241-245.

Helm-Clark, C.M., Rodgers, D.W., and Smith, R.P., 2004, Borehole geophysical techniques to define stratigraphy, alteration and aquifers in basalt: Journal of Applied Geophysics, v. 55, p. 3-38.

Hobbs, R.W., Flecha, I., Carbonell, R., and Pearse, S., 2009, Does size matter?, in Varming, T., and Ziska, H., eds., Faroe Islands Exploration Conference: Proceedings of the 2nd Conference, Annales Societatis Scientarium Faroensis, supplementum, Volume 50, p. 333-345.

Hodgetts, D., 2009, LiDAR in the Environmental Sciences: Geological Applications, in Heritage, G., and Large, A., eds., Laser Scanning for the Environmental Sciences, Blackwell, p. 165-179.

Holliger, K., 1996, Upper-crustal seismic velocity heterogeneity as derived from a variety of P-wave sonic logs: Geophysical Journal International, v. 125, p. 813-829.

Huang, J., and Turcotte, D.L., 1989, Fractal Mapping of Digitized Images: Application to the Topography of Arizona and Comparisons With Synthetic Images: J. Geophys. Res., v. 94, p. 7491-7495.

Izenman, A.J., 1991, Recent developments in nonparametric density estimation: Journal of the American Statistical Association, v. 86, p. 205-224.

Kennett, B.L.N., 1983, Seismic wave propogation in stratified media, Cambridge University Press.

Japsen, P., Andersen, C., Andersen, H.L., Andersen, M.S., Boldreel, L.O., Mavko, G., Mohammed, N.G., Pedersen, J.M., Petersen, U.K., and Rasmussen, R., 2005, Preliminary results from investigations of seismic and petrophysical properties of Faroes basalts in the SeiFaBa project, in Doré, A.G., and Vining, B.A., eds., Petroleum Geology: North-West Europe and Global Perspectives - Proceedings of the 6th Petroleum Geology Conference, p. 1461-1470.

Jerram, D.A., 2002, Volcanology and facies architecture of flood basalts, in Menzies, M.A., Klemperer, S.L., Ebinger, C.J., and Baker, J., eds., Volcanic rifted margins. Geological Society of America Special Paper, Volume 362, p. 119-132.

Jerram, D.A., Mountney, N., Holzforster, F., and Stollhofen, H., 1999, Internal stratigraphic relationships in the Etendeka Group in the Huab Basin, NW Namibia: understanding the onset of flood volcanism: Journal of Geodynamics, v. 28, p. 393-418.

Jerram, D.A., and Robbe, O., 2001, Building a 3-D geologic model of a Flood Basalt: an example from the Etendeka, NW Namibia: Electronic Geosciences, v. 6, p. 1.

Jerram, D.A., Single, R.T., Hobbs, R.W., and Nelson, C.E., 2009, Understanding the offshore flood basalt sequence using onshore volcanic facies analogues: an example from the Faroe-Shetland basin: Geological Magazine, p. doi:10.1017/S0016756809005974.

Jerram, D.A., and Smith, S.A.F., 2010, How to build a 3D volcano: Geoscientist, v. February 2010.

Jerram, D.A., and Widdowson, M., 2005, The anatomy of Continental Flood Basalt Provinces: geological constraints on the processes and products of flood volcanism: Lithos, v. 79, p. 385-405.

Kattenhorn, S.A., and Schaefer, C.J., 2008, Thermal-mechanical modeling of cooling history and fracture development in inflationary basalt lava flows: Journal of Volcanology and Geothermal Research, v. 170, p. 181-197.

Kearey, P., Brooks, M., and Hill, I., 2002, An Introduction to Geophysical Exploration: Oxford, Blackwell Science Publications.

Kessler, H., Mathers, S., and Sobisch, H.G., 2009, The capture and dissemination of integrated 3D geospatial knowledge at the British Geological Survey using GSI3D software and methodology: Computers & Geosciences, v. 35, p. 1311-1321.

Keszthelyi, L., 2002, Classification of the mafic lava flows from ODP Leg 183., in Frey, F.A., Coffin, M., Wallace, P., and Quilty, P., eds., Proceedings of the Ocean Drilling Program, Scientific Results, Volume 183

Keszthelyi, L., Thordarson, T., McEwen, A., Haack, H., Guilbaud, M.N., Self, S., and Rossi, M.J., 2004, Icelandic analogs to Martian flood lavas: Geochemistry Geophysics Geosystems, v. 5.

Kieffer, B., Arndt, N., Lapierre, H., Bastien, F., Bosch, D., Pecher, A., Yirgu, G., Ayalew, D., Weis, D., Jerram, D.A., Keller, F., and Meugniot, C., 2004, Flood and shield basalts from Ethiopia: Magmas from the African superswell: Journal of Petrology, v. 45, p. 793-834.

Kumar, D., Bastia, R., and Guha, D., 2004, Prospect hunting below Deccan basalt: imaging challenges and solutions: First Break, v. 22, p. 35-39.

Labourdette, R., and Jones, R.R., 2007, Characterization of fluvial architectural elements using a three-dimensional outcrop data set: Escanilla braided system, South-Central Pyrenees, Spain: Geosphere, v. 3, p. 422-434.

Laier, T., Nycroft, H.P., Jørgensen, O., and Isaksen, G.H., 1997, Hydrocarbon traces in the Tertiary basalts of the Faeroe Islands: Marine and Petroleum Geology, v. 14, p. 257-266.

Larsen, H.C., Saunders, A. D., Clift, P.D. and Shipboard Scientific Party, 1994, Proceedings of the Ocean Drilling Program, Initial Reports, College Station, TX (Ocean Drilling Program).

Leathard, M., McHugo, S., and Hoare, R., 2009, Imaging Below Faroese Basalts Using Over/under Acquisition., in Varming, T., and Ziska, H., eds., Faroe Islands Exploration Conference: Proceedings of the 2nd Conference, Annales Societatis Scientarium Faroensis, supplementum, Volume 50, p. 61-66.

Lelliott, M.R., Bridge, D., Kessler, H., Price, S.J., and Seymour, K.J., 2006, The application of 3D geological modelling to aquifer recharge assessments in an urban environment: Quarterly Journal of Engineering Geology & Hydrogeology, v. 39, p. 293.

Li, X.R., 1999, Probability, random signals and statistics, CRC Press.

Maresh, J., 2004, The Seismic Expression of Paleogene Basalts on the Atlantic Margin [PhD thesis], Cambridge University.

Maresh, J., and White, R.S., 2005, Seeing through a glass, darkly: strategies for imaging through basalt: First Break, v. 23, p. 27-33.

Maresh, J., White, R.S., Hobbs, R.W., and Smallwood, J.R., 2006, Seismic attenuation of Atlantic margin basalts: Observations and modeling: Geophysics, v. 71, p. B211-B221.

Martini, F., and Bean, C.J., 2002, Application of pre-stack wave equation datuming to remove interface scattering in sub-basalt imaging: First Break, v. 20, p. 395-403.

Martini, F., Hobbs, R.W., Bean, C.J., and Single, R., 2005, A complex 3-D volume for subbasalt imaging: First Break, v. 23, p. 41–51.

Mathers, S., and Kessler, H., 2008, GSI3D: the software and methodology to build systematic near-surface 3-D geological models - Version 2.6., British Geological Survey, (OR/08/064) 130pp.

McCaffrey, K.J.W., Feely, M., Hennessy, R., and Thompson, J., 2008, Visualization of folding in marble outcrops, Connemara, western Ireland: An application of virtual outcrop technology: Geosphere, v. 4, p. 588-599.

McCaffrey, K.J.W., Jones, R.R., Holdsworth, R.E., Wilson, R.W., Clegg, P., Imber, J., Holliman, N., and Trinks, I., 2005, Unlocking the spatial dimension: digital technologies and the future of geoscience fieldwork: Journal of the Geological Society, v. 162, p. 927-938.

Menzies, M.A., Klemperer, S.L., Ebinger, C.J., and Baker, J., 2002, Characteristics of volcanic rifted margins, in Menzies, M.A., Klemperer, S.L., Ebinger, C.J., and Baker, J., eds., Volcanic Rifted Margins, Volume 362, Geological Society of America Special Paper, p. 1-14.

Merritt, J., Monaghan, A., Entwisle, D., Hughes, A., Campbell, D., and Browne, M., 2007, 3D attributed models for addressing environmental and engineering geoscience problems in areas of urban regeneration: a case study in Glasgow, UK: First Break, p. 79-84.

Miyamoto, H., and Sasaki, S., 1998, Numerical simulations of flood basalt lava flows: Roles of parameters on lava flow morphologies: Journal of Geophysical Research, v. 103, p. 27489-27502.

Naylor, P.H., Bell, B.R., Jolley, D.W., Durnall, P., and Fredsted, R., 1999, Palaeogene magmatism in the Faeroe-Shetland Basin: influences on uplift history and sedimentation, in Fleet, A.J., and Boldy, S.A.R., eds., Petroleum Geology of Northwest Europe: Proceedings of the 5th Conference., p. 545–558.

Oppenheimer, C., and Francis, P., 1998, Implications of longeval lava lakes for geomorphological and plutonic processes at Erta 'Ale volcano, Afar: Journal of Volcanology and Geothermal Research, v. 80, p. 101-111.

Passey, S.R., 2004, The Volcanic and Sedimentary Evolution of the Faroe Plateau Lava Group, Faroe Islands and Faroe-Shetland Basin, NE Atlantic [PhD thesis], University of Glasgow.

—, 2009, Recognition of a faulted basalt lava flow sequence through the correlation of stratigraphic marker units, Skopunarfjørður, Faroe Islands, in Varming, T., and Ziska, H., eds., Faroe Islands Exploration Conference: Proceedings of the 2nd Conference, Annales Societatis Scientarium Faroensis, supplementum, Volume 50, p. 174-204.

Passey, S.R., and Bell, B.R., 2007, Morphologies and emplacement mechanisms of the lava flows of the Faroe Islands Basalt Group, Faroe Islands, NE Atlantic Ocean: Bulletin of Volcanology, v. 70, p. 139-156.

Planke, S., 1994, Geophysical response of flood basalts from analysis of wire line logs: Ocean Drilling Program Site 642, Vøring Volcanic Margin: Journal of Geophysical Research-Solid Earth, v. 99, p. 9279-9296.

Planke, S., Alvestad, E., and Skogseid, J., 1999, Seismic characteristics of basaltic extrusive and intrusive rocks: The Leading Edge, v. 18, p. 342-348.

Planke, S., Symonds, P.A., Alvestad, E., and Skogseid, J., 2000, Seismic volcanostratigraphy of large-volume basaltic extrusive complexes on rifted margins: Journal of Geophysical Research-Solid Earth, v. 105, p. 19335-19351.

Planke, S., Rasmussen, T., Rey, S.S., and Myklebust, R., 2005, Seismic characteristics and distribution of volcanic intrusions and hydrothermal vent complexes in the Vøring and Møre basins, *in* Doré, A.G., and Vining, B.A., eds., Petroleum Geology: North-West Europe and Global Perspectives - Proceedings of the 6th Petroleum Geology Conference, p. 833–844.

Rasmussen, J., and Noe-Nygaard, A., 1970, Geology of the Faeroe Islands (Pre-Quaternary): Copenhagen, Geological Survey of Denmark.

Reading, H.G., 1986, Sedimentary environments and facies: Oxford, Blackwell Scientific Publication.

Rider, M., 1996, The Geological Interpretation of Wireline Logs, Whittles, 280 p.

Roberts, A.W., White, R.S., and Christie, P.A.F., 2009, Imaging igneous rocks on the North Atlantic rifted continental margin: Geophysical Journal International, v. 179, p. 1024-1038.

Rogers, C.D.F., Chapman, D.N., Entwisle, D., Jones, L., Kessler, H., Metje, N., Mica, L., Morey, M., Pospisil, P., Price, S., Raclavsky, J., Raines, M., Scott, H., and Thomas, A.M., 2009, Predictive mapping of soil geophysical properties for GPR utility location surveys, 5th International Workshop on

Advanced Ground Penetrating Radar, Granada, Spain, 27-29 May 2009. 60-67. (Unpublished). http://nora.nerc.ac.uk/7898/

Rotevatn, A., Buckley, S.J., Howell, J.A., and Fossen, H., 2009, Overlapping faults and their effect on fluid flow in different reservoir types: A LIDAR-based outcrop modeling and flow simulation study: AAPG Bulletin, v. 93, p. 407-427.

Royer, J.J., 2004, 3D Modeling and Visualization, 9th International CODATA Conference: Data Visualization - Earth and Geo Science: Berlin.

Royse, K.R., Reeves, H.J., and Gibson, A.R., 2008, The modelling and visualization of digital geoscientific data as a communication aid to land-use planning in the urban environment: an example from the Thames Gateway: Geological Society, London, Special Publications, v. 305, p. 89-106.

Sain, K., Zelt, C.A., and Reddy, P.R., 2002, Imaging of subvolcanic Mesozoics in the Saurashtra peninsula of India using traveltime inversion of wide-angle seismic data: Geophysical Journal International, v. 150, p. 820-826.

Saupe, D., 1988, Algorithms for random fractals, in Peitgen, H., and Saupe, D., eds., The science of fractal images: New York, Springer-Verlag.

Self, S., Jay, A.E., Widdowson, M., and Keszthelyi, L.P., 2008, Correlation of the Deccan and Rajahmundry Trap lavas: Are these the longest and largest lava flows on Earth?: Journal of Volcanology and Geothermal Research, v. 172, p. 3-19.

Self, S., Keszthelyi, L., and Thordarson, T., 1998, The importance of pahoehoe: Annual Review of Earth and Planetary Sciences, v. 26, p. 81-110.

Self, S., Thordarson, T., and Keszthelyi, L., 1997, Emplacement of continental flood basalt lava flows, in Mahoney, J.J., and Coffin, M.F., eds., Large Igneous Provinces: Continental, Oceanic and Planetary Flood Volcanism, Volume 100, American Geophysical Union Geophysical Monograph, p. 381-410.

Self, S., Thordarson, T., Keszthelyi, L., Walker, G.P.L., Hon, K., Murphy, M.T., Long, P., and Finnemore, S., 1996, A new model for the emplacement of

Columbia River Basalts as large, inflated pahoehoe lava flow fields: Geophysical Research Letters, v. 23, p. 2689-2692.

Self, S., Widdowson, M., Thordarson, T., and Jay, A.E., 2006, Volatile fluxes during flood basalt eruptions and potential effects on the global environment: A Deccan perspective: Earth and Planetary Science Letters, v. 248, p. 518-532.

Shaw, F., Worthington, M.H., White, R.S., Andersen, M.S., and Petersen, U.K., 2008, Seismic attenuation in Faroe Islands basalts: Geophysical Prospecting, v. 56, p. 5-20.

Single, R.T., 2004, The facies architecture of large igneous provinces: an integrated geological and geophysical approach to the characterisation of volcanic successions in 3-D. [PhD thesis], Durham University.

Single, R.T., and Jerram, D.A., 2004, The 3D facies architecture of flood basalt provinces and their internal heterogeneity: examples from the Palaeogene Skye Lava Field.: Journal of the Geological Society, v. 161, p. 911-926.

Smallwood, J.R., and Maresh, J., 2002, The properties, morphology and distribution of igneous sills: modelling, borehole data and 3D seismic from the Faroe-Shetland area, in Jolley, D.W., and Bell, B.R., eds., The North Atlantic Igneous Province: Stratigraphy, Tectonic, Volcanic and Magmatic Processes, Volume 197, Geological Society, London, Special Publications, p. 271-306.

Thomson, K., 2005, Volcanic features of the North Rockall Trough: application of visualisation techniques on 3D seismic reflection data: Bulletin of Volcanology, v. 67, p. 116-128.

Thomson, K., and Schofield, N., 2008, Lithological and structural controls on the emplacement and morphology of sills in sedimentary basins: Geological Society, London, Special Publications, v. 302, p. 31-44.

Thordarson, T., and Hoskuldsson, A., 2002, Iceland (Classic Geology in Europe, 3): Terra, Harpenden.

Thordarson, T., and Self, S., 1993, The Laki (Skaftar-Fires) and Grimsvotn eruptions in 1783-1785: Bulletin of Volcanology, v. 55, p. 233-263.

—, 1998, The Roza Member, Columbia River Basalt Group- A gigantic pahoehoe lava flow field formed by endogenous processes?: Journal of Geophysical Research, v. 103, p. 27411-27446.

Turcotte, D.L., 1989, Fractals in Geology and Geophysics: Pure and Applied Geophysics, v. 131, p. 171-196.

Waagstein, R., 1988, Structure, composition and age of the Faeroe basalt plateau, in Morton, A.C., and Parson, L.M., eds., Early Tertiary Volcanism and the Opening of the NE Atlantic. Geological Society, London, Special Publications, Volume 39, p. 225-238.

Walia, R.K., and Bull, J.M., 1997, Modelling rough interfaces on seismic reflection profiles - The application of fractal concepts: Geophysical Research Letters, v. 24, p. 2067-2070.

Walker, G.P.L., 1971, Compound and simple lava flows and flood basalts: Bulletin of Volcanology, v. 35, p. 579-590.

Welch, P., 1967, The use of fast Fourier transform for the estimation of power spectra: a method based on time averaging over short, modified periodograms: IEEE Transactions on Audio and Electroacoustics, v. 15, p. 70-73.

Wessel, P., and Smith, W.H.F., 2009, The Generic Mapping Tools (GMT) version 4.5.0 Technical Reference & Cookbook, SOEST/NOAA, http://gmt.soest.hawaii.edu/.

White, J.C., 2009, Development and application of the phase-screen seismic modelling code [Unpublished PhD thesis], Durham University.

White, R.S., and McKenzie, D., 1989, Mantle plumes and flood basalts: Journal of Geophysical Research, v. 100, p. 17543-17585.

White, R.S., Spitzer, R., Christie, P.A.F., Roberts, A., Lunnon, Z., Maresh, J., and Group, i.W., 2005, Seismic imaging through basalt flows on the Faroes Shelf, in Ziska, H., Varming, T., and Bloch, D., eds., Proceedings of the 1st Faroe Islands Exploration Conference, Volume Supplementum 43: Tórshavn,

Annales Societatis Scientarium Faeroensis (Faroese Society of Science and Humanities), p. 11-31.

Wild, A.J., Hobbs, R.W., and Frenje, L., 2000, Modelling complex media: an introduction to the phase-screen method: Physics of the Earth and Planetary Interiors, v. 120, p. 219-225.

Wilson, P., Hodgetts, D., Rarity, F., Gawthorpe, R.L., and Sharp, I.R., 2009, Structural geology and 4D evolution of a half-graben: New digital outcrop modelling techniques applied to the Nukhul half-graben, Suez rift, Egypt: Journal of Structural Geology, v. 31, p. 328-345.

Wu, R.S., and Aki, K., 1988, Introduction: Seismic wave scattering in three-dimensionally heterogeneous earth: Pure and Applied Geophysics, v. 128, p. 1-6.

Young, P., and Wadge, G., 1990, FLOWFRONT: simulation of a lava flow: Computers & Geosciences, v. 16, p. 1171-1191.

Ziolkowski, A., Hanssen, P., Gatliff, R., Jakubowicz, H., Dobson, A., Hampson, G., Li, X.Y., and Liu, E., 2003, Use of low frequencies for sub-basalt imaging: Geophysical Prospecting, v. 51, p. 169-182.

Index of Appendices

APPENDIX 1: PAPERS PUBLISHED IN SUPPORT OF THE THESIS 181

NELSON ET AL., GEOSPHERE 181

NELSON ET AL., 2009, PETROLEUM GEOSCIENCE 203

NELSON ET AL., 2009, FIEC PROCEEDINGS 215

APPENDIX 2: BOREHOLE INTERPRETATIONS 235

LOPRA-1/1A 236

GLYVURSNES-1 246

VESTMANNA-1 252

ODP HOLE 642E 258

ODP HOLE 917A 264

WELL 164/07-1 267

APPENDIX 3: WORKFLOWS 271

3.1 HOW TO SCAN WITH THE RIEGL Z420I LASER SCANNER 271

3.1.1 Setting up the scanner 271

3.1.2 Positioning the reflectors 271

3.1.3 Scanning 271

3.1.4 Tilting the scanner 272

3.1.5 Improving precision 272

3.2 DATA PROCESSING 273

3.2.1 Processing scan sequences 273

3.2.2 Merging scans 273

3.2.3 Tidying the data 274

3.3 HOW TO PICK LINES IN A DRAWING PACKAGE AND USE THEM IN RISCAN PRO 275

3.4 SURFACE BUILDING USING GSI3D 278

3.5 GMT WORKFLOW FOR SPECTRAL ANALYSIS 279

3.6 GOCAD WORKFLOWS FOR CHAPTER 7 280

3.6.1 Method for tabular model 280

3.6.2 Method for adding random noise 284

APPENDIX 4: LIST OF FILES ON DVD 286

Appendix 1: Papers published in support of the thesis

Reconstructing flood basalt lava flows in 3D using terrestrial laser scanning

Accepted for publication, Geosphere, June 2010

Catherine E. Nelson[1], Dougal A. Jerram[1], Richard W. Hobbs[1], Ricky Terrington[2], Holger Kessler[2]

[1]Department of Earth Sciences, Durham University, South Road, Durham, DH1 3LE, UK

[2]British Geological Survey, Keyworth, Nottingham, NG12 5GG

ABSTRACT

We present a new method for reconstructing flood basalt lava flows from outcrop data, using terrestrial laser scanning (TLS) to generate 3D models. Case studies are presented from the Faroe Islands and the Isle of Skye (UK), both part of the North Atlantic Igneous Province (NAIP). These were analysed to pick out lava flow tops and bases, as well as dykes, lava tubes and sedimentary layers. 3D surfaces were then generated using the GSI3D software, a modelling package developed by the British Geological Survey (BGS) and INSIGHT GmbH, and 3D geological models constructed. Finally, the models were interrogated to give data on flow thickness and crust to core ratio.

The aim of this research is to obtain quantitative data on the internal heterogeneity of a sequence of flood basalt lava flows, and to provide high resolution information about flow geometries and volcanic facies variations in 3D. Lava flow sequences display complex stacking patterns, and these are difficult to understand from photos or outcrop observations. Laser scanning allows us to study inaccessible outcrops, while avoiding the perspective distortion in conventional photography. The data from this study will form part of larger models of flood basalt provinces, which will be used to improve seismic imaging in areas of basalt cover, and aid our understanding of facies architecture in flood basalts.

INTRODUCTION

Flood basalt volcanology has developed significantly over recent years, with studies moving from more traditional geochemically-driven research to the development and understanding of emplacement models (e.g. Self et al., 1997), studies looking at the facies architecture of the volcanic units (e.g. Passey and Jolley, 2009; Passey and Bell, 2007; Single and Jerram, 2004), and the types and distributions of volcanic units in offshore environments (e.g. Planke et al., 2000; Jerram et al., 2009). Much of this research has been driven by a realization that the internal architecture of flood basalt provinces is not a simple layer-cake sequence (Jerram and Widdowson, 2005). Moreover, the internal architecture is heterogeneous and complex, with a variety of different stacking patterns. These can be observed at a number of scales, and vary

both laterally and vertically. The aim of this work is to identify and quantify the 3D facies variations present in flood basalt outcrops, and this is facilitated by the use of terrestrial laser scanning.

Recent advances in mapping technology have permitted the construction of3D "virtual outcrops" (McCaffrey et al., 2005; Xu et al., 2000), allowing accurate measurements of an outcrop in a digital environment. These studies use high resolution laser scanning to capture the geological landscape in a format that can be manipulated in 3D, in order to interpret the internal facies and facies variations within the rocks. The term "virtual outcrop" has come to mean a 3D triangulated mesh with a draped photograph, providing an easily interpreted representation of the original outcrop. Such 3D geological models are used in areas such as fluid flow modeling (e.g. Rotevatn et al., 2009) and reservoir modeling (Pringle et al., 2004). Until recently much of the work developing and using virtual outcrops has been aimed at sedimentary problems (e.g. Bellian et al. 2005; Labourdette and Jones, 2007), and structural problems (Wilson et al., 2009; McCaffrey et al., 2008), with few examples in the field of volcanology. Previous studies have documented in detail the workflow used to capture and process TLS data (e.g. Hodgetts, 2009; Buckley et al. 2008; Enge et al. 2007). Our workflow mostly follows that of previous studies with slight site-specific variations highlighted in the text. Strictly, our models are not virtual outcrops in the sense that no triangulated surfaces are made, but they represent the outcrop in a digital format allowing interpretation.

In this study, we construct the first 3D point clouds of flood basalt lava flows from terrestrial laser scanning data, and use the GSI3D software (Kessler et al., 2009) developed by the British Geological Survey (BGS) and INSIGHT GmbH to construct 3D geological models of lava flows. This allows the accurate measurement of the size and shape of multiple flows, and the reconstruction of flow tops and flow bases between outcrops. Locations of the case studies are shown in Figure1. We also discuss the potential of this approach for further volcanological studies.

3D geological models and facies analysis

This study is motivated by a need for more accurate characterization of flood basalt lava flows in 3D. Hydrocarbon exploration is increasingly focusing on volcanic rifted margins associated with flood volcanism. In the North Atlantic, many potentially prospective sedimentary basins extend under areas of flood basalt lava flows (e.g. the Faroe-Shetland Basin, Naylor et al., 1999) where seismic imaging provides poor results compared to most other rock types. Much research has focused on optimizing exploration strategies to improve seismic imaging, using methods such as collecting wide-angle or long-offset seismic data, and these have met with some success (e.g. Roberts et al., 2005).

However, seismic imaging is still hampered by the very heterogeneous nature of a basalt sequence, and this is one of the largest challenges to successful imaging. The large difference in rock properties (P-wave velocity or V_p, density and so on) between the core and crust of a basalt lava flow leads to a very variable velocity profile. This causes scattering and attenuation of the seismic wave, especially at high frequencies, and as a result little energy is returned from below a basalt sequence. Images of sedimentary sequences below the basalt are therefore poor.

The work presented here allows quantification of this heterogeneity by creating detailed 3D geological models which can then be populated accurately with rock properties such as V_p, density or acoustic impedance. The shape, size and internal structures within flood lavas also provide important information for volcanological research (e.g. Single and Jerram 2004).

Although outcrops provide high resolution data, the scale at which they are exposed is typically in the region of hundreds of metres. Therefore to make outcrop scale observations and models applicable to an entire province (that may be hundreds of kilometres in extent) the use of facies analysis can be employed. A number of volcanic facies have been identified that are found in many flood basalt provinces (Jerram, 2002), and each facies displays common physical characteristics. The two major facies types encountered in this study are compound-braided lava flows and tabular-classic lava flows, both of which occur in large volumes in the NAIP. Compound-braided lava flows are thin (<3m), anastomosing flows of limited lateral extent. Tabular-classic flows are much thicker (up to several tens of metres) and may extend for 10s to 100s of kilometres. They have a simple internal structure of a massive flow core and a vesicular, fractured crust, as shown in Figure 2. Tabular-classic and compound-braided flows are often found close together, either vertically or laterally, probably related to changes in lava eruption rates and volumes. Other facies types include intrusions, ponded flows and volcaniclastic sediments, all of which are present throughout the NAIP. Volcanic facies are described in more detail in Nelson et al. (2009b) and Jerram (2002).

Case studies

In order to test the applicability of TLS to the study of flood basalt facies, and the potential for successful reconstruction of lava sequences, we selected two case studies. Both are located within the North Atlantic Igneous Province, and are taken to be representative of compound-braided flows both onshore and offshore in this province. It was important that the case study areas met certain criteria to make a successful 3D model, including:

- Detailed facies architecture in 3D.
- Composed of typical flood basalt facies.
- Being of a scale that our equipment could cope with, and having good accessibility to enable the heavy laser scanning equipment to be relatively easily deployed.

The first case study, located near Ljosa, Eysturoy, Faroe Islands, is a quarried outcrop approximately 75m by 20m. Its location is shown in Figure 1. It is an extremely well-exposed section through compound-braided lava flows, comprising two flows which extend across the entire outcrop and several more which pinch out within the exposure. It is not a true 3D exposure as the two faces are at right angles, but a 3D model can be built by extending the interpretations laterally. The relative simplicity of the flow geometries and the small number of flows made this an excellent case study for developing the methods used in this work.

The second case study is located in Talisker Bay, Skye, Scotland (Figure 1). Here, two sea stacks and a cliff section display well-exposed sections through a lava sequence. This location had previously been mapped in detail by Single (2004)

which aided our interpretations (also see Single and Jerram 2004). We selected this location because the sea stacks and the cliff section contain exposures of the same lava flows, and it is therefore possible to correlate between them. This allowed us to build a comprehensive 3D geological model once the data had been collected. The tidal nature of this location did, unfortunately, limit the amount of data we were able to collect, as well as posing a logistical problem.

The GSI3D software

GSI3D (Geological Surveying and Investigation in 3 Dimensions) has been developed by the BGS and INSIGHT GmbH, and is now used extensively by the BGS for the construction of detailed 3D geological models. GSI3D uses cross-sections, mapped outlines and a digital terrain model to produce a solid model made up of triangulated objects. Its main function is to produce 3D geological models from existing geological maps and borehole data (e.g. Kessler et al., 2009). For example, detailed models of quaternary sediments have been constructed to give information on groundwater flow (Lelliott et al., 2006).

To produce a 3D geological model in GSI3D, the user must first construct cross-sections through the units of interest. Then, the outline extents must be defined in a map view. Once these have been defined, the software triangulates surfaces satisfying the cross-sections and map extents, and the DTM forms the top of the model. All these steps are fully controlled by the user, allowing the user to apply their geological knowledge to construct a realistic final model. This level of control makes the software potentially ideal for use with TLS data, and one of the additional goals of this study is to test the use of TLS data within the GSI3D environment. The process of constructing the models is described in detail below.

GEOLOGICAL SETTING

In this section, we briefly review the geological setting of the two case studies, putting them into their regional context. Both case studies are located within the North Atlantic Igneous Province (NAIP), a large igneous province with an approximate areal extent of $1.3x10^6 km^2$ (Eldholm and Grue, 1994). Map locations are shown in Figure 1. The NAIP consists of a variety of facies including flood basalt lava flows, thick hyaloclastite sequences, central volcanoes, sills and dykes. The majority of the flood basalt sequences were emplaced between 60.5Ma and 54.5Ma (Jolley and Bell, 2002), however subaerial volcanism continues in the North Atlantic to the present day in Iceland.

The Faroe Islands study area

The Faroe Islands are almost entirely formed of the Faroe Islands Basalt Group (FIBG), part of the NAIP, which was emplaced between approximately 60.6 and 57.5Ma (Ellis et al., 2002). The FIBG is subdivided into four main volcanic formations: from uppermost to lowest, the Enni, Malinstindur, Beinisvorð and Lopra formations (Passey and Jolley, 2009). The formations display a variety of facies: the Enni Formation contains tabular-classic and compound-braided lava flows; the Malinstindur Formation mainly contains compound-braided flows and the

Beinisvorð Formation is dominated by tabular-classic flows. The Lopra Formation is known only from the Lopra 1/1A borehole (Berthelsen, 1984; Chalmers and Waagstein, 2006) and is dominated by hyaloclastites. For a comprehensive description of the FIBG and a discussion of its emplacement mechanisms, see Passey and Bell (2007).

Our case study is located on the island of Eysturoy, within the Malinstindur formation. The quarry near Ljosa cuts through a sequence of thin (up to 3m) compound-braided basaltic lava flows, giving excellent exposure. The flow cores and crusts are easily identified, and the location is an excellent example of the complex flow architecture of the compound-braided facies.

Skye

The Isle of Skye, located off the west coast of Scotland, contains excellent exposures of flood basalt lava flows forming part of the NAIP. The Skye Lava Field covers much of the island, with the main sequence erupted between ~61-59 Ma, and in the west of Skye this can be divided into three sequences based on facies types (Single and Jerram, 2004). These are: lower compound-braided lavas; transitional lavas; and upper tabular lavas.

The Talisker Bay case study is located in the Minginish district on the west coast of Skye, within the lower compound-braided lavas. This area has been mapped in detail by Single (2004) and it is also the basis for a fine-scale facies classification scheme for flood basalt lava flows (Single and Jerram, 2004). In this study, we incorporate these detailed observations into a 3D reconstruction.

DATA COLLECTION AND PROCESSING

Figure 3 summarises the steps followed to produce the 3D geological models. Data collection is followed by interpretation, surface construction and finally model interrogation. The workflow described below has become standard over recent years, and is described in more detail in Hodgetts (2009), Buckley et al. (2008) and Enge et al. (2007).

TLS data collection

Terrestrial laser scanning has become increasingly popular amongst geologists, as it allows 3D data to be captured which can be analysed away from a field situation. 3D point clouds thus obtained can be analysed to provide quantitative structural or geological data (e.g. McCaffrey et al. 2005, 2008). The laser scanner measures the XYZ coordinates of points on the outcrop at specified intervals. These points can then be coloured from digital photos to give an accurate representation of the outcrop, which can then be viewed from any angle and features on it can be measured. This is particularly useful for inaccessible parts of outcrops. Multiple scans from different angles are obtained to minimise shadow areas where parts of the outcrop hide other areas from the scanner viewpoint. Reflectors are used to provide common points of reference between scan and photo, and between scans.

Data for this study were collected during fieldwork in June 2007 (Faroe Islands) and September 2008 (Skye) using a Riegl LMS-Z420i terrestrial laser scanner combined with a calibrated Nikon D70 digital camera. The Z420i equipment is capable of an accuracy of up to 10mm and a precision of up to 4mm (http://www.riegl.com). The scanning range can be up to 1000m for highly reflective objects, however the maximum range falls as the reflectivity of the target decreases. We found that the dark colour of weathered basalt and the often wet nature of the outcrops reduced the range to less than 200m, suggesting the reflectivity is likely to be 10% or less based on data from http://www.riegl.com. The camera has a resolution of 6MP, and lenses with a variety of focal lengths are available to produce the best possible picture.

Ljosa quarry

At this location, three scans were required to collect all the required data. The quarry is extremely well-exposed, and the surfaces are relatively smooth. This means there are few shadow areas to cause problems, and the three scans were required primarily to obtain good photos for interpretation. Figure 4 shows the quarry layout and the scan setup. The three scans collected a total of approximately 8,600,000 points, at an angular resolution of 0.03°, giving a spacing of approximately 10mm between points on the quarry wall. Points were duplicated between scans. A total of 60 digital photos were taken, at focal lengths of either 14mm or 50mm depending on the distance from the scanner to the quarry walls.

Talisker Bay

Five laser scans were acquired here, however many more could have been acquired to provide a more complete coverage of the outcrops. Unfortunately the other locations were inaccessible due to the tidal nature of the site. The five scans obtained provided a good coverage of the outcrops and allowed us to correlate flows between the outcrops. In total, approximately 10,020,000 points were collected at an angular resolution of 0.05-0.06°. 84 digital photos were taken, again using either the 14mm or 50mm lenses.

Data processing

The steps required to produce a coloured 3D point cloud are now well-documented (e.g. Hodgetts, 2009; Buckley et al., 2008) and are described only briefly here. Once the point clouds and digital photos were collected at each site, a common frame of reference was needed. This was provided by the reflectors, as shown in Figures 4 and 6. These were identified in both the scans and the photos, and an adjustment carried out to establish the relative locations of the scanner and camera, and the relative locations of the various scan positions. A common coordinate system was thus established for the whole project. The point clouds could then be coloured from the images, and the scans merged to give one point cloud, as shown in Figure 7.

The 3D point clouds at this stage are made up of millions of points, making it difficult for software to handle. Unwanted areas of the outcrop were removed to leave only the areas of interest. The data were then filtered using an Octree filter (e.g. McCaffrey et al., 2008) to leave around 10,000 points, suitable for importing into

GOCAD®. In the case of the Ljosa quarry data this was achieved by giving the resulting points a spacing of 20cm spacing; whereas the point spacing for the Talisker Bay data was 50cm.

BUILDING AND ANALYSING THE 3D MODELS

Picking key horizons

At this point, our workflow differs slightly from that of Buckley et al. (2008) and Enge et al. (2007). In their workflows, a triangulated mesh is formed from the point cloud, and the photographs are draped onto this. This allows detailed interpretation not possible on the point cloud itself, as the photograph is at a higher resolution than the point cloud. Enge et al. (2007) show the difficulty of making detailed interpretations directly onto the point cloud. The process of meshing the point data is extremely time-consuming, and becomes more so when the geometry of the site is complex. The Talisker Bay case study is extremely complex, and attempts to build a triangulated mesh were hampered by the high level of computing power required. Accordingly, a simpler method for interpreting the data was devised.

It was decided to draw interpretations directly onto the digital photographs, and then project the altered photographs onto the point cloud. The point clouds generated are at a resolution of around 50 points/metre, whereas the photographs have 300 or more pixels/metre, so much more detailed interpretation is possible. Lines drawn on the photograph had a width of approximately 10cm when projected onto the point cloud, covering 4 or 5 points. The lines from the photos are projected into the correct position on the point cloud, and can easily be seen, so 3D lines could be drawn directly onto the point cloud then exported. Figure 2 gives an example of the digital photo and its interpretation.

The purpose of our 3D geological models is to show the different volcanic facies present in the outcrops, and provide data on flow thicknesses and crust to core ratios. The high quality digital photographs, accompanied by detailed field observations, allowed us to identify flow tops, bases and crust/core boundaries, as well as dykes, sills, lava tubes and boles. The loss of 10cm of accuracy is acceptable in this situation, as very high accuracy is not required, but this workflow would not be suitable for other uses.

Extending the horizons laterally

The .dxf files produced in the previous step were imported into GOCAD®, and the fault modelling package used to produce rough surfaces. In the case of the Talisker data, flows from different outcrops had already been correlated, and their top surfaces were constructed using the interpreted lines as edges. Where each horizon only had one interpreted line, this was extended laterally by treating the line as a fault centre line. The triangulated surfaces were then exported to GSI3D. GSI3D, unlike GOCAD®, places no limitations on where surfaces are constructed. This allowed us to extend surfaces to where no data was available, and to use our geological experience to determine where the surfaces should go. While this introduced a much higher level of uncertainty, it allowed us to extend the surfaces

and construct a useful block model. The finished model of Ljosa quarry is shown in Figure 9. Lighter colours are flow crusts and darker colours are flow cores.

For the Talisker Bay case study, two final models were constructed. The first is a palaeoreconstruction of the lava flows between the sea stacks and cliff section, constructed as detailed above. The second uses a GOCAD® surface of the topography, generated from the filtered laser scan point cloud, to display only the present-day flows. The GOCAD® surface is shown in Figure 10. All overhanging areas have been replaced by vertical sections to make it compatible with the GSI3D software. The final models are shown in Figure 11. It has also been possible to include lava tubes, a sill and a dyke in this model, making it possible to determine what proportion of the total volume is made up of these features.

Interrogating the block models

The completed geological models can be analysed in a number of ways. Virtual boreholes and cross-sections can be obtained for any area of the model to give an idea of the heterogeneity, which is useful in showing how complex the stacking patterns of lava flows may be. An example of a synthetic borehole is given in Figure 12.

It is also easy to obtain volumes and map areas for each unit. While the volume is a function of the size of the model, and therefore not useful in determining the original flow volume, it can be used with the flow area to calculate an average thickness. We have calculated average flow thicknesses and crust to core ratios for the Ljosa quarry model, and these are given in Table 1. In the case of the Talisker Bay model, it was not possible to identify crusts for the majority of flows; however volumes and average thicknesses were calculated. These are given in Table 2. The use of these data is described in the next section.

DISCUSSION AND CONCLUSIONS

The 3D geological models presented here accurately capture the heterogeneity present in a complex sequence of compound-braided lava flows. The internal flow structure can be identified, and irregular features such as dykes, sills and lava tubes can be visualized. Quantitative data on lava flow thicknesses, volumes and crust to core ratios can be easily obtained from the final models, and virtual boreholes constructed in any location.

This work builds on previous detailed facies analysis of flood basalt sequences (e.g. Single & Jerram 2004; Passey and Bell 2007). The use of TLS technology and associated software packages provides many advantages over traditional “paper-based” methods, as summarised by Buckley et al. (2008). For our purposes, it is useful to capture 3D data quickly and accurately, allowing for lab-based analysis. Additionally, the level of detail and accuracy provided by TLS makes it possible to correlate lava flows between inaccessible parts of outcrops.

The workflow presented here provides a relatively simple way to construct 3D models, albeit with a slight loss in accuracy. It reduces the computer memory and processing power required compared to workflows such as that of Buckley et al. (2008). The loss of accuracy may make the workflow unsuitable for detailed structural analysis, but the interpretations have an uncertainty of around 10cm, making them suitable for facies analysis.

This study forms part of ongoing work to construct realistic geological and geophysical models of flood basalt provinces. The models generated in this study can be used to populate larger sequences where the distribution of such facies is known (e.g. Jerram et al., 2009). The fine-scale modelling is required to capture all the heterogeneity present in a flood basalt sequence, and the models also need to include lateral variations. Future work will also incorporate geophysical data from boreholes on the Faroe Islands, as well as data on lava flow surface roughness from other laser scans and 3D models of other facies types.

ACKNOWLEDGEMENTS

Nick Schofield and an anonymous reviewer are thanked for their thorough and constructive reviews, which resulted in substantial improvements to this manuscript. The authors would like to thank Richard Walker, Terry Spry, Mike Lewis and Jo Garland for valuable assistance with fieldwork. Charlotte Vye at the BGS is thanked for suggesting we use the GSI3D software. The Faroese authorities are thanked for not filling in Ljosa quarry until the day after we had collected the data. Research was supported by funding provided to DAJ by TOTAL GRC (while DAJ was the TOTAL lecturer at Durham University) and the EU 5th Framework Project SIMBA (CONTRACT N°: ENK6-CT-2000-00075).

REFERENCES

Bellian, J.A., Kerans, C., and Jennette, D.C., 2005, Digital Outcrop Models: Applications of Terrestrial Scanning Lidar Technology in Stratigraphic Modeling: Journal of Sedimentary Research, v. 75, p. 166-176.

Berthelsen, O., Noe-Nygaard, A. & Rasmussen, J. (eds), 1984, The deep drilling project 1980-1981 in the Faeroe Islands.: Annales Societatis Scientarium Faeroensis, Supplementum, v. IX, p. 158pp.

Buckley, S.J., Howell, J.A., Enge, H.D., and Kurz, T.H., 2008, Terrestrial laser scanning in geology: data acquisition, processing and accuracy considerations. Journal of the Geological Society, v. 165, p. 625-638.

Chalmers, J.A., and Waagstein, R., 2006, Scientific results from the deepened Lopra-1 borehole, Faroe Islands. Geological Survey of Denmark and Greenland Bulletin 9.

Eldholm, O., and Grue, K., 1994, North Atlantic volcanic margins: Dimensions and production rates: Journal of Geophysical Research, v. 99, p. 2955-2968.

Ellis, D., Bell, B.R., Jolley, D.W., and O'Callaghan, M., 2002, The stratigraphy, environment of eruption and age of the Faroes Lava Group, NE Atlantic Ocean, *in* Jolley, D.W., and Bell, B.R., eds., The North Atlantic Igneous Province: Stratigraphy, Tectonic, Volcanic and Magmatic Processes, Volume 197, Geological Society, London, Special Publications, p. 253-269.

Enge, H.D., Buckley, S.D., Rotevatn, A., and Howell, J., 2007. From outcrop to reservoir simulation model: Workflow and procedures: Geosphere, v. 3, p. 469-490.

Hodgetts, D., 2009, LiDAR in the environmental sciences: geological applications, *in* Heritage, G.L. and Large, A.R.G., eds., Laser Scanning for the Environmental Sciences: Chichester, United Kingdom, Wiley-Blackwell, p. 165-179.

Jerram, D.A., 2002, Volcanology and facies architecture of flood basalts, *in* Menzies, M.A., Klemperer, S.L., Ebinger, C.J., and Baker, J., eds., Volcanic rifted margins. Geological Society of America Special Paper, Volume 362, p. 119-132.

Jerram, D.A., Single, R.T., Hobbs, R.W., and Nelson, C.E., 2009, Understanding the offshore flood basalt sequence using onshore volcanic facies analogues: an example from the Faroe-Shetland basin: Geological Magazine, v. 146, p. 353-367.

Jerram, D.A., and Widdowson, M., 2005, The anatomy of Continental Flood Basalt Provinces: geological constraints on the processes and products of flood volcanism: Lithos, v. 79, p. 385-405.

Jolley, D.W., and Bell, B.R., 2002, The evolution of the North Atlantic Igneous Province and the opening of the NE Atlantic rift, *in* Jolley, D.W., and Bell, B.R., eds., The North Atlantic Igneous Province: Stratigraphy, Tectonic, Volcanic and Magmatic Processes: Geological Society of London Special Publications 197, p. 1-13.

Kessler, H., Mathers, S., and Sobisch, H.G., 2009, The capture and dissemination of integrated 3D geospatial knowledge at the British Geological Survey using GSI3D software and methodology: Computers & Geosciences, v. 35, p. 1311-1321.

Labourdette, R., and Jones, R.R., 2007, Characterization of fluvial architectural elements using a three-dimensional outcrop data set: Escanilla braided system, South-Central Pyrenees, Spain: Geosphere, v. 3, p. 422-434.

Lelliott, M., Bridge, D., Kessler, H., Price, S., and Seymour, K., 2006, The application of 3D geological modelling to aquifer recharge assessments in an urban environment: Quarterly Journal of Engineering Geology & Hydrogeology, v. 39, p. 293.

McCaffrey, K., Feely, M., Hennessy, R., and Thompson, J., 2008, Visualization of folding in marble outcrops, Connemara, western Ireland: An application of virtual outcrop technology: Geosphere, v. 4, p. 588.

McCaffrey, K.J.W., Jones, R.R., Holdsworth, R.E., Wilson, R.W., Clegg, P., Imber, J., Hollman, N., and Trinks, I., 2005, Unlocking the spatial dimension: digital technologies and the future of geoscience fieldwork: Journal of the Geological Society, v. 162, p. 927-938.

Naylor, P.H., Bell, B.R., Jolley, D.W., Durnall, P., and Fredsted, R., 1999, Palaeogene magmatism in the Faeroe-Shetland Basin: influences on uplift history and sedimentation, *in* Fleet, A.J., and Boldy, S.A.R., eds., Petroleum Geology of Northwest Europe: Proceedings of the 5th Conference., p. 545–558.

Nelson, C.E., Jerram, D.A., and Hobbs, R.W., 2009a, Flood basalt facies and borehole data: implications for prospectivity and volcanology in volcanic rifted margins: Petroleum Geoscience, v. 15, p.313-324.

Nelson, C.E., Jerram, D.A., Single, R.T., and Hobbs, R.W., 2009b, Understanding the facies architecture of flood basalts and volcanic rifted margins and its effect on geophysical properties., *in* Varming, T., and Ziska, H., eds., Faroe Islands Exploration Conference: Proceedings of the 2nd Conference, Annales Societatis Scientarium Faroensis, supplementum, Volume 48, p. 84-103.

Passey, S., and Jolley, D., 2009, A revised lithostratigraphic nomenclature for the Palaeogene Faroe Islands Basalt Group, NE Atlantic Ocean: Earth and Environmental Science Transactions of the Royal Society of Edinburgh, v. 99, p. 127-158.

Passey, S.R., and Bell, B.R., 2007, Morphologies and emplacement mechanisms of the lava flows of the Faroe Islands Basalt Group, Faroe Islands, NE Atlantic Ocean: Bulletin of Volcanology, v. 70, p. 139-156.

Planke, S., Symonds, P.A., Alvestad, E., and Skogseid, J., 2000, Seismic volcanostratigraphy of large-volume basaltic extrusive complexes on rifted margins: Journal of Geophysical Research-Solid Earth, v. 105, p. 19335-19351.

Pringle, J.K., Westerman, A.R., Clark, J.D., Drinkwater, N.J., and Gardiner, A.R., 2004, 3D high-resolution digital models of outcrop analogue study sites to constrain reservoir model uncertainty: an example from Alport Castles, Derbyshire, UK: Petroleum Geoscience, v. 10, p. 343-352.

Roberts, A.W., White, R.S., Lunnon, Z.C., Christie, P.A.F., Spitzer, R., and Team, i., 2005, Imaging magmatic rocks on the Faroes Margin, *in* Doré, A.G., and Vining, B.A., eds., Petroleum Geology: North-West Europe and Global Perspectives - Proceedings of the 6th Petroleum Geology Conference, p. 755-766.

Rotevatn, A., Buckley, S.J., Howell, J.A., and Fossen, H., 2009, Overlapping faults and their effect on fluid flow in different reservoir types: A LIDAR-based outcrop modeling and flow simulation study: AAPG Bulletin, v. 93, p. 407-427.

Self, S., Thordarson, T., and Keszthelyi, L., 1997, Emplacement of continental flood basalt lava flows, *in* Mahoney, J.J., and Coffin, M.F., eds., Large Igneous Provinces: Continental, Oceanic and Planetary Flood Volcanism, Volume 100, American Geophysical Union Geophysical Monograph, p. 381-410.

Single, R.T., 2004, The facies architecture of large igneous provinces: an integrated geological and geophysical approach to the characterisation of volcanic successions in 3-D. [PhD thesis], Durham University.

Single, R.T., and Jerram, D.A., 2004, The 3D facies architecture of flood basalt provinces and their internal heterogeneity: examples from the Palaeogene Skye Lava Field: Journal of the Geological Society, v. 161, p. 911-926.

Wilson, P., Hodgetts, D., Rarity, F., Gawthorpe, R.L., and Sharp, I.R., 2009, Structural geology and 4D evolution of a half-graben: New digital outcrop

modelling techniques applied to the Nukhul half-graben, Suez Rift, Egypt: Journal of Structural Geology, v. 31, p. 328-345.

Xu, X., Aiken, C., Bhattacharya, J., Corbeanu, R., Nielsen, K., McMechan, G., and Abdelsalam, M., 2000, Creating virtual 3-D outcrop: The Leading Edge, v. 19, p. 197-202.

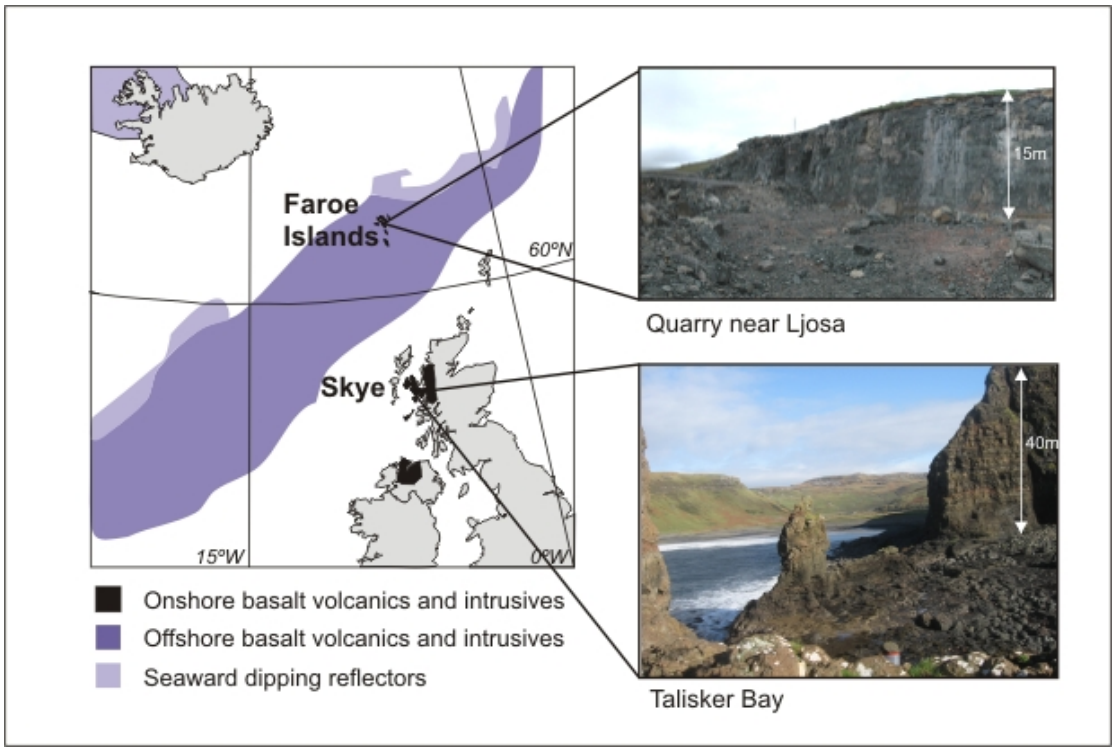

Figure 1 Map of part of the NAIP and locations of case studies.

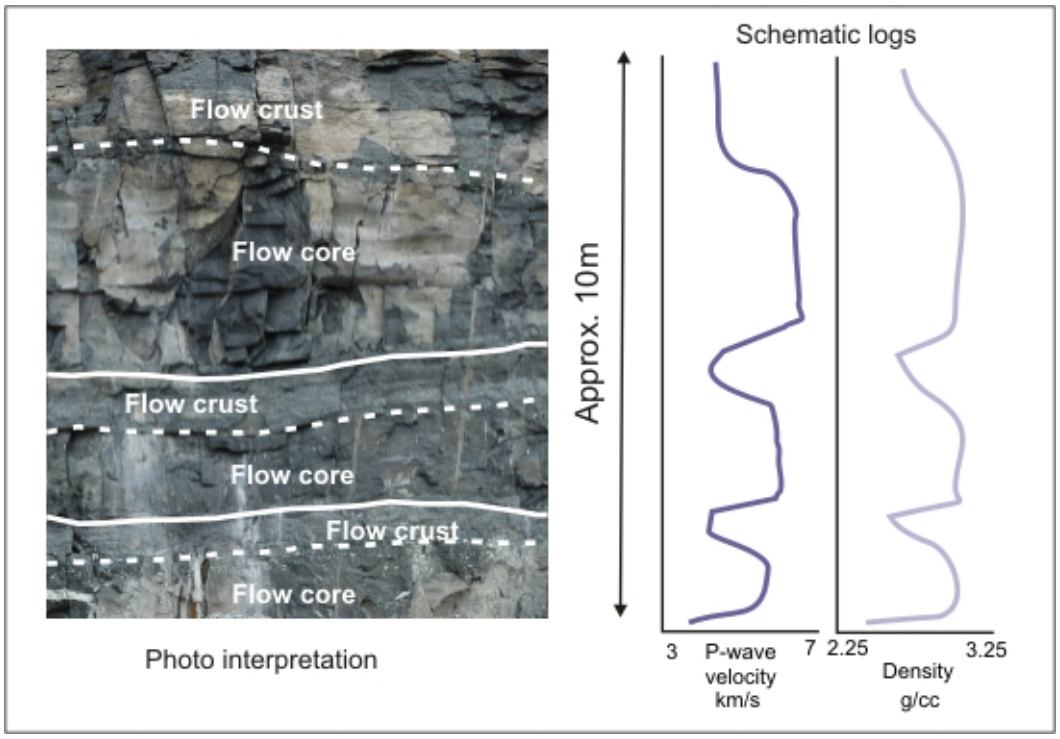

Figure 2 Photo interpretation from Ljosa quarry, Faroe Islands, and schematic geophysical logs. The photo was taken by the scanner-mounted camera. The schematic logs show the large variation between flow crust and core, and the values are based on data from Nelson et al. (2009a).

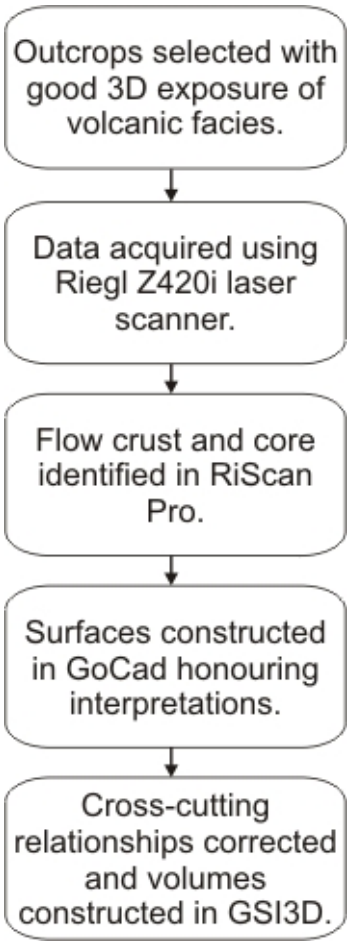

Figure 3 Summary of the workflow used in this study. The data collection and processing steps follow standard procedures (e.g. Buckley et al., 2008). Enge et al. (2007) provide a similar workflow for model building.

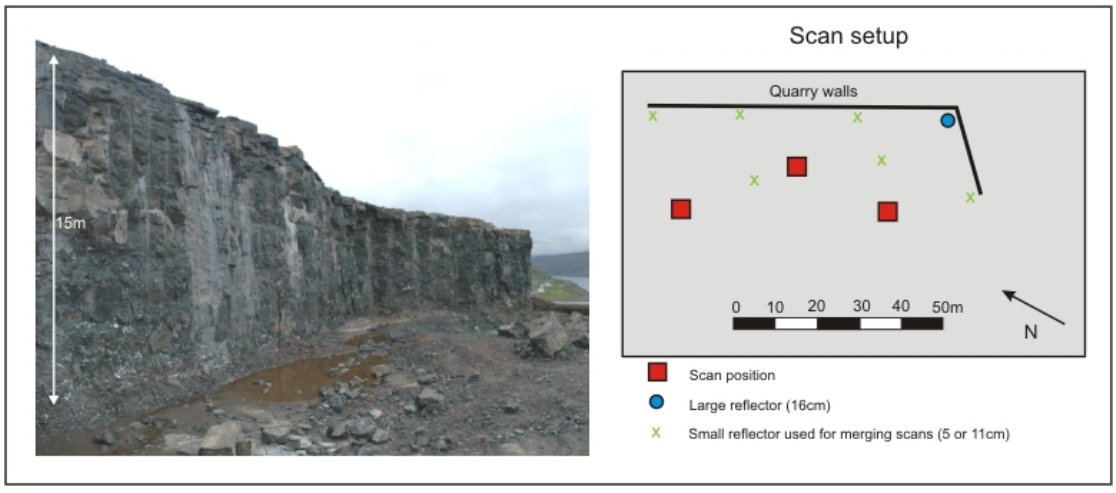

Figure 4 Overview photo of Ljosa quarry and map of the scanning setup, showing the scan positions and the reflector positions.

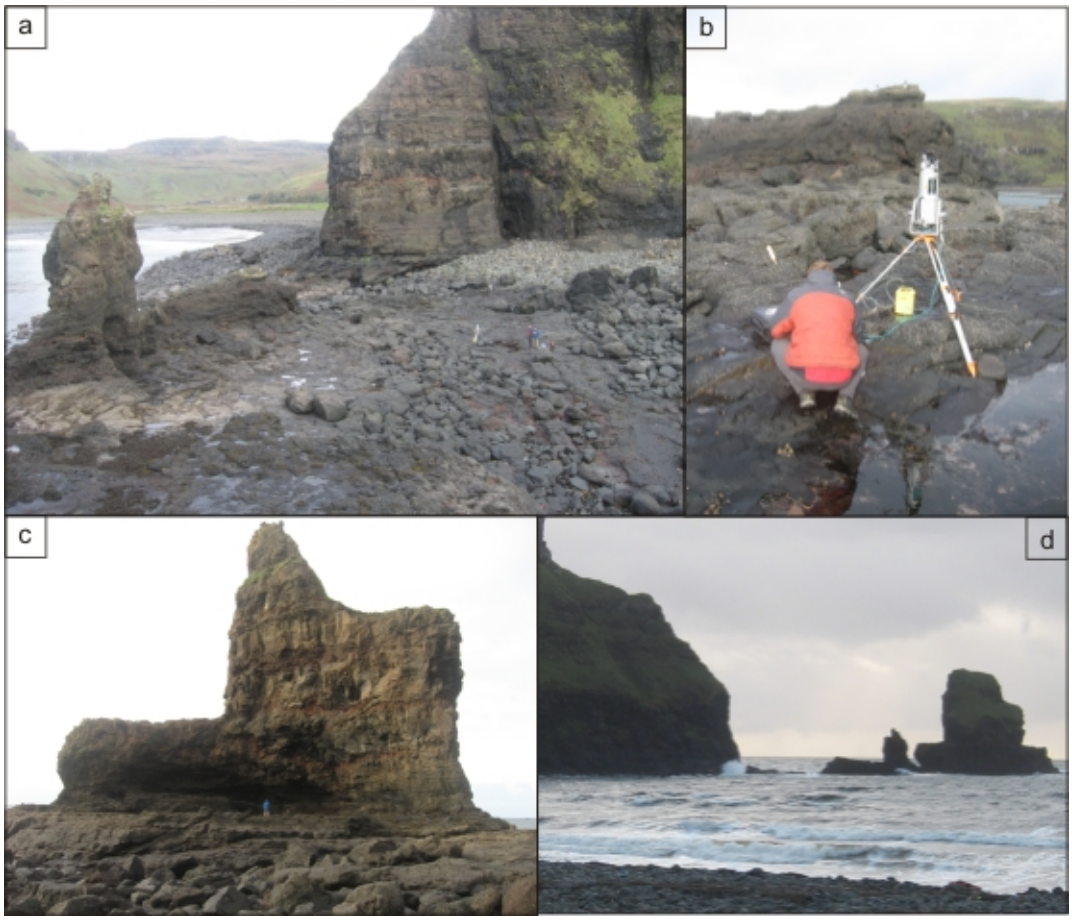

Figure 5 a) Overview photo of the Talisker Bay case study, showing the small sea stack, cliff section and wave-cut platform. **b)** The TLS equipment in action. **c)** The large sea stack. **d)** The case study area at high tide, showing the cliff section and both sea stacks.

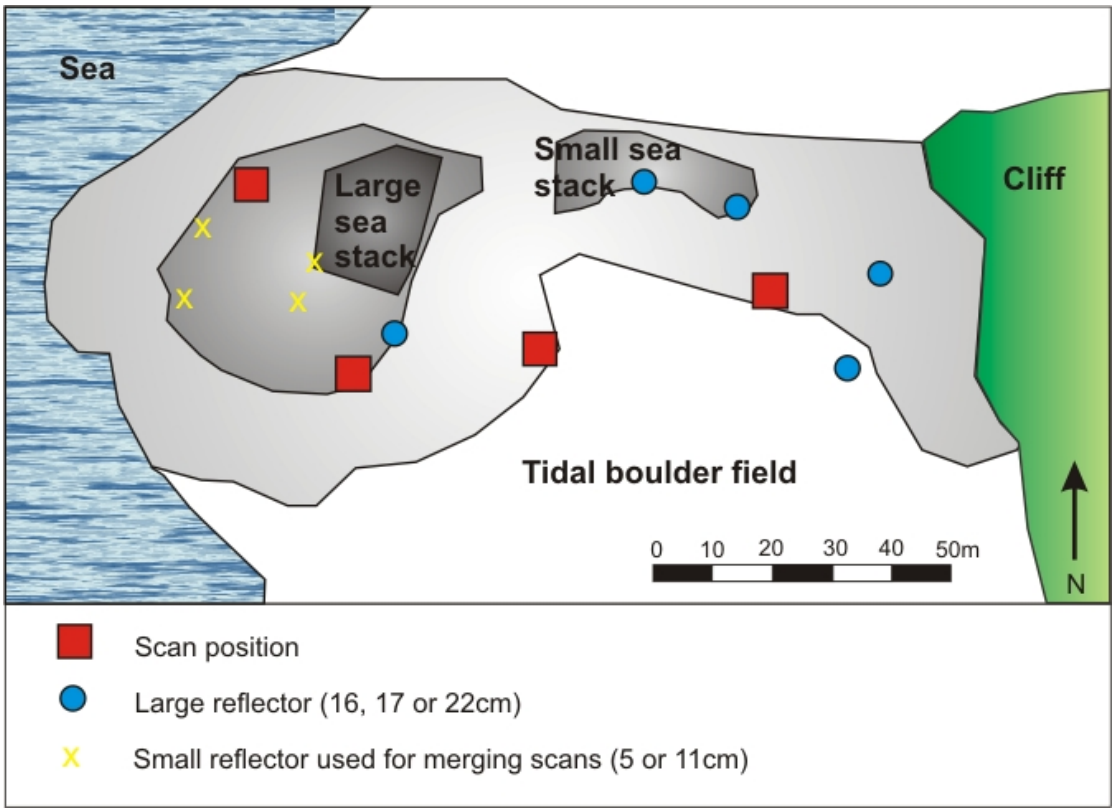

Figure 6 Map of the scan setup at Talisker Bay. The complex layout meant several scans were carried out; two on the platform halfway up the large sea stack. Two scans were carried out at one position, one of which was tilted at an angle of 30° to the horizontal, in order to capture the top of the sea stack.

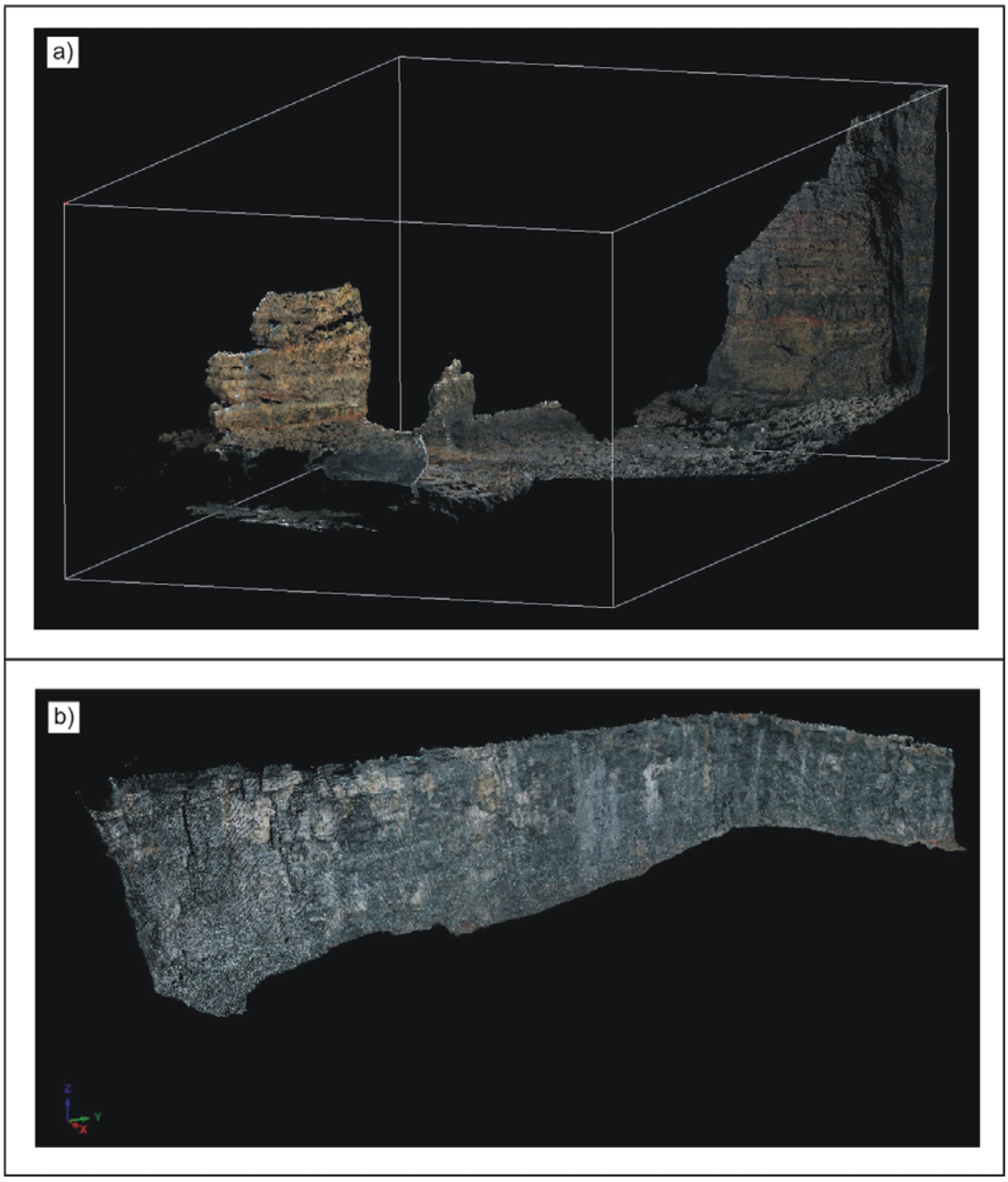

Figure 7 The completed laser scan point clouds, coloured from the digital photos. **a)** Talisker Bay data**. b)** Ljosa Quarry data. Animations of both are available.

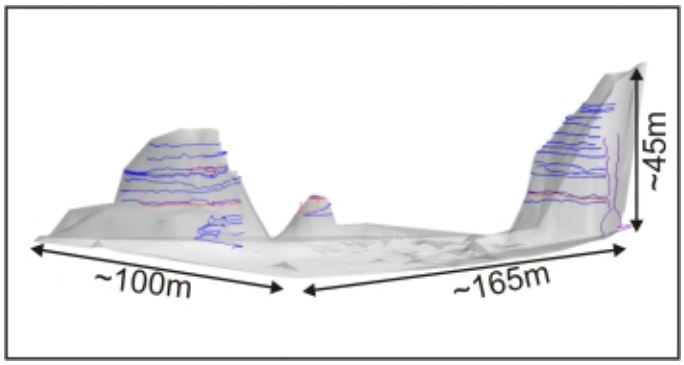

Figure 8 Interpreted 3D lines from the Talisker Bay case study.

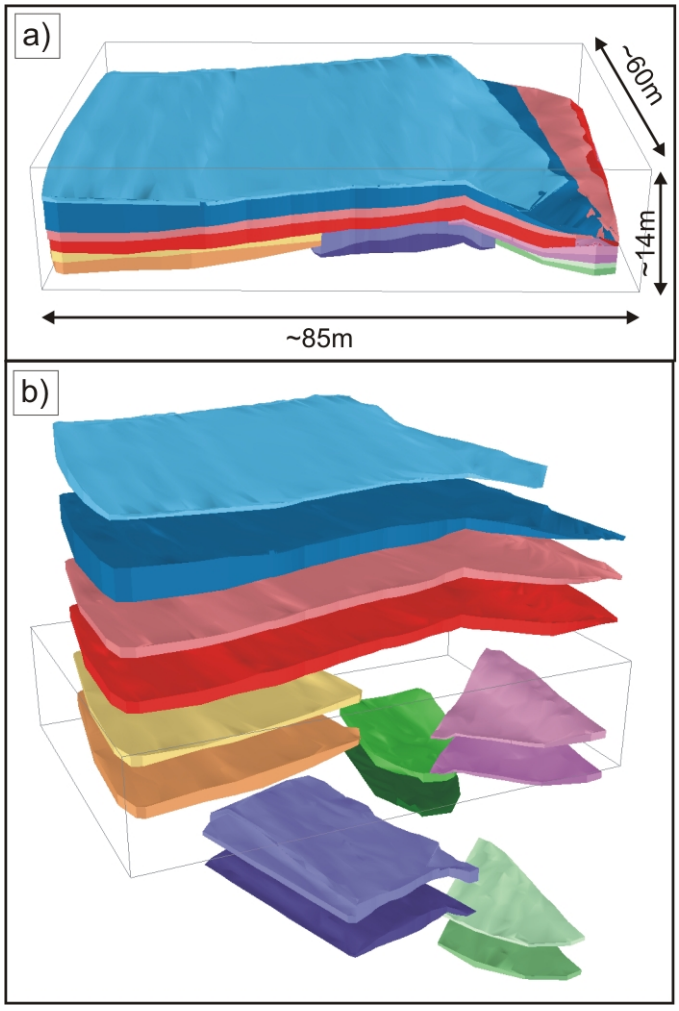

Figure 9 The completed 3D model of the Ljosa Quarry case study constructed in GSI3D. **a)** Final model - lighter colours are flow crusts and darker colours are flow

cores. **b)** Expanded model to show the full distribution of each layer. Animated versions available.

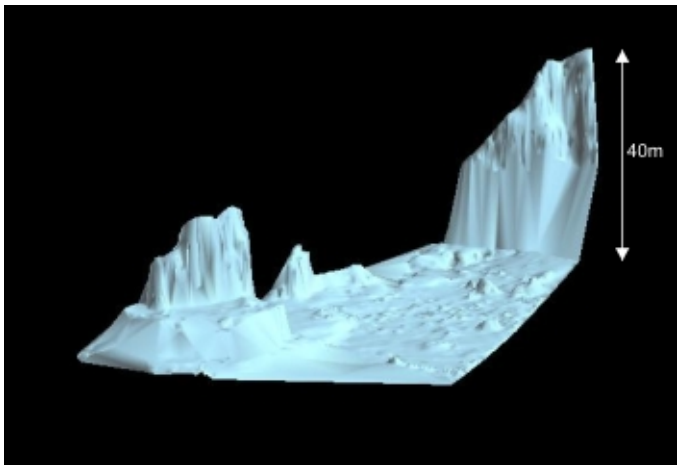

Figure 10 The GOCAD® surface used to construct the Talisker Bay model.

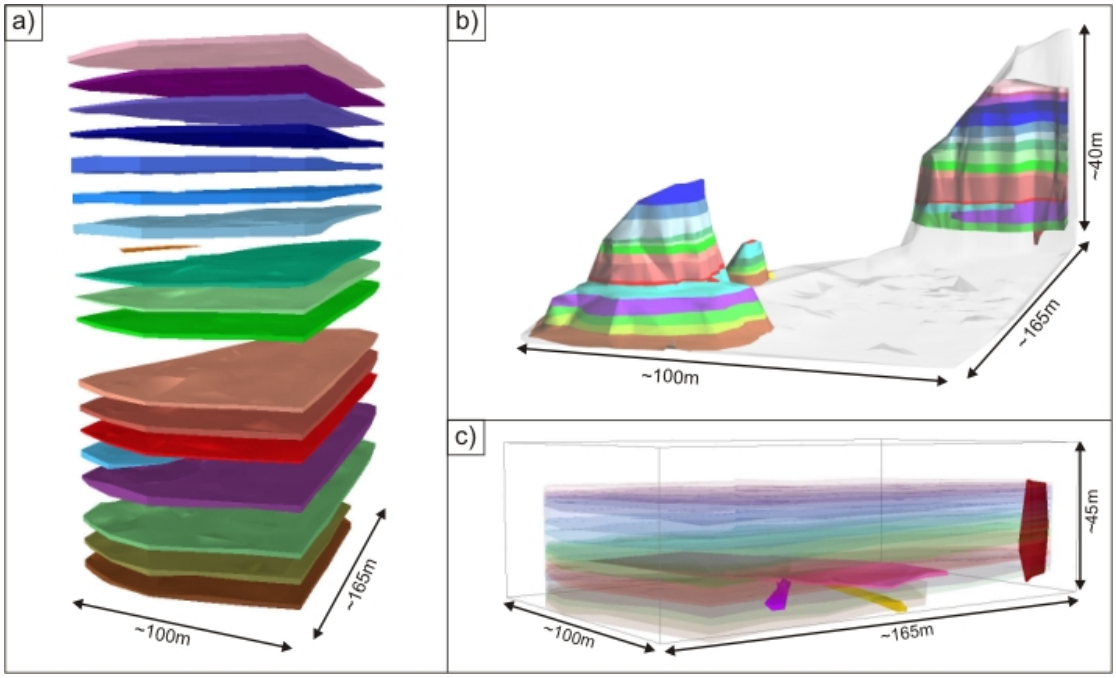

Figure 11 Completed GSI3D models of the Talisker Bay case study. Animated versions available. **a)** Exploded view of the lava flows and sedimentary units. **b)** The

3D volumes cut to the present day topography. **c)** Transparent view of the entire model highlighting the sill, dyke and lava tubes.

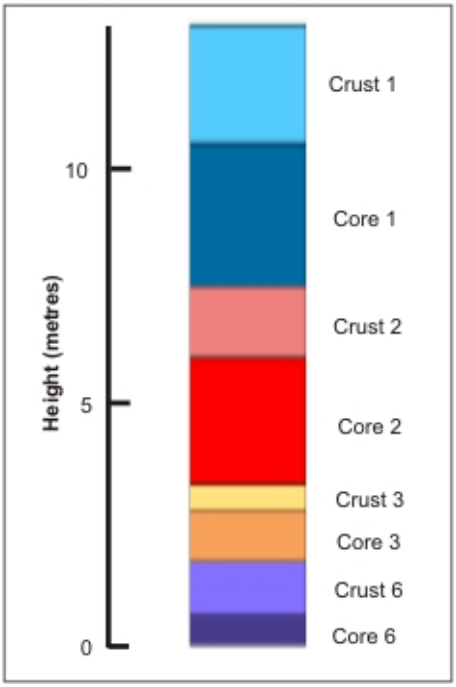

Figure 12 Synthetic borehole through Ljosa quarry model.

	Area (m^2)	Volume (m^3)	Average thickness (m)	Crust:core ratio
Crust1	3050	7575	2.483	
Core1	3303	9336	2.826	0.532
Crust2	3621	4907	1.355	
Core2	3656	6890	1.884	0.582
Crust3	1441	1107	0.768	
Core3	1434	2725	1.900	0.712
Crust4	554	529	0.955	
Core4	551	745	1.353	0.586
Crust5	544	827	1.521	

Core5	538	478	0.888	0.369
Crust6	1091	2305	2.113	
Core6	1085	2219	2.045	0.492
Crust7	483	357	0.739	
Core7	478	487	1.020	0.580

Table 1 Details of flows from Ljosa quarry model.

	Area (m^2)	Volume (m^3)	Average thickness (m)	Crust:core ratio
Flow 17	11140	20419	1.83	
Flow 16	11140	13714	1.23	
Flow 15	11140	18809	1.67	
Flow 14	11140	22996	2.06	
Flow 13	11140	45107	4.05	
Flow 12	11140	31387	2.82	
Flow 11	11140	31915	2.86	
Red Bole 2	397.54	127.64	0.32	
Flow 10	11140	16998	1.53	
Crust 9	11140	19605	1.76	0.554
Core 9	11140	24368	2.19	
Crust 7	11140	19390	1.74	0.672
Core 7	11140	39761	3.57	
Red Bole 1	11140	8599.6	0.77	
Flow 6	6047.4	13383	2.21	
Flow 5	9620.5	28832	3.00	
Flow 4	1613.7	2243.4	1.39	
Flow 3	11140	20655	1.85	
Flow 2	8381.7	9848.4	1.17	
Flow 1	8723.3	22517	2.58	
Sill	2111.7	2365.1	1.12	

Table 2 Details of flows from Talisker Bay model.

Flood basalt facies from borehole data: implications for prospectivity and volcanology in volcanic rifted margins

Catherine E. Nelson*, Dougal A. Jerram and Richard W. Hobbs
Department of Earth Sciences, Durham University, South Road, Durham DH1 3LE, UK
**Corresponding author (e-mail: c.e.nelson@durham.ac.uk)*

ABSTRACT: Flood basalt successions cover many potentially prospective sedimentary basins world-wide, and a few instances exist of intra-basalt petroleum discoveries. However, little is known about the architecture and rock properties of the lava flows, intrusions and other lithologies that make up these successions. We present a simple, effective method of obtaining information from borehole data on the different volcanic facies within a flood basalt succession. Our aims are: (1) to provide a means of determining proportions of different volcanic facies without detailed examination of borehole data or where borehole data are limited; (2) to explore the relationship between onshore and offshore observations. The facies classification scheme providing the framework for this research includes tabular-classic lava flows, compound-braided lava flows, hyaloclastites and intrusions. We show how this scheme can increase our knowledge of the offshore succession and can be useful in hydrocarbon exploration.

In the Faroe Islands, three different basalt formations display a range of facies onshore. Boreholes have been drilled through these, and several kilometres' depth of log data collected. The proximity of these boreholes to onshore observations allows the identification of different facies within the wireline log data. This work demonstrates that histograms of P-wave velocities provide an efficient method of identifying the different facies, and we also explore why these distributions are so different. When applied to borehole data from published ODP wells and one commercial well, it is possible to estimate proportions of the different volcanic facies using the velocity distributions alone.

KEYWORDS: *North Atlantic Igneous Province, Faroe Islands, lava flows, wireline logs, volcaniclastic*

INTRODUCTION

Continental flood basalt provinces (CFBPs) have complex internal architectures and are often associated with sedimentary basins, preserving vital information about palaeoenvironments and the onset of flood volcanism (Mountney *et al.* 1999; Jerram *et al.* 2000; Ellis *et al.* 2002). CFBPs and their associated volcanic rifted margins cover a significant area of the Earth's surface and represent some of the largest volcanic events in the Earth's history (Mahoney & Coffin 1997). The Palaeogene North Atlantic Igneous Province (NAIP), for example, covers an area of approximately 1.3×10^6 km^2 (Eldholm & Grue 1994), of which the majority now lies offshore (Fig. 1). In locations where these vast flood volcanics are found in offshore settings, such as the NAIP, problems are encountered in the interpretation of geophysical data to identify the size and nature of the sedimentary basins beneath. Poor seismic imaging due to the basalt cover, the so-called 'sub-basalt imaging problem' (e.g. Roberts *et al.* 2005), and concerns with technical issues associated with drilling through basalts in often deep-water settings, require a better understanding of the internal architectures of flood basalt sequences (Jerram & Widdowson 2005).

The data available to study flood basalts in offshore regions are limited to remote sensing tools, such as core and wireline log information, and also seismic data and other geophysical remote sensing tools, such as magnetotelluric data (Planke *et al.* 2000; Hautot *et al.* 2007). In order to improve our understanding of the internal architecture and development of flood basalt sequences, it is therefore necessary to link onshore observations with the offshore data in a similar way to that of sedimentary facies and facies associations (Jerram *et al.* 2009; Nelson *et al.* 2009). As exploration in volcanic rifted margins increases, seismic data shot over significant lava cover become more available; however, the velocity and density characteristics of layered flood basalt sequences are highly variable. To generate an accurate velocity model for a basalt sequence, it is essential to understand its velocity structure, which in turn will help to establish its thickness, and also provide constraints for models that try to determine what may lie beneath the basalt sequence.

In this study we investigate the relationship between flood basalt facies and rock properties by examining well-constrained

Petroleum Geoscience, Vol. **15** 2009, pp. 313–324
DOI 10.1144/1354-079309-842

1354-0793/09/$15.00 © 2009 EAGE/Geological Society of London

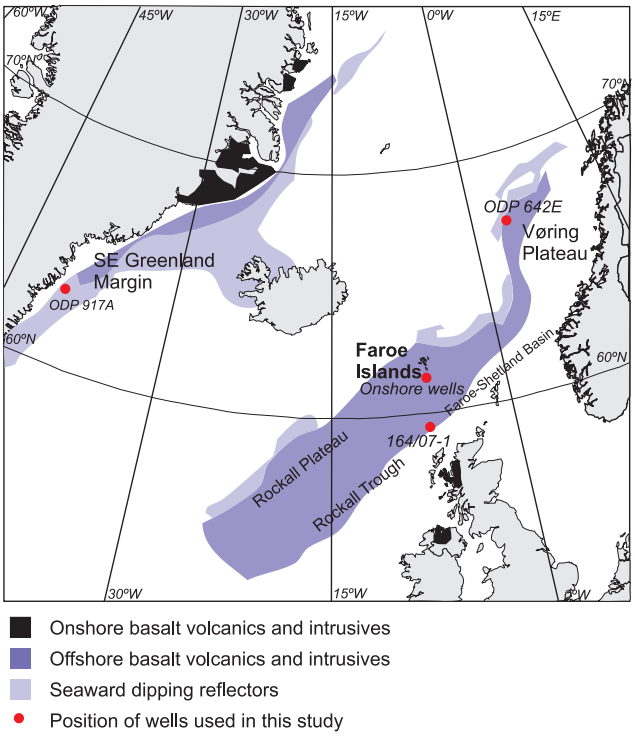

Fig. 1. Map of the NAIP showing the locations of the boreholes used in this study. For the locations of the other Faroese onshore boreholes, see Figure 4. Adapted from Saunders *et al.* (1997).

borehole data where the true lava facies are known. The wireline log responses for tabular-classic and compound-braided flows, hyaloclastites and intrusions are investigated using boreholes from the Faroe Islands to assess whether these facies can be identified by the statistical distribution of their rock properties. Published ODP/IODP boreholes that have encountered significant flood volcanic sequences are used to further constrain the relationships. Finally, we present a method of linking key flood basalt facies with offshore borehole data based on their key responses, and explore the implications for hydrocarbon exploration in areas of flood basalt cover.

VOLCANIC FACIES IN FLOOD BASALT SEQUENCES

While the technique of facies analysis is usually associated with sedimentary successions, it can also be very successful in describing volcanic successions (Cas & Wright 1987). It is becoming clear that the internal architecture of flood basalt sequences is markedly heterogeneous (Jerram & Widdowson 2005; Jerram *et al.* 2009; Nelson *et al.* 2009), an observation which had received little attention until the late 1990s (Self *et al.* 1997; Jerram *et al.* 1999), with the majority of previous studies focusing on the geochemistry of flood basalts.

Planke *et al.* (2000) described volcanological facies at the seismic scale, defining variations at the kilometre to hundreds of kilometre scale. Facies described by Planke *et al.* (2000) included seaward-dipping reflectors and lava deltas. These were identified and mapped on the Norwegian Margin by Berndt *et al.* (2001), showing the distribution and associations of the various seismic facies. Jerram (2002) developed a facies and facies association framework for continental flood basalt provinces at the metre to kilometre scale, building on the previous work of Walker (1971). This is of particular use as it provides a framework to compare direct onshore observations with the offshore setting. Figure 2 highlights, with examples, some of the common facies that can be identified within flood basalts and provides the key flood basalt facies for the present study.

On a smaller scale still, individual lava flow lobes can also be divided into their component parts. Aubele *et al.* (1988) recognized a three-part vertical structure consisting of an upper vesicular zone, a middle non-vesicular zone and a lower vesicular zone. Self *et al.* (1997) developed this for continental flood basalts based on observations in the Columbia River Basalt Group and divided flows into a crust, core and basal zone. This three-part zonation is observed in other flood basalt provinces including the NAIP (Passey & Bell 2007) and the Deccan Volcanic Province (Self *et al.* 2007) (Fig. 3). Developing this further, Single & Jerram (2004) developed a classification scheme for variations at the scale of individual flow lobes. These intrafacies included flow cores, crusts, boles and small intrusions. These intrafacies can be identified from field observations, and were applied to the characterization of lava flows in Talisker Bay, Skye (Single & Jerram 2004). Andersen & Boldreel (2009) characterized the basalt succession in eight wells in the Faroe–Shetland channel and the Rockall Trough, describing five classes of units. Helm-Clark *et al.* (2004) provide a detailed study of the uses and limitations of various wireline logging tools, using data from the Deccan Traps and Columbia River flood basalt provinces amongst others.

While we mainly consider subaerial and nearshore environments in this study, many flood basalt provinces were emplaced into deeper water. Bartetzko *et al.* (2001, 2002) defined facies such as pillow basalts in wireline log data from ODP holes in oceanic crust. This is of use when considering oceanic large igneous provinces such as the Wrangellia oceanic plateau, Canada, where significant submarine pillow sequences exist (Greene *et al.* 2009) and the approaches taken in this study could be extended to these provinces as additional datasets become available.

Terminology

A **flow lobe** is 'an individual package of lava that is surrounded by a chilled crust' (Self *et al.* 1997). Flow lobes can be identified easily in the field by the presence of this chilled crust. Most flow lobes in CFBPs show a three-part vertical division into an upper **crust**, a **core** and a lower crust or **base** (Self *et al.* 1998). This is illustrated in Figure 3. The crust is highly vesicular and extensively fractured, while the core is massive with few vesicles. This three-part structure is largely independent of flow thickness, though the upper crust may be fully or partially eroded if the lobe top is exposed at the surface for a significant amount of time. The smallest lobes (below 50 cm) may have vesicular cores. A **lava flow** is defined as 'the product of a single continuous outpouring of lava' (Self *et al.* 1997). This may be very difficult to recognize in ancient flood basalt provinces, as a lava flow can be made up of one or more flow lobes.

Volcanic facies at a metre to kilometre scale

Volcanic facies provide a useful way of characterizing the internal architecture of a CFBP. These key facies have been identified from a variety of provinces world-wide and are described based on their internal and external geometries (Jerram 2002; also see Fig. 2 and Nelson *et al.* 2009).

Tabular-classic flows contain thick flow lobes, up to 50 m or more in thickness. Their lateral extent can be several kilometres, with a few examples known of hundreds of kilometres (e.g. Self *et al.* 2007). They show a low level of lateral

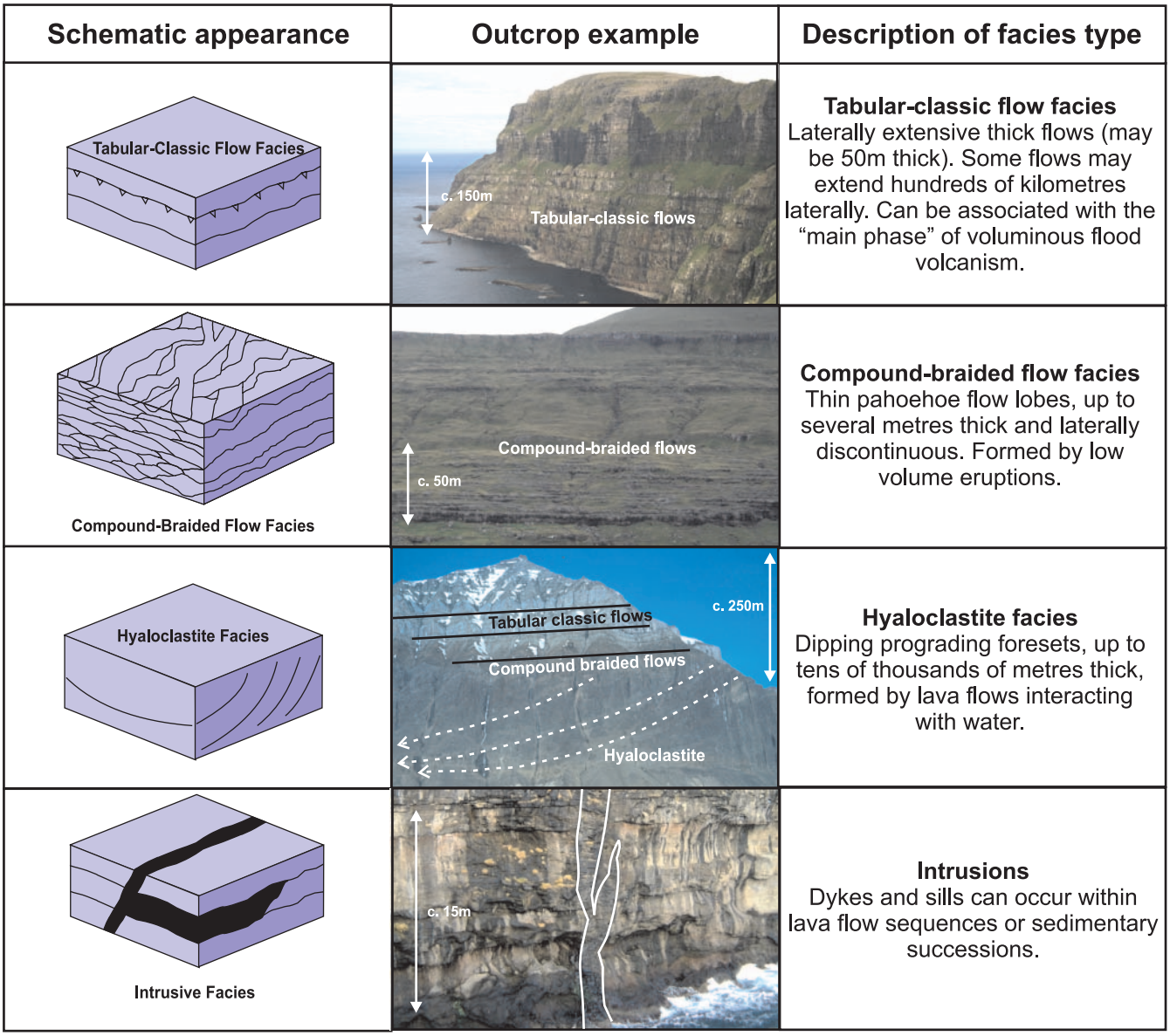

Fig. 2. Summary of the facies classification scheme of Jerram (2002) showing onshore examples. Other facies include ponded flows. Photographs: Tabular-classic flows from Suðuroy, Faroe Islands, courtesy of Richard Walker. Compound braided from Eidi, Eysturoy, Faroe Islands. Hyaloclastite from Greenland, courtesy of Graham Pearson. Dyke at Gjógv, Eysturoy, Faroe Islands.

heterogeneity. **Compound-braided flows**, in contrast, contain thin anastomosing flow lobes. Thicknesses are up to a few metres and lateral complexity is high. The **intrusive** facies comprises dykes and sills, which are internally homogeneous, and show lateral continuity mainly in two dimensions. **Hyaloclastites** consist of quench-fragmented glass, formed by eruption into water, and contain prograding foreset bedding.

Interpreting wireline log data in flood basalt provinces

Several Ocean Drilling Program (ODP) boreholes have penetrated flood basalt lava flows in the North Atlantic. The first to have its log data fully analysed was Hole 642E (Leg 104) on the Vøring margin (Planke 1994). Its location is shown in Figure 1. The data from Hole 642E showed wide variations in the sonic, density, neutron porosity and resistivity logs. Planke (1994) recognized a cyclic response in these logs related to the internal structure of the flow lobes – the velocity and density are low at the flow top, gradually increase to a maximum in the flow core and decrease sharply at the flow base. This within-lobe variation maps onto the crust–core–base sequences often observed in flood basalt facies described above (Fig. 3). This cyclical pattern is caused by the vertical variations in vesicularity and fracturing that characterize a flood basalt flow lobe. In the crust, vesicle density and fracturing are high, thus reducing sonic velocity and bulk density. The crust often shows a greater degree of alteration than the rest of the lobe, resulting in a high gamma-ray value. The flow core has a low degree of fracturing and vesicularity is also low, so velocity and density are high. The thin flow bases generally show a return to high values of fracturing and vesicularity.

As ODP boreholes have a full set of cores as well as wireline log data, they are invaluable for linking geophysical data to geological observations. Bücker *et al.* (1998) confirmed the link between the cyclical pattern in log data and the internal flow structure, using data from ODP Holes 553A (Leg 81), 642E (Leg 104) and 917A (Leg 152). It was also shown that geographically distant boreholes demonstrated the same cyclical pattern, which was also unaffected by core size (Bücker *et al.*

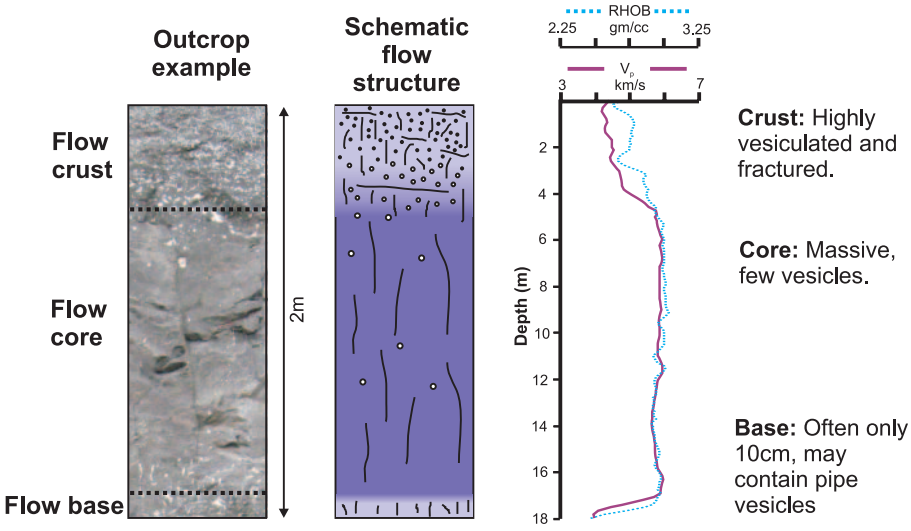

Fig. 3. Principles of interpreting wireline log data. As discussed in the text, variation in velocity and density can be used to subdivide lava flows into their crust, core and base regions. Photo from Ljosa quarry, Eysturoy, Faroe Islands. This is at a different scale to the log data, but this three-part division has been shown to be independent of scale (e.g. Self *et al.* 1997). Schematic flow structure from Self *et al.* (1997). Log data from the Lopra-1/1A borehole.

1998). This suggests that this pattern in wireline log data is common to all areas of the NAIP, and possibly to other flood basalt provinces, and may be used to identify intraflow structures in areas of no core recovery.

Several more recent studies have used this cyclical pattern to identify flow lobes where no core has been recovered. Archer *et al.* (2005) identified individual flow lobes in well 164/07-1, in the Rockall Trough, using the cyclical pattern present in sonic and density logs. Boldreel (2006) used this technique to construct a detailed stratigraphy for the Lopra 1/1A borehole, Faroe Islands. 'Flow units', minor compound flows, intrusions and a hyaloclastite sequence were observed in this borehole, aided by the lithological analysis of Hald & Waagstein (1984).

FAROESE CASE STUDY

A set of key borehole data from the Faroe Islands provides a vital case study for this work. The proximity of the boreholes to the onshore basalt equivalents allows a full investigation into the use of the borehole signatures to identify key flood basalt facies. In turn, it helps us determine a strategy for the interpretation of boreholes from areas where no close onshore analogues exist. We will describe the facies relationships found in the Faroe Islands and then introduce the borehole data used in this study and their analysis.

Facies relationships in the Faroe Islands

Onshore, the Faroe Islands Basalt Group (FIBG) has been the target of recent studies, prompted by hydrocarbon prospecting in the area. The onshore distribution of the FIBG is presented in Figure 4. Passey & Bell (2007) described the facies architecture of the FIBG from field observations using the classification scheme of Jerram (2002), and comparisons were made between onshore and offshore volcanic facies (Jerram *et al.* 2009). The basalt stratigraphy of the Faroe Islands is divided into four main formations: the Lopra Formation (LF), Beinisvørð Formation (BF), Malinstindur Formation (MF) and Enni Formation (EF). The LF is known only from the Lopra 1/1A onshore borehole and is interpreted as being dominated by hyaloclastites formed by lava flowing into water (Ellis *et al.* 2002; Boldreel 2006). The entire formation is thought to have been erupted into an estuarine environment (Ellis *et al.* 2002). The BF is exposed onshore as well as being found in the Lopra 1/1A borehole, and mostly demonstrates a tabular-classic facies architecture (Passey & Bell 2007). The MF, on the other hand, is dominated by compound flows, while the EF contains a mixture of tabular and compound facies. The characteristics of the facies (flow size, morphology and so on) were found to be consistent between the formations, but their relative proportions varied.

Analysis of the Lopra-1/1A, Vestmanna-1, and Glyvursnes-1 borehole data

The purpose of this study is to investigate the link between wireline log data and volcanic facies observed onshore. In order to do this, three recently released onshore boreholes in the Faroe Islands (Lopra-1/1A, Vestmanna-1 and Glyvursnes-1) were selected for this study, and their locations are shown in Figure 4. Examples of log data from these boreholes are given in Figure 5. These boreholes are ideally suited for studying the wireline log responses of altered flood basalt lava flows, as they are in close proximity to well-exposed onshore flows. The facies architecture of the flows penetrated by the boreholes is therefore well-constrained. The Faroe Islands exhibit a variety of facies architectures in onshore exposures: the EF is a mixture of tabular-classic and compound-braided flows; the MF is dominated by compound-braided flows; the BF is dominated by tabular-classic flows; and the LF by hyaloclastites.

The Lopra-1/1A borehole was drilled to a depth of 2.2 km on the island of Suðuroy, Faroe Islands, in 1981 and deepened to 3.6 km in 1996 (Hald & Waagstein 1984). The entire depth of this borehole was within the FIBG, and two formations were encountered: the subaerial Beinisvørð Formation and the near-shore Lopra Formation. The BF is dominated by tabular flows, and the LF by hyaloclastites (Passey & Bell 2007). The entire borehole was logged in 1996, and data between 180 m and 3550 m depth are used in this study. The approximate depths of all three boreholes within the FIBG stratigraphy are shown in Figure 4.

The Vestmanna-1 borehole was drilled in 1980 on the island of Streymoy (Berthelsen *et al.* 1984). Its original total depth was 660 m, but in 2002 it was reamed and logged to 590 m as part of the SeiFaBa project (Japsen *et al.* 2005). It encountered the bottom 550 m of the MF and the top 100 m of the BF. The MF mainly consists of compound-braided flows.

The Glyvursnes-1 borehole was also drilled as part of the SeiFaBa project in 2002. It reached a total depth of 700 m and sampled the bottom 250 m of the EF and the top 450 m of the MF (Japsen *et al.* 2005).

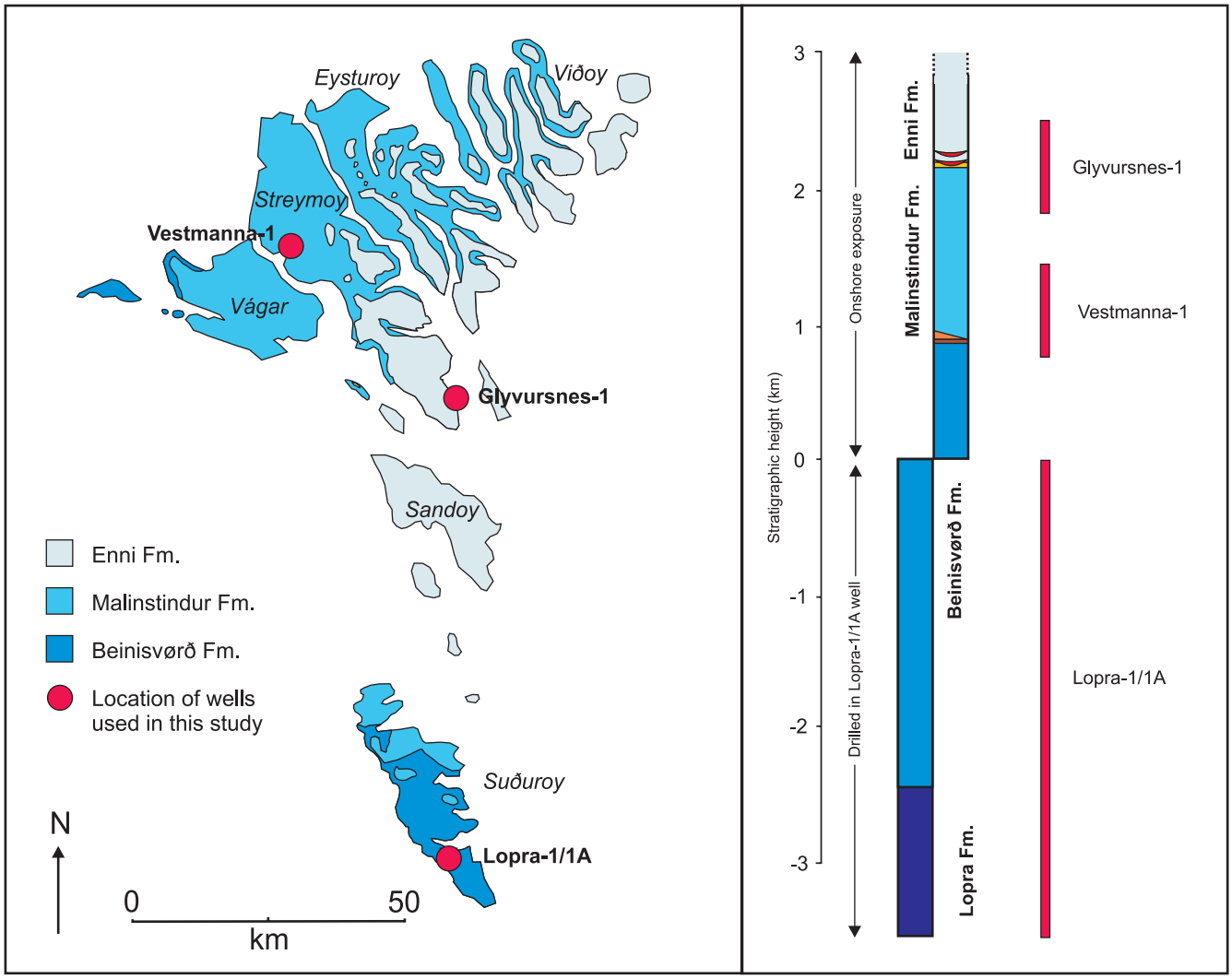

Fig. 4. Location map of Faroese onshore boreholes and their stratigraphic positions. After Passey & Bell (2007). Borehole depths from Japsen *et al.* (2005).

Methodology

Velocity distributions are useful in geophysical analysis and modelling, as they are a primary 'parameter' determining the seismic response of the medium (Holliger 1996). As wireline log data are sampled at constant intervals (usually 15.24 cm), a histogram is representative of the velocity structure of the borehole. A histogram can thus be constructed easily by counting the frequency of measurements for the desired intervals. This is shown in Figure 6.

The shape of a histogram is known to be sensitive to the bin size. Larger bins produce more robust shapes but may mask finer details of the data. Accordingly, we use the method of Freedman & Diaconis (1981, summarized in Izenman 1991). This gives bin sizes based on the number of samples and their inter-quartile range (IQR). We selected the largest bin size calculated for the various facies (0.8 km s^{-1}), and used this in all histograms to allow us to compare the histograms easily. Choosing a smaller bin size would either mean that the shapes of some histograms were not robust, or that the histograms were difficult to compare.

The relevant data for each facies were identified by combining previous work on the boreholes with interpretations of the data. Data were filtered to remove caved intervals identified in the calliper log, where available. Flow lobes can be identified by the cyclical velocity pattern described in the introduction and Figure 3 (Planke 1994). Boldreel (2006) identified the transition between the BF (known to be dominated by tabular-classic flows) and the LF (composed of hyaloclastites) in the Lopra 1/1A borehole. Boldreel (2006) also identified two dykes which provide the data for the dyke facies shown in Figure 6. Logging data characteristics for tabular-classic flows, intrusions and hyaloclastites were identified from the Lopra-1/1A borehole and are summarized below. From previous studies, the boundary between the EF and MF in the Glyvursnes-1 borehole, and the boundary between the MF and BF in the Vestmanna-1 borehole, can be identified. These were used, together with the known facies from outcrop examples, to divide the boreholes into the appropriate facies. Examples of logs from the different facies are given in Figure 5. The exact details of the data used are given in Table 1.

Results of data analysis

Investigations of the wireline logging data from the three Faroese boreholes showed that each volcanic facies has a characteristic velocity histogram. This allows a link to be made between onshore observations and logging data from boreholes. The velocity distributions for the various volcanic facies are shown in Figure 6. Table 2 gives a mathematical description

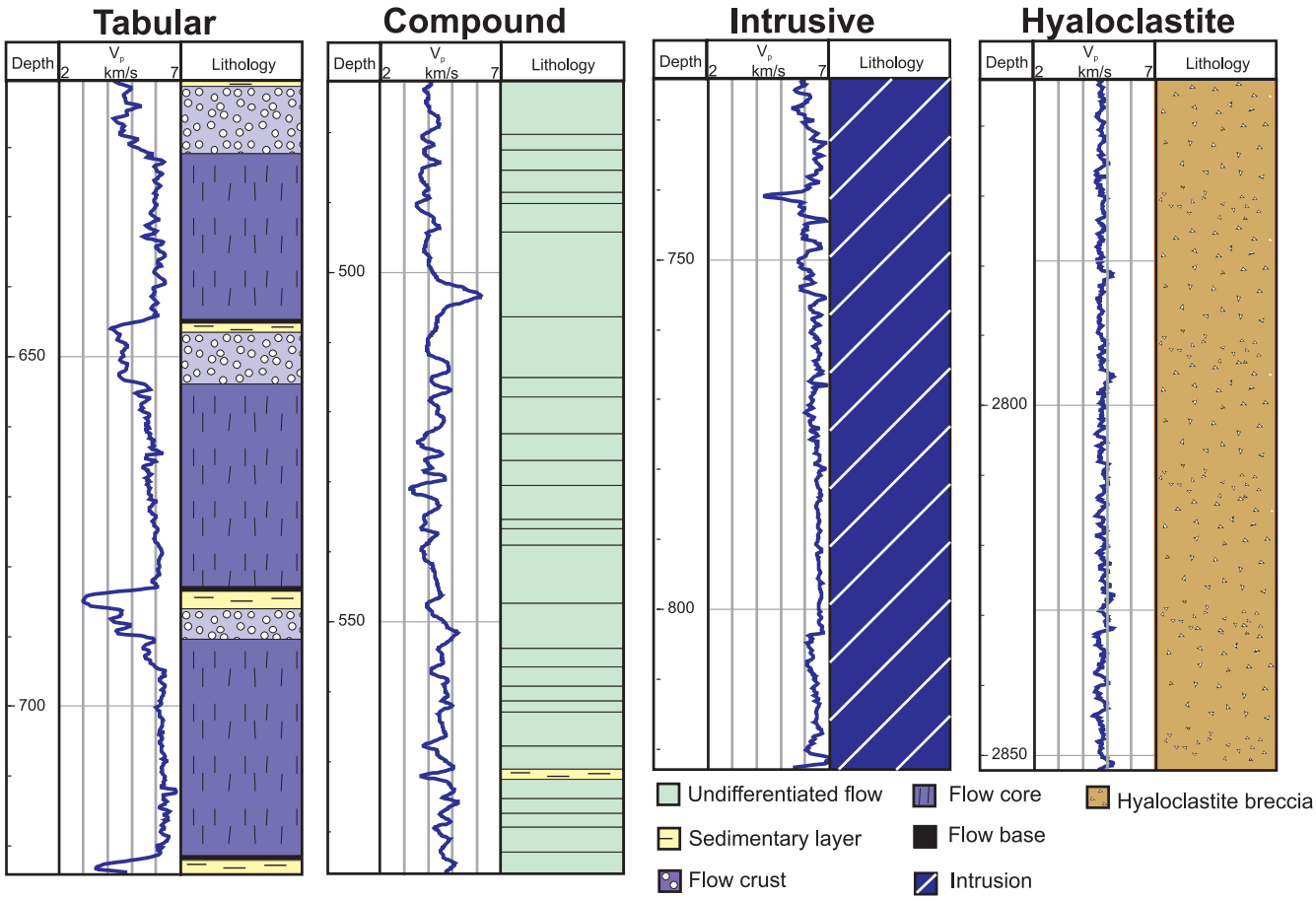

Fig. 5. Examples of P-wave velocity (V_p) data from different volcanic facies, divided into individual lava flows and showing intraflow variations where appropriate. Compound data from the Glyvursnes-1 borehole, other data from the Lopra-1/1A borehole.

Table 1. *Data used in this study*

Facies	Well	Depth range (MD)	Number of samples	Logs available
Tabular-classic	Lopra-1/1A	184–2467, omitting the intrusive intervals below	13573	V_p, V_s, RHOB, SGR, CAL
Compound-braided	Glyvursnes-1	354–697	1715	V_p, V_s, RHOB, SGR, CAL, NPHI, RES, TEMP
Intrusive	Lopra-1/1A	494–610; 724–823	1413	V_p, V_s, RHOB, SGR, CAL
Hyaloclastite	Lopra-1/1A	2596–2886	1902	V_p, V_s, RHOB, SGR, CAL
Mixed	164/07-1	2242–2952	4660	V_p, RHOB, GR, CAL, RMLL
Mixed	917A	238–546	2020	V_p, RHOB, SGR, CAL, SFLU
Mixed	642E	416–1068	4255	V_p, RHOB, SGR, CGR, GR, CAL, NPHI, SFLU, ILD, ILM

of the shape of these distributions in terms of their mean, modality and skewness.

It can be seen from Figure 6 that the volcanic facies show very different velocity distributions. Intrusions show a high peak, with a very small spread of data. Hyaloclastites surprisingly also have a small spread, but a lower peak velocity. Both lava flow facies (tabular-classic and compound-braided) have a large spread of data; however, the shapes of their distributions are very different. Tabular-classic flows produce a negatively-skewed distribution with a high single mode, whereas compound-braided flows produce a largely symmetrical distribution with two modes. Data from compound-braided flows in the Vestmanna-1 borehole gave a similar histogram to those from the Glyvursnes-1 borehole.

Intrusive sills and dykes have a high mode and narrow distribution because of their homogeneous nature, low porosity and low fracture density. Hyaloclastites show a high level of heterogeneity, sometimes including lava flows (e.g. Ellis *et al.* 2002). In other places, the V_p is relatively constant, probably responding to zones of hyaloclastite breccia. We use a section of hyaloclastite breccia for this type example. This has a low spread because of its homogeneity, and the inclusion of the lava flows would have increased the spread of the data.

Sedimentary units are found in all boreholes used; however, their data are not separated from the facies in which they occur. Their velocity distribution is not shown in Figure 6 because they make up only a small proportion of the data analysed. When taken separately, their velocity distribution is

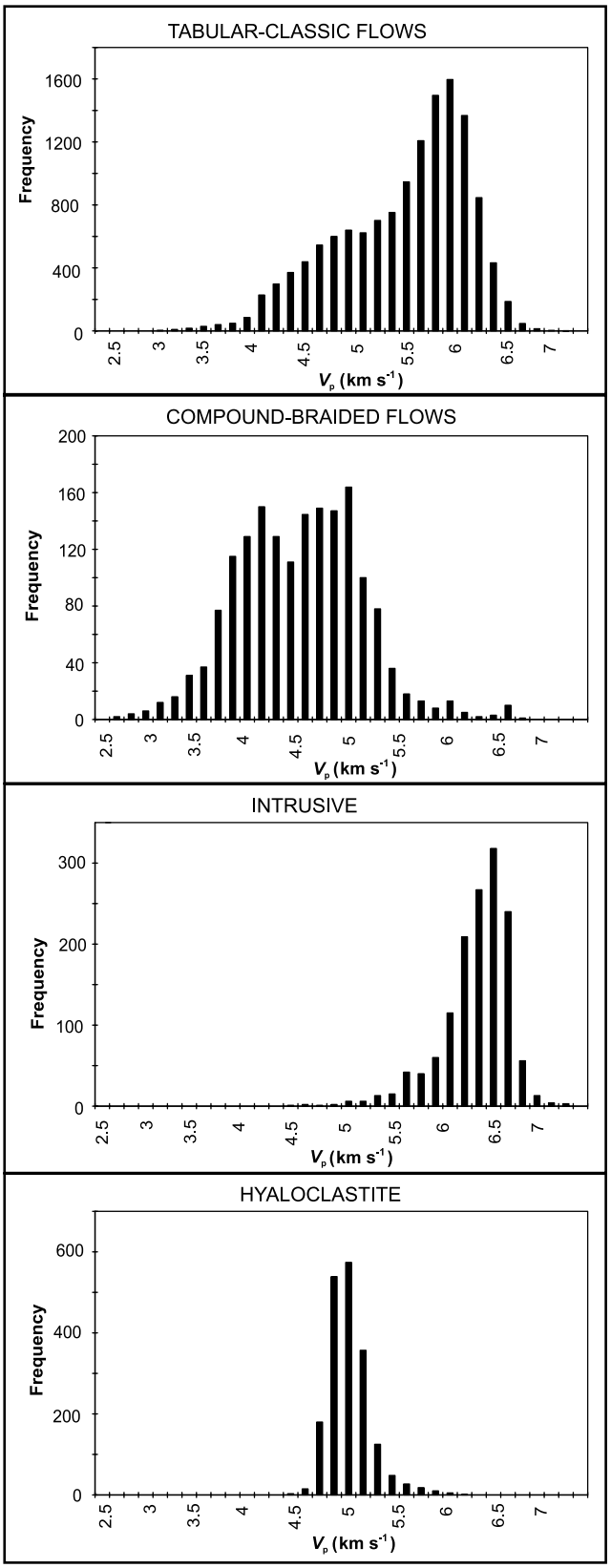

Fig. 6. Velocity histograms of various volcanic facies. Tabular-classic, hyaloclastite and dyke data from the Lopra-1/1A borehole; compound-braided data from the Glyvursnes-1 borehole.

symmetrical, with a peak at 3.25 km s^{-1}. The sedimentary layers account for the slower velocity 'tails' of the compound and tabular distributions. In the next section, we explore the reasons for the difference between the tabular-classic and compound-braided distributions.

Table 2. *Statistics for the velocity distributions for the various facies*

	Facies			
	Tabular-classic	Compound-braided	Dyke	Hyaloclastite
Number of modes	1	2	1	1
Modal value(s)	5.9–6.05	3.95–4.1; 4.4–4.55	6.35–6.5	4.85–5.0
IQR (spread)	0.991	0.934	0.381	0.259
Fisher skewness	−0.689	0.212	−1.342	1.339

Tabular-classic, hyaloclastite and dyke data from the Lopra-1/1A borehole; compound-braided data from the Glyvursnes-1 borehole. IQR is inter-quartile range. Fisher skewness is a measure of the asymmetry of the distribution. A positive number indicates an asymmetric tail extending towards larger values, while a negative number indicates that the asymmetric tail extends towards smaller values.

Understanding the lava flow signature: comparing tabular-classic and compound-braided facies

For each of the major subaerial formations in the Faroe Islands, flow thicknesses and core proportions were calculated to identify the causes of the different velocity distributions. Recalling from Figure 6, tabular-classic flows have a negatively-skewed distribution with a high mode. Compound-braided flows have a more symmetrical distribution. The peak at 5.75–6 km s^{-1} in the tabular-classic distribution is due to the many measurements recorded in the fully degassed core of the tabular flows. If the core proportion varies between tabular-classic and compound-braided flows, this would explain the difference between the distributions. Another contributing factor may be that the cores of tabular-classic flows are fully degassed, resulting in a higher velocity, while the cores of compound-braided flows are slightly more vesicular.

In order to investigate the flow lobe thickness and core to crust ratio, the Glyvursnes-1, Vestmanna-1 and Lopra-1/1A borehole data were subdivided into individual flow lobes, then into lobe crusts and cores. Boldreel (2006) plotted individual flow lobes and flow crusts for the Lopra 1/1A borehole, and we repeat this work to obtain core to crust ratios. This work uses a modified version of the zones identified by Bücker *et al.* (1998) and Planke (1994) to divide this stratigraphy into lava flows and their component parts. The transition zone identified by Planke (1994) is not used in this study for simplicity and because it is not often observed in the density log, and it may be an 'edge effect' of the deep penetrating sonic logging tool (Rider 1996). The transition zone is not generally observed in the field, where a relatively sharp divide is commonly observed between the crust and core. This zone is included in the crust. Sonic, density and gamma-ray logs have proved most useful for interpreting log data and were available for all datasets used in this study. Available data are summarized in Table 1. The lack of neutron porosity data for some wells meant we were unable to use the 'cross over technique' of Boldreel (2006). The criteria we used for identifying the zones are summarized in Table 3.

The proportion of core in each flow is plotted against flow thickness for all the formations in Figure 7, and data are summarized in Table 4. This displays a trend in the minimum value of the core proportion: thick flows do not have a low core proportion, whereas thin flows display a wide range of core proportions. When combined with data on flow thicknesses in

Table 3. *Criteria for dividing flow lobes into separate zones*

Flow lobe component	V_P	Density	GR
Crust	Relatively low. Below *c.* 4 km s^{-1}	Relatively low. Below *c.* 2600 kg m^{-3}	Often shows a peak of 10–20 API at flow top
Core	Relatively high. Above *c.* 5 km s^{-1}	Relatively high. Above *c.* 2600 kg m^{-3}	Low, <10 API
Base	Decreasing	Decreasing	Increasing

After Planke (1994), Bücker *et al.* (1998) and Boldreel (2006).

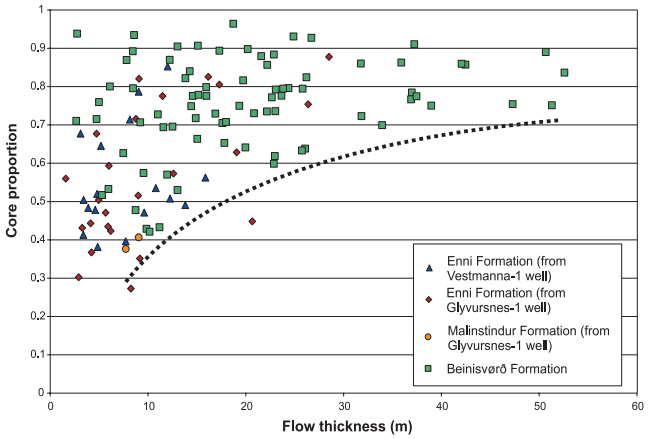

Fig. 7. Plot of core proportion (core thickness divided by total flow thickness) versus flow thickness. Beinisvørð Formation data from the Lopra-1/1A borehole.

Table 4. *Flow thickness statistics from the BF, MF and EF*

Formation	Mean flow thickness (m)	Standard deviation (m)	Percentage of total core thickness made up of flows >5 m thick
Beinisvørð Formation (BF)	12.6	12.6	91
Malinstindur Formation (MF)	3.46	2.24	36
Enni Formation (EF)	6.39	6.55	73

Mean and standard deviation accurate to 3 significant figures; percentages to 2 significant figures.

Table 4, it is predicted that core proportions in the MF are low compared to the BF. The EF shows intermediate flow thickness values, as expected for a mixture of compound and tabular flows.

In summary, we suggest that the significant differences between tabular-classic and compound-braided velocity distributions are due to the differences in flow thickness and thus core proportion. In tabular-classic flows, relatively more measurements are recorded in the massive, faster flow core, whereas in compound-braided flows relatively more measurements come from the vesicular, slower crust. In compound-braided flows, the flow core may also be less well degassed than that of tabular flows, resulting in a lower velocity peak for core values.

IDENTIFYING FACIES DISTRIBUTIONS IN UNCONSTRAINED DATA

This study has shown that the key flood volcanic facies (tabular-classic, compound-braided, hyaloclastites and intrusions) have characteristic velocity distributions for examples where the facies is well known. The next step is to investigate whether these distributions can be used to identify volcanic facies in areas with no nearby onshore exposure, or where data are limited (e.g. little or no core data). Three offshore boreholes were available: ODP Hole 642E, ODP Hole 917A and the commercial borehole 164/07-1 (Fig. 1). These are described in detail below.

ODP Hole 642E (Leg 104) was drilled in 1985 through a sequence of seaward-dipping reflectors (SDR) on the Vøring margin (Eldholm *et al.* 1987). This study uses approximately 700 m of logging data from a layered terrestrial tholeiitic basalt sequence, which was also cored. ODP Hole 917A (Leg 152) was also drilled through a SDR sequence, this time on the SE Greenland margin (Duncan *et al.* 1996). The basalt sequence was terrestrial, and 370 m of wireline logging data were obtained.

Well 164/07-1 was drilled in the UK sector of the Rockall Trough, penetrating a 1.2 km sequence of lava flows (Archer *et al.* 2005). Approximately 300 m of this was interpreted as subaqueous, the rest being subaerial. As we wish to test our methods on data that have not been interpreted previously, we attempt to identify the volcanic facies within the subaerial data only. The geological history is similar to the Faroe–Shetland basin – the lavas are a subaerial flood basalt sequence. The borehole also contained approximately 70 dolerite sills, although data for these were not available.

Velocity distributions for the unconstrained boreholes

Velocity frequency distributions for well 164/07-1 and ODP Holes 917A and 642E are plotted in Figure 8, and statistics for these distributions are given in Table 5. The distributions do not correspond to any single distribution in Figure 6, as they contain multiple modes and show a high spread of data. A possible hypothesis from these features is that these boreholes penetrate a mixture of compound-braided and tabular-classic flows. Based on the relative heights of the modal velocities, it is suggested that ODP Hole 642E has mainly compound flows, while ODP Hole 917A has around 25% tabular flows. The data from well 164/07-1 are taken as an example to test the hypothesis.

We constructed histograms from the Faroe Islands data showing tabular and compound data combined in different proportions (Fig. 9). Data from well 164/07-1 are plotted in an attempt to derive proportions of tabular and compound flows by fitting the borehole data to the closest constructed histograms. It was found that the peak corresponding to the lava flow cores from the Lopra-1/1A data was at a higher velocity than the interpreted core peak from the 164/07-1 data, resulting in a poor fit between the modes of the datasets, but with a similar overall range. Such differences in absolute velocity between different datasets would be expected if the composition of the basalt was different between boreholes. Composition data from Hald & Waagstein (1984), Waagstein

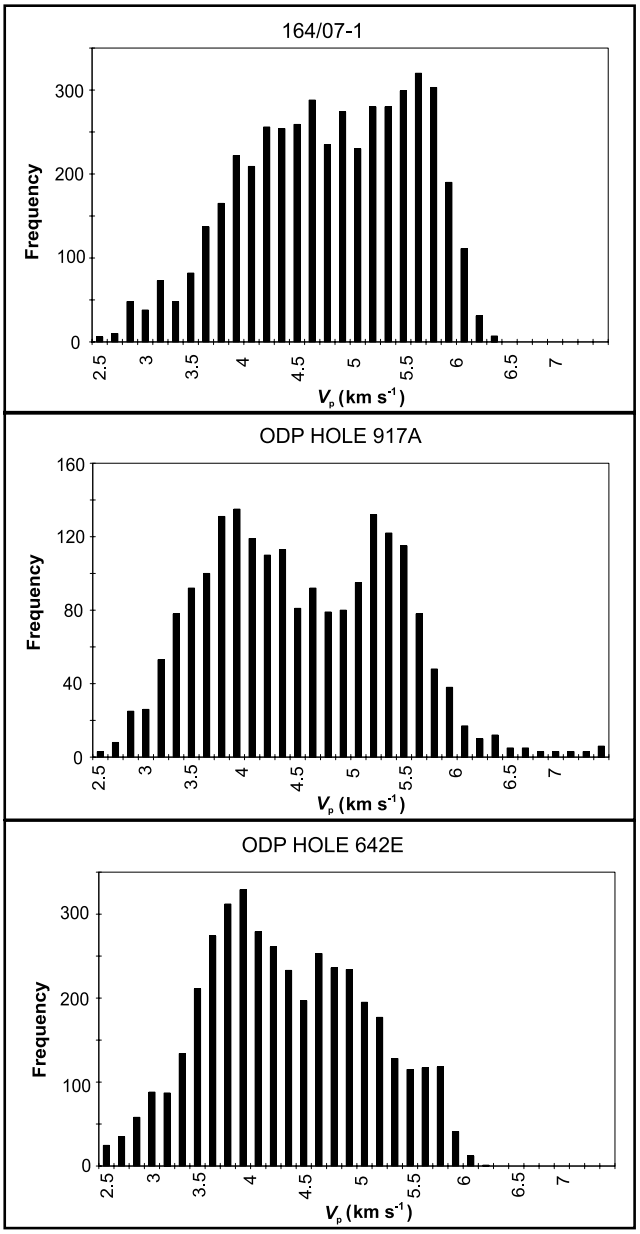

Fig. 8. Velocity histograms for the boreholes with no nearby onshore analogues, as described in the text.

Table 5. *Statistics for the borehole s unconstrained by nearby onshore analogues*

	Borehole		
	164/07-1	917A	642E
Number of modes	2	2	2
Modal values	4.4–4.55; 5.45–5.6	3.65–3.8; 5–5.15	3.65–3.8; 4.4–4.55
IQR (spread)	1.326	1.356	1.215
Fisher skewness	−0.317	0.255	−0.064

(1988) (Lopra-1/1A borehole) and Archer *et al.* (2005) (164/07-1 data) were used to calculate a theoretical density following the method of Hall (1987). The calculated density was significantly higher than other boreholes for data from the Lopra-1/1A borehole, indicating that the rock composition variation is responsible for the slightly higher velocity values in the Lopra-1/1A borehole. Other possible causes of a high flow

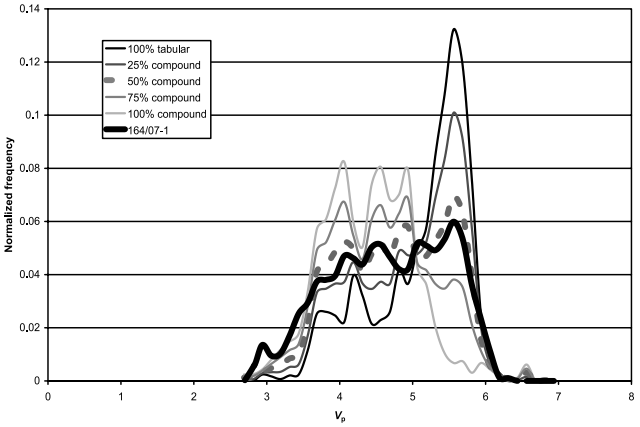

Fig. 9. Well 164/07-1 histogram plotted with synthetic histograms constructed from tabular-classic and compound-braided data. The tabular data are a 300 m selection from the Lopra-1/1A borehole of almost entirely tabular flows, while the compound data are a 150 m selection from the Glyvursnes-1 borehole. These are normalized to the number of sample points.

core velocity would include a lower level of fracturing in the borehole or a lower proportion of vesicles in the core (i.e. a more degassed core). A more degassed core is unlikely, because the same increase in average velocity is found in data from the flow crust, suggesting a mechanism that affects both crust and core.

To account for the higher overall velocity in the Lopra-1/1A data, we can overlay the velocity distributions by matching their flow core peaks. In Figure 9 the combination of different mixes of tabular-classic vs. compound-braided facies is presented, representing the distributions expected from lava stratigraphy that contained different amounts of each facies (normalized to the core peak values). An overlay of the natural distribution from the 164/07-1 data (Fig. 9) shows that the best fit to the 164/07-1 data is a mixture of 50% compound flows and 50% tabular flows.

As a further test of this result a detailed (flow-by-flow) volcanological interpretation of the 164/07-1 wireline logging data found that compound flows totalled 361 m out of the 710 m analysed, or 51%. The velocity distributions of key facies and their relative abundances can be used as a way of estimating proportions of the different facies in wireline datasets, and has the potential to be developed further when used to map out the distributions of these facies in 2D or 3D.

DISCUSSION

Identification of key volcanic facies helps us constrain the 3D nature of flood basalt sequences. For example, if tabular-classic flows are identified in a borehole, we can expect that they extend laterally for hundreds of metres. This will also affect the seismic response of the sequence, as shown in Figure 2. Tabular-classic flows show laterally continuous, high amplitude reflectors (e.g. Jerram *et al.* 2009), which may allow better imaging of structures below than the diffuse, complex reflectors of compound-braided flows. Knowledge of volcanic facies in boreholes also provides a control for inter-basalt seismic imaging. This is of particular importance in exploration, as it allows a better definition of the velocity distribution within basalt to help in defining the true base basalt and the likely basalt thickness.

It can be demonstrated that the key facies used in this study are found in a wide selection of known sections through flood basalt provinces world-wide (e.g. Fig. 10a). In each example

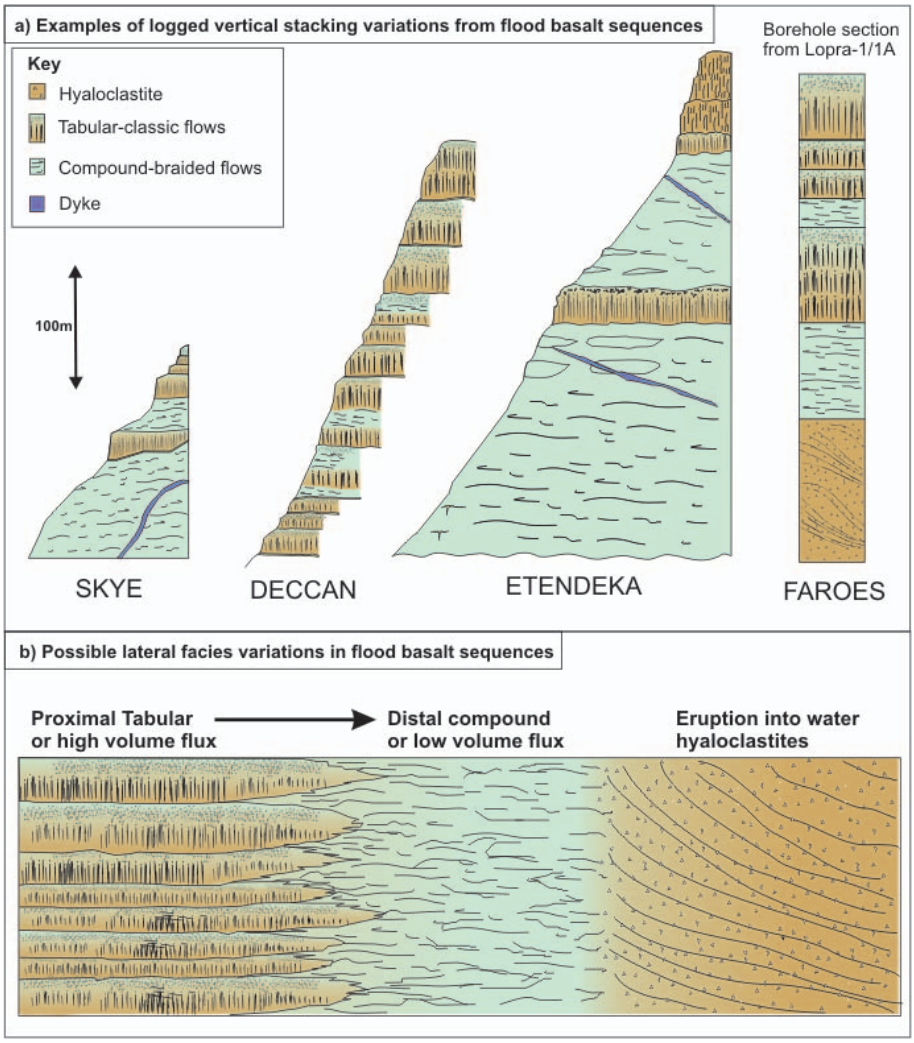

Fig. 10. Examples of the vertical and lateral heterogeneity in flood basalt provinces. (**a**) Vertical heterogeneity. Skye, Deccan (India) and Etendeka (Namibia) sections from field sketches; Faroes section from Lopra borehole data, approximately 2190–2550 md. Note that all sections are at the same scale. After Nelson *et al.* (2009). (**b**) Schematic representation of the lateral heterogeneity possible within a flood basalt province.

there is a wide variation in the amounts and distributions of these facies. Where good onshore analogues and field data allow, such facies variations and facies architectures can be mapped (e.g. Jerram & Widdowson 2005). In this study we have provided a means of detecting such facies variations from limited data, such as borehole signatures. With improved coverage, and linked to additional information (such as seismic data), our method may allow a better understanding of the facies variations and associations in the sequences now preserved offshore.

There are also implications for research into the physical volcanology of flood basalt provinces. If the key facies types we describe can be identified over a wide area, we can begin to build up a picture of the 3D architecture of the province, and characterize its lateral heterogeneity (e.g. Fig. 10b). We might expect thick tabular flows proximal to the vent to develop into thinner compound facies in distal areas (Fig. 10b). The presence of different facies types could also be linked to the original volumes of magma flux in the system. Mapping the hyaloclastite distribution within the volcanic system is also of vital importance. This can highlight palaeo-shorelines and the transition from lava flows to volcaniclastic-dominated parts of the basin (e.g. Jerram *et al.* 2009). One of the limitations of our method, however, is that we cannot classify flows into a'a and pahoehoe. To date, these have not been identified by log data alone; it has been necessary to identify the characteristic vesicle shapes from core sections (e.g. Keszthelyi 2002; Garcia *et al.* 2007).

We have demonstrated that the key volcanic facies (intrusions, hyaloclastites, tabular-classic flows and compound-braided flows) have characteristic velocity histograms. These type distributions have also been used to interpret data from areas without nearby onshore analogues. While the same interpretations could be made by subdividing each borehole into individual lava flows, using the velocity distributions is far quicker and more efficient. We hope that our method will be useful to those involved in hydrocarbon exploration in understanding the structure of a flood basalt sequence. There are also implications for the process of drilling through a flood basalt sequence: the rock properties of tabular and compound flows are very different and will require drilling strategies to take this into account. If these key facies can be defined, the occurrences of significant thick 'hard' basalt sections interspersed with softer basalt sections can be better predicted when drilling exploration wells. It is hoped that future work will use these velocity distributions as a tool in the interpretation of wireline logs in flood basalt terrains. This work could also be extended by looking at a smaller 'window' of, say, several hundred metres' thickness within a borehole and investigating the change in facies throughout the borehole.

Reviews by Morten S. Andersen, Simon Passey and an anonymous reviewer resulted in a substantial improvement to this manuscript. This work was completed while DAJ was the TOTAL Lecturer at the Department of Earth Sciences, Durham University. Research

was supported by funding provided to DAJ by Elf/TOTAL GRC and the EU 5th Framework Project SIMBA (CONTRACT Nº: ENK6-CT-2000-00075). RWH is a NERC Advanced Research Fellow (NER/J/S/2002/00745).

REFERENCES

Andersen, M.S. & Boldreel, L.O. 2009. *Log responses in basalt successions in 8 wells from the Faroe–Shetland Channel – a classification scheme for interpretation of geophysical logs and case studies. In:* Faroe Islands Exploration Conference: Proceedings of the 2nd Conference, Annales Societatis Scientarium Faroensis.

Archer, S.G., Bergman, S.C., Iliffe, J., Murphy, C.M. & Thornton, M. 2005. Palaeogene igneous rocks reveal new insights into the geodynamic evolution and petroleum potential of the Rockall Trough, NE Atlantic Margin. *Basin Research*, **17**, 171–201.

Aubele, J.C., Crumpler, L.S. & Elston, W.E. 1988. Vesicle zonation and vertical structure of basalt flows. *Journal of Volcanology and Geothermal Research*, **35**, 349–374.

Bartetzko, A., Pezard, P., Goldberg, D., Sun, Y. & Becker, K. 2001. Volcanic stratigraphy of DSDP/ODP Hole 395A: An interpretation using well-logging data. *Marine Geophysical Researches*, **22**, 111–127.

Bartetzko, A., Pechnig, R. & Wohlenberg, J. 2002. Interpretation of well-logging data to study lateral variations in young oceanic crust: DSDP/ODP Holes 504B and 896A, Costa Rica Rift. *In:* Lovell, M. & Parkinson, N. (eds) *Geological Applications of Well Logs*. AAPG Methods in Exploration, **13**, 213–228.

Berndt, C., Planke, S., Alvestad, E., Tsikalas, F. & Rasmussen, T. 2001. Seismic volcanostratigraphy of the Norwegian Margin: constraints on tectonomagmatic break-up processes. *Journal of the Geological Society, London*, **158**, 413–426.

Berthelsen, O., Noe-Nygaard, A. & Rasmussen, J. (eds) 1984. The deep drilling project 1980–1981 in the Faeroe Islands. *Annales Societatis Scientarium Faeroensis, Supplementum*, **IX**, 1–158.

Boldreel, L.O. 2006. Wire-line log-based stratigraphy of flood basalts from the Lopra-1/1A well, Faroe Islands. *In:* Chalmers, J.A. & Waagstein, R. (eds) *Scientific results from the deepened Lopra-1 borehole, Faroe Islands*. Geological Survey of Denmark and Greenland Bulletin, **9**, 7–22.

Bücker, C.J., Delius, H., Wohlenberg, J. & Leg 163 Shipboard Scientific Party. 1998. Physical signature of basaltic volcanics drilled on the northeast Atlantic volcanic rifted margins. *In:* Harvey, P.K. & Lovell, M.A. (eds) *Core–Log Integration*. Geological Society, London, Special Publications, **136**, 363–374.

Cas, R.A.F. & Wright, J.V. 1987. *Volcanic Successions: Modern and Ancient*. Allen & Unwin, Boston.

Duncan, R.A., Larsen, H.C. & Allan, J.F. *et al.* 1996. *Proceedings of the Ocean Drilling Program, Initial Reports*, **163**. College Station, TX (Ocean Drilling Program).

Eldholm, O. & Grue, K. 1994. North Atlantic volcanic margins: Dimensions and production rates. *Journal of Geophysical Research*, **99**, 2955–2968.

Eldholm, O., Thiede, J., Taylor, E. & Shipboard Scientific Party. 1987. *Proceedings of the Ocean Drilling Program, Initial Reports*, **104**. College Station, TX (Ocean Drilling Program).

Ellis, D., Bell, B.R., Jolley, D.W. & O'Callaghan, M. 2002. The stratigraphy, environment of eruption and age of the Faroes Lava Group, NE Atlantic Ocean. *In:* Jolley, D.W. & Bell, B.R. (eds) *The North Atlantic Igneous Province: Stratigraphy, Tectonic, Volcanic and Magmatic Processes*. Geological Society, London, Special Publications, **197**, 253–269.

Freedman, D. & Diaconis, P. 1981. On the histogram as a density estimator: L_2 theory. *Probability Theory and Related Fields*, **57**, 453–476.

Garcia, M.O., Haskins, E.H., Stolper, E.M. & Baker, M. 2007. Stratigraphy of the Hawai'i Scientific Drilling Project core (HSDP2): Anatomy of a Hawaiian shield volcano. *Geochemistry, Geophysics, Geosystems*, **8**, DOI: 10.1029/2006GC001379.

Greene, A.R., Scoates, J.S., Weis, D., Nixon, G.T. & Kieffer, B. 2009. Melting history and magmatic evolution of basalts and picrites from the accreted Wrangellia Oceanic Plateau, Vancouver Island, Canada. *Journal of Petrology*, DOI: 10.1093/petrology/egp008.

Hald, N. & Waagstein, R. 1984. Lithology and chemistry of a 2-km sequence of Lower Tertiary tholeiitic lavas drilled on Suðuroy, Faeroe Islands (Lopra-1). *In:* Berthelsen, O., Noe-Nygaard, A. & Rasmussen, J. (eds) *The Deep Drilling Project 1980–1981 in the Faeroe Islands*. Annales Societatis Scientiarum Faeroensis, Supplementum, **IX**, 15–38.

Hall, A. 1987. *Igneous Petrology*. Longman Scientific & Technical, Harlow.

Hautot, S., Single, R.T. & Watson, J. *et al.* 2007. 3-D magnetotelluric inversion and model validation with gravity data for the investigation of flood basalts and associated volcanic rifted margins. *Geophysical Journal International*, **170**, 1418–1430.

Helm-Clark, C., Rodgers, D. & Smith, R. 2004. Borehole geophysical techniques to define stratigraphy, alteration and aquifers in basalt. *Journal of Applied Geophysics*, **55**, 3–38.

Holliger, K. 1996. Upper-crustal seismic velocity heterogeneity as derived from a variety of P-wave sonic logs. *Geophysical Journal International*, **125**, 813–829.

Izenman, A. 1991. Recent developments in nonparametric density estimation. *Journal of the American Statistical Association*, **86**, 205–224.

Japsen, P., Andersen, C. & Andersen, H.L. *et al.* 2005. Preliminary results from investigations of seismic and petrophysical properties of Faroes basalts in the SeiFaBa project. *In:* Doré, A.G. & Vining, B.A. (eds) *Petroleum Geology: North-West Europe and Global Perspectives – Proceedings of the 6th Petroleum Geology Conference*. Geological Society, London, 1461–1470.

Jerram, D.A. 2002. Volcanology and facies architecture of flood basalts. *In:* Menzies, M.A., Klemperer, S.L., Ebinger, C.J. & Baker, J. (eds) *Volcanic Rifted Margins*. Geological Society of America Special Paper, **362**, 119–132.

Jerram, D.A. & Widdowson, M. 2005. The anatomy of Continental Flood Basalt Provinces: geological constraints on the processes and products of flood volcanism. *Lithos*, **79**, 385–405.

Jerram, D.A., Mountney, N., Holzforster, F. & Stollhofen, H. 1999. Internal stratigraphic relationships in the Etendeka Group in the Huab Basin, NW Namibia: understanding the onset of flood volcanism. *Journal of Geodynamics*, **28**, 393–418.

Jerram, D., Mountney, N., Howell, J., Long, D. & Stollhofen, H. 2000. Death of a sand sea: an active aeolian erg systematically buried by the Etendeka flood basalts of NW Namibia. *Journal of the Geological Society, London*, **157**, 513–516.

Jerram, D.A., Single, R.T., Hobbs, R.W. & Nelson, C.E. 2009. Understanding the offshore flood basalt sequence using onshore volcanic facies analogues: an example from the Faroe–Shetland basin. *Geological Magazine*, **146**, DOI: 10.1017/S0016756809005974.

Keszthelyi, L. 2002. Classification of the mafic lava flows from ODP Leg 183. *In:* Frey, F.A., Coffin, M., Wallace, P. & Quilty, P. (eds) *Proceedings of the Ocean Drilling Program, Scientific Results*, **183**, Available from World Wide Web: http://www-odp.tamu.edu/publications/183_SR/012/012.htm (downloaded 31 March 2009).

Mahoney, J. & Coffin, M. (eds) 1997. *Large Igneous Provinces: Continental, Oceanic, and Planetary Flood Volcanism*. AGU Geophysical Monograph, **100**.

Mountney, N., Howell, J., Flint, S. & Jerram, D. 1999. Climate, sediment supply and tectonics as controls on the deposition and preservation of the aeolian-fluvial Etjo Sandstone Formation, Namibia. *Journal of the Geological Society, London*, **156**, 771–777.

Nelson, C.E., Jerram, D.A., Single, R.T. & Hobbs, R.W. 2009. Understanding the facies architecture of flood basalts and volcanic rifted margins and its effect on geophysical properties. *In:* Varming, T. & Ziska, H. (eds) *Faroe Islands Exploration Conference: Proceedings of the 2nd Conference*. Annales Societatis Scientarium Faroensis, supplementum, **48**, 84–103.

Passey, S.R. & Bell, B.R. 2007. Morphologies and emplacement mechanisms of the lava flows of the Faroe Islands Basalt Group, Faroe Islands, NE Atlantic Ocean. *Bulletin of Volcanology*, **70**, 139–156.

Planke, S. 1994. Geophysical response of flood basalts from analysis of wire line logs – Ocean Drilling Program Site 642, Vøring Volcanic Margin. *Journal of Geophysical Research-Solid Earth*, **99**, 9279–9296.

Planke, S., Symonds, P.A., Alvestad, E. & Skogseid, J. 2000. Seismic volcanostratigraphy of large-volume basaltic extrusive complexes on rifted margins. *Journal of Geophysical Research-Solid Earth*, **105**, 19 335–19 351.

Rider, M. 1996. *The Geological Interpretation of Wireline Logs*. Whittles, Caithness.

Roberts, A.W., White, R.S., Lunnon, Z.C., Christie, P.A.F., Spitzer, R. & Team i. 2005. Imaging magmatic rocks on the Faroes Margin. *In:* Doré, A.G. & Vining, B.A. (eds) *Petroleum Geology: North-West Europe and Global Perspectives – Proceedings of the 6th Petroleum Geology Conference*. Geological Society, London, 755–766.

Saunders, A.D., Fitton, J.G., Kerr, A.C., Norry, M.J. & Kent, R.W. 1997. The North Atlantic Igneous Province. In: Mahoney, J. & Coffin, M. (eds) *Large Igneous Provinces: Continental, Oceanic, and Planetary Flood Volcanism*. AGU Geophysical Monograph, **100**, 45–93.

Self, S., Thordarson, T. & Keszthelyi, L. 1997. Emplacement of continental flood basalt lava flows. *In:* Mahoney, J.J. & Coffin, M.F. (eds) *Large Igneous Provinces: Continental, Oceanic and Planetary Flood Volcanism*. AGU Geophysical Monograph, **100**, 381–410.

Self, S., Keszthelyi, L. & Thordarson, T. 1998. The importance of pahoehoe. *Annual Review of Earth and Planetary Sciences*, **26**, 81–110.

Self, S., Jay, A.E., Widdowson, M. & Keszthelyi, L.P. 2008. Correlation of the Deccan and Rajahmundry Trap lavas: Are these the longest and largest lava flows on Earth? *Journal of Volcanology and Geothermal Research*, **172**, 3–19.

Single, R.T. & Jerram, D.A. 2004. The 3D facies architecture of flood basalt provinces and their internal heterogeneity: examples from the Palaeogene Skye Lava Field. *Journal of the Geological Society, London*, **161**, 911–926.

Waagstein, R. 1988. Structure, composition and age of the Faeroe basalt plateau. *In:* Morton, A.C. & Parson, L.M. (eds) *Early Tertiary Volcanism and the Opening of the NE Atlantic*. Geological Society, London, Special Publications, **39**, 225–238.

Walker, G.P.L. 1971. Compound and simple lava flows and flood basalts. *Bulletin of Volcanology*, **35**, 579–590.

Received 14 November 2008; revised typescript accepted 2 April 2009.

Understanding the facies architecture of flood basalts and volcanic rifted margins and its effect on geophysical properties

CATHERINE E. NELSON[1]*, DOUGAL A. JERRAM[1], RICHARD T. SINGLE[2] AND RICHARD W. HOBBS[1]

[1] Dept. of Earth Sciences, The University of Durham, South Rd., Durham DH1 3LE, UK.
* Email: c.e.nelson@durham.ac.uk
[2] Senior Geofysiker, Det norske oljeselskap ASA, Bryggegata 9, 0250 Oslo, Norway

ABSTRACT

A review is presented of the current developments in our understanding of the facies architecture of flood basalts and volcanic rifted margins. Basalt sequences are sometimes considered to consist of uniform, homogeneous layers of basalt; however heterogeneity in basalt sequences exists at every scale from that of a lava flow, through lava flow stacking patterns, up to the basin or province scale. The main scales addressed in this review comprise: intrafacies - heterogeneity on a lava flow scale; facies/facies associations – variations on a lava field scale; and seismic facies – the sub-province scale. These scales of heterogeneity are important in the interpretation of flood basalt sequences from a variety of different settings. Examples from the North Atlantic Igneous Province, Paranã-Etendeka, Deccan and Ethiopia are presented, which suggest that there are common facies elements in the generation of flood basalt provinces associated with volcanic rifted margins. Research into facies architecture has the potential to improve imaging beneath basalt sequences through better understanding of the loss of seismic energy caused by the basalt sequence. This is due to both the high impedance contrast between the basalt sequence and the overlying sedimentary succession, and the scattering and production of multiples by the heterogeneity within the basalt sequence. Recent studies have shown that the internal heterogeneity causes more energy loss than the impedance contrast at the surface of the basalt sequence. Accordingly, characterising this internal heterogeneity and incorporating it into 3D models allows the generation of synthetic seismic data, and hence improved strategies for data acquisition and processing.

1 Introduction

Three quarters of the Atlantic rifted margins are estimated to be volcanic, and perhaps as much as 90% of rifted margins worldwide (Menzies *et al*., 2002). In places along these margins, subaerial lava flows were erupted to form flood basalt provinces, especially where the positions of mantle melting anomalies were coincident with the rifted margin (e.g. North Atlantic Igneous Province, Paranã-Etendeka, White and McKenzie, 1989, Jerram and Widdowson, 2005). Substantial volumes of material were also added to the underside of the continental crust via magmatic underplating (Cox 1980; 1993). The distribution of several of the main Cenozoic and Mesozoic flood basalt provinces is highlighted in Figure 1a. These provinces contain enormous volumes of lava; for example the Deccan Volcanic Province has an estimated maximum extrusive volume of c. $1x10^6$ km^3 (Self *et al*., 2006). The North Atlantic Igneous Province (NAIP) (Figure 1b), when its volcanic rifted margins are included, is estimated to have a volume of $1.8x10^6$ km^3 covering an area of $1.3x10^6$ km^2 (Eldholm and Grue, 1994). Provinces such as the NAIP cover some sedimentary basins which are thought to have a high potential for hydrocarbon discovery. Volcanism coincided with the deposition of Palaeocene sediments in the Faroe-Shetland Basin, which contain the Foinaven and

Schiehallion fields in areas without basalt cover (Naylor *et al*. 1999), and the Rosebank discovery within the edge of the basalts. Similar areas are associated with other flood basalt provinces, such as the Kudu Gas Field, offshore Namibia (Jerram *et al*., 1999), associated with the Paranã-Etendeka flood basalts. Areas covered by the Deccan Volcanic Province such as the Saurashtra Peninsula, western India (Sain *et al.*, 2002) and the Kutch Basin, offshore to the west of India (Kumar *et al*., 2004) have also been identified as sub-basalt hydrocarbon prospects. Therefore, a major target in hydrocarbon exploration is to exploit areas with flood basalt cover, which specifically requires good seismic imaging of the structure beneath the basalt sequence, often over 1 km thick.

The aim of this overview is to look at how a facies architecture approach to the study of flood

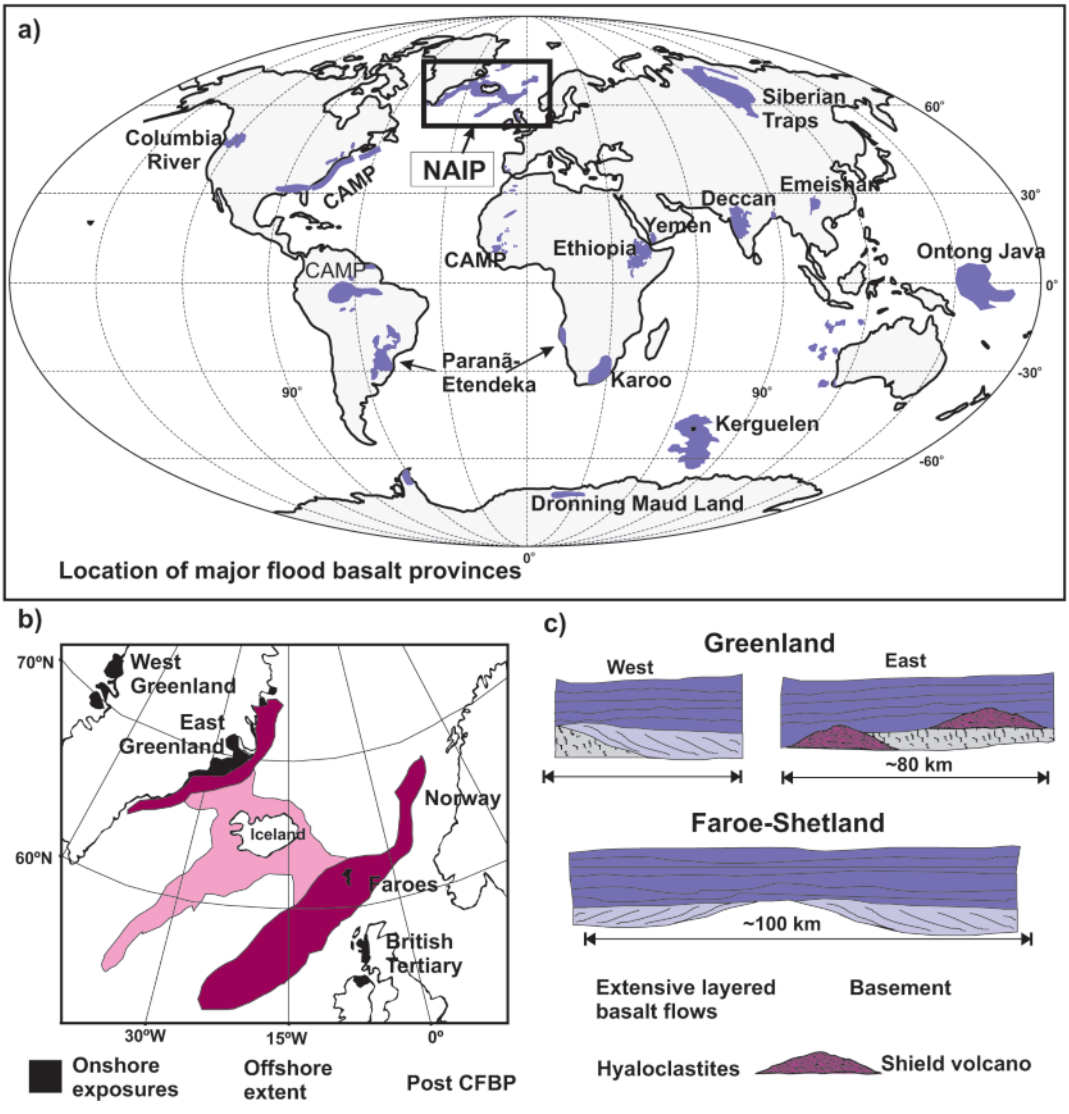

Figure 1. a) Location map of major flood basalt provinces, North Atlantic Igneous Province (NAIP) is highlighted. **b**) Schematic map of the NAIP showing location of onshore exposure. **c**) Schematic E-W cross-section from Greenland to Shetland, showing large scale lateral facies variations (adapted from Jerram and Widdowson, 2005).

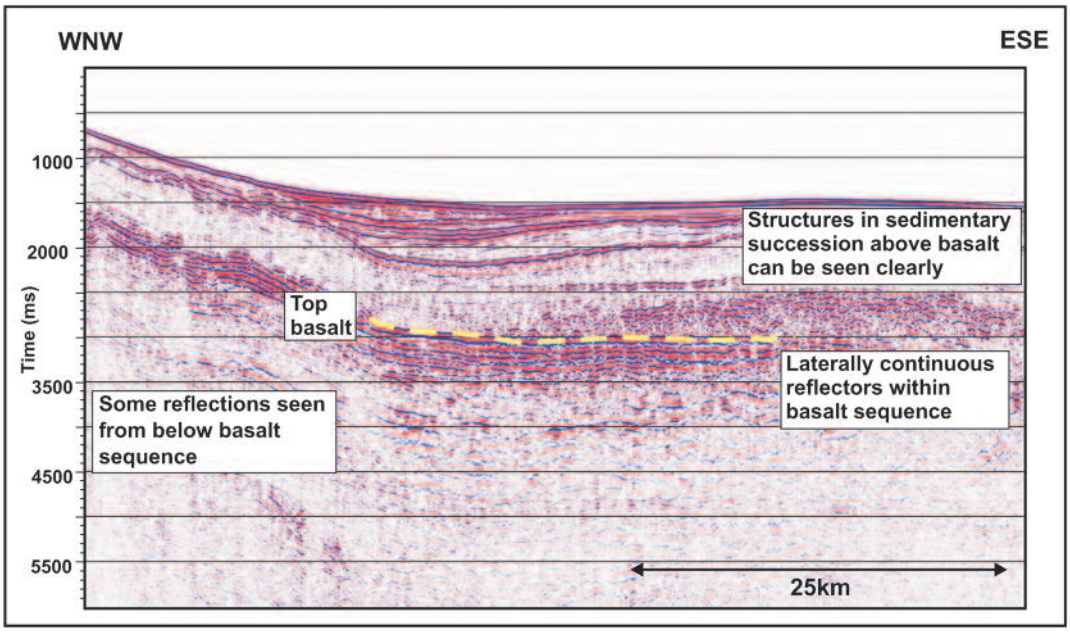

Figure 2. Seismic reflection data from the FAST profile, Faroe-Shetland Basin (England *et al*., 2005). The source was designed to maximise penetration through basalts, using large airguns to increase low-frequency energy. A long offset was used, allowing better multiple suppression by normal moveout strategies.

basalts is of importance in understanding their temporal and spatial evolution in a basin wide context, with specific focus on the potential problems and implications to the successful exploration of sub-basalt basins. Firstly, we will outline some of the problems associated with exploration in flood basalt terrains, and introduce the developing field of flood basalt facies analysis. Focus will then be on the different scales of heterogeneity through the volcanic pile, which will have major effects on remote sensing techniques through such media. These range from heterogeneities at the 0.1 to 10 metre, or lava flow scale (intrafacies), through flow facies variations at the metre to kilometre scale and facies associations up to the seismic scale (km to 10 km). Figure 1c shows schematically how extensive these facies variations can be on a basin-wide scale. Finally, the potential effect of these heterogeneities on geophysical surveying is presented.

1.1 Exploration problems in flood basalts, volcanic rifted margins and associated basins

Seismic reflection surveying has proved good at sub-surface imaging in layered sedimentary sequences. Unfortunately, the presence of thick, layered basalt sequences (consisting predominantly of lava flows and associated lithologies) in flood basalt provinces and volcanic rifted margins creates an environment where very few clear reflections are returned from below the basalt sequence, as demonstrated in Figure 2. The poor imaging below the basalt sequence is due to loss of seismic energy by scattering and attenuation. This is caused by the high impedance contrast between sediments and basaltic lava flows at the top of the basalt succession, and by energy loss within the basalt sequence from its internal heterogeneity. This internal heterogeneity causes more of a problem than the high impedance contrast (Martini and Bean, 2002), causing the production of multiples, scattering due to layering and rubbly flow tops, and transmissions and mode conversions at flow boundaries (Maresh *et al*.,

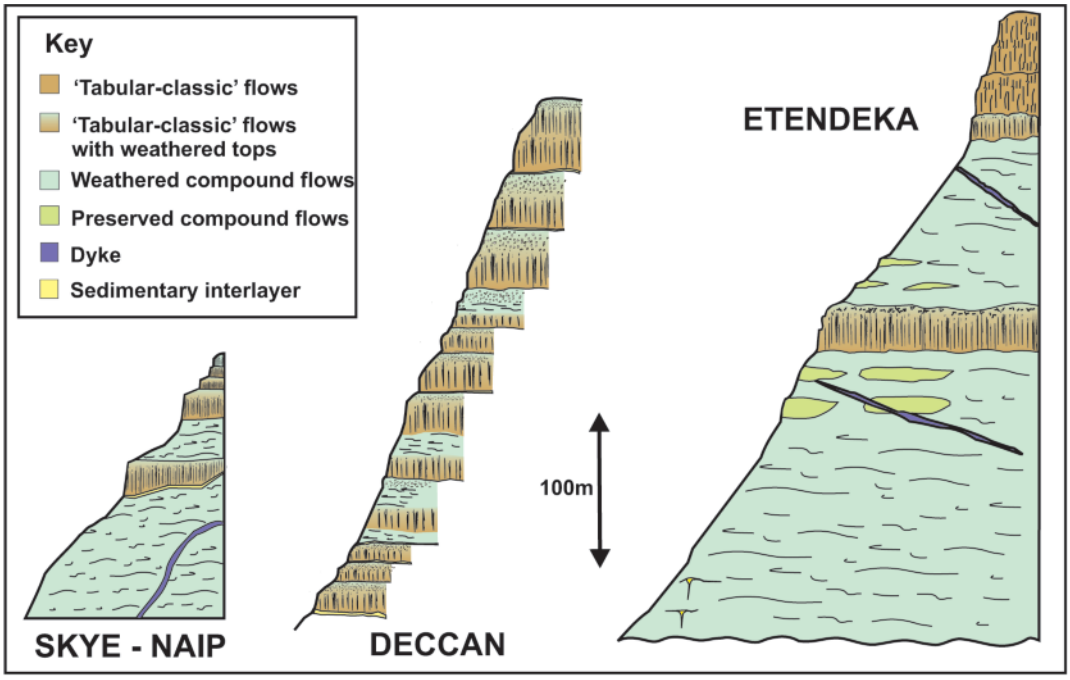

Figure 3. Examples of the internal heterogeneity present in flood basalt provinces. Sections were produced from field sketches. Note that the scale is the same for each example. It can be seen that there is a wide variation in the internal architecture of a flood basalt province - flow thicknesses, numbers and associations all vary within a province and between provinces. Provinces are, however, made of the same "building blocks" allowing classification schemes to be developed, as discussed in Section 2.

2006). The net effect is that higher frequencies are preferentially attenuated.

Recent research by Maresh *et al*. (2006) investigated the cause of the attenuation in layered basaltic lava flows, using a vertical seismic profile from Well 164/07-1. The measured attenuation was considerably higher than predicted from laboratory basalt samples, indicating that either the impedance contrasts caused by layering, or the scattering caused by the rugose interfaces between flows, contributed to the attenuation. Modelling synthetic seismograms showed that the layering caused more attenuation than the rubbly surfaces, and the layering alone could account for the observed attenuation in the borehole data. However, this study only considered the effect of one rubbly surface, and the combined effect of many such interfaces may be significant.

Due to the loss of high frequencies through attenuation, strategies for imaging below basalt sequences have concentrated on the use of low frequencies. Wide-angle surveys have also had some success in imaging the base of the basalt sequence, as fewer interbed multiples are present in long-offset data (White *et al*., 2005). Work has also focussed on optimizing the source and receivers to obtain better low frequency data. Ziolkowski *et al*. (2003) argued for the use of larger airguns and for towing both the seismic source and receiver at a depth of around 20 m below the sea surface. Towing the source at a greater depth allows a reflection from the sea surface, to increase constructive interference at low frequencies (Maresh and White, 2005).

Martini *et al*. (2005) highlighted the need for synthetic seismic data based on realistic 3D geology. A 3D model of a basalt succession could be used for the simulation of realistic seismic data, to test seismic acquisition and processing techniques. This would help to improve imaging

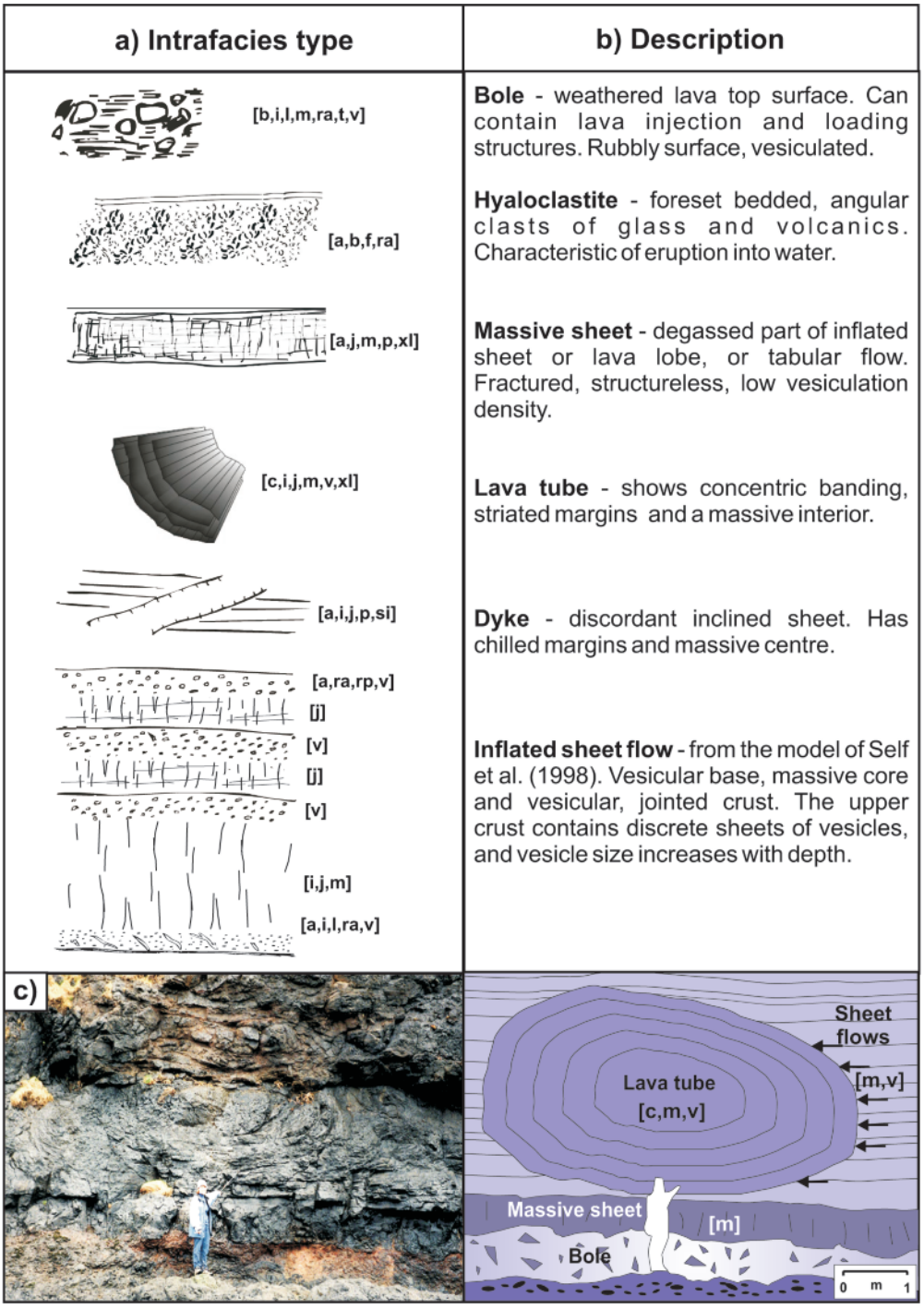

Figure 4. The intrafacies classification scheme. **a**) The components which make up the various facies are indicated next to the diagrams. The abbreviations are as follows: **a** aphanitic margin, **b** bole material, **c** concentric banding, **f** foreset bedding, **i** injection structure, **j** regular jointing, **l** loading structure, **m** massive, **p** porphyritic texture, **ra** rubbly surface, **rp** ropy surface, **si** inclined sheet, **t** tuffaceous material, **v** vesiculated, **xl** medium to coarsely crystalline. Other intrafacies include Flow base, Flow top (unweathered), Sill, Pillow lava and Volcaniclastic. **b**) Descriptions of the different intrafacies shown in a). **c**) An example of various intrafacies from Talisker Bay, Skye, NAIP. There is a high degree of complexity evident in this one small area. For further details on all the intrafacies and their components, see Single and Jerram, 2004.

below the basalt sequence, and provides the purpose for current work outlined in this contribution.

1.2 The developing field of detailed facies analysis in flood basalt terrains

As discussed above, it is the internal heterogeneity of the flood basalt provinces and volcanic rifted margins that give rise to imaging problems. Figure 3 shows three logged sections highlighting the vertical stacking of lava flows preserved in onshore examples of flood basalt sequences. Each lava flow contains internal heterogeneities and this, together with the stacking variations, would give rise to complex seismic characteristics in the offshore setting. Clearly, a simple solid block of massive basalt would present very different seismic characteristics (e.g. an intrusive sill). Characterising this internal heterogeneity would give valuable information on the effect of the basalt sequence on the passage of seismic energy. An additional problem affecting exploration of such areas is the prediction of inter- and intraflow variations. Here, a clear understanding of the volcanic facies distributions and their physical properties is of vital importance.

Although borehole data gives a vertical section, the existence of lateral variations (e.g. Passey, 2004) requires us to use onshore analogues where much more data is available to characterise the 3D nature. Recent studies have investigated the physical characteristics of continental flood basalt provinces, and classification schemes have been developed (see below). No onshore analogues are available for the parts of volcanic rifted margins found further offshore; facies here (such as the outer seaward dipping reflectors facies of Planke *et al*., 2000) have been classified based on their shape and characteristic reflections in seismic data. However, the use of 3D seismic data has led to successful imaging of the structure of sill complexes (e.g. Corfield *et al*., 2004; Thomson, 2005, Smallwood and Maresh, 2002).

The facies concept, used extensively in describing sedimentary rocks, was first applied to volcanic rocks by Cas and Wright (1987). A facies is defined as a body of rock with specified characteristics (Reading, 1986), and these characteristics are definable and distinguish the rock from other facies. The facies is considered to

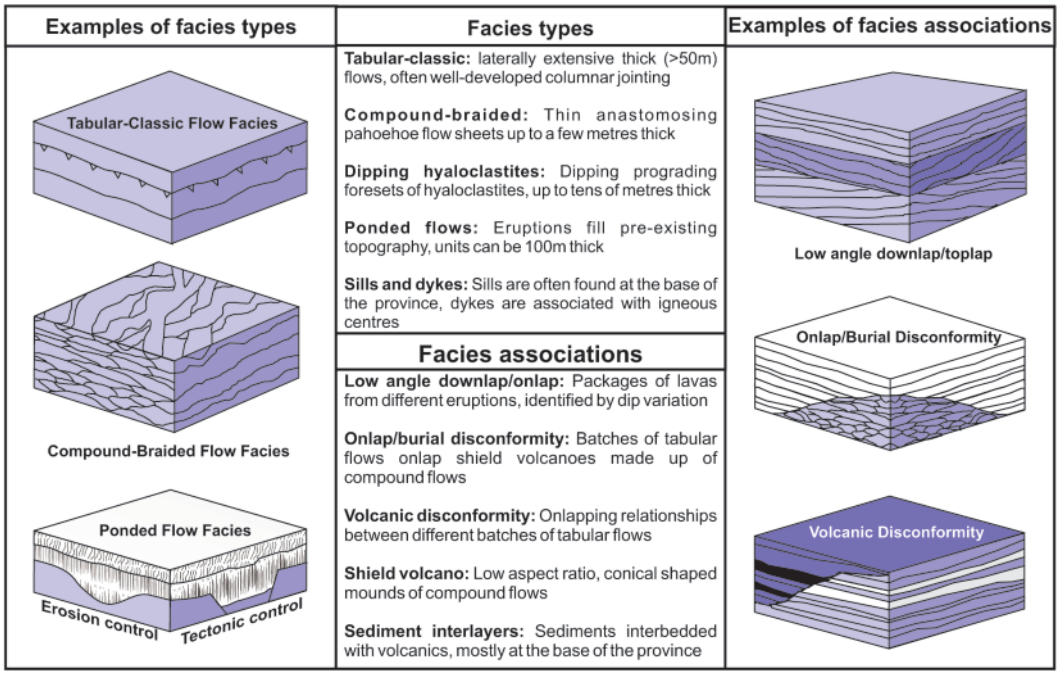

Figure 5. The facies classification scheme. 3D examples of different facies are shown, together with a list of the facies from the classification scheme of Jerram (2002).

be the product of a particular set of conditions (Cas and Wright 1987). In volcanic successions different styles of volcanism, different magma compositions, topographic variations or differences in rates of eruption, produce the various facies (e.g. Jerram, 2002). An understanding of the evolution of a province can thus be gained from facies analysis.

Facies variation has been observed at scales from the individual lava flow to the seismic scale. Classification schemes have been developed by Single and Jerram (2004) (Figure 4) at the intrafacies scale (flow scale variation), at the facies scale (e.g. Jerram, 2002) (Figure 5) and at the seismic scale (e.g. Planke *et al*., 2000) (Table 1). Although these schemes are not fully inclusive of all facies types found in flood basalt provinces, they provide a conceptual means of defining volcanic heterogeneities and comparing between different flood basalt provinces, thus providing a systematic framework for observations. In the following section we will summarise these conceptual facies models and show key examples from a number of onshore flood basalt provinces.

2 Flood basalts and volcanic rifted margins – a facies architecture approach

2.1 How to define key volcanic facies

Cas and Wright (1987) suggested that facies should be defined by two major groups of characteristics. Firstly, the geometry of the facies should be considered - the volume, shape, pre-existing relief and flow direction. Secondly, the lithology is equally important - the composition and the texture. The lithology is subject to later modification by processes such as erosion and alteration. Deformation may also be important as flood basalt provinces are often situated at sites of later rifting. Flood basalt provinces are massive outpourings of predominantly tholeiitic basalt, but also basaltic andesite lava which cover several thousands of square kilometres, and build to a thickness of up to a few kilometres. Yet they are made up of many hundreds or thousands of individual lava flows, with associated sills and dyke facies which vary on the scale of metres and in some cases centimetres. Therefore, it is useful to consider the heterogeneities present at different scales of observation. Below, we consider scales of heterogeneity from 1) intrafacies variations, 2) facies variations and associations and 3) seismic scale variations.

2.1.1 Scales of heterogeneity 1 - intrafacies

To understand the volcanology and physical characteristics of flood basalts it is important to look beyond their geochemical variations, and quantify them from a volcanological perspective. For example, in attempting to understand lava emplacement mechanisms, Self *et al*. (1996; 1997) divided flows into an upper crust, core and basal zone, based on vesicle patterns, jointing style and petrographic texture. The abundance of flows with this three-part structure led to an emplacement model of inflating pahoehoe flows whereby liquid lava is injected under a solidifying crust. This model was proposed as the standard way of emplacing large pahoehoe lava fields (e.g. Self *et al*., 1996).

A similar approach was taken by Single and Jerram (2004), who developed a classification scheme for small-scale heterogeneity within lava flows, which built on the core-crust observations to include bole horizons, lava tubes, small intrusions and so on. Within this scheme, known as the 'intrafacies' scheme (Single and Jerram, 2004), information on rock properties important for geophysical modelling are also included, providing a systematic method of characterising features in lava sequences and allowing comparisons to be made between provinces. A summary of the different intrafacies components is shown in Figure 4.

This intrafacies classification scheme is based on field observations and covers heterogeneities visible at the smallest scale of field observation: the 0.1-10 m scale. These intrafacies can provide information on the method of emplacement, for example if vesicle patterns characteristic of inflated pahoehoe flows are present (e.g. Cashman and Kauahikaua, 1997), and give information on the association of flow breakouts, inflation textures and lava feeder systems (e.g. Single and

Jerram, 2004). Intrafacies components are identified by changes in properties such as fracturing, vesiculation, shape of the feature, and the presence of palaeosols. The effect of these properties on geophysical parameters such as seismic velocity, density and magnetic susceptibility is discussed further in Section 3.1.

2.1.2 Scales of heterogeneity 2 - flow facies and facies associations

Studies of heterogeneity at the facies scale are somewhat more common than those at the intrafacies scale, but they are still relatively few in number. Walker (1972) proposed the terms "simple" and "compound" for describing two very different types of lava flow, based on observations of numerous recent and ancient lava flows. Compound flows are defined as those that are divisible into smaller flow lobes, whereas simple flows are composed of only one flow unit.

Jerram (2002) outlined the major facies types and facies associations providing a systematic way of describing heterogeneity at the metre to kilometre scale (summarised in Figure 5). Facies types described in this scheme include different types of lava flow (incorporating the terminology of Walker, 1972), hyaloclastites, ponded flows, sills and dykes, based on observations made in the Etendeka, Karoo, Columbia River, Ethiopia, Deccan and British Palaeogene provinces. Sedimentary units may also be present as interbeds, and would thus be included in this

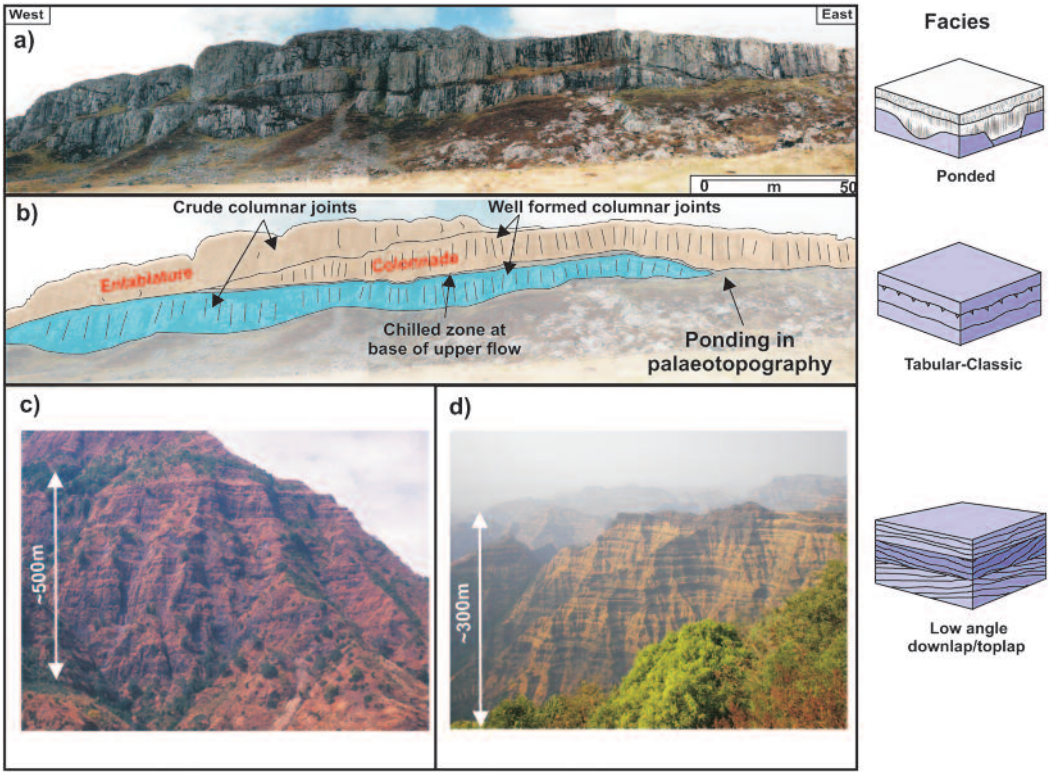

Figure 6. Examples of facies types. **a**) is a cliff section from Talisker Bay, Skye, NAIP. **b**) shows the interpretation. Two flows are present, both showing the tabular-classic facies type. The upper flow shows a well-developed entablature and colonnade structure. The ponded flow facies type is also present here, on the right of the photograph. Also note the onlapping relationship between the two flows a) and b) Examples of ponding and pinch out in thick flows Talisker area, NAIP. Examples of facies associations: Large scale onlap-offlap facies variations in Ethiopia and Deccan. **c**) is from the Ethiopian Traps, Africa. **d**) is from the Deccan Traps, India. Note that the scale is similar - in both areas, this facies association is present on a scale of hundreds of metres. Modified from Jerram 2002; Jerram and Widdowson 2005.

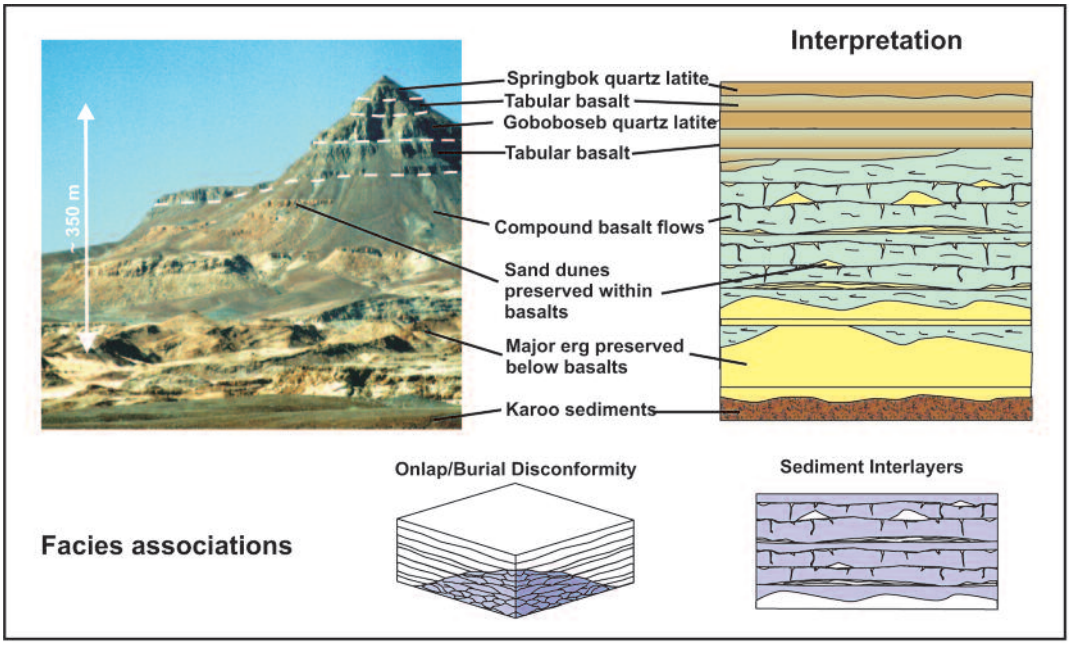

Figure 7. Section through the Etendeka flood basalts, NW Namibia. Compound-braided and tabular-classic flow facies can both be observed here, as well as onlap disconformity and sediment interlayer facies associations.

classification scheme. Examples are shown in Figures 6 and 7. These facies are identified by their characteristic physical properties, and are made up of the intrafacies described above. In common with facies analysis in sedimentary successions, their interpretation is based on analogues with present-day examples. The eruptions of Kilauea, Hawaii, and Laki, Iceland, are the most commonly used analogues, with preserved flood basalt lavas which range in size from examples similar to modern day occurrences to flows that are orders of magnitude larger (Jerram, 2002), with the largest flows having volumes of 1000s of km^3 (e.g. the Roza Member, Columbia River, Self *et al*., 1997).

The study of the relationships between these facies is particularly important when considering offshore examples. Geometrical stacking patterns may be seen on seismic scales, so if we know what causes these patterns in well-exposed onshore examples, we can then begin to identify facies offshore. Characteristic stacking patterns include disconformities, downlap and shield volcanoes. Examples are given in Figures 6 and 7.

The facies classification scheme has been applied successfully in several flood basalt provinces. In the NAIP, Passey and Bell (2007) characterised the morphologies of the Faroe Islands Basalt Group, incorporating a facies approach such as the scheme of Jerram (2002). The three main eruptive sequences (the Beinisvørð, Malinstindur and Enni formations) demonstrate a variety of different facies architectures. The Beinisvørð (previously Lower) Formation is dominated by a 'tabular-classic' facies architecture, which is interpreted as indicating that the flows were erupted as single continuous flows from fissure systems. In contrast, the Malinstindur (previously Middle) formation consists mainly of 'compound-braided' flows, suggesting a different eruptive style whereby flows were not erupted continuously, but at longer time intervals from separate shield volcanoes. The Enni (previously Upper) formation has a mixture of the two facies architectures. Hyaloclastite and sill facies are also present (Ellis *et al.*, 2002; Rasmussen and Noe-Nygaard, 1970). Single (2004) also studied the NAIP - in this case, the facies architecture of the Talisker Bay area, Skye.

A series of tabular-classic flows was found overlying compound-braided flows, with a transitional sequence in between.

Jerram and Widdowson (2005) showed how facies variations may successfully be compared across different provinces. The architecture of the Deccan, the Paranã-Etendeka and the NAIP was considered; despite many differences between the provinces, there are some key similarities. All show initial low-volume eruptions followed by a main phase of relatively short duration (1-5Ma). This main phase is often characterised by large volume, extensive tabular flows.

The characteristic associations of these facies are important in developing models of the basin as a whole. In the NAIP and the Paranã-Etendeka, early shield volcanoes were buried by later large-volume flat-lying tabular flows, creating volcanic disconformities (Jerram and Widdowson, 2005). The Ethiopian flood basalt province, where the top of the flood basalt sequence is preserved, contains a series of flood basalts overlain by large shield volcanoes (Kieffer *et al*., 2004). Clearly the relative abundance and distribution of key facies within flood basalt sequences will help define their evolution both spatially and temporally, particularly below the resolution of or in the absence of geochronological markers.

2.1.3 Scales of heterogeneity 3 - seismic scale

Seismic imaging can pick out features greater than 50 m thick, so individual lava flows (typically 5-30 m thick) cannot be identified. A certain amount of heterogeneity is, however, still apparent within processed seismic data. This has been characterised by Planke *et al*. (1999; 2000) who developed a facies classification scheme at the seismic scale (1 to 10's of kilometres). Their scheme is summarised in Table 1, and is based on seismic reflection data from the Atlantic and Western Australia volcanic rifted margins. The different facies were identified by their gross form, and the reflection characteristics of their boundaries and internal reflections.

In order to gain a better understanding of offshore basaltic successions, the use of onshore

Facies	**Shape**	**Characteristics**	**Probable flow scale components**
Inner flows	Sheet	High amplitude top reflector, high amplitude parallel internal reflectors	Mixture of compound and tabular facies and volcaniclastics; subaqueous.
Lava delta	Bank	Prograding clinoform internal reflectors	Hyaloclastites and volcaniclastics; coastal
Landward flows	Sheet	High amplitude top reflector, high amplitude parallel internal reflectors	Mixture of compound and tabular facies; subaerial.
Inner Seaward Dipping Reflectors (SDR)	Wedge	Divergent-arcuate internal reflectors, toplap seen on top reflector	Mixture of compound and tabular facies; subaerial.
Outer high	Mound	Strong top reflector, chaotic internal reflector	Hyaloclastites and volcaniclastics; shallow marine
Outer SDR	Wedge	Divergent-arcuate internal reflectors, weaker than Inner SDR	Deep marine compound facies, pillow lavas, sediments and sills.

Table 1. Summary of the seismic scale facies of Planke *et al.* (1999; 2000) and their probable flow scale components (e.g equivalents of Jerram 2002).

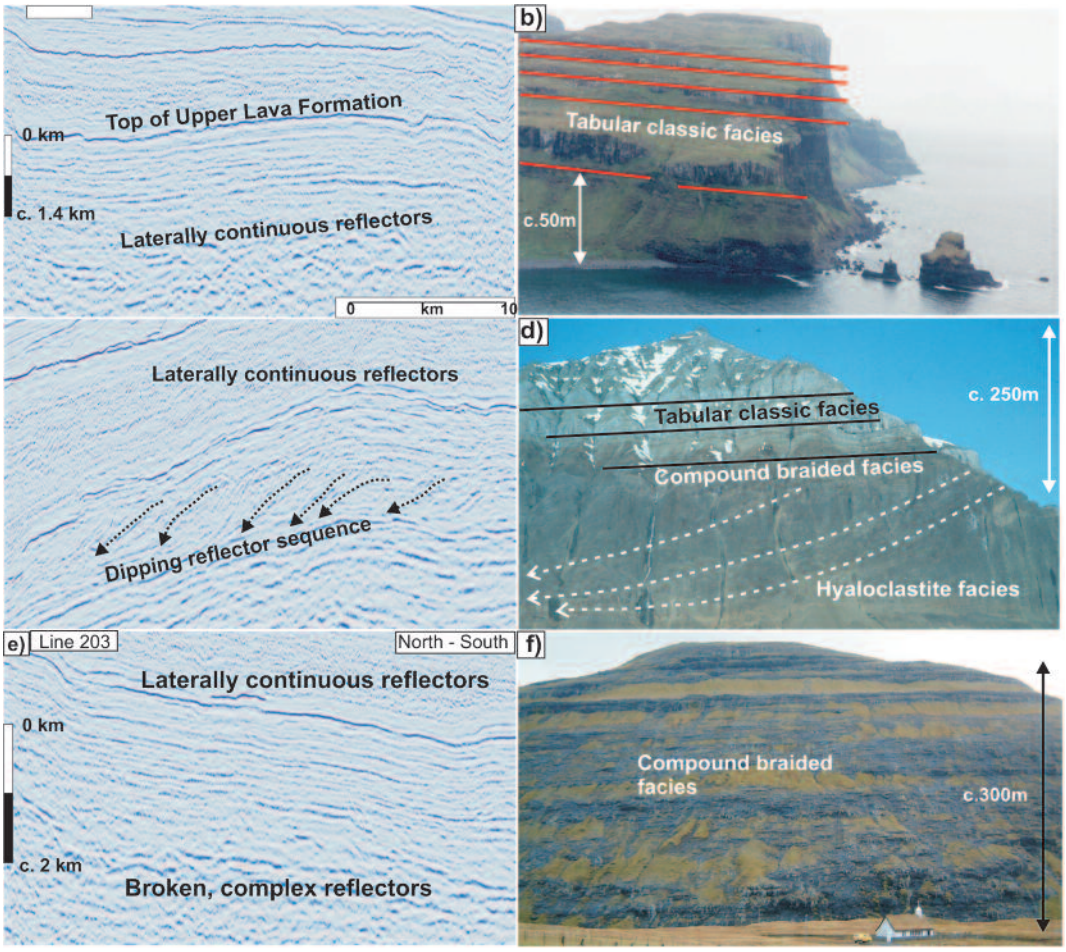

Figure 8. Facies observed in seismic sections and onshore analogues. **a**) Section of GFA-99 line 205 interpreted as showing tabular-type facies. The GFA-99 seismic data was collected approximately 60km SE of the Faroe Islands in the Faroe-Shetland Basin. **b**) Example of thick tabular flows from Talisker Bay, Skye. **c**) Section of GFA-99 line 107 showing dipping reflector sequences interpreted as hyaloclastite facies. Section changed from W-E to E-W for comparison with onshore analogue. **d**) Cliff section in the Nausuaq area, West Greenland shows hyaloclastites dipping and prograding eastwards onto Jurassic sediments. The hyaloclastites are covered by subaerial compound and tabular flows; this section is interpreted as filling a water-filled basin. Photograph courtesy of D.G. Pearson. **e**) Section of GFA-99 line 203 showing contrasting seismic signatures. **f**) These different seismic signatures are interpreted as compound braided facies overlain by tabular classic facies. An example of compound braided facies is shown from NW Streymoy, Faroe Islands. Seismic data courtesy of Western-Geco.

analogues is crucial to the interpretation of seismic data. In table 1 we consider the possible flow scale components which make up the seismic scale facies described by Planke *et al.* (1999; 2000). In the offshore region around the Faroe Islands, it has proved possible to correlate onshore observations with offshore seismic data. Ellis *et al.* (2002) determined the offshore extent of the Lower, Middle and Upper Lava Formations from seismic data. Passey (2004) correlated material from Well 214/04-1 (240 km east of the Faroe Islands) with the Lower Basalt Formation, based on geochemical data, although there is also evidence of a lateral facies change. Seismic interpretation

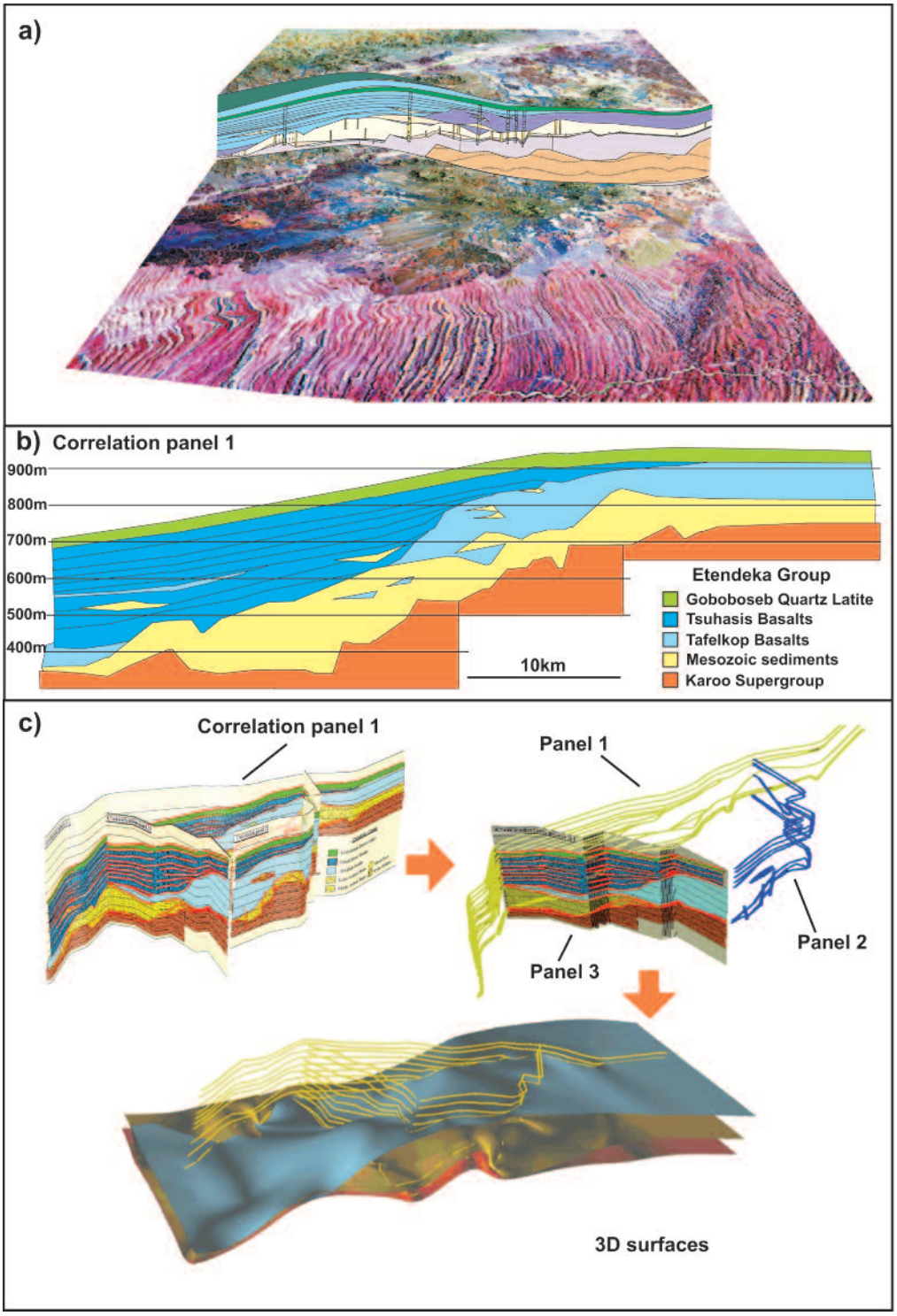

Figure 9. Construction of a 3-D model from surfaces identified on correlation panels. **a**) Fully geo-spatially constrained logs and correlation panels. Data based on detailed satellite located logs. 3D data collected for key surfaces through the lava sequence can include many types of data such as satellite, laser scanning, 3D located logs and so on. **b**) A correlation panel of key surfaces is constructed through logged data (e.g. Jerram *et al*., 1999). **c**) Panels orientated into true 3-D position, key surfaces identified from the 3 correlation panels, and 3-D surfaces reconstructed as GoCad™ interpolated surfaces (adapted from Jerram and Robbe, 2001).

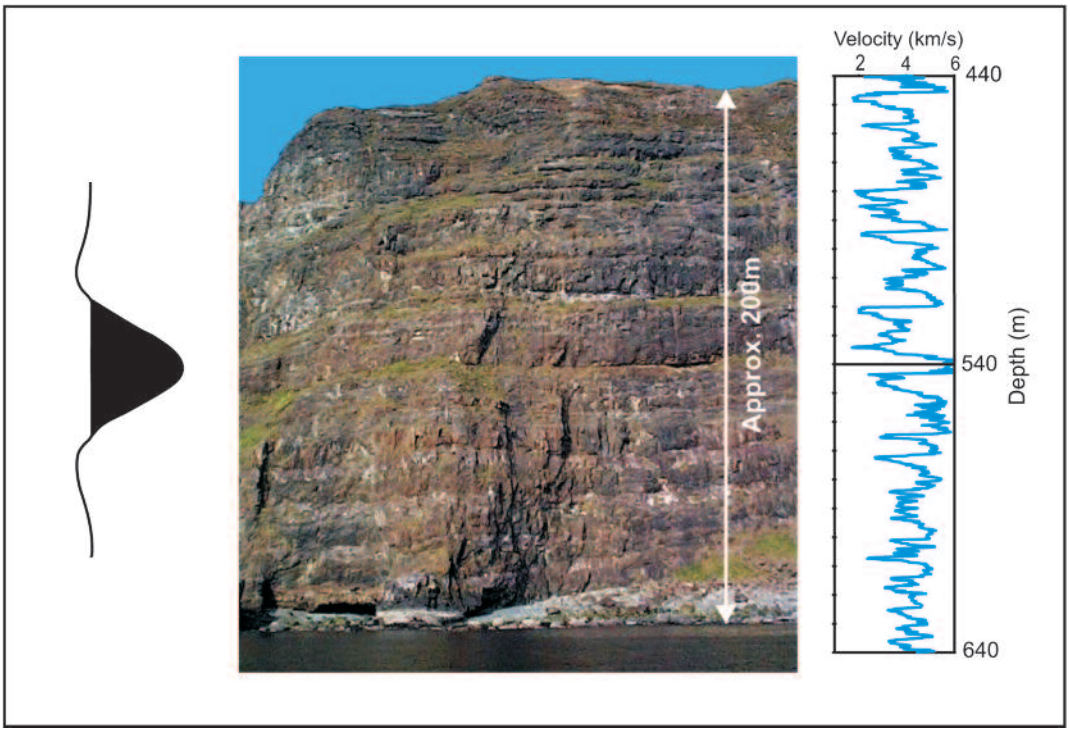

Figure 10. Schematic representation of the effects of basalt heterogeneity on the velocity profile through a lava pile. All elements of this diagram are on approximately the same scale. Photo from Skye Main Lava Series showing a typical layered basalt sequence. A seismic wavelet is included for comparison. The velocity profile is taken from ODP Hole 642E (Eldholm *et al*., 1987) and shows the wide and rapid variation in P-wave velocity.

by Single (2004) identified tabular lavas, delta fans, compound braided flows and hyaloclastites, with direct analogues onshore (Figure 8). These facies were identified by their characteristic shapes and internal reflections. The thickness and areal extent of these facies were also calculated with the aid of gravity models along the seismic lines.

2.2 3D geological models

As can be seen from the facies associations of Jerram (2002), heterogeneity within a flood basalt sequence is not limited to 1D layering. The protracted build-up of lava packages results in marked lateral variations within the provinces (e.g. Jerram and Widdowson, 2005). These lateral facies variations exist and must be taken into account in geophysical modelling of areas with flood basalt cover. Constructing 3D models allows improved geophysical modelling (see Section 3), as well as improved understanding of the evolution of flood basalt provinces. As yet, limited examples of 3D geological models of flood basalt basins exist. However, there is promising initial work on reconstructing onshore flood basalt basin analogues. This aims to capture further information on heterogeneities and facies distributions as well as providing realistic geometries for geophysical modelling. Jerram and Robbe (2001) produced a 3D geological model in GoCad™ for the Etendeka region in Namibia (Figure 9), and were able to use this to map out a palaeo-shield volcanic feature in the sequence. Further detailed examples have been constructed for the Skye lavas in the British Palaeogene (e.g. Single and Jerram, 2004), and for the offshore Faroe-Shetland (Single 2004).

3 A geophysical perspective

To improve sub-basalt imaging, it is necessary to understand the effect of a layered, heterogeneous basalt sequence on the seismic wave. This is currently poorly constrained; it is known that a flood basalt sequence causes scattering and preferentially attenuates high frequencies (Maresh *et al*., 2006). Knowledge of how the heterogeneity within the basalt sequence affects the seismic wave will enable optimisation of the seismic method. Figure 10 schematically highlights some of the geophysical problems that a thick basalt sequence would cause. Accordingly, in the following section some of the issues related to the geophysical response of basaltic sequences will be explored.

3.1 Relating basaltic facies to geophysical properties

To ascertain how the geological heterogeneity affects geophysical data, it becomes necessary to link physical rock properties to the different facies. Methods to distinguish between facies include the amount of vesiculation, jointing, flow thickness, colour, shape of the feature and so on. We must determine which of these also affect geophysical data. The different physical properties that affect geophysical surveying methods are summarised in Table 2.

We can say qualitatively that these rock properties affect the various geophysical methods, based on our knowledge of, for example, the relationship between jointing and seismic velocity. Unfortunately, no studies have yet quantified the relationship between the physical properties and the geophysical data. The rock properties are complex and change dramatically over centimetre scales.

However, the effect of the variations in rock properties can be observed in borehole data. Both commercial and academic boreholes have penetrated thick basalt sequences and wireline logs recorded include sonic, density, gamma ray and resistivity. Site 642 of Ocean Drilling Program (ODP) Leg 104, on the Vøring margin, was one of the first drill holes to penetrate deeply into a volcanic margin sequence. Approximately 687m of basaltic lava flows were cored and logged, and 137 individual lava flows were identified (Eldholm *et al.*, 1987). The internal structure of the lava flows was identified from the core, and Planke (1994) correlated variations in logging measurements with the internal structure of the lava flows. A cyclic pattern was observed in the velocity, density, resistivity, porosity and gamma ray logs, and an example of the cyclicity present in the velocity log is presented in Figure 10.

This cyclic pattern has also been observed in other drill holes. Planke and Cambray (1998) reported similar data from Hole 917A (East

Geophysical method	Operative physical property	Rock properties which may affect this
Seismic	Seismic velocity and density	Vesicularity, jointing, geochemistry, degree of alteration, size of flow, shape of flow
Gravity	Density	Vesicularity, geochemistry, degree of alteration
Resistivity	Electrical conductivity	Vesiculation, geochemistry, degree of alteration, jointing, pore fluid
Magnetic	Magnetic susceptibility and remanence	Geochemistry, degree of alteration

Table 2. Adapted from Kearey *et al*. (2002) and Single (2004).

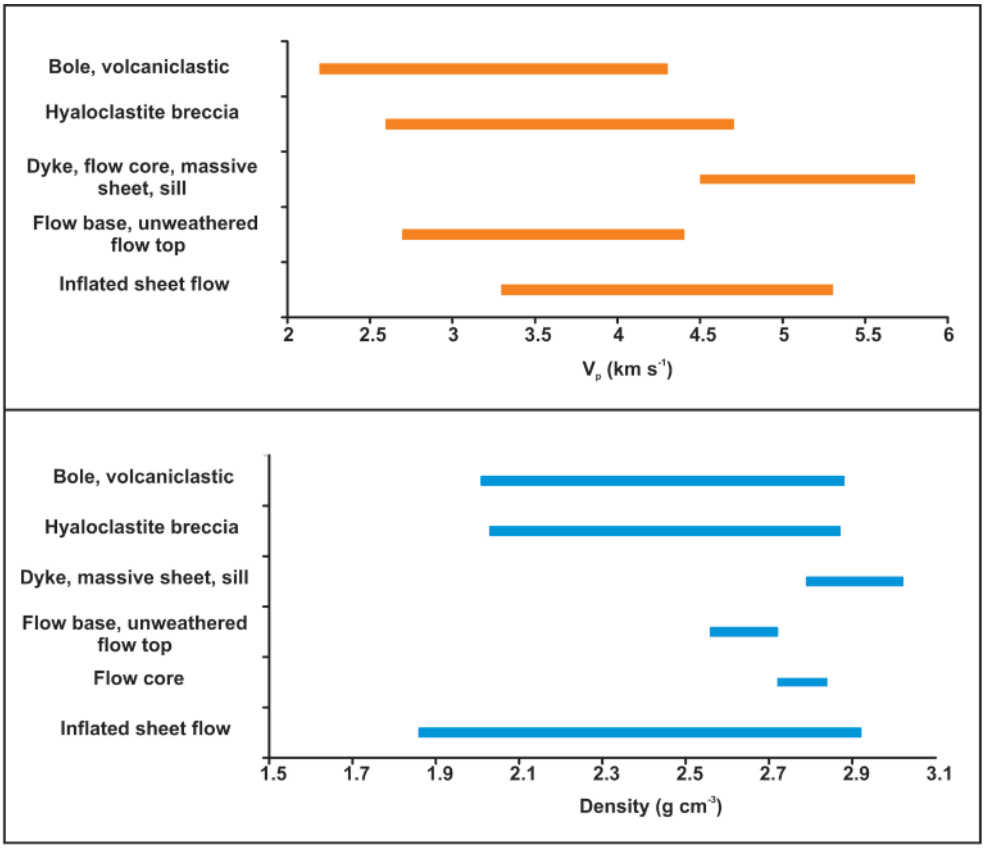

Figure 11. Physical properties of different intrafacies. **a**) P-wave velocities for the different intrafacies. It can be seen that there is a wide velocity range. Massive intrafacies such as dykes and flow cores are faster, while more vesicular intrafacies such as boles are slower. The inflated sheet flow shows a range. **b**) Densities for the different intrafacies. Again, there is a wide range, from high density flow cores to low density boles. Data from the SIMBA database.

Greenland Margin). Bücker *et al.* (1998) summarised the data from ODP Holes 553A and 990A, where the cyclic pattern is also observed. A similar pattern can also be seen in Well 164/7-1 in the Rockall Trough (Archer *et al.*, 2005) and the Lopra 1/1A borehole on the Faroe Islands (Boldreel, 2006).

In all cases where core was also recovered, a strong correlation was found between the flow structure and the log responses. The log response reflects the three-part structure commonly observed in basalt flows, described by Self *et al.* (1997) and summarised in Section 2.1.1 above. The flow core corresponds to a high velocity, high density, and low gamma ray interval on the wireline log data (e.g. Planke 1994; Boldreel 2006). The flow crust is correlated to a lower velocity, lower density, and high gamma ray interval. This correlation is possible because the internal structure of the basalt flows is present as variations in the amount of vesicles, jointing and weathering of the basalt. These variations also indicate the boundaries between flows and strongly affect conventional logging tools.

As yet, few studies have linked this borehole data to the facies observed onshore. The EU 5th Framework SIMBA (ENK6-CT-2000-00075) project collated a database from various wells in the North Atlantic (Single, 2004). From this, the range of P-wave velocities and densities present for the different intrafacies has been identified, and the results are shown in Figure 11. It is

immediately apparent that there is a wide velocity range within a basalt succession, which must be taken into account in geophysical models involving basalt sequences. Boles, volcaniclastics, flow bases and flow tops all have a relatively low P-wave velocity (around 2.5-4.5 km s^{-1}) whereas dykes, flow cores and sills have a relatively high P-wave velocity (around 4.5-6 km s^{-1}. A similar pattern is observed for density, although boles, volcaniclastics and hyaloclastites have a wide range. It can also be seen that the different intrafacies cannot be distinguished by the range of velocities and densities alone. Fully characterising the different facies in terms of their logging properties would be an important step towards building accurate geophysical models of basalt sequences.

3.2 How does heterogeneity affect seismic data?
We have seen in previous sections that basalt sequences are heterogeneous at a variety of scales. As discussed in section 1.1, a basalt sequence causes attenuation of high frequency seismic waves by scattering and the production of multiples. In this section, the theoretical basis for the effect of heterogeneity on the seismic wave is examined, focussing in particular on the different types of scattering caused by different scales of heterogeneity. A heterogeneity, as discussed in this section, is for example a lava flow crust, which is different to the flow core above and below it. A flow crust is typically of the order of one to ten metres thick, depending on the overall flow thickness, so an average heterogeneity for a lava crust could be considered as 5 m.

Figure 12 shows the interplay between the size of the heterogeneity, the seismic wavelength of the input pulse, and the length of the travel path of the seismic wave. The labelled boxes correspond to the approximations that can be used to correct for the scattering, and thus obtain clear reflections. "Geometric optics" are the simple rules of reflection and refraction. The heterogeneity (a) is large relative to the wavelength (λ) and the travel path (L). Therefore, a coherent reflection is received from the boundary of the heterogeneity, and it can be imaged. In the "Diffraction theory" region, it is still possible to image the heterogeneity, provided that diffraction is taken into account and single scattering approximations (e.g. Born theory, Aki and Richards, 1980) can be used.

"Quasi-homogeneous" means that the seismic wave only responds to the average properties of the region it travels through - the heterogeneity is so small relative to the wavelength that it does not affect the seismic wave. No measurable reflection is received from the boundary of the heterogeneity.

In the "Saturated region", the seismic wave encounters a large number of heterogeneities that are large relative to the wavelength. The seismic energy undergoes multiple reflection events creating a complex path, which can no longer be analysed by conventional approximations. The saturated region expands or contracts depending on the scattering strength - this is greater if the heterogeneities exhibit a large velocity and density contrast. Figure 12 shows how the saturated region expands for a material with a high scattering strength such as a layered basalt sequence.

If we consider a layered basalt sequence with a thickness of 2000 m, the two-way travel path of a seismic wave through this sequence (L) has a value of 4000 m. A typical heterogeneity size (a), for example a flow crust as described above, would be around 5 m. $\frac{L}{a}$ in this case is 800, which plots on the y-axis of Figure 12. If a high frequency seismic wave, with a frequency of 40 Hz, passes through the basalt sequence, λ is 100m if the average velocity is 4000 m s^{-1}. ka (on the x-axis) is thus approximately 0.3 (Point A on Figure 12). If a low frequency seismic wave (10 Hz) passes through this basalt sequence, ka is approximately 0.79 (Point B on Figure 12). It can be seen that a low frequency wave (Point B) falls within the "Diffraction regime", whereas a high frequency wave falls on the boundary of the "Saturated region". This more complex scattering at high frequencies explains why low frequency waves have produced better imaging through basalt sequences.

Figure 12 may also be able to predict which approximations could be used when attempting to image the different facies. It may be able to give information on which facies can be better imaged.

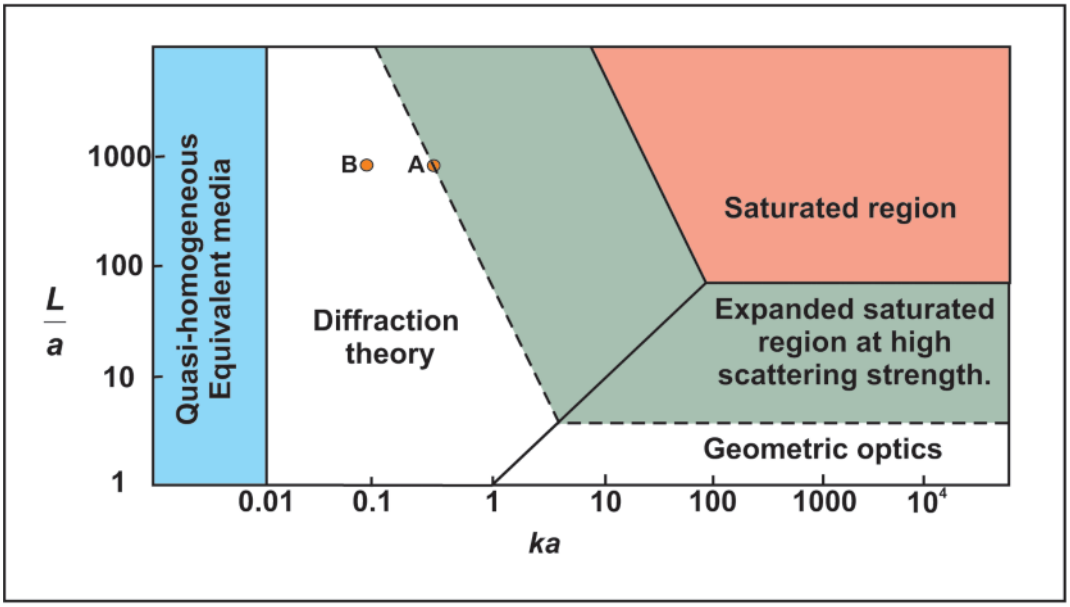

Figure 12. Classification of scattering problems in heterogeneous media. Regions where different methods of analysis can be used are highlighted. *L* is the extent of the heterogeneous region, or the distance the seismic wave travels (the travel path). *a* is the size of the heterogeneity. *k* (the wavenumber) is where λ is the wavelength. Adapted from Wu and Aki, 1988.

For example, a hyaloclastite sequence has small internal impedance contrasts, so it has a weak scattering strength. The saturated region is smaller in this case, so the likelihood of clear imaging is greater. A sequence comprising compound-braided facies would contain many strong impedance contrasts between the flow crust and the flow core. Its scattering strength would therefore be stronger, and the saturated region would be larger. More work is needed to characterise the size of the heterogeneities in the different facies, the average velocity within the facies, and the thickness of the sequence. This will allow the construction of diagrams similar to Figure 12, with appropriately sized regions depending on the scattering strength.

4 Summary and closing remarks

Understanding flood basalts and volcanic rifted margins in terms of their properties (size and geometry of key facies, physical properties of the rocks) and how these relate to their geophysical responses is an important emerging subject. It is also useful to consider whether the inverse is possible: can we derive information on facies from geophysical data? There are still relatively few studies of the facies architecture of flood basalts and volcanic rifted margins, but they have the potential to help improve sub-basalt imaging and our knowledge of the development of the lava sequences.

Improved data on geometric and facies changes within basalt sequences will enable the creation of more robust models of flood basalt provinces, which in turn will help us understand how they relate to geophysical problems. This will facilitate better data acquisition and processing. Within this context, much more information is required about the scale of flood basalt lavas. Current information is often skewed to data from the few largest lava flows (e.g. Roza Mbr, Columbia River Basalts; Self *et al*., 1996), as these have been well mapped out. Current data on 3D geometries and volumes is limited for the various facies types described in this contribution.

The role of hyaloclastites in the onset of flood

volcanism should be another focus for future research. In many cases, for example in the NAIP, the occurrence of thick hyaloclastite sequences (up to 700 m in Greenland) requires deep waterways. The presence of such deep waterways needs to be accounted for in our models of uplift due to plume impact (e.g. White and McKenzie, 1989). They can also be mapped out to define the palaeo-environments immediately prior to flood basalt eruption. Additionally, the role of hyaloclastites as potential hydrocarbon reservoirs warrants further investigation.

The incorporation of additional imaging techniques such as MT and Gravity (e.g. Hautot *et al*., 2007) has proved successful, and multidisciplinary studies such as SIMBA (CONTRACT N°: ENK6-CT-2000-00075; EU 5th Framework), have provided a template for the integrated approach we must take to understanding flood basalts and associated basins in the offshore setting. Strength may be gained by the combined approach to characterising flood volcanic sequences and their associated margins. With geologists and geophysicists working together, it will be possible to overcome some of the main issues and to develop new strategies for further exploration.

Acknowledgements

DAJ is the TOTAL lecturer at Durham University. This work was supported by funding provided to DAJ by Elf/TOTAL GRC and the EU 5th Framework Project SIMBA (CONTRACT N°: ENK6-CT-2000-00075). The GFA-99 survey data were acquired by WesternGeco and made available to the SIMBA project researchers. RWH is a NERC Advanced Research Fellow (NERC/J/S/2002/00745).

References

Aki, K. and Richards, P.G. 1980. *Quantitative seismology: theory and methods Volume II*. W.H Freeman and Company, San Francisco.

Archer, S.G., Bergman, S.C., Iliffe, J., Murphy, C.M. and Thornton, M. 2005. Palaeogene igneous rocks reveal new insights into the geodynamic evolution and petroleum potential of the Rockall Trough, NE Atlantic Margin. *Basin Research* 17: 171-201.

Boldreel, L.O. 2006. Wireline log-based stratigraphy of flood basalts from the Lopra-1/1A well, Faroe Islands. *In*: Chalmers, J.A. and Waagstein, R. (eds) *Scientific results from the deepened Lopra-1 borehole, Faroe Islands*. Geological Survey of Denmark and Greenland Bulletin 9: 7-22.

Bücker, C.J., Delius, H., Wohlenberg, J. and Leg 163 Shipboard Scientific Party. 1998. Physical signature of basaltic volcanics drilled on the northeast Atlantic volcanic rifted margins. *In*: Harvey, P.K. and Lovell, M.A. (eds) *Core-Log Integration*, Geological Society, London, Special Publications 136: 363-374.

Cas, R.A.F. and Wright, J.V. 1987. *Volcanic successions: modern and ancient.* Allen and Unwin, London.

Cashman, K.V. and Kauahikaua, J.P. 1997. Reevaluation of vesicle distributions in basaltic lava flows. *Geology* 25: 419-422.

Corfield, S.M., Wheeler, W., Karpuz, R., Wilson, M. and Helland, R. 2004. Exploration 3D seismic over the Gjallar Ridge, Mid-Norway: visualization of structures on the Norwegian volcanic margin from Moho to seafloor. *In*: Davies, R.J., Cartwright, J.A., Stewart, S.A., Lappin, M., Underhill, J.R. (eds) *3D Seismic Technology: Application to the Exploration of Sedimentary Basins*. Geological Society, London, Memoirs 29: 177-185.

Cox, K.G. 1980. A model for flood basalt volcanism. *Journal of Petrology* 21: 629-650.

Cox, K.G. 1993. Continental magmatic underplating. *Philosophical transactions of the Royal Society of London A* 342: 155-166.

Eldholm, O., Thiede, J., Taylor, E. and Shipboard Scientific Party, 1987. *Proceedings of the Ocean Drilling Program, Initial Reports* 104: College Station, TX (Ocean Drilling Program).

Eldholm, O. and Grue, K. 1994. North Atlantic volcanic margins: dimensions and production rates. *Journal of Geophysical Research* 99: 2955-2968.

Ellis, D., Bell, B. R., Jolley, D. W. and O'Callaghan, M. 2002. The stratigraphy, environment of eruption and age of the Faroes Lava Group, NE Atlantic Ocean. *In*: Jolley, D.W. and Bell, B.R. (eds) *The North Atlantic Igneous Province: Stratigraphy, Tectonic, Volcanic and Magmatic Processes*. Geological Society, London, Special Publications 197: 253-269.

England, R.W., McBride, J.H. and Hobbs, R.W. 2005. The role of Mesozoic rifting in the opening of the NE Atlantic: evidence from deep seismic profiling across the Faroe-Shetland Trough. *Journal of the Geological Society, London* 162: 661-673.

Hautot, S., Single, R. T., Watson, J., Harrop, N., Jerram, D. A., Tarits, P., Whaler K. and Dawes, G. 2007 3-D magnetotelluric inversion and model validation with gravity data for the investigation of flood basalts and associated volcanic rifted margins *Geophys. J. Int*. 170: 1418-1430.

Jerram, D.A., Mountney, N. and Stollhofen, H. 1999. Facies architecture of the Etjo Sandstone Fm. and its interaction with the Basal Etendeka flood basalts of NW Namibia: implications for offshore analogues. *In*: Cameron, N., Bate, R. and Clure, V. (eds) *The oil and gas habitats of the South Atlantic*. Geological Society, London, Special Publications 153: 367-380.

Jerram, D.A. and Robbe, O. 2001. Building a 3-D geologic model of a Flood Basalt: an example from the Etendeka, NW Namibia. *Electronic Geosciences* 6:1.

Jerram, D.A. 2002. Volcanology and facies architecture of flood basalts. *In*: Menzies, M.A., Klemperer, S.L., Ebinger, C.J. and Baker, J. (eds) *Volcanic Rifted Margins*. Geological Society of America Special Paper 362: 121-135.

Jerram, D.A. and Widdowson, M. 2005. The anatomy of Continental Flood Basalt Provinces: geological constraints on the processes and products of flood volcanism. *Lithos* 79: 385-405.

Kearey, P., Brooks, M. and Hill, I. 2002. *An Introduction to Geophysical Exploration*. Third Edition, Blackwell Science Publications, Oxford.

Kieffer, B., Arndt, N. Lapierre, H. Bastien, F., Bosch, D., Pecher, A., Yirgu, G., Ayalew, D., Weis, D., Jerram, D.A., Keller, F. and Meugniot, C. 2004. Flood and Shield Basalts from Ethiopia: Magmas from the African Superswell. *Journal of Petrology* 45: 793-834.

Kumar, D., Bastia, R. and Guha, D. 2004. Prospect hunting below Deccan basalt: imaging challenges and solutions. *First Break* 22: 35-39.

Maresh, J. and White, R.S. 2005. Seeing through a glass, darkly: strategies for imaging through basalt. *First Break* 23: 27-33.

Maresh, J., White, R.S., Hobbs, R.W. and Smallwood, J.R. 2006. Seismic attenuation of Atlantic margin basalts: Observations and modelling. *Geophysics* 71: B211-B221.

Martini, F. and Bean, C.J. 2002. Application of pre-stack wave equation datuming to remove interface scattering in sub-basalt imaging. *First Break* 20: 395-403.

Martini, F., Hobbs, R.W., Bean, C.J. and Single, R.T. 2005. A complex 3D volume for sub-basalt imaging. *First Break* 23: 41-51.

Menzies, M.A., Klemperer, S.L., Ebinger, C.J. and Baker, J. 2002. Characteristics of volcanic rifted margins. *In*: Menzies, M.A., Klemperer, S.L., Ebinger, C.J. and Baker, J. (eds) *Volcanic Rifted Margins*. Geological Society of America Special Paper 362: 1-14.

Naylor, P.H., Bell, B.R., Jolley, D.W., Durnall, P. and Fredsted, R. 1999. Palaeogene magmatism in the Faroe-Shetland Basin: influences on uplift history and sedimentation. *In*: Fleet, A.J. and Boldy, S.A.R. (eds) *Petroleum Geology of Northwest Europe: Proceedings of the 5th Conference*: 545-558.

Passey, S.R. 2004. *The Volcanic and Sedimentary Evolution of the Faroe Plateau Lava Group, Faroe Islands and Faroe-Shetland Basin, NE Atlantic.* PhD thesis, University of Glasgow.

Passey, S.R. and Bell, B.R. 2007. Morphologies and emplacement mechanisms of the lava flows of the Faroe Islands Basalt Group, Faroe Islands, NE Atlantic Ocean. *Bulletin of Volcanology* DOI: 10.1007/s00445-007-0125-6.

Planke, S. 1994. Geophysical response of flood basalts from analysis of wireline logs: Ocean Drilling Project Site 642, Vøring volcanic margin. *Journal of Geophysical Research* 99: 9263-9278.

Planke, S., Cambray, H. 1998. Seismic properties of flood basalts from Hole 917A downhole data, Southeast Greenland volcanic margin. *In*: Saunders, A.D., Larsen, H.C. and Wise, S.W. (eds) *Proceedings of the Ocean Drilling Program, Scientific Results*. Volume 152: 453-462.

Planke, S., Alvestad, E. and Skogseid, J. 1999. Seismic characteristics of basaltic extrusive and intrusive rocks. *The Leading Edge* 18: 342-348.

Planke, S., Symonds, P.A., Alvestad, E. and Skogseid, J. 2000. Seismic volcanostratigraphy of large-volume basaltic extrusive complexes on rifted margins. *Journal of Geophysical Research* 105: 19335-19351.

Rasmussen, J. and Noe-Nygaard, A. 1970. *Geology of the Faeroe Islands (Pre-Quaternary).* Trans: Henderson, G. Geological Survey of Denmark, Copenhagen 1/25.

Reading, H.G. 1986. *Sedimentary Environments and Facies*. Second Edition, Blackwell Scientific Publications, Oxford.

Sain, K., Zelt, C.A. and Reddy, P.R. 2002. Imaging of subvolcanic Mesozoics in the Saurashtra peninsula of India using traveltime inversion of wide-angle seismic data. *Geophysical Journal International* 150: 820-826.

Self, S., Thordarson, T., Kesthelyi, L., Walker, G.P.L., Hon, K., Murphy, M.T., Long, P. and Finnemore, S. 1996. A new model for the emplacement of Columbia River basalts as large, inflated pahoehoe lava flow fields. *Geophysical Research Letters* 23: 2689-2692.

Self, S., Thordarson, T. and Keszthelyi, L. 1997. Emplacement of continental flood basalt lava flows. In: Mahoney, J. J. and Coffin, M. F. (eds) *Large Igneous Provinces: Continental, Oceanic, and Planetary Flood Volcanism*. American Geophysical Union Geophysical Monograph 100: 381-410.

Self, S., Widdowson, M., E Thordarson, T. and Jay, A.E. 2006. Volatile fluxes during flood basalt eruptions and potential effects on the global environment: A Deccan perspective. Earth and Planetary Science Letters, Volume 248, Issues 1-2, Pages 518-532.

Single, R.T. 2004. *The facies architecture of large ig-*

neous provinces: an integrated geological and geophysical approach to the characterisation of volcanic successions in 3-D. PhD thesis, University of Durham.

Single, R.T. and Jerram, D.A., 2004. The 3-D facies architecture of flood basalt provinces and their internal heterogeneity: examples from the Palaeogene Skye Lava Field. *Journal of the Geological Society, London,* 161: 911-926.

Smallwood, J.R. and Maresh, J. 2002. The properties, morphology and distribution of igneous sills: modelling, borehole data and 3D seismic from the Faroe-Shetland area. *In*: Jolley, D.W. and Bell, B.R. (eds) *The North Atlantic Igneous Province: Stratigraphy, Tectonic, Volcanic and Magmatic Processes*. Geological Society, London, Special Publications 197: 271-306.

Thomson, K. 2005. Volcanic features of the North Rockall Trough: application of visualisation techniques on 3D seismic reflection data. *Bulletin of Volcanology* 67: 116-128.

Walker, G.P.L., 1972. Compound and Simple Lava Flows and Flood Basalts. *Bulletin of Volcanology* 35: 579-590.

White, R.S. and McKenzie, D. 1989. Mantle plumes and flood basalts. *Journal of Geophysical Research* 100: 17543-17585.

White, R.S., Spitzer, R., Christie, P.A.F., Roberts, A., Lunnon, Z., Maresh, J. and iSIMM Working Group 2005. Seismic imaging through basalt flows on the Faroes Shelf. *In*: Ziska, H., Varming, T. and Bloch, D. (eds) *Proceedings of the 1st Faroe Islands Exploration Conference* Annales Societatis Scientiarum Færoensis (Faroese Society of Science and Humanities), Tórshavn, Supplementum 43: 11-31.

Wu, R.S. and Aki, K., 1988. Introduction: Seismic Wave Scattering in Three-dimensionally Heterogeneous Earth. *Pure and Applied Geophysics* 128: 1-6.

Ziolkowski, A., Hanssen, P., Gatcliff, R., Jakubowicz, H., Dobson, A., Hampson, G., Li, X.-Y. and Liu, E. 2003. Use of low frequencies for sub-basalt imaging. *Geophysical Prospecting* 51: 169-182.

Appendix 2: Borehole interpretations

This appendix contains interpretations of all six boreholes described in the text: Lopra-1/1A, Glyvursnes-1, Vestmanna-1, ODP 642E, ODP 917A and Well 164/07-1. Samples of the data are also given, in the form of screenshots from Oilfield Data Manager.

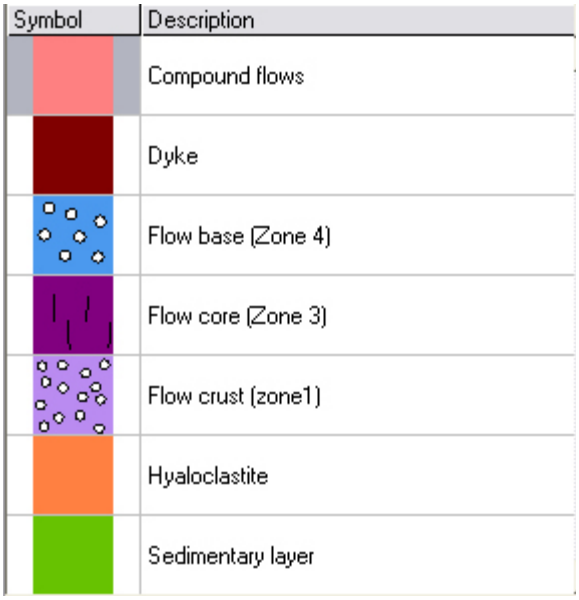

Key to the lithologies shown in the sample data in this appendix.

Lopra-1/1A

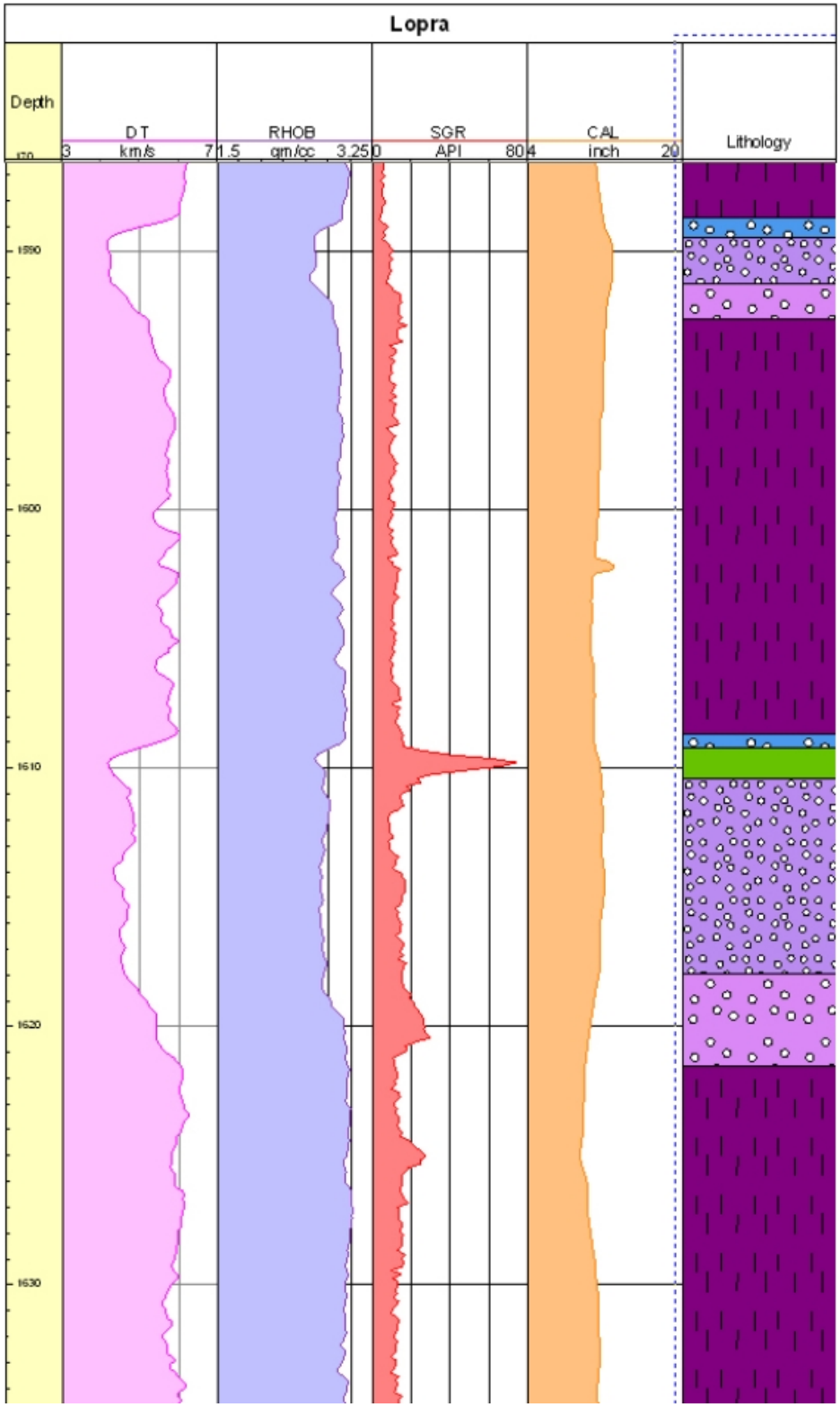

Sample data from Lopra-1/1A

Lopra-1/1A					
Top Depth (m)	**Base Depth (m)**	**Lithotype**	**Unit thickness (m)**	**Core proportion**	**Flow thickness (m)**
184.17	185.20	Sedimentary layer	1.03		
185.20	185.79	Flow crust	0.59		
185.79	189.18	Flow core	3.39	0.71518987	4.74
189.18	189.94	Flow base	0.76		
189.94	191.41	Flow crust	1.47		
191.41	209.55	Flow core	18.14	0.8980198	20.2
209.55	210.14	Flow base	0.59		
210.14	210.81	Sedimentary layer	0.67		
210.81	211.25	Flow crust	0.44		
211.25	213.14	Flow core	1.89	0.71052632	2.66
213.14	213.47	Flow base	0.33		
213.47	218.50	Flow crust	5.03		
218.50	222.72	Flow core	4.22	0.42886179	9.84
222.72	223.31	Flow base	0.59		
223.31	224.31	Sedimentary layer	1		
224.31	229.40	Flow crust	5.09		
229.40	236.30	Flow core	6.9	0.52995392	13.02
236.30	237.33	Flow base	1.03		
237.33	245.50	Flow crust	8.17		
245.50	268.51	Flow core	23.01	0.72290292	31.83
268.51	269.16	Flow base	0.65		
269.16	272.83	Flow crust	3.67		
272.83	283.51	Flow core	10.68	0.71774194	14.88
283.51	284.04	Flow base	0.53		
284.04	285.10	Sedimentary layer	1.06		
285.10	293.08	Flow crust	7.98		
293.08	306.77	Flow core	13.69	0.59860079	22.87
306.77	307.97	Flow base	1.2		
307.97	308.99	Sedimentary layer	1.02		
308.99	312.76	Flow crust	3.77		
312.76	334.36	Flow core	21.6	0.82442748	26.2
334.36	335.19	Flow base	0.83		
335.19	338.92	Compound flow	3.73		
338.92	339.60	Flow crust	0.68		
339.60	350.23	Flow core	10.63	0.86988543	12.22
350.23	351.14	Flow base	0.91		
351.14	353.43	Flow crust	2.29		
353.45	356.19	Flow core	2.74	0.51698113	5.3
356.19	356.46	Flow base	0.27		
356.46	357.58	Sedimentary layer	1.12		
357.58	362.81	Compound flow	5.23		
362.81	366.19	Flow crust	3.38		

Lopra-1/1A					
Top Depth (m)	**Base Depth (m)**	**Lithotype**	**Unit thickness (m)**	**Core proportion**	**Flow thickness (m)**
366.19	374.89	Flow core	8.7	0.69544365	12.51
374.89	375.32	Flow base	0.43		
375.32	376.63	Sedimentary layer	1.31		
376.63	380.33	Flow crust	3.7		
380.33	400.84	Flow core	20.51	0.79465324	25.81
400.84	402.44	Flow base	1.6		
402.44	410.32	Flow crust	7.88		
410.32	424.53	Flow core	14.21	0.618633	22.97
424.53	425.41	Flow base	0.88		
425.41	427.12	Compound flow	1.71		
427.12	428.64	Compound flow	1.52		
428.64	430.66	Compound flow	2.02		
430.66	434.00	Compound flow	3.34		
434.00	436.35	Flow crust	2.35		
436.35	441.03	Flow core	4.68	0.62650602	7.47
441.03	441.47	Flow base	0.44		
441.47	444.03	Flow crust	2.56		
444.03	455.34	Flow core	11.31	0.77572016	14.58
455.34	456.05	Flow base	0.71		
456.05	458.95	Compound flow	2.9		
458.95	460.74	Compound flow	1.79		
460.74	463.40	Compound flow	2.66		
463.40	466.09	Flow crust	2.69		
466.09	478.48	Flow core	12.39	0.77582968	15.97
478.48	479.37	Flow base	0.89		
479.37	480.36	Flow crust	0.99		
480.36	494.05	Flow core	13.69	0.90662252	15.1
494.05	494.47	Flow base	0.42		
494.47	610.60	Dyke	116.13		
610.60	611.31	Sedimentary layer	0.71		
611.31	620.91	Flow crust	9.6		
620.91	644.65	Flow core	23.74	0.69946965	33.94
644.65	645.25	Flow base	0.6		
645.25	646.59	Sedimentary layer	1.34		
646.59	653.92	Flow crust	7.33		
653.92	682.93	Flow core	29.01	0.7844781	36.98
682.93	683.57	Flow base	0.64		
683.57	686.15	Sedimentary layer	2.58		
686.15	690.44	Flow crust	4.29		
690.44	721.41	Flow core	30.97	0.86267409	35.9
721.41	722.05	Flow base	0.64		
722.05	724.03	Sedimentary layer	1.98		
724.03	823.25	Dyke	99.22		

Lopra-1/1A					
Top Depth (m)	**Base Depth (m)**	**Lithotype**	**Unit thickness (m)**	**Core proportion**	**Flow thickness (m)**
823.25	826.36	Compound flow	3.11		
826.36	828.68	Compound flow	2.32		
828.68	831.42	Compound flow	2.74		
831.42	833.70	Compound flow	2.28		
833.70	835.23	Flow crust	1.53		
835.23	854.21	Flow core	18.98	0.87951807	21.58
854.21	855.28	Flow base	1.07		
855.28	856.60	Compound flow	1.32		
856.60	859.68	Compound flow	3.08		
859.68	861.73	Compound flow	2.05		
861.73	862.84	Sedimentary layer	1.11		
862.84	867.56	Compound flow	4.72		
867.56	869.27	Compound flow	1.71		
869.27	872.88	Flow crust	3.61		
872.88	887.38	Flow core	14.5	0.74974147	19.34
887.38	888.61	Flow base	1.23		
888.61	890.08	Sedimentary layer	1.47		
890.08	891.88	Flow crust	1.8		
891.88	904.62	Flow core	12.74	0.79874608	15.95
904.62	906.03	Flow base	1.41		
906.03	907.28	Flow crust	1.25		
907.28	922.74	Flow core	15.46	0.89364162	17.3
922.74	923.33	Flow base	0.59		
923.33	924.72	Sedimentary layer	1.39		
924.72	932.58	Compound flow	7.86		
932.58	936.76	Flow crust	4.18		
936.76	964.09	Flow core	27.33	0.86024551	31.77
964.09	964.35	Flow base	0.26		
964.35	965.50	Sedimentary layer	1.15		
965.50	970.94	Compound flow	5.44		
970.94	975.44	Flow crust	4.5		
975.44	985.42	Flow core	9.98	0.66356383	15.04
985.42	985.98	Flow base	0.56		
985.98	987.33	Sedimentary layer	1.35		
987.33	990.51	Flow crust	3.18		
990.51	998.54	Flow core	8.03	0.6940363	11.57
998.54	998.90	Flow base	0.36		
998.90	999.93	Sedimentary layer	1.03		
999.93	1004.10	Compound flow	4.17		
1004.10	1006.58	Compound flow	2.48		
1006.58	1009.59	Compound flow	3.01		
1009.59	1015.24	Compound flow	5.65		

Lopra-1/1A					
Top Depth (m)	**Base Depth (m)**	**Lithotype**	**Unit thickness (m)**	**Core proportion**	**Flow thickness (m)**
1015.24	1020.32	Compound flow	5.08		
1020.32	1025.77	Flow crust	5.45		
1025.77	1042.71	Flow core	16.94	0.73588184	23.02
1042.71	1043.34	Flow base	0.63		
1043.34	1045.12	Sedimentary layer	1.78		
1045.12	1048.48	Flow crust	3.36		
1048.48	1060.29	Flow core	11.81	0.77851022	15.17
1060.29	1061.21	Sedimentary layer	0.92		
1061.21	1063.09	Compound flow	1.88		
1063.09	1066.59	Compound flow	3.5		
1066.59	1073.24	Compound flow	6.65		
1073.24	1074.99	Sedimentary layer	1.75		
1074.99	1075.35	Flow crust	0.36		
1075.35	1082.89	Flow core	7.54	0.89230769	8.45
1082.89	1083.44	Flow base	0.55		
1083.44	1084.20	Flow crust	0.76		
1084.32	1091.11	Flow core	6.79	0.86939821	7.81
1091.11	1091.37	Flow base	0.26		
1091.37	1092.89	Sedimentary layer	1.52		
1092.89	1093.06	Flow crust	0.17		
1093.06	1095.64	Flow core	2.58	0.93818182	2.75
1095.64	1097.95	Flow crust	2.31		
1097.95	1108.75	Flow core	10.8	0.74895978	14.42
1108.75	1110.06	Flow base	1.31		
1110.06	1113.66	Sedimentary layer	3.6		
1113.66	1118.76	Compound flow	5.1		
1118.76	1120.28	Compound flow	1.52		
1120.28	1121.60	Compound flow	1.32		
1121.60	1122.64	Flow crust	1.04		
1122.64	1134.42	Flow core	11.78	0.9047619	13.02
1134.42	1134.62	Flow base	0.2		
1134.62	1135.45	Sedimentary layer	0.83		
1135.45	1138.39	Compound flow	2.94		
1138.39	1141.72	Flow crust	3.33		
1141.72	1159.99	Flow core	18.27	0.79228101	23.06
1159.99	1161.45	Flow base	1.46		
1161.45	1163.03	Compound flow	1.58		
1163.03	1164.62	Compound flow	1.59		
1164.62	1166.41	Compound flow	1.79		
1166.41	1168.39	Compound flow	1.98		
1168.39	1171.73	Compound flow	3.34		
1171.73	1175.27	Compound flow	3.54		

Lopra-1/1A					
Top Depth (m)	**Base Depth (m)**	**Lithotype**	**Unit thickness (m)**	**Core proportion**	**Flow thickness (m)**
1175.27	1179.90	Flow crust	4.63		
1179.90	1197.40	Flow core	17.5	0.7719453	22.67
1197.40	1197.94	Flow base	0.54		
1197.94	1198.98	Sedimentary layer	1.04		
1198.98	1202.67	Flow crust	3.69		
1202.67	1214.99	Flow core	12.32	0.7294257	16.89
1214.99	1215.87	Flow base	0.88		
1215.87	1221.33	Flow crust	5.46		
1221.33	1257.74	Flow core	36.41	0.85731104	42.47
1257.74	1258.34	Flow base	0.6		
1258.34	1259.52	Sedimentary layer	1.18		
1259.52	1267.93	Flow crust	8.41		
1267.93	1296.22	Flow core	28.29	0.76666667	36.9
1296.22	1296.42	Flow base	0.2		
1296.42	1298.55	Sedimentary layer	2.13		
1298.55	1307.37	Flow crust	8.82		
1307.37	1336.61	Flow core	29.24	0.75032076	38.97
1336.61	1337.52	Flow base	0.91		
1337.52	1338.56	Flow crust	1.04		
1338.56	1345.30	Flow core	6.74	0.7957497	8.47
1345.30	1345.99	Flow base	0.69		
1345.99	1350.26	Sedimentary layer	4.27		
1350.26	1357.86	Flow crust	7.6		
1357.86	1386.88	Flow core	29.02	0.77469301	37.46
1386.88	1387.72	Flow base	0.84		
1387.72	1390.16	Flow crust	2.44		
1390.16	1410.37	Flow core	20.21	0.88369042	22.87
1410.37	1410.59	Flow base	0.22		
1410.59	1411.55	Sedimentary layer	0.96		
1411.55	1417.09	Flow crust	5.54		
1417.09	1421.93	Flow core	4.84	0.43291592	11.18
1421.93	1422.73	Flow base	0.8		
1422.73	1424.04	Sedimentary layer	1.31		
1424.04	1433.11	Flow crust	9.07		
1433.11	1449.74	Flow core	16.63	0.63814275	26.06
1449.74	1450.10	Flow base	0.36		
1450.10	1451.01	Sedimentary layer	0.91		
1451.01	1451.30	Flow crust	0.29		
1451.30	1469.35	Flow core	18.05	0.9642094	18.72
1469.35	1469.73	Flow base	0.38		

Lopra-1/1A					
Top Depth (m)	**Base Depth (m)**	**Lithotype**	**Unit thickness (m)**	**Core proportion**	**Flow thickness (m)**
1469.73	1471.11	Sedimentary layer	1.38		
1471.11	1475.71	Flow crust	4.6		
1475.71	1482.53	Flow core	6.82	0.57023411	11.96
1482.53	1483.07	Flow base	0.54		
1483.07	1484.07	Sedimentary layer	1		
1490.95	1503.75	Flow core	12.8	0.64128257	19.96
1503.75	1504.03	Flow base	0.28		
1504.03	1505.06	Sedimentary layer	1.03		
1505.06	1506.55	Flow crust	1.49		
1506.55	1518.54	Flow core	11.99	0.84022425	14.27
1518.54	1519.33	Flow base	0.79		
1519.33	1522.23	Compound flow	2.9		
1522.23	1523.50	Sedimentary layer	1.27		
1523.50	1528.05	Flow crust	4.55		
1528.05	1543.27	Flow core	15.22	0.7303263	20.84
1543.27	1544.34	Flow base	1.07		
1544.34	1545.59	Flow crust	1.25		
1545.59	1570.36	Flow core	24.77	0.92736803	26.71
1570.36	1571.05	Flow base	0.69		
1571.05	1571.84	Sedimentary layer	0.79		
1571.84	1576.25	Flow crust	4.41		
1576.25	1588.66	Flow core	12.41	0.70511364	17.6
1588.66	1589.44	Flow base	0.78		
1589.44	1592.56	Flow crust	3.12		
1592.59	1608.70	Flow core	16.11	0.81652306	19.73
1608.70	1609.20	Flow base	0.5		
1609.20	1610.39	Sedimentary layer	1.19		
1610.39	1621.52	Flow crust	11.13		
1621.52	1660.06	Flow core	38.54	0.75126706	51.3
1660.06	1661.69	Flow base	1.63		
1677.49	1679.83	Flow crust	2.34		
1679.83	1713.73	Flow core	33.9	0.910556	37.23
1713.73	1714.72	Flow base	0.99		
1714.72	1715.87	Sedimentary layer	1.15		
1715.87	1718.87	Flow crust	3		
1718.87	1726.88	Flow core	8.01	0.72752044	11.01
1726.96	1728.00	Sedimentary layer	1.04		
1728.00	1729.67	Compound flow	1.67		
1729.67	1733.57	Compound flow	3.9		
1733.57	1737.94	Compound flow	4.37		

Lopra-1/1A					
Top Depth (m)	**Base Depth (m)**	**Lithotype**	**Unit thickness (m)**	**Core proportion**	**Flow thickness (m)**
1737.94	1743.72	Compound flow	5.78		
1743.72	1746.83	Flow crust	3.11		
1746.83	1752.31	Flow core	5.48	0.57442348	9.54
1752.31	1753.26	Flow base	0.95		
1753.26	1761.75	Flow crust	8.49		
1761.75	1778.05	Flow core	16.3	0.63325563	25.74
1778.05	1779.00	Flow base	0.95		
1779.00	1785.06	Flow crust	6.06		
1785.06	1796.69	Flow core	11.63	0.65300393	17.81
1796.69	1796.81	Flow base	0.12		
1796.81	1797.64	Sedimentary layer	0.83		
1797.64	1798.20	Flow crust	0.56		
1798.20	1806.21	Flow core	8.01	0.93465578	8.57
1806.21	1808.29	Sedimentary layer	2.08		
1808.29	1813.19	Flow crust	4.9		
1813.19	1829.48	Flow core	16.29	0.7351083	22.16
1829.48	1830.45	Flow base	0.97		
1830.45	1832.12	Compound flow	1.67		
1832.12	1833.10	Flow crust	0.98		
1833.10	1837.99	Flow core	4.89	0.80032733	6.11
1837.99	1838.23	Flow base	0.24		
1838.23	1839.22	Sedimentary layer	0.99		
1839.22	1839.78	Flow crust	0.56		
1839.78	1843.57	Flow core	3.79	0.75951904	4.99
1843.57	1844.21	Flow base	0.64		
1844.21	1846.59	Compound flow	2.38		
1846.59	1848.72	Compound flow	2.13		
1848.72	1854.61	Compound flow	5.89		
1854.71	1856.33	Flow crust	1.62		
1856.33	1867.69	Flow core	11.36	0.82199711	13.82
1867.69	1868.53	Flow base	0.84		
1868.53	1869.45	Sedimentary layer	0.92		
1869.45	1874.10	Flow crust	4.65		
1874.10	1878.38	Flow core	4.28	0.42125984	10.16
1878.38	1879.61	Flow base	1.23		
1899.96	1905.11	Flow crust	5.15		
1905.11	1941.27	Flow core	36.16	0.85951985	42.07
1941.27	1942.03	Flow base	0.76		
1942.03	1943.14	Sedimentary layer	1.11		
1943.14	1946.58	Flow crust	3.44		
1946.58	1950.75	Flow core	4.17	0.47766323	8.73
1950.75	1951.87	Flow base	1.12		
1951.87	1953.93	Flow crust	2.06		

Lopra-1/1A					
Top Depth (m)	**Base Depth (m)**	**Lithotype**	**Unit thickness (m)**	**Core proportion**	**Flow thickness (m)**
1953.93	1957.10	Flow core	3.17	0.53277311	5.95
1957.10	1957.82	Flow base	0.72		
1957.82	1960.08	Flow crust	2.26		
1960.08	1966.59	Flow core	6.51	0.70684039	9.21
1966.59	1967.03	Flow base	0.44		
1967.03	1968.45	Sedimentary layer	1.42		
1968.45	1971.11	Compound flow	2.66		
1971.11	1972.73	Compound flow	1.62		
1972.73	1976.27	Compound flow	3.54		
1976.27	1979.71	Compound flow	3.44		
1979.71	1982.36	Compound flow	2.65		
1982.36	1985.37	Compound flow	3.01		
1985.37	1988.03	Flow crust	2.66		
1988.03	2007.04	Flow core	19.01	0.8566922	22.19
2007.04	2007.56	Flow base	0.52		
2007.56	2008.78	Sedimentary layer	1.22		
2008.78	2019.92	Flow crust	11.14		
2019.92	2055.59	Flow core	35.67	0.75428209	47.29
2055.59	2056.07	Flow base	0.48		
2056.07	2056.66	Sedimentary layer	0.59		
2056.66	2064.63	Flow crust	7.97		
2064.63	2108.62	Flow core	43.99	0.83647081	52.59
2108.62	2109.25	Flow base	0.63		
2125.79	2129.95	Flow crust	4.16		
2129.95	2148.31	Flow core	18.36	0.77632135	23.65
2148.31	2149.44	Flow base	1.13		
2149.44	2154.02	Flow crust	4.58		
2154.02	2173.42	Flow core	19.4	0.79606073	24.37
2173.42	2173.81	Flow base	0.39		
2173.81	2174.85	Sedimentary layer	1.04		
2174.85	2178.68	Flow crust	3.83		
2178.68	2191.40	Flow core	12.72	0.70745273	17.98
2191.40	2192.83	Flow base	1.43		
2192.83	2198.07	Flow crust	5.24		
2198.07	2243.19	Flow core	45.12	0.89029203	50.68
2243.19	2243.51	Flow base	0.32		
2243.51	2244.94	Sedimentary layer	1.43		
2244.94	2249.71	Compound flow	4.77		
2249.71	2250.12	Flow crust	0.41		
2250.12	2273.28	Flow core	23.16	0.93086817	24.88
2273.28	2274.59	Flow base	1.31		
2274.59	2277.37	Flow crust	2.78		
2277.37	2296.30	Flow core	18.93	0.79471033	23.82

Lopra-1/1A					
Top Depth (m)	**Base Depth (m)**	**Lithotype**	**Unit thickness (m)**	**Core proportion**	**Flow thickness (m)**
2296.30	2298.41	Flow base	2.11		
2298.41	2303.51	Compound flow	5.1		
2303.51	2306.36	Compound flow	2.85		
2306.36	2311.19	Compound flow	4.83		
2311.19	2319.23	Compound flow	8.04		
2319.23	2328.99	Compound flow	9.76		
2329.08	2332.82	Compound flow	3.74		
2332.82	2338.04	Flow crust	5.22		
2338.04	2400.29	Flow core	62.25	0.90505961	68.78
2400.29	2401.60	Flow base	1.31		
2401.60	2404.14	Compound flow	2.54		
2404.14	2407.25	Compound flow	3.11		
2407.25	2415.68	Compound flow	8.43		
2415.68	2418.20	Compound flow	2.52		
2418.20	2427.70	Compound flow	9.5		
2427.70	2433.98	Compound flow	6.28		
2433.98	2436.17	Compound flow	2.19		
2436.17	2438.32	Compound flow	2.15		
2438.32	2441.52	Compound flow	3.2		
2441.52	2443.65	Compound flow	2.13		
2443.65	2447.62	Compound flow	3.97		
2447.62	2451.09	Compound flow	3.47		
2451.09	2456.55	Compound flow	5.46		
2456.55	2464.22	Compound flow	7.67		
2464.22	2468.09	Compound flow	3.87		

Glyvursnes-1

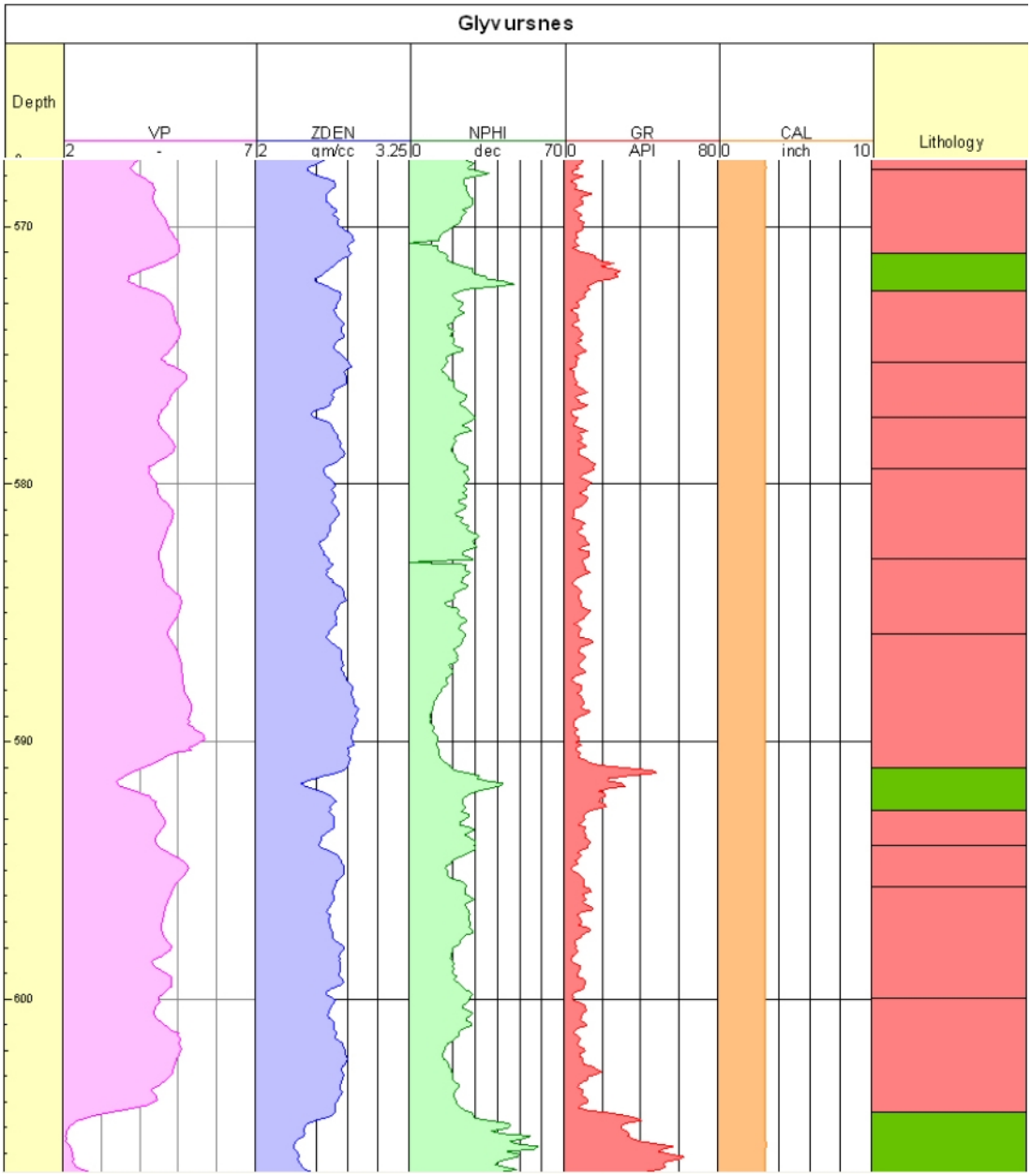

Sample data from Glyvursnes-1

Glyvursnes-1					
Top Depth (m)	**Base Depth (m)**	**Lithotype**	**Unit thickness (m)**	**Core proportion**	**Flow thickness (m)**
21.83	28.78	Flow core	6.95		
28.78	29.26	Flow base	0.48		
29.26	34.97	Flow crust	5.71		
34.97	38.19	Flow core	3.22	0.35114504	9.17
38.19	38.43	Flow base	0.24		
38.43	44.24	Sedimentary layer	5.81		
44.24	49.73	Flow crust	5.49		
49.73	51.98	Flow core	2.25	0.27272727	8.25
51.98	52.49	Flow base	0.51		
52.49	54.37	Flow crust	1.88		
54.37	57.93	Flow core	3.56	0.59333333	6
57.93	58.49	Flow base	0.56		
58.49	59.57	Flow crust	1.08		
59.57	62.78	Flow core	3.21	0.67721519	4.74
62.78	63.23	Flow base	0.45		
63.23	66.23	Flow crust	3		
66.23	80.16	Flow core	13.93	0.80520231	17.3
80.16	80.53	Flow base	0.37		
80.53	83.63	Flow crust	3.1		
83.63	108.65	Flow core	25.02	0.87758681	28.51
108.65	109.04	Flow base	0.39		
109.04	111.33	Flow crust	2.29		
111.33	120.24	Flow core	8.91	0.77545692	11.49
120.24	120.53	Flow base	0.29		
120.53	122.68	Flow crust	2.15		
122.68	125.18	Flow core	2.5	0.50403226	4.96
125.18	125.49	Flow base	0.31		
125.49	127.18	Flow crust	1.69		
127.18	128.06	Flow core	0.88	0.3024055	2.91
128.06	128.40	Flow base	0.34		
128.40	134.64	Flow crust	6.24		
134.64	146.62	Flow core	11.98	0.62854145	19.06
146.62	147.46	Flow base	0.84		
147.46	149.36	Compound flows	1.9		
149.36	152.60	Flow crust	3.24		
152.60	155.22	Flow core	2.62	0.42326333	6.19
155.22	155.55	Flow base	0.33		
155.55	158.22	Flow crust	2.67		
158.22	160.89	Flow core	2.67	0.47089947	5.67
160.89	161.22	Flow base	0.33		
161.22	164.18	Flow crust	2.96		
164.18	166.75	Flow core	2.57	0.43485618	5.91
166.75	167.13	Flow base	0.38		
167.13	177.53	Flow crust	10.4		
177.53	186.79	Flow core	9.26	0.4482091	20.66
186.79	187.79	Flow base	1		
187.79	190.91	Compound flows	3.12		

Glyvursnes-1					
Top Depth (m)	**Base Depth (m)**	**Lithotype**	**Unit thickness (m)**	**Core proportion**	**Flow thickness (m)**
190.91	192.45	Flow crust	1.54		
192.45	193.86	Flow core	1.41	0.43119266	3.27
193.86	194.18	Flow base	0.32		
194.18	196.48	Flow crust	2.3		
196.48	198.03	Flow core	1.55	0.36729858	4.22
198.03	198.40	Flow base	0.37		
198.40	200.42	Flow crust	2.02		
200.42	202.25	Flow core	1.83	0.44309927	4.13
202.25	202.53	Flow base	0.28		
202.53	203.00	Flow crust	0.47		
203.00	203.89	Flow core	0.89	0.55974843	1.59
203.89	204.12	Flow base	0.23		
204.12	207.87	Flow crust	3.75		
207.87	212.51	Flow core	4.64	0.51555556	9
212.51	213.12	Flow base	0.61		
213.12	216.50	Compound flows	3.38		
216.50	218.00	Compound flows	1.5		
218.00	222.17	Compound flows	4.17		
222.17	224.14	Compound flows	1.97		
224.14	227.82	Compound flows	3.68		
227.82	233.41	Flow crust	5.59		
233.41	253.30	Flow core	19.89	0.75398029	26.38
253.30	254.20	Flow base	0.9		
254.20	255.83	Flow crust	1.63		
255.83	263.28	Flow core	7.45	0.82048458	9.08
263.28	266.28	Compound flows	3		
266.28	267.44	Compound flows	1.16		
267.44	269.17	Flow crust	1.73		
269.17	282.51	Flow core	13.34	0.82549505	16.16
282.51	283.60	Flow base	1.09		
283.60	288.60	Flow crust	5		
288.60	295.82	Flow core	7.22	0.57301587	12.6
295.82	296.20	Flow base	0.38		
296.20	298.63	Sedimentary layer	2.43		
298.63	300.07	Compound flows	1.44		
300.07	304.64	Compound flows	4.57		
304.64	308.05	Compound flows	3.41		
308.05	310.00	Compound flows	1.95		
310.00	314.24	Compound flows	4.24		
314.24	319.24	Compound flows	5		
319.24	321.68	Compound flows	2.44		
321.68	323.15	Compound flows	1.47		
323.15	324.89	Compound flows	1.74		
324.89	326.52	Compound flows	1.63		
326.52	328.11	Compound flows	1.59		
328.11	331.05	Compound flows	2.94		
331.05	333.43	Compound flows	2.38		

Glyvursnes-1					
Top Depth (m)	**Base Depth (m)**	**Lithotype**	**Unit thickness (m)**	**Core proportion**	**Flow thickness (m)**
333.43	334.10	Compound flows	0.67		
334.10	335.45	Compound flows	1.35		
345.92	347.86	Flow crust	1.94		
347.86	354.13	Flow core	6.27	0.71575342	8.76
354.13	354.68	Flow base	0.55		
354.68	356.51	Sedimentary layer	1.83		
356.51	360.87	Compound flows	4.36		
360.87	364.11	Compound flows	3.24		
364.11	365.42	Compound flows	1.31		
365.42	368.51	Compound flows	3.09		
368.51	372.31	Compound flows	3.8		
372.31	376.54	Compound flows	4.23		
376.54	380.71	Flow crust	4.17		
380.71	383.62	Flow core	2.91	0.37645537	7.73
383.62	384.27	Flow base	0.65		
384.27	385.91	Compound flows	1.64		
385.91	387.55	Compound flows	1.64		
387.55	389.24	Compound flows	1.69		
389.24	399.74	Compound flows	10.5		
399.74	402.69	Compound flows	2.95		
402.69	404.19	Compound flows	1.5		
404.19	406.21	Compound flows	2.02		
406.21	407.94	Compound flows	1.73		
407.94	412.27	Compound flows	4.33		
412.27	413.67	Compound flows	1.4		
413.67	415.88	Compound flows	2.21		
415.88	417.19	Compound flows	1.31		
417.19	418.50	Compound flows	1.31		
418.50	422.30	Compound flows	3.8		
422.30	425.28	Compound flows	2.98		
425.28	427.01	Compound flows	1.73		
427.01	428.33	Compound flows	1.32		
428.33	429.73	Compound flows	1.4		
429.73	430.43	Sedimentary layer	0.7		
430.43	432.26	Compound flows	1.83		
432.26	434.09	Compound flows	1.83		
434.09	437.65	Compound flows	3.56		
437.65	440.31	Compound flows	2.66		
440.31	443.26	Compound flows	2.95		
443.26	446.24	Compound flows	2.98		
446.24	447.18	Compound flows	0.94		
447.18	448.73	Compound flows	1.55		
448.73	450.74	Compound flows	2.01		
450.74	453.37	Compound flows	2.63		
453.37	454.63	Compound flows	1.26		
454.63	460.58	Compound flows	5.95		
460.58	463.49	Compound flows	2.91		

Glyvursnes-1					
Top Depth (m)	**Base Depth (m)**	**Lithotype**	**Unit thickness (m)**	**Core proportion**	**Flow thickness (m)**
463.49	468.41	Flow crust	4.92		
468.41	472.09	Flow core	3.68	0.40662983	9.05
472.09	472.54	Flow base	0.45		
472.54	480.30	Compound flows	7.76		
480.30	482.49	Compound flows	2.19		
482.49	485.39	Compound flows	2.9		
485.39	488.60	Compound flows	3.21		
488.60	490.10	Compound flows	1.5		
490.10	494.26	Compound flows	4.16		
494.26	506.28	Compound flows	12.02		
506.28	515.09	Compound flows	8.81		
515.09	517.81	Compound flows	2.72		
517.81	523.14	Compound flows	5.33		
523.14	526.88	Compound flows	3.74		
526.88	530.46	Compound flows	3.58		
530.46	535.28	Compound flows	4.82		
535.28	536.64	Compound flows	1.36		
536.64	539.07	Compound flows	2.43		
539.07	547.34	Compound flows	8.27		
547.34	553.84	Compound flows	6.5		
553.84	556.51	Compound flows	2.67		
556.51	559.19	Compound flows	2.68		
559.19	561.33	Compound flows	2.14		
561.33	562.84	Compound flows	1.51		
562.84	567.80	Compound flows	4.96		
567.80	571.04	Compound flows	3.24		
571.04	572.51	Sedimentary layer	1.47		
572.51	575.26	Compound flows	2.75		
575.26	577.41	Compound flows	2.15		
577.41	579.42	Compound flows	2.01		
579.42	582.88	Compound flows	3.46		
582.88	585.85	Compound flows	2.97		
585.85	591.05	Compound flows	5.2		
591.05	592.68	Sedimentary layer	1.63		
592.68	594.04	Compound flows	1.36		
594.04	595.65	Compound flows	1.61		
595.65	599.95	Compound flows	4.3		
599.95	604.39	Compound flows	4.44		
604.39	607.21	Sedimentary layer	2.82		
607.21	609.68	Compound flows	2.47		
609.68	610.80	Compound flows	1.12		
610.80	613.92	Compound flows	3.12		
613.92	622.92	Compound flows	9		
622.92	623.99	Compound flows	1.07		
623.99	627.49	Compound flows	3.5		
627.49	628.95	Compound flows	1.46		
628.95	632.79	Compound flows	3.84		

Glyvursnes-1					
Top Depth (m)	**Base Depth (m)**	**Lithotype**	**Unit thickness (m)**	**Core proportion**	**Flow thickness (m)**
632.79	634.79	Compound flows	2		
634.79	636.93	Compound flows	2.14		
636.93	641.11	Compound flows	4.18		
641.11	644.88	Compound flows	3.77		
644.88	648.04	Compound flows	3.16		
648.09	655.24	Compound flows	7.15		
655.24	658.90	Compound flows	3.66		
658.90	664.24	Compound flows	5.34		
664.24	670.27	Compound flows	6.03		
670.27	673.39	Compound flows	3.12		
673.39	678.35	Compound flows	4.96		
678.35	681.65	Compound flows	3.3		

Vestmanna-1

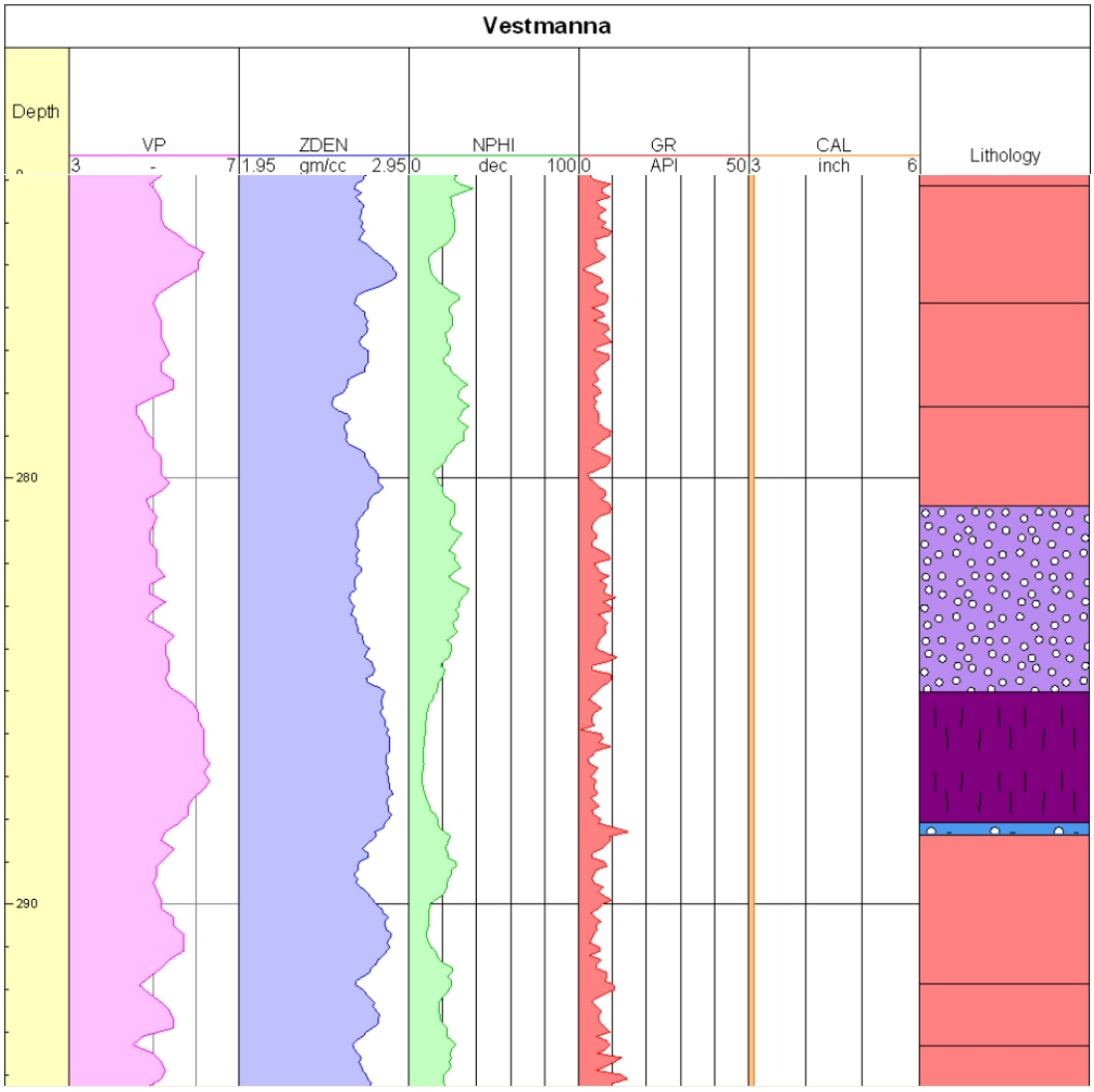

Sample data from Vestmanna-1

Vestmanna-1					
Top Depth (m)	**Base Depth (m)**	**Lithotype**	**Unit thickness (m)**	**Core proportion**	**Flow thickness (m)**
22.21	24.03	Compound flows	1.82		
24.03	25.34	Compound flows	1.31		
25.34	27.43	Compound flows	2.09		
27.43	30.79	Compound flows	3.36		
30.79	34.61	Compound flows	3.82		
34.61	37.71	Compound flows	3.1		
37.71	41.24	Compound flows	3.53		
41.24	44.02	Compound flows	2.78		
44.02	47.26	Compound flows	3.24		
47.26	48.85	Compound flows	1.59		
48.85	50.41	Compound flows	1.56		
50.41	52.59	Compound flows	2.18		
52.59	54.96	Compound flows	2.37		
54.96	58.17	Compound flows	3.21		
58.17	60.04	Compound flows	1.87		
60.04	61.23	Compound flows	1.19		
61.23	62.54	Flow crust	1.31		
62.54	65.89	Flow core	3.35	0.64547206	5.19
65.89	66.42	Flow base	0.53		
66.42	67.80	Compound flows	1.38		
67.80	68.35	Compound flows	0.55		
68.35	72.00	Compound flows	3.65		
72.00	74.20	Compound flows	2.2		
74.20	77.04	Compound flows	2.84		
77.04	79.97	Compound flows	2.93		
79.97	81.46	Compound flows	1.49		
81.46	82.36	Compound flows	0.9		
82.36	86.09	Compound flows	3.73		
86.09	88.82	Compound flows	2.73		
88.82	93.69	Compound flows	4.87		
93.69	94.98	Compound flows	1.29		
94.98	100.57	Compound flows	5.59		
100.57	104.21	Compound flows	3.64		
104.21	106.99	Compound flows	2.78		
106.99	109.19	Compound flows	2.2		
109.19	110.29	Compound flows	1.1		
110.29	110.94	Compound flows	0.65		
110.94	111.99	Compound flows	1.05		
111.99	116.95	Compound flows	4.96		
116.95	119.38	Compound flows	2.43		
119.38	120.70	Compound flows	1.32		
120.70	121.71	Compound flows	1.01		
121.71	124.96	Compound flows	3.25		
124.96	126.84	Compound flows	1.88		
126.84	128.09	Compound flows	1.25		

Vestmanna-1					
Top Depth (m)	**Base Depth (m)**	**Lithotype**	**Unit thickness (m)**	**Core proportion**	**Flow thickness (m)**
128.09	128.93	Compound flows	0.84		
128.93	130.52	Compound flows	1.59		
130.52	132.61	Compound flows	2.09		
132.61	135.76	Compound flows	3.15		
135.76	138.46	Compound flows	2.7		
138.46	140.08	Compound flows	1.62		
140.08	141.88	Compound flows	1.8		
141.88	144.71	Compound flows	2.83		
144.71	146.19	Compound flows	1.48		
146.19	147.25	Compound flows	1.06		
147.25	149.74	Compound flows	2.49		
149.74	152.94	Compound flows	3.2		
152.94	155.27	Compound flows	2.33		
155.27	156.35	Compound flows	1.08		
156.35	158.24	Compound flows	1.89		
158.24	160.33	Compound flows	2.09		
160.33	161.86	Compound flows	1.53		
161.86	163.03	Compound flows	1.17		
163.03	166.15	Compound flows	3.12		
166.15	168.61	Compound flows	2.46		
168.61	170.92	Compound flows	2.31		
170.92	174.28	Compound flows	3.36		
174.28	176.87	Compound flows	2.59		
176.87	183.04	Compound flows	6.17		
183.04	186.59	Compound flows	3.55		
186.59	188.12	Compound flows	1.53		
188.12	190.82	Flow crust	2.7		
190.82	192.67	Flow core	1.85	0.3814433	4.85
192.67	192.97	Flow base	0.3		
192.97	198.23	Flow crust	5.26		
198.23	204.45	Flow core	6.22	0.5077551	12.25
204.45	205.22	Flow base	0.77		
205.22	208.93	Compound flows	3.71		
208.93	210.17	Compound flows	1.24		
210.17	211.58	Compound flows	1.41		
211.58	213.93	Compound flows	2.35		
213.93	215.76	Compound flows	1.83		
215.76	217.66	Compound flows	1.9		
217.66	219.52	Compound flows	1.86		
219.52	220.34	Compound flows	0.82		
220.34	223.57	Compound flows	3.23		
223.57	225.52	Flow crust	1.95		
225.52	227.72	Flow core	2.2	0.47826087	4.6
227.72	228.17	Flow base	0.45		
228.20	230.42	Compound flows	2.22		
230.42	231.16	Compound flows	0.74		
231.16	233.20	Flow crust	2.04		

Vestmanna-1					
Top Depth (m)	**Base Depth (m)**	**Lithotype**	**Unit thickness (m)**	**Core proportion**	**Flow thickness (m)**
235.95	237.04	Compound flows	1.09		
237.04	238.20	Flow crust	1.16		
238.20	239.92	Flow core	1.72	0.50439883	3.41
239.92	240.45	Flow base	0.53		
240.45	241.59	Compound flows	1.14		
241.59	243.34	Flow crust	1.75		
243.34	249.16	Flow core	5.82	0.71411043	8.15
249.16	249.74	Flow base	0.58		
249.74	251.65	Compound flows	1.91		
251.65	252.79	Compound flows	1.14		
252.79	254.49	Compound flows	1.7		
254.49	255.91	Compound flows	1.42		
255.91	256.60	Compound flows	0.69		
256.60	258.14	Compound flows	1.54		
258.14	259.49	Compound flows	1.35		
259.49	260.84	Compound flows	1.35		
260.84	262.05	Compound flows	1.21		
262.05	262.90	Compound flows	0.85		
262.90	264.42	Compound flows	1.52		
264.42	265.42	Compound flows	1		
265.42	267.12	Compound flows	1.7		
267.12	269.68	Compound flows	2.56		
269.68	273.14	Compound flows	3.46		
273.14	275.89	Compound flows	2.75		
275.89	278.33	Compound flows	2.44		
278.33	280.65	Compound flows	2.32		
280.65	285.03	Flow crust	4.38		
285.03	288.09	Flow core	3.06	0.39637306	7.72
288.09	288.37	Flow base	0.28		
288.37	291.86	Compound flows	3.49		
291.86	293.33	Compound flows	1.47		
293.33	294.39	Compound flows	1.06		
294.39	296.61	Compound flows	2.22		
296.61	299.58	Compound flows	2.97		
299.58	301.04	Compound flows	1.46		
301.04	302.79	Compound flows	1.75		
302.79	304.11	Compound flows	1.32		
304.11	305.26	Compound flows	1.15		
305.26	306.19	Compound flows	0.93		
306.19	306.81	Flow crust	0.62		
306.81	308.91	Flow core	2.1	0.67741935	3.1
308.91	309.29	Flow base	0.38		
309.29	315.91	Flow crust	6.62		
315.91	324.84	Flow core	8.93	0.56269691	15.87
324.84	325.16	Flow base	0.32		
325.16	329.38	Compound flows	4.22		
329.38	331.23	Compound flows	1.85		

Vestmanna-1					
Top Depth (m)	**Base Depth (m)**	**Lithotype**	**Unit thickness (m)**	**Core proportion**	**Flow thickness (m)**
331.23	332.13	Compound flows	0.9		
332.13	334.73	Compound flows	2.6		
334.73	335.57	Compound flows	0.84		
335.57	343.26	Compound flows	7.69		
343.26	352.79	Compound flows	9.53		
352.79	355.33	Compound flows	2.54		
355.33	359.69	Flow crust	4.36		
359.69	365.47	Flow core	5.78	0.53518519	10.8
365.47	366.13	Flow base	0.66		
366.13	368.01	Compound flows	1.88		
368.01	369.49	Compound flows	1.48		
369.49	372.46	Compound flows	2.97		
372.46	373.34	Compound flows	0.88		
373.34	374.58	Compound flows	1.24		
374.58	376.17	Compound flows	1.59		
376.17	379.91	Compound flows	3.74		
379.91	384.56	Compound flows	4.65		
384.56	387.41	Compound flows	2.85		
387.41	389.83	Compound flows	2.42		
389.83	394.27	Compound flows	4.44		
394.27	397.43	Compound flows	3.16		
397.43	401.02	Compound flows	3.59		
401.02	409.92	Compound flows	8.9		
409.92	412.69	Compound flows	2.77		
412.69	414.66	Compound flows	1.97		
414.66	416.03	Compound flows	1.37		
416.03	417.94	Compound flows	1.91		
417.94	421.55	Compound flows	3.61		
421.55	424.43	Compound flows	2.88		
424.43	429.73	Compound flows	5.3		
429.73	431.01	Compound flows	1.28		
431.01	435.96	Compound flows	4.95		
435.96	437.24	Compound flows	1.28		
437.24	441.65	Compound flows	4.41		
447.44	453.75	Flow crust	6.31		
453.75	460.53	Flow core	6.78	0.49094859	13.81
460.53	461.25	Flow base	0.72		
461.25	463.09	Compound flows	1.84		
463.09	466.96	Compound flows	3.87		
466.96	473.29	Compound flows	6.33		
473.29	476.79	Compound flows	3.5		
476.79	478.91	Compound flows	2.12		
478.91	481.08	Compound flows	2.17		
481.08	487.80	Compound flows	6.72		
487.80	489.46	Compound flows	1.66		
489.46	491.80	Compound flows	2.34		
491.80	494.54	Compound flows	2.74		

Vestmanna-1					
Top Depth (m)	**Base Depth (m)**	**Lithotype**	**Unit thickness (m)**	**Core proportion**	**Flow thickness (m)**
494.54	495.98	Compound flows	1.44		
495.98	498.69	Compound flows	2.71		
498.69	501.31	Compound flows	2.62		
501.31	503.38	Compound flows	2.07		
503.38	505.66	Compound flows	2.28		
505.66	511.23	Compound flows	5.57		
511.23	515.10	Compound flows	3.87		
515.10	520.73	Compound flows	5.63		
520.73	521.82	Compound flows	1.09		
521.82	523.24	Compound flows	1.42		
523.24	527.40	Compound flows	4.16		
527.40	531.12	Compound flows	3.72		
531.12	532.48	Compound flows	1.36		
532.48	533.92	Compound flows	1.44		
533.92	535.42	Compound flows	1.5		
535.42	537.86	Compound flows	2.44		
537.86	542.22	Flow crust	4.36		
542.22	546.75	Flow core	4.53	0.47138398	9.61
546.75	547.47	Flow base	0.72		
547.47	552.91	Compound flows	5.44		
552.91	554.08	Compound flows	1.17		
554.08	555.69	Compound flows	1.61		
555.69	557.63	Sedimentary layer	1.94		
557.63	558.95	Flow crust	1.32		
558.98	569.22	Flow core	10.24	0.85262281	12.01
569.22	569.67	Flow base	0.45		
569.67	570.81	Compound flows	1.14		
570.81	572.45	Flow crust	1.64		
572.45	574.33	Flow core	1.88	0.48329049	3.89
574.33	574.70	Flow base	0.37		
574.70	576.42	Flow crust	1.72		
576.42	577.82	Flow core	1.4	0.41297935	3.39
577.82	578.09	Flow base	0.27		
578.09	579.73	Flow crust	1.64		
579.73	586.85	Flow core	7.12	0.78674033	9.05
586.85	587.14	Flow base	0.29		

ODP Hole 642E

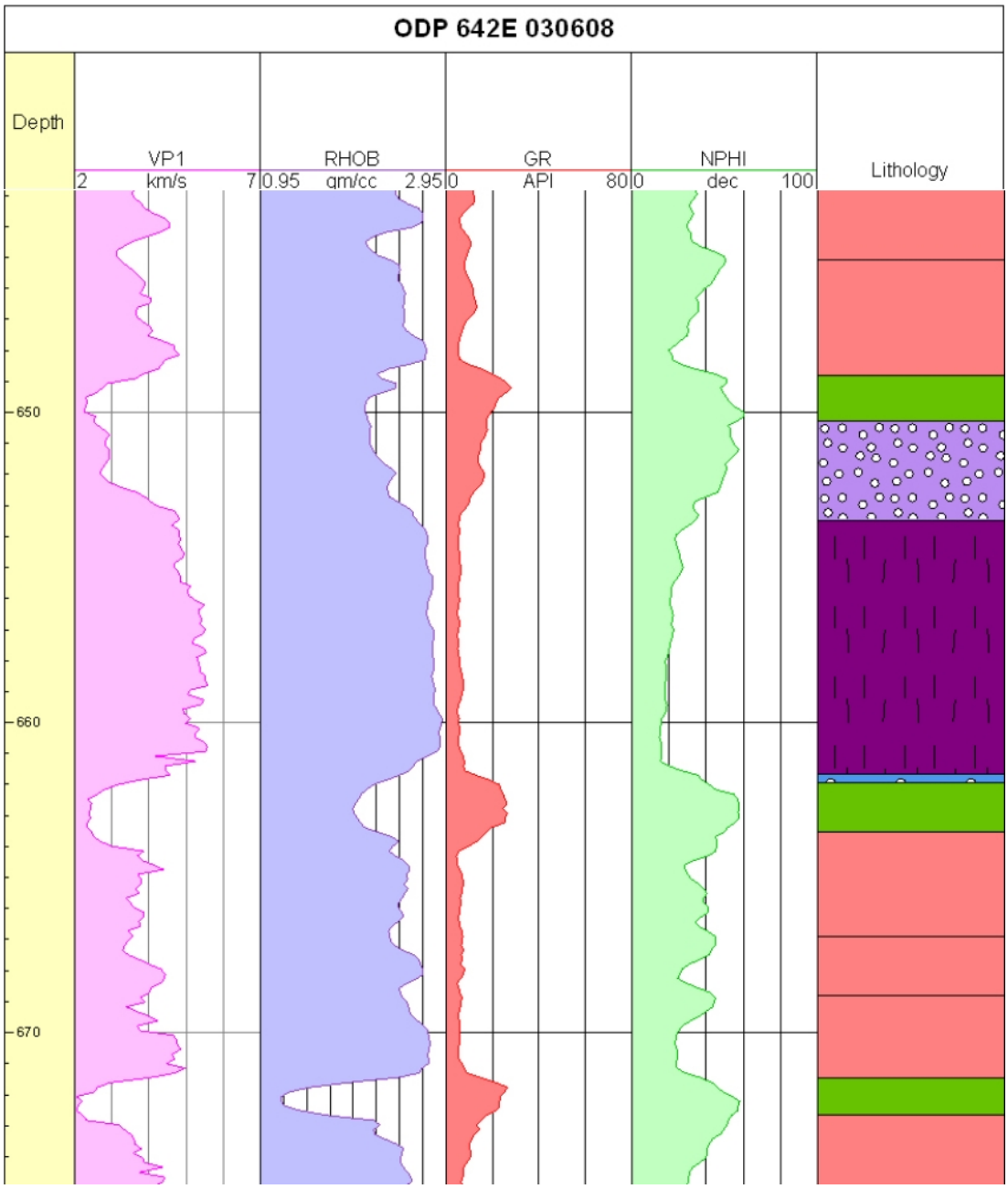

Sample data from ODP Hole 642E

ODP Hole 642E					
Top Depth (m)	**Base Depth (m)**	**Lithotype**	**Unit thickness (m)**	**Core proportion**	**Flow thickness (m)**
416.34	418.00	Sedimentary layer	1.66		
418.00	419.63	Compound flows	1.63		
419.63	428.20	Compound flows	8.57		
428.20	429.37	Flow crust	1.17		
429.37	436.74	Flow core	7.37	0.82254464	8.96
436.74	437.16	Flow base	0.42		
437.16	439.59	Flow crust	2.43		
439.59	446.12	Flow core	6.53	0.71055495	9.19
446.12	446.35	Flow base	0.23		
446.35	449.27	Sedimentary layer	2.92		
449.27	451.31	Flow crust	2.04		
451.31	456.45	Flow core	5.14	0.68624833	7.49
456.45	456.76	Flow base	0.31		
456.76	457.59	Sedimentary layer	0.83		
457.59	462.35	Compound flows	4.76		
462.35	465.53	Compound flows	3.18		
465.53	468.35	Compound flows	2.82		
468.35	472.87	Compound flows	4.52		
472.87	476.45	Compound flows	3.58		
476.45	479.87	Compound flows	3.42		
479.87	482.63	Sedimentary layer	2.76		
482.63	485.20	Compound flows	2.57		
485.20	485.81	Sedimentary layer	0.61		
485.81	494.49	Compound flows	8.68		
494.49	495.74	Sedimentary layer	1.25		
495.74	498.35	Flow crust	2.61		
498.35	506.98	Flow core	8.63	0.75043478	11.5
506.98	507.24	Flow base	0.26		
507.24	510.75	Compound flows	3.51		
510.75	513.21	Compound flows	2.46		
513.21	514.32	Flow crust	1.11		
514.32	520.00	Flow core	5.68	0.76653171	7.41
520.00	520.62	Flow base	0.62		
520.62	522.24	Sedimentary layer	1.62		
522.24	525.92	Compound flows	3.68		
525.92	529.25	Compound flows	3.33		
529.25	533.54	Compound flows	4.29		
533.54	536.10	Compound flows	2.56		
536.10	539.26	Flow crust	3.16		
539.26	544.24	Flow core	4.98	0.56590909	8.8
544.24	544.90	Flow base	0.66		
544.90	550.30	Flow crust	5.4		

ODP Hole 642E					
Top Depth (m)	**Base Depth (m)**	**Lithotype**	**Unit thickness (m)**	**Core proportion**	**Flow thickness (m)**
550.30	564.12	Flow core	13.82	0.70618293	19.57
564.12	564.47	Flow base	0.35		
564.47	565.85	Flow crust	1.38		
565.85	571.80	Flow core	5.95		
571.80	573.16	Sedimentary layer	1.36		
573.16	576.17	Flow crust	3.01		
576.17	583.36	Flow core	7.19	0.66512488	10.81
583.36	583.97	Flow base	0.61		
583.97	586.08	Compound flows	2.11		
586.08	588.18	Compound flows	2.1		
588.18	589.13	Compound flows	0.95		
589.13	590.80	Compound flows	1.67		
590.80	593.35	Compound flows	2.55		
593.35	594.74	Flow crust	1.39		
594.74	600.77	Flow core	6.03	0.77406932	7.79
600.77	601.14	Flow base	0.37		
601.14	603.98	Compound flows	2.84		
603.98	605.84	Compound flows	1.86		
605.84	607.11	Compound flows	1.27		
607.17	608.87	Flow crust	1.7		
608.87	613.93	Flow core	5.06	0.71468927	7.08
613.93	614.25	Flow base	0.32		
614.25	617.21	Compound flows	2.96		
617.21	618.42	Sedimentary layer	1.21		
618.42	624.97	Compound flows	6.55		
624.97	625.71	Sedimentary layer	0.74		
625.71	631.50	Compound flows	5.79		
631.58	635.83	Compound flows	4.25		
635.83	640.51	Compound flows	4.68		
640.51	645.07	Compound flows	4.56		
645.07	648.82	Compound flows	3.75		
648.82	650.27	Sedimentary layer	1.45		
650.27	653.48	Flow crust	3.21		
653.48	661.66	Flow core	8.18	0.70034247	11.68
661.66	661.95	Flow base	0.29		
661.95	663.53	Sedimentary layer	1.58		
663.53	666.91	Compound flows	3.38		
666.91	668.82	Compound flows	1.91		
668.82	671.49	Compound flows	2.67		
671.49	672.65	Sedimentary layer	1.16		
672.65	675.84	Compound flows	3.19		
675.84	677.09	Sedimentary layer	1.25		

ODP Hole 642E					
Top Depth (m)	**Base Depth (m)**	**Lithotype**	**Unit thickness (m)**	**Core proportion**	**Flow thickness (m)**
677.09	681.81	Flow crust	4.72		
681.81	689.98	Flow core	8.17	0.6198786	13.18
689.98	690.27	Flow base	0.29		
690.27	697.09	Compound flows	6.82		
697.09	701.62	Compound flows	4.53		
701.62	707.38	Compound flows	5.76		
707.38	709.47	Flow crust	2.09		
709.47	712.17	Flow core	2.7	0.53677932	5.03
712.17	712.41	Flow base	0.24		
712.41	713.39	Sedimentary layer	0.98		
713.39	717.33	Compound flows	3.94		
717.33	721.41	Flow crust	4.08		
721.41	725.22	Flow core	3.81	0.44405594	8.58
725.22	725.91	Flow base	0.69		
725.91	726.86	Sedimentary layer	0.95		
726.86	729.24	Flow crust	2.38		
729.24	731.78	Flow core	2.54	0.46863469	5.42
731.78	732.28	Flow base	0.5		
732.28	734.63	Flow crust	2.35		
734.63	738.24	Flow core	3.61	0.54531722	6.62
738.24	738.90	Flow base	0.66		
738.90	739.43	Sedimentary layer	0.53		
739.43	742.79	Flow crust	3.36		
742.79	747.15	Flow core	4.36	0.52657005	8.28
747.15	747.71	Flow base	0.56		
747.71	749.91	Flow crust	2.2		
749.91	751.76	Flow core	1.85	0.404814	4.57
751.76	752.28	Flow base	0.52		
752.28	753.63	Sedimentary layer	1.35		
753.63	757.84	Compound flows	4.21		
757.84	762.53	Sedimentary layer	4.69		
762.53	763.22	Flow crust	0.69		
763.22	770.65	Flow core	7.43	0.81025082	9.17
770.65	771.70	Flow base	1.05		
771.70	775.30	Flow crust	3.6		
775.30	781.62	Flow core	6.32	0.60769231	10.4
781.62	782.10	Flow base	0.48		
782.10	785.19	Compound flows	3.09		
785.19	789.07	Compound flows	3.88		
789.07	794.06	Sedimentary layer	4.99		
794.49	797.98	Flow core	3.49		
797.98	798.19	Flow base	0.21		

ODP Hole 642E					
Top Depth (m)	**Base Depth (m)**	**Lithotype**	**Unit thickness (m)**	**Core proportion**	**Flow thickness (m)**
798.19	799.00	Sedimentary layer	0.81		
799.00	803.42	Compound flows	4.42		
803.42	805.60	Compound flows	2.18		
805.60	807.54	Compound flows	1.94		
807.54	808.89	Flow crust	1.35		
808.89	817.19	Flow core	8.3	0.807393	10.28
817.19	817.82	Flow base	0.63		
817.82	826.50	Compound flows	8.68		
826.50	829.30	Sedimentary layer	2.8		
829.30	832.43	Flow crust	3.13		
832.43	838.35	Flow core	5.92	0.62119622	9.53
838.35	838.83	Flow base	0.48		
838.83	841.47	Compound flows	2.64		
841.47	843.93	Compound flows	2.46		
844.09	847.93	Compound flows	3.84		
847.93	851.23	Compound flows	3.3		
851.23	856.79	Compound flows	5.56		
856.79	863.81	Compound flows	7.02		
863.81	866.69	Flow crust	2.88		
866.69	869.97	Flow core	3.28	0.49848024	6.58
869.97	870.39	Flow base	0.42		
870.39	872.23	Flow crust	1.84		
872.23	879.26	Flow core	7.03	0.74	9.5
879.26	879.89	Flow base	0.63		
879.89	881.70	Flow crust	1.81		
881.70	885.31	Flow core	3.61	0.62456747	5.78
885.31	885.67	Flow base	0.36		
885.67	886.65	Compound flows	0.98		
886.65	888.51	Compound flows	1.86		
888.51	891.01	Compound flows	2.5		
891.01	894.00	Compound flows	2.99		
894.00	895.87	Flow crust	1.87		
895.87	907.38	Flow core	11.51	0.84322344	13.65
907.38	907.65	Flow base	0.27		
907.65	910.93	Compound flows	3.28		
910.93	913.17	Flow crust	2.24		
913.17	916.04	Flow core	2.87	0.52468007	5.47
916.04	916.40	Flow base	0.36		
916.40	923.49	Compound flows	7.09		
923.49	925.43	Compound flows	1.94		
925.43	927.64	Compound flows	2.21		
927.64	929.59	Sedimentary layer	1.95		
929.59	932.00	Flow crust	2.41		
932.00	935.40	Flow core	3.4	0.55105348	6.17
935.40	935.76	Flow base	0.36		

ODP Hole 642E					
Top Depth (m)	**Base Depth (m)**	**Lithotype**	**Unit thickness (m)**	**Core proportion**	**Flow thickness (m)**
935.76	940.09	Flow crust	4.33		
940.09	943.51	Flow core	3.42	0.41555286	8.23
943.51	943.99	Flow base	0.48		
943.99	949.94	Compound flows	5.95		
949.94	952.99	Compound flows	3.05		
952.99	953.64	Flow crust	0.65		
953.64	956.80	Flow core	3.16	0.7745098	4.08
956.80	957.07	Flow base	0.27		
957.07	961.43	Flow crust	4.36		
961.43	969.64	Flow core	8.21	0.63495746	12.93
969.64	970.00	Flow base	0.36		
970.00	974.40	Compound flows	4.4		
974.40	978.47	Compound flows	4.07		
978.47	979.68	Sedimentary layer	1.21		
979.68	986.16	Compound flows	6.48		
986.16	991.43	Flow crust	5.27		
991.43	997.35	Flow core	5.92	0.51388889	11.52
997.35	997.68	Flow base	0.33		
997.68	1001.49	Flow crust	3.81		
1001.49	1009.75	Flow core	8.26	0.65659777	12.58
1009.75	1010.26	Flow base	0.51		
1010.26	1011.46	Sedimentary layer	1.2		
1011.46	1011.96	Flow crust	0.5		
1012.08	1015.49	Flow core	3.41	0.77853881	4.38
1015.49	1015.96	Flow base	0.47		
1015.96	1016.64	Sedimentary layer	0.68		
1016.64	1021.13	Compound flows	4.49		
1021.13	1024.44	Compound flows	3.31		
1024.44	1025.95	Flow crust	1.51		
1025.95	1028.14	Flow core	2.19	0.53940887	4.06
1028.14	1028.50	Flow base	0.36		
1028.50	1029.10	Sedimentary layer	0.6		
1029.10	1035.51	Flow crust	6.41		
1035.51	1041.93	Flow core	6.42	0.48895659	13.13
1041.93	1042.23	Flow base	0.3		
1042.23	1043.72	Compound flows	1.49		
1043.72	1049.23	Compound flows	5.51		
1049.23	1051.94	Flow crust	2.71		
1051.94	1056.53	Flow core	4.59	0.57160648	8.03
1056.53	1057.26	Flow base	0.73		
1057.26	1061.91	Compound flows	4.65		
1061.91	1064.38	Flow crust	2.47		
1064.38	1067.63	Flow core	3.25	0.50309598	6.46
1067.63	1068.37	Flow base	0.74		

ODP Hole 917A

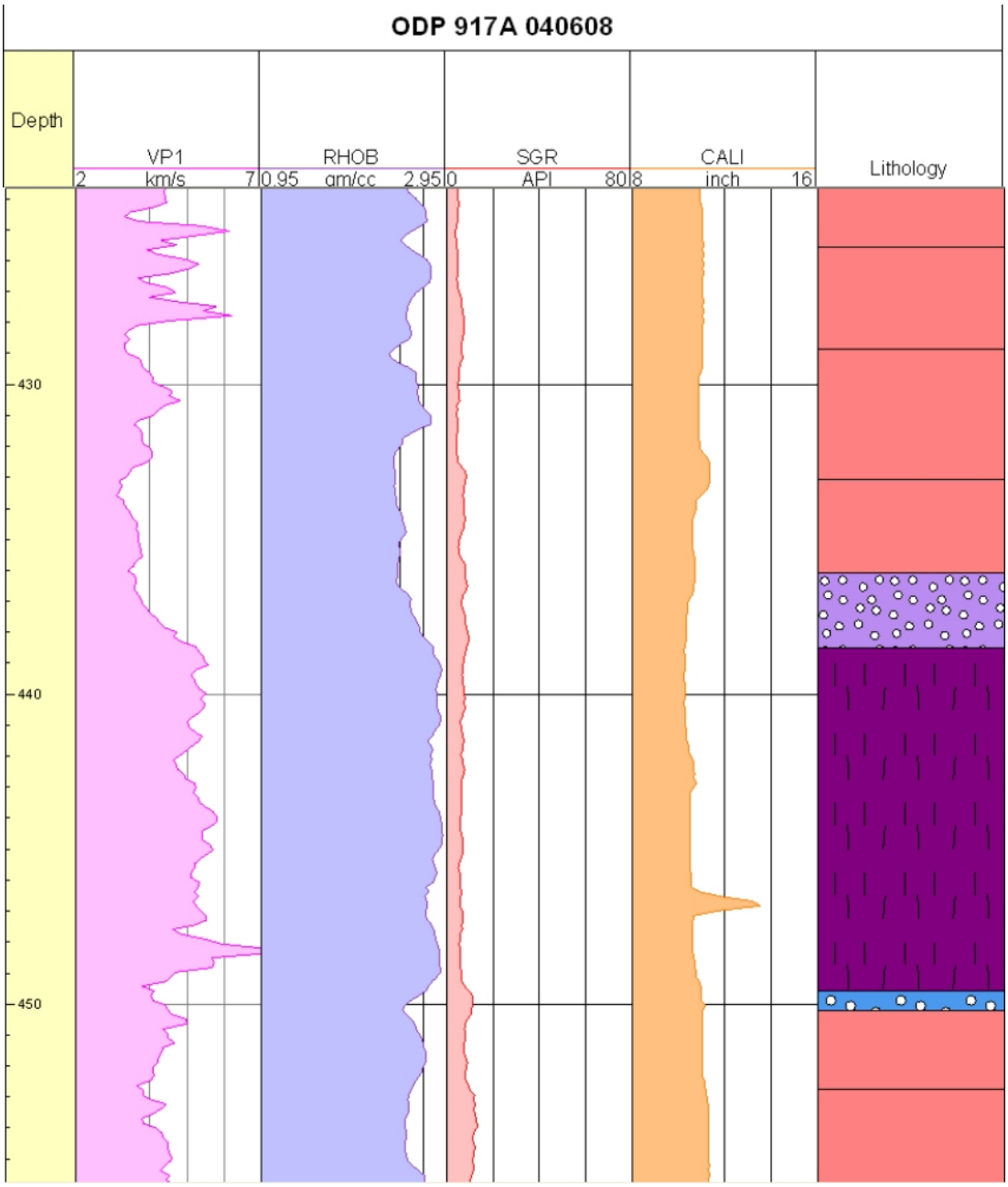

Sample data from ODP Hole 917A

ODP Hole 917A					
Top Depth (m)	**Base Depth (m)**	**Lithotype**	**Unit thickness**	**Core proportion**	**Flow thickness**
238.27	244.42	Compound flows	6.15		
244.42	250.77	Compound flows	6.35		
250.77	253.87	Compound flows	3.1		
253.87	259.19	Compound flows	5.32		
259.19	262.69	Compound flows	3.5		
262.69	266.26	Compound flows	3.57		
266.26	269.75	Compound flows	3.49		
269.75	270.92	Flow crust	1.17		
270.92	273.83	Flow core	2.91	0.670507	4.34
273.83	274.09	Flow base	0.26		
274.09	276.61	Flow crust	2.52		
276.61	315.04	Flow core	38.43	0.911311	42.17
315.04	316.26	Flow base	1.22		
358.77	359.88	Flow crust	1.11		
359.88	369.03	Flow core	9.15	0.851955	10.74
369.03	369.51	Flow base	0.48		
369.51	372.99	Compound flows	3.48		
372.99	380.49	Compound flows	7.5		
380.49	381.47	Flow crust	0.98		
381.47	388.51	Flow core	7.04	0.810127	8.69
388.51	389.18	Flow base	0.67		
389.18	394.66	Flow crust	5.48		
394.66	403.13	Flow core	8.47	0.578552	14.64
403.13	403.82	Flow base	0.69		
403.82	405.23	Compound flows	1.41		
405.23	413.01	Compound flows	7.78		
413.01	419.24	Compound flows	6.23		
419.24	423.21	Compound flows	3.97		
423.21	425.56	Compound flows	2.35		
425.56	428.85	Compound flows	3.29		
428.85	433.06	Compound flows	4.21		
433.06	436.09	Compound flows	3.03		
436.09	438.49	Flow crust	2.4		
438.49	449.58	Flow core	11.09	0.7843	14.14
449.58	450.23	Flow base	0.65		
450.23	452.76	Compound flows	2.53		
452.76	457.28	Compound flows	4.52		
457.28	458.83	Compound flows	1.55		
458.83	468.44	Flow crust	9.61		
468.44	474.47	Flow core	6.03	0.368132	16.38
474.47	475.21	Flow base	0.74		
475.21	478.13	Compound flows	2.92		
478.13	485.79	Compound flows	7.66		
494.41	497.98	Flow crust	3.57		
497.98	504.76	Flow core	6.78	0.634831	10.68
504.76	505.09	Flow base	0.33		
505.09	507.51	Sedimentary layer	2.42		

ODP Hole 917A					
Top Depth (m)	**Base Depth (m)**	**Lithotype**	**Unit thickness**	**Core proportion**	**Flow thickness**
507.51	513.19	Flow crust	5.68		
513.22	531.65	Flow core	18.43	0.751938	24.51
531.65	532.05	Flow base	0.4		
532.05	534.23	Compound flows	2.18		

Well 164/07-1

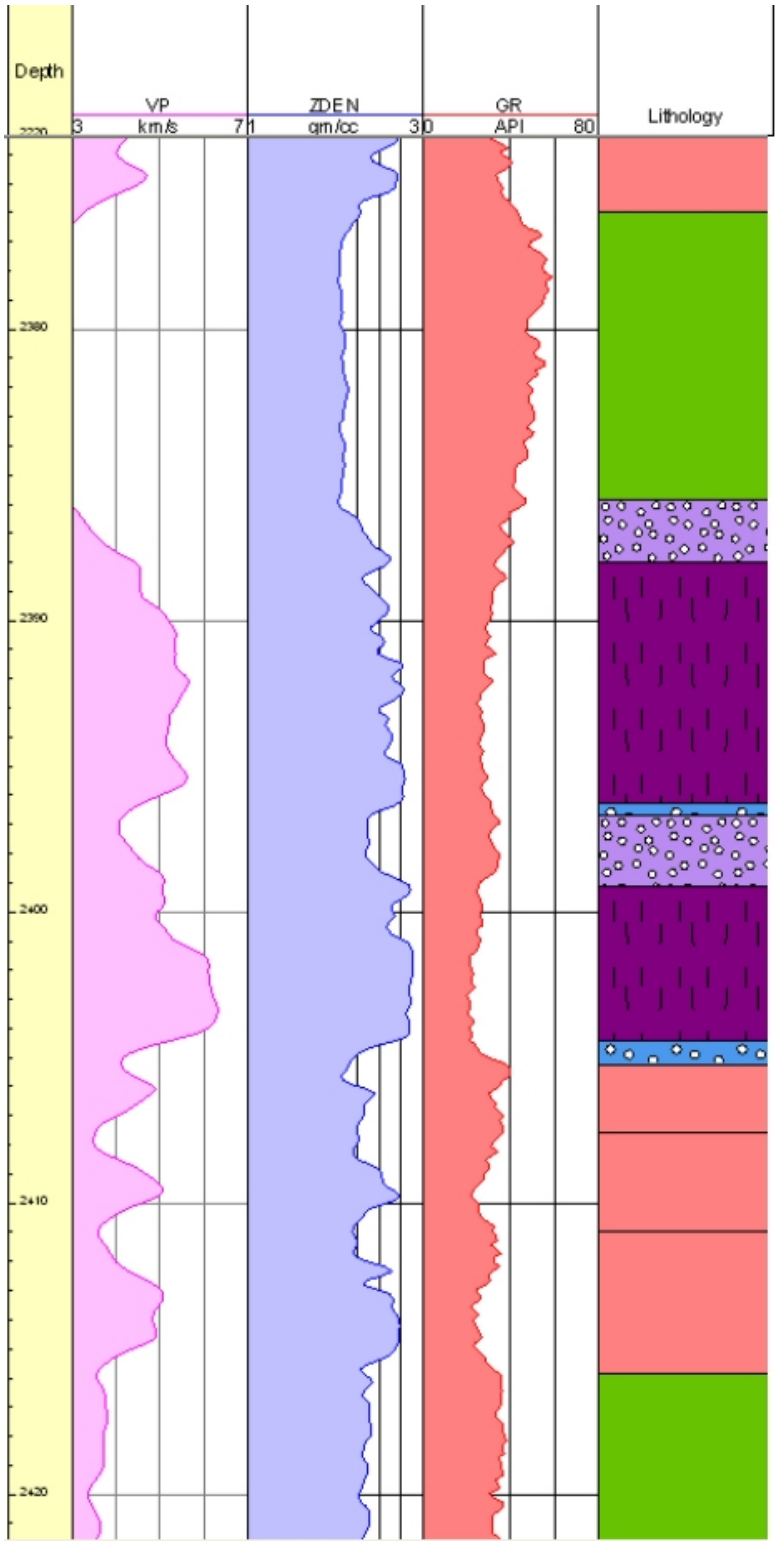

Sample data from Well 164/07-1

Well 164/07-1					
Top Depth (m)	**Base Depth (m)**	**Lithotype**	**Unit thickness (m)**	**Core proportion**	**Flow thickness (m)**
2242.60	2244.20	Flow crust	1.6		
2244.20	2258.27	Flow core	14.07	0.8674476	16.22
2258.27	2258.82	Flow base	0.55		
2258.82	2261.76	Compound flows	2.94		
2261.76	2262.72	Flow crust	0.96		
2262.72	2273.28	Flow core	10.56	0.88	12
2273.28	2273.76	Flow base	0.48		
2273.76	2277.76	Compound flows	4		
2277.76	2278.49	Flow crust	0.73		
2278.49	2285.91	Flow core	7.42	0.8451025	8.78
2285.91	2286.54	Flow base	0.63		
2286.54	2288.29	Flow crust	1.75		
2288.29	2298.42	Flow core	10.13	0.7744648	13.08
2298.42	2299.62	Flow base	1.2		
2299.62	2301.55	Flow crust	1.93		
2301.55	2311.13	Flow core	9.58	0.8010033	11.96
2311.13	2311.58	Flow base	0.45		
2311.58	2315.97	Compound flows	4.39		
2315.97	2319.64	Compound flows	3.67		
2319.64	2321.45	Flow crust	1.81		
2321.45	2332.03	Flow core	10.58	0.7978884	13.26
2332.03	2332.90	Flow base	0.87		
2332.90	2333.49	Flow crust	0.59		
2333.49	2341.48	Flow core	7.99	0.8741794	9.14
2341.48	2342.04	Flow base	0.56		
2342.04	2345.19	Compound flows	3.15		
2345.19	2347.65	Compound flows	2.46		
2347.65	2353.41	Flow crust	5.76		
2353.41	2370.88	Flow core	17.47	0.7148118	24.44
2370.88	2372.09	Flow base	1.21		
2372.09	2375.97	Compound flows	3.88		
2375.97	2385.85	Sedimentary layer	9.88		
2385.85	2388.00	Flow crust	2.15		
2388.00	2396.28	Flow core	8.28	0.7631336	10.85
2396.28	2396.70	Flow base	0.42		
2396.70	2399.11	Flow crust	2.41		
2399.11	2404.40	Flow core	5.29	0.6194379	8.54
2404.40	2405.24	Flow base	0.84		
2405.24	2407.57	Compound flows	2.33		
2407.57	2410.98	Compound flows	3.41		
2410.98	2415.83	Compound flows	4.85		
2415.85	2430.91	Sedimentary layer	15.06		
2430.91	2434.10	Compound flows	3.19		
2434.10	2440.33	Compound flows	6.23		
2440.33	2446.16	Compound flows	5.83		
2446.16	2449.06	Compound flows	2.9		

Well 164/07-1					
Top Depth (m)	**Base Depth (m)**	**Lithotype**	**Unit thickness (m)**	**Core proportion**	**Flow thickness (m)**
2449.06	2451.80	Compound flows	2.74		
2451.80	2456.53	Compound flows	4.73		
2456.53	2458.68	Flow crust	2.15		
2458.68	2464.60	Flow core	5.92	0.6742597	8.78
2464.60	2465.31	Flow base	0.71		
2465.31	2474.68	Sedimentary layer	9.37		
2474.68	2476.78	Compound flows	2.1		
2476.78	2479.72	Compound flows	2.94		
2479.72	2483.45	Compound flows	3.73		
2483.45	2491.98	Compound flows	8.53		
2491.98	2496.15	Compound flows	4.17		
2496.15	2498.97	Compound flows	2.82		
2498.97	2504.29	Compound flows	5.32		
2504.29	2528.47	Compound flows	24.18		
2528.47	2529.94	Compound flows	1.47		
2529.94	2534.51	Compound flows	4.57		
2534.51	2538.99	Compound flows	4.48		
2538.99	2544.99	Compound flows	6		
2544.99	2547.87	Sedimentary layer	2.88		
2547.87	2550.23	Flow crust	2.36		
2550.23	2559.67	Flow core	9.44	0.7369243	12.81
2559.67	2560.68	Flow base	1.01		
2560.68	2565.89	Compound flows	5.21		
2565.89	2569.81	Compound flows	3.92		
2569.81	2576.24	Compound flows	6.43		
2576.24	2580.61	Compound flows	4.37		
2580.61	2583.11	Compound flows	2.5		
2583.11	2588.19	Compound flows	5.08		
2588.19	2589.75	Flow crust	1.56		
2589.75	2596.28	Flow core	6.53	0.7412032	8.81
2596.28	2597.00	Flow base	0.72		
2597.00	2597.74	Flow crust	0.74		
2597.74	2608.90	Flow core	11.16	0.8985507	12.42
2608.90	2609.42	Flow base	0.52		
2609.42	2613.59	Flow crust	4.17		
2613.59	2620.79	Flow core	7.2	0.5882353	12.24
2620.79	2621.66	Flow base	0.87		
2621.66	2626.95	Sedimentary layer	5.29		
2626.95	2631.32	Compound flows	4.37		
2631.32	2636.40	Compound flows	5.08		
2636.40	2645.49	Compound flows	9.09		
2645.49	2650.73	Compound flows	5.24		
2650.73	2654.03	Compound flows	3.3		
2654.03	2657.48	Compound flows	3.45		
2657.48	2660.77	Compound flows	3.29		

Well 164/07-1					
Top Depth (m)	**Base Depth (m)**	**Lithotype**	**Unit thickness (m)**	**Core proportion**	**Flow thickness (m)**
2660.77	2665.74	Compound flows	4.97		
2665.74	2671.22	Compound flows	5.48		
2671.22	2672.92	Compound flows	1.7		
2672.92	2675.23	Compound flows	2.31		
2675.23	2678.12	Compound flows	2.89		
2678.12	2681.36	Compound flows	3.24		
2681.36	2683.02	Flow crust	1.66		
2683.02	2698.77	Flow core	15.75	0.8467742	18.6
2698.77	2699.96	Flow base	1.19		
2699.96	2705.13	Compound flows	5.17		
2705.13	2706.80	Flow crust	1.67		
2706.80	2720.32	Flow core	13.52	0.8223844	16.44
2720.32	2721.57	Flow base	1.25		
2721.57	2731.75	Compound flows	10.18		
2731.75	2739.26	Compound flows	7.51		
2739.26	2742.19	Flow crust	2.93		
2742.19	2767.54	Flow core	25.35	0.8660745	29.27
2767.54	2768.53	Flow base	0.99		
2768.53	2773.65	Compound flows	5.12		
2773.65	2783.30	Compound flows	9.65		
2783.30	2786.08	Compound flows	2.78		
2786.08	2793.94	Compound flows	7.86		
2793.94	2803.35	Compound flows	9.41		
2803.35	2811.37	Compound flows	8.02		
2811.37	2815.70	Compound flows	4.33		
2815.70	2822.10	Compound flows	6.4		
2822.10	2825.43	Compound flows	3.33		
2825.43	2829.04	Compound flows	3.61		
2829.04	2839.68	Compound flows	10.64		
2839.68	2844.57	Compound flows	4.89		
2844.57	2847.42	Compound flows	2.85		
2847.42	2854.13	Compound flows	6.71		
2854.13	2856.68	Compound flows	2.55		
2856.68	2866.04	Compound flows	9.36		
2866.04	2871.60	Compound flows	5.56		
2871.60	2874.26	Compound flows	2.66		
2874.26	2877.32	Compound flows	3.06		
2877.32	2889.82	Compound flows	12.5		
2889.82	2892.32	Compound flows	2.5		
2892.32	2894.28	Compound flows	1.96		
2894.28	2897.74	Flow crust	3.46		
2897.74	2904.28	Flow core	6.54	0.5989011	10.92
2904.28	2905.20	Flow base	0.92		
2905.20	2906.62	Sedimentary layer	1.42		
2906.62	2913.34	Flow crust	6.72		
2913.34	2932.32	Flow core	18.98	0.6988218	27.16
2932.32	2933.78	Flow base	1.46		

Well 164/07-1					
Top Depth (m)	**Base Depth (m)**	**Lithotype**	**Unit thickness (m)**	**Core proportion**	**Flow thickness (m)**
2933.78	2938.17	Flow crust	4.39		
2938.17	2951.34	Flow core	13.17	0.6994158	18.83
2951.34	2952.61	Flow base	1.27		
2952.61	3206.57	Hyaloclastite	253.96		

Appendix 3: Workflows

These workflows give exact commands used in the software described in the main text, and an overview of details of how to capture laser scan data.

3.1 How to scan with the Riegl Z420i laser scanner

3.1.1 Setting up the scanner

1. Set up tripod, make sure it is level.
2. Open scanner box, attach handle to back. Put scanner on tripod, make sure it is still level. Don't put fingers on the scanner lenses
3. Tilt scanner to allow easy attachment of cables and camera. Attach camera to scanner, scanner to battery, scanner to laptop, camera to laptop.
4. Turn on battery and laptop, wait for scanner to turn.

3.1.2 Positioning the reflectors

- Choose type depending on distance from scanning position. Don't forget the 2 on the box.
- Don't put reflectors directly behind the handle.
- Think about the angle of the scanner, and where subsequent scans will be.
- Try to get a wide angle of coverage
- Nearby reflectors are good for tying in photos, more distant ones are good for tying scans together.
- Can use other things instead of reflectors if you know exactly where they are – e.g. fence post. Fine scan them.

3.1.3 Scanning

1. Open the default project C:/documents and settings/rrguser/My Documents/riegl scans/default_grl_z420i_994790_nikond70_14_85mm
2. Save the project with a new name. This automatically creates a new folder.
3. Set up a new tripod position. Right click on Scans – New scanposition. For the first tripod and scanner positions, call this TriPos1_ScanPos1. On the Scaling Correction tab, select the Z420i and put in the temperature as 15ºC.
4. Right click on this new scan position – New single scan. In the next window, click on Panorama. This gives 2 million points and takes 4 minutes. Use the resolution values it suggests. Go! [Beam widening – this defocuses the laser so that there are no gaps between the beams. If small reflectors are far away, you might miss them e.g. 5cm reflectors at 100m. However, this also gives a smaller range.]
5. At some point, a new mounting calibration must be created. Calibrations – Mounting – 14mm. Right click on this – new mounting calibration – import from the default project or the current project. Ok – should appear in the list of mounting calibrations. Rename it to TriPos01_14mm or similar depending on camera lens and tripod position.

6. Take photos. Turn the camera on, take the lens cap off. Right click on the panorama scan – Image acquisition. Change the mounting calibration to the one you just created. Go!
7. Find the reflectors. Right click on the panorama scan – Find reflectors. Use the default values – 50% sensitivity, 0.100 threshold. Look at the panorama scan; check that you can see all the reflectors. Check that they are all in the tiepoint list (TPL_SOCS). If there are extra, delete them from the tiepoint list. If one is missing, find it on the panorama scan and create a new tiepoint (left click on position, right click and add to TPL). If you still can't find them, change the sensitivity and threshold. If this still doesn't work, fine scan area where reflectors are. Make sure you don't remove existing tiepoints.
8. Fine scan the reflectors. Go to the TPL; find the button that says "Finescan selected tiepoints". As it runs, check that it's finding the right things. If not, change the sensitivity or create them yourself.
9. Detailed scan. Right click on the panorama scan – New single scan. Alt – click – drag over area of interest. Change the resolution based on the time available, this is displayed on the right of the window. Press the = button to get the vertical and horizontal resolution the same. Go!

3.1.4 Tilting the scanner

1. Tilt the scanner to the required angle. Think about the path the scanner will take when setting up reflectors.
2. Right click on Scans – New scanposition. On the tilt mount tab, make sure the tilt mount is ticked. Assign tilt mount.

A new mounting calibration is only needed if the camera has been removed.

3.1.5 Improving precision

Instead of New single scan, use New scansequence. Generally, 3 or 4 are useful. Only scan a small area. Again, the resolution is dictated by the amount of time available for the scan.

3.2 Data Processing

1. Copy data and work on the copy.
2. Open project.rsp from the copied folder.
3. In the project manager bar, find the digital photos. (SCANS – name of scan position - SCANPOSIMAGES)
4. Click on the “Show TPL SOCS” button – it’s black and white, on the top right.
5. Zoom in to the reflector. Left click on the centre of it. Right click on the cross that appears, then “Add point to TPL”. Rename the point to the same name as the reflector tiepoint (SOCS_xxx) and choose the appropriate type of reflector.
6. Shift and drag to select both the new point and the original point that the scanner found. Right click – “Link tiepoints together”.
7. Go to the mounting calibration that was created during setup (Mount_Tripos or similar). Right click – attributes – readjust. Try and minimise the pixel distance. Aim for a mean around 1, and a maximum less than 2. Usually, adjusting the rotation and translation, and least squares fitting will give the best results.
8. Right click on the scan. Colour from images. Task Manager tells you when big tasks like this are done.
9. View the scan! (3D, true colour, linearscaled). F11 gives a full screen view.

3.2.1 Processing scan sequences

Processing the data is generally the same as you have already done previously, but there is one specific thing in relation to "Scan Sequences" (remember, we used "Scan Sequences" rather than "Single Scans" for the detailed data capture from Tripos1 and Tripos3).

Before you can add colour to a Scan Sequence, you need to "resample" it to average out the individual scans in the sequence. Right-click and choose "Resample...". See attached JPEG for the suggested settings to use. This produces a new "average" scan which you can colour as before.

3.2.2 Merging scans

- Use reflectors that appear in both scans (at least 5)
- Each scan position has its own coordinate system (SOCS). The camera position is matched to this by a transformation matrix.
- When scans are merged, one of these SOCS is used as the project coordinate system (PRCS). Other scans are converted to this using another transformation matrix.
- Another transformation matrix takes you to a global coordinate system (GLCS).
- Scans can either be merged using their geometry (default) or by labelling the reflectors with a unique name.
- SOP = scanner’s own position (matrix from SOCS to PRCS). COP = camera’s own position. POP matrix takes us to the global coordinate system.

1. Take a copy of what has already been done and rename it.

2. Right click on the first scan, define it as registered. A globe icon appears. This is now PRCS.
3. Use the tiepoint list to define which reflectors to tie between scans. Make sure all the reflectors are listed as the correct type (cylinder, flat etc)
4. In the second scan TPL, click the "Find corresponding points" button. Mode – Minimize error (use by name if this doesn't work). The program will rename the tiepoints. Match at least 5, error up to 10cm.
5. Look at the error and standard deviation, they should only be a few cm.

3.2.3 Tidying the data

- Make sure you can see all the toolbars.
- Use the coloured data from the detailed scan.
- Changing the background colour and/or the point size can be useful.

In selection mode, you can't change position but can select data. You don't want to change the raw scan, so do the following:

1. Select the area you want to work with (Select rectangle/polyline)
2. Create new polydata object.
3. Drag the polydata object from the project manager window to a new view.

Pick surfaces using the polyline tool. Left click to add a node; right click to finish the line.

Use the Octree filter to reduce the number of points (using e.g. 5cm)

3.3 How to pick lines in a drawing package and use them in RiScan Pro

Sometimes, it's not very easy to see the features you're interested in on a scan, but you can see them very well on the photos. This workflow explains how to get lines picked on photos onto your scan. It's probably not so useful for structural work where high precision is important and outcrops are more complex shapes, but works well for picking out lava flow tops and bases on fairly flat outcrops.

1. Import your scan photos into CorelDraw. They're found in the SCANS/TriPos01_ScanPos01/SCANPOSIMAGES directory.
2. Rotate them so they're upright. Mark on your lines – the Polyline tool is good for this. A width of 4pts and a bright colour usually works well for me, but experiment.
3. Draw a rectangle around the edge of the photo. Change the outline thickness to None and the fill to None. Delete the photo. Save this.
4. Open Corel PhotoPaint. Open the scan photo that you've used to pick the lines. Go to File – Import then select the .cdr file. Set the image height to 2000 pixels and maintain aspect ratio. It should have the settings shown in Figure 1.
5. Click OK then click anywhere on the photo. It should now look like Figure 2.
6. Go to Object – Combine – Combine all objects with background. Save the file with the settings in Figure 3.
7. When you've done this for all your photos, go back to RiScan. Select Colour from images as normal. You should get something that looks like Figure 4. You can now use this to pick your lines in RiScan, so you get the detail from the photos and the 3D shape from the scan.

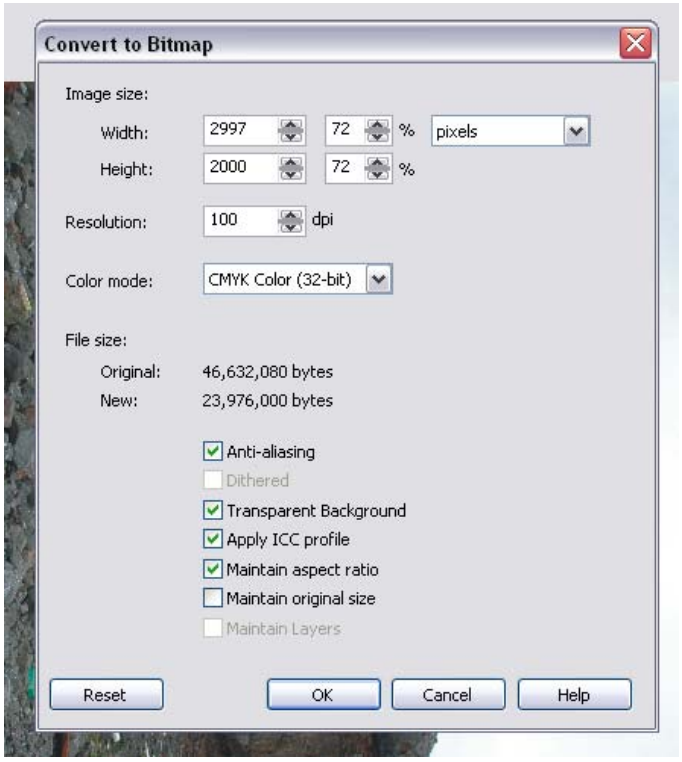

Figure 1

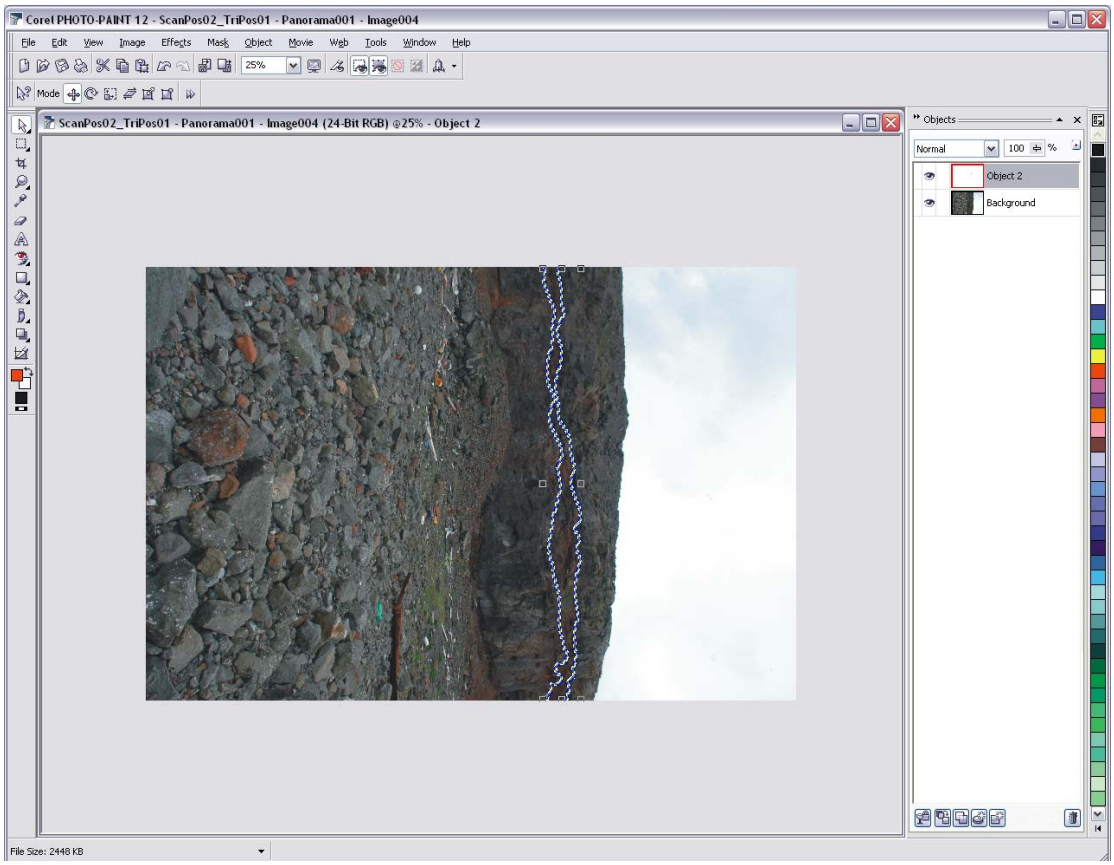

Figure 2

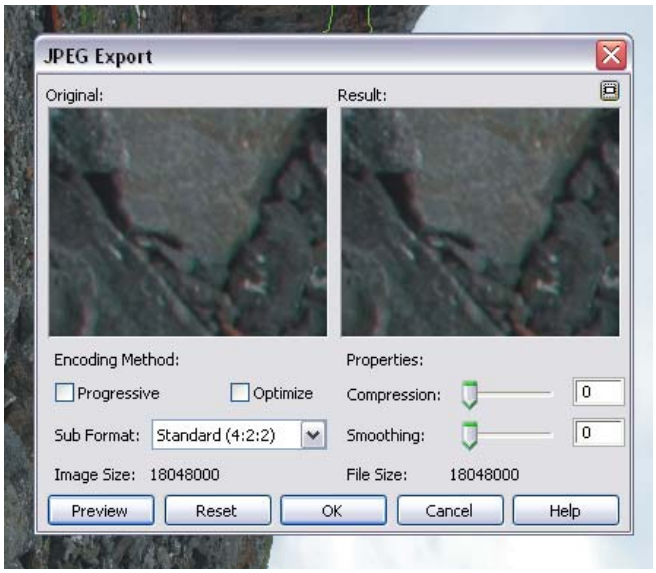

Figure 3

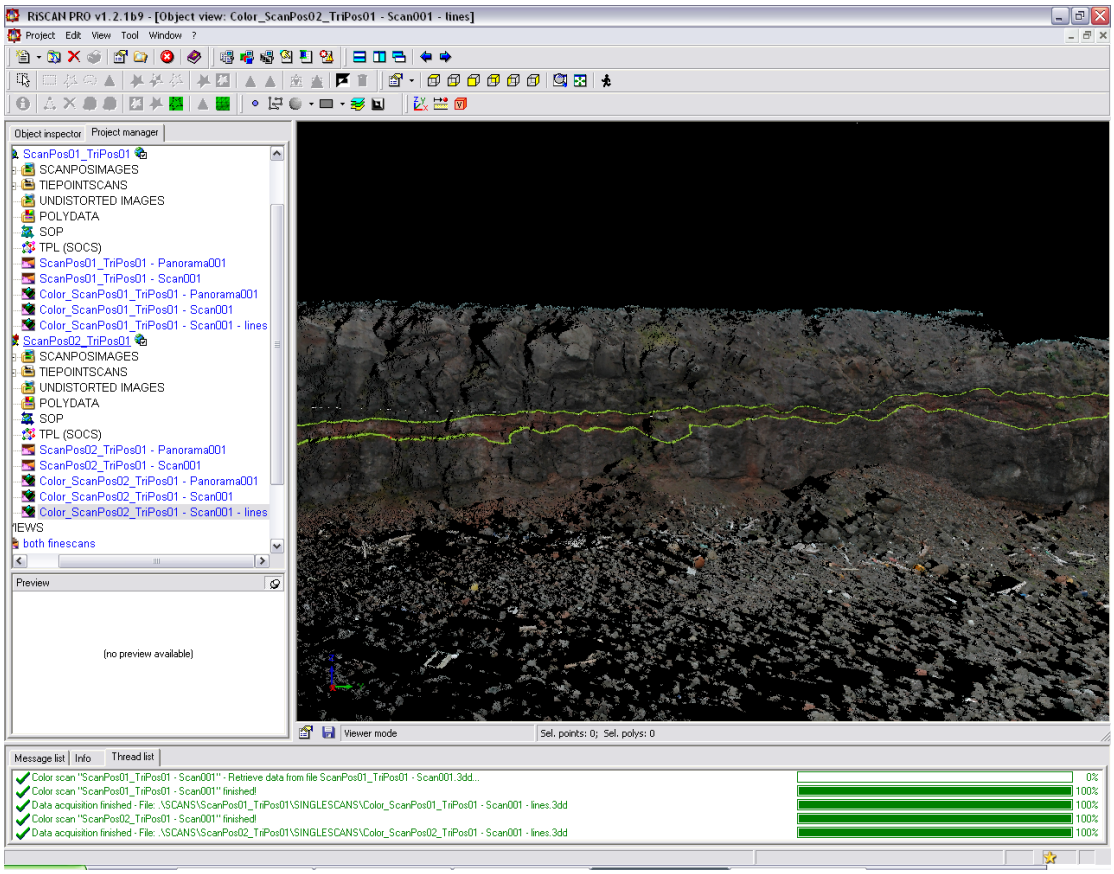

Figure 4

3.4 Surface building using GSI3D

Export the interpreted lines from Riscan Pro as Ascii files, then do the following:

In ArcGIS:

Make a buffer line around the interpreted line following the model space.

- To make buffer: Toolbox – Analysis tools – Proximity – Buffer.
- Set to 20m, dissolve type = all.
- Seems to only work if based on 2d line.
- To export as 2D shp files, right click on Toolbox. Environments – general – disable output z values and m values.
- Toolbox – data management tools – features – copy features: gives 2D shape.

In GOCAD:

Make a rough surface:

- Import buffer curves – cultural data.
- Make sure curves are one part – merge all parts
- Structural modelling – data management. Set data type as fault centre lines. Advanced – set extent (-10 to 10m) and dip – measure from scan.
- Fault modelling – build surfaces. Create new outline, fit only the outline lateral extension. 0.5m size seems to not take too long/crash repeatedly.
- Copy surfaces before cutting.
- Surface – edit – cut - by curves. X,Y = 0; Z = 50. Tick two ways box.
- Show parts. Edit – part – keep selection.
- Apply script to move all surfaces to positive values.
- Save objects as – export surfaces as .ts files

In GSI3D:

Follow standard steps for constructing models as described in the manual:

- Set up GVS and GLEG files
- Create new geological units for each surface.
- Import Gocad surfaces as base
- Draw line for cross-section.
- Construct cross-sections for all units
- Calculate units to obtain the 3D model.

3.5 GMT workflow for spectral analysis

The following workflow was used in GMT to produce the power spectra in Chapter 6. 1D profiles were exported from Riscan Pro or Global Mapper as ASCII files, and the following commands were used:

`sample1d` samples the data at a constant interval, for use when the data are not sampled at regular intervals.

`spectrum1d` produces a power spectrum for a 1D profile.

`minmax` returns the minimum and maximum data values.

`psxy` plots a PostScript image.

The commands take the following arguments:

```
sample1d *.txt -Fc -H1 -I0.05 -S0.0 -T0 >*dump.txt
```

-Fc: use cubic spline

-H1: there is 1 header row

-I0.05: sampling interval (in metres in this case).

-S0.0: start at 0.

-T0: Set column number of independent variable (x).

```
spectrum1d *dump.txt -S512 -C -H1 -D0.05 -N*spec
```

-S: segment size – bigger for more points.

-C: read first two columns.

-H: input file has a header

-D: sampling interval in metres

-N: name of output file.

```
minmax *spec.ypower
```

```
psxy *spec.ypower -JX20l/20l -Rmin_col-1/max_col-1/min_col-2/max_col-2 -B1g1/1g1 -Sc0.1 -Ey >*_ypower.ps
```

-Jx: x-y plot, l=log, 20=size of box

-R: range for axes – make sure everything fits

-B: boundary/tickmark annotations

-Sc: Symbol is circle; size.

-Ey: y-axis error bars.

-K: keep open for more to be added later

-O: overlay onto existing plot (needs >> to same file name).

-G255/255/255: fill colour of circles.

3.6 GOCAD workflows for Chapter 7

3.6.1 Method for tabular model

1. Import surfaces.

2. Translate surfaces in Z to desired spacing (`Surface – Compute – Apply script on object`). e.g. Z=Z-30;

3. Build voxet. `Voxet – New From Corners`. Put in desired boundaries, making sure it is smaller than the surfaces in X and Y, and bigger in Z. Decide on cell size and put in number of nodes accordingly.

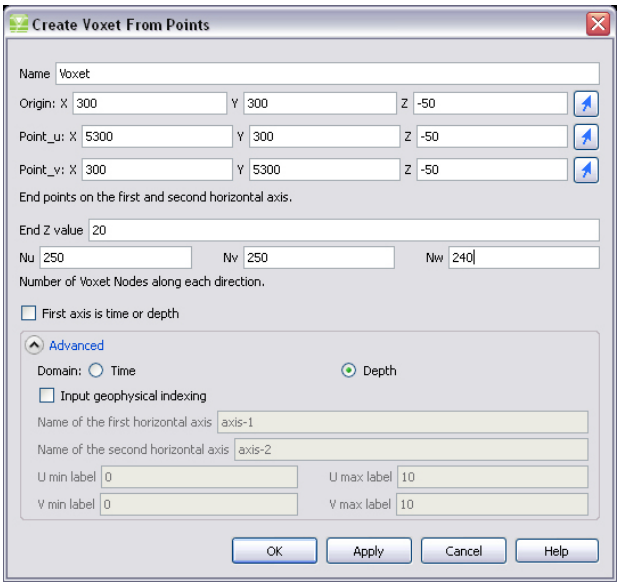

4. Right click on the model within the Voxet you have made, `Model – Add surfaces`.

Voxet with surfaces:

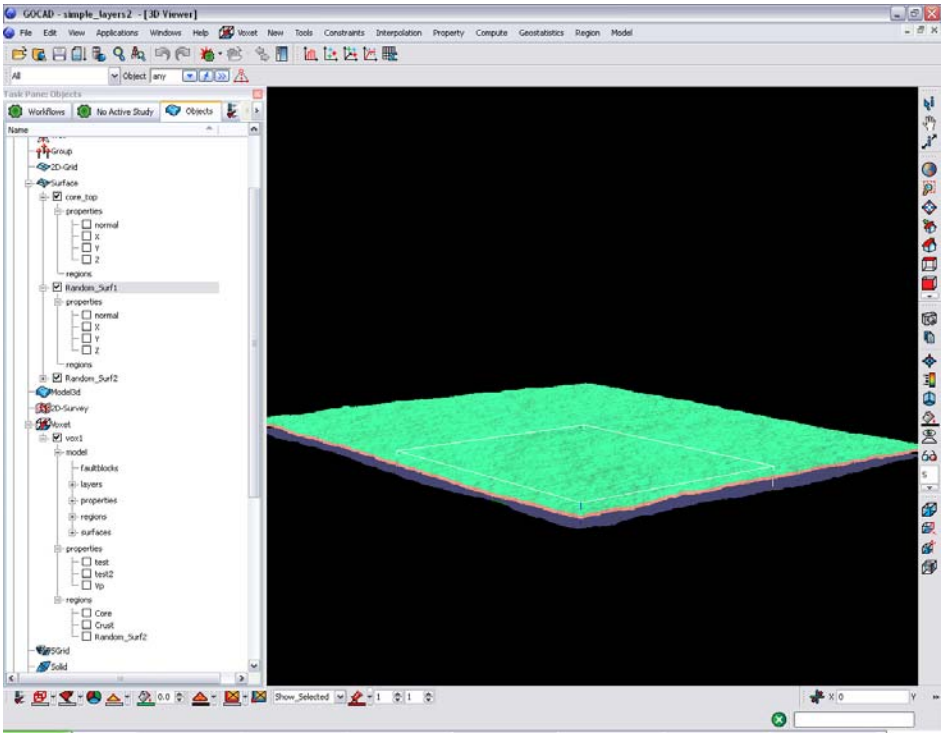

5. Right click on voxet model – `Build.` Switch off Layers only option.

6. Find desired regions within Voxet menu, not Model submenu. Rename them to something useful. 2 regions shown below.

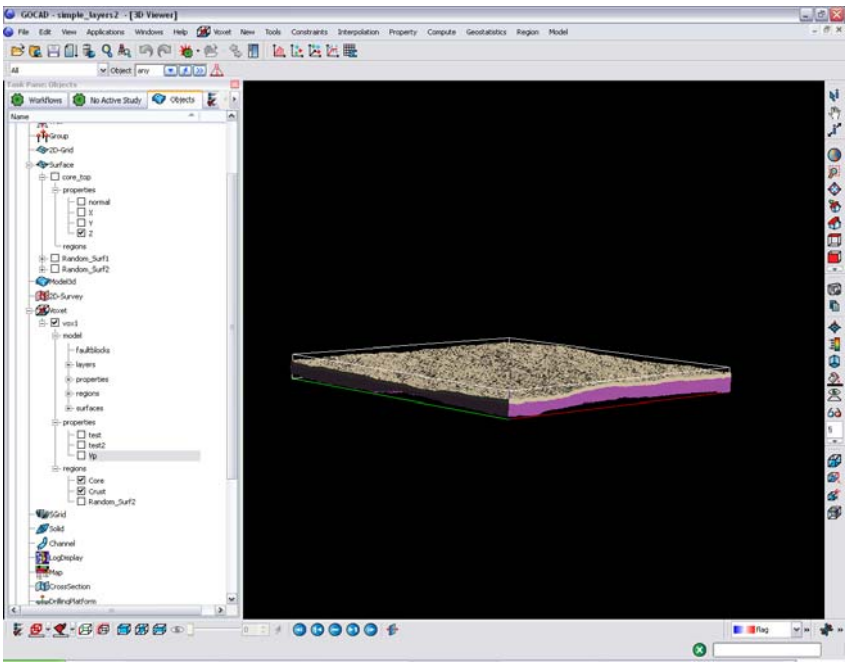

7. Right click on properties within Voxet menus – Create.

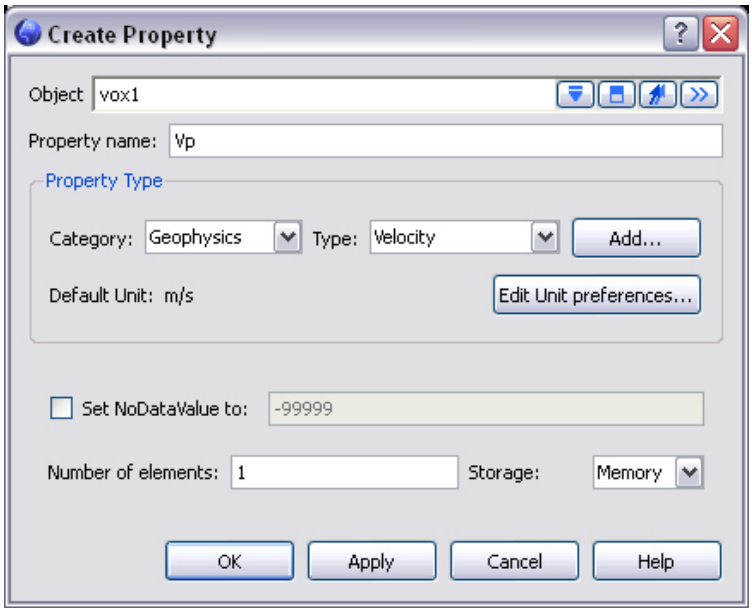

8. Apply script to generate desired property on desired regions (e.g. crust, core):

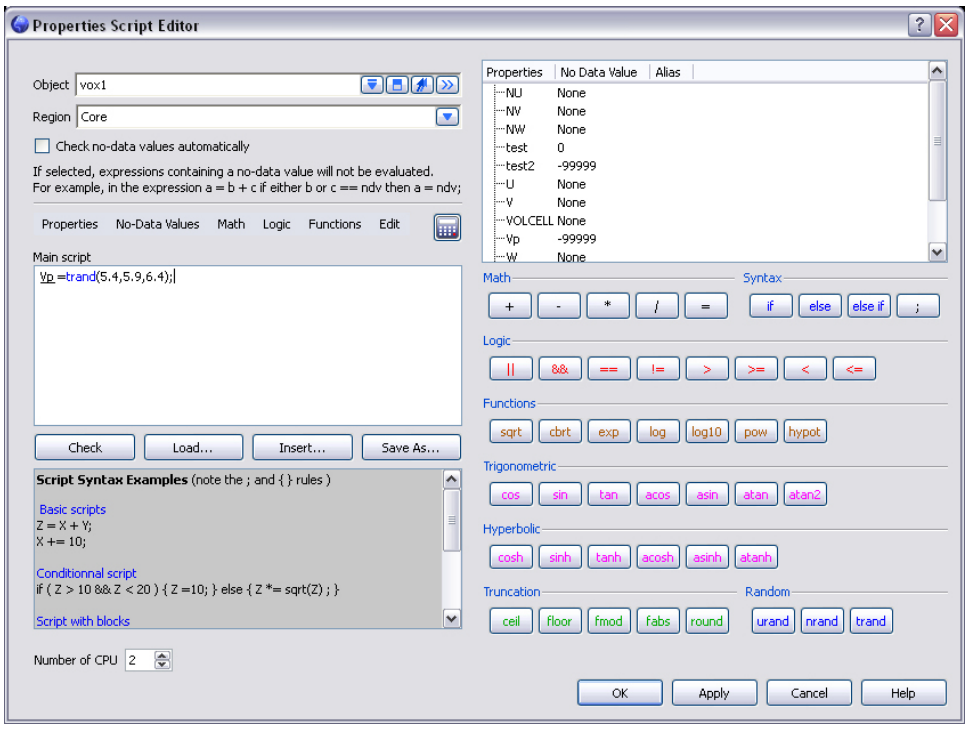

To create a trend, create a new property (e.g. `calcdist`) then `calculate the distance from a surface`, feeding the answer into this new property. To normalise this, divide by the distance between surfaces (e.g. `reldist=calcdist/3.5;`). Then, use this to calculate Vp.

9. Repeat for other regions.

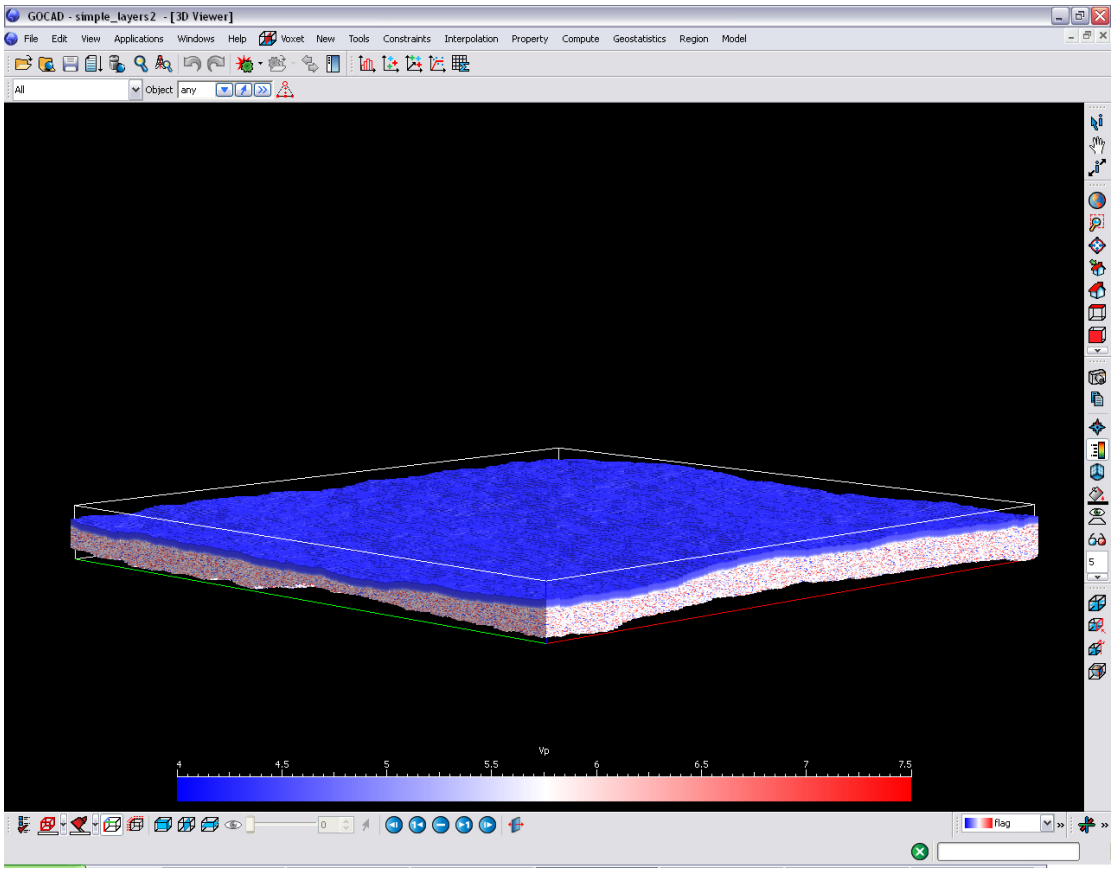

3.6.2 Method for adding random noise

1. Import GSI3D surfaces, clean up if necessary.
2. Import random surfaces.
3. Right click on GSI3D surface – `Split all` to create smaller triangles. Repeat a couple of times.
4. Create a new property on the GSI3D surface e.g. `rough.`
5. `Property – Transfer vertically.`

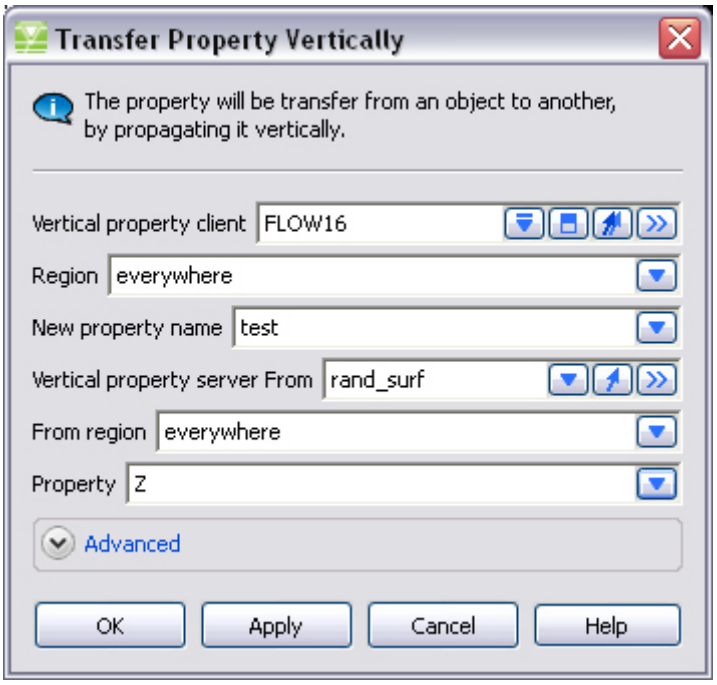

6. Apply script on GSI3D surface: `z=z+rough;`
7. Repeat on all surfaces.

Memory saving tips: the surfaces are always loaded into memory so delete random surfaces when finished. Keep the regions turned off (invisible) when calculating.

Appendix 4: DVD files

The following files are included on a DVD:

SEGY files: GOCAD voxets exported as .sgy files. Tabular models will stack up, with 3 at the top, then 4, then 5 at the base.

GOCAD models: Compound GOCAD models with rough surfaces

GSI3D models: Completed GSI3D files and stand-alone Subsurface Viewer models.

Laser scans: data from Ljosa Quarry and Talisker Bay.

Borehole interpretations: spreadsheet of the data in Appendix 2.